NATIONAL TECHNICAL UNIVERSITY OF ATHENS

AERODYNAMICS LABORATORY

A THESIS SUBMITTED FOR THE DEGREE OF DOCTOR OF ENGINEERING

Hovering helicopter interaction with the ground and bluff bodies: A CFD based investigation

Theologos Andronikos

23 February 2022

Hovering helicopter interaction with the ground and bluff bodies: A CFD based investigation

Ph.D. Thesis
Theologos Andronikos

Examination Committee:

1. K. Belibasakis, Professor, NTUA, School of Naval Architecture and Marine Engineering

2. D. Bouris* Associate Professor, NTUA, School of Mechanical Engineering

3. K. Giannakoglou, Professor, NTUA, School of Mechanical Engineering

4. I. Nikolos, Professor, TUC, School of Production Engineering and Management

5. G. Papadakis, Assistant Professor, NTUA, School of Naval Architecture and Marine Engineering

6. V. Riziotis (Supervisor) *, Associate Professor, NTUA, School of Mechanical Engineering

7. S. Voutsinas *, Professor, NTUA, School of Mechanical Engineering

 * Member of the Advisory Committee

Acknowledgements

At the beginning of my PH.D. thesis I was under the misapprehension that my accomplishments would be mine alone. The truth is that I would not have succeeded if there were not some important people in my life.

First and mostly I would like to thank my supervisor Associate Professor Vasilis Riziotis. He gave me an amazing opportunity almost 7 years ago and during these years his help was priceless and with no limits. He was always by my side along the way, supporting me and inspiring me. Besides a great professor and scientist, his is also a great teacher, since he is the reason I decided to get involved with fluid dynamics in the first place. My admiration of his personality, his knowledge and his mentality can not be expressed.

Next, I would like to thank the other two members of the advisory committee, Professor Spyros Voutsinas and Associate Professor Demetri Bouri, for their useful comments that helped in shaping my thesis.

A special thank you is in order for Professor Spyros Voutsinas. When the knowledge meets the wisdom a mentor is created. All these years, he was there for me either as my harshest critic or my biggest supporter. Our talks were endless, both on professional and personal level. His advises are so helpful and his interest is genuinely focused on the progress and improvement of all of his students.

I also express my gratitude to the members of the examination committee for reading the thesis and making constructive comments on the presented work.

A really important person without whom I could not grow as a scientist and as a person is Professor George Papadakis. His help was of the most importance since my thesis is based on the incredible work of his.

During all these years at the Laboratory of Aerodynamics, I was lucky enough to meet such great co-workers that I can also call them friends: Marinos Manolessos, Dimitris Manolas, Kostas Diakakis, John Prospathopoulos, Petros Chasapogiannis, Giannis Serafeim, Dimitris Ntouras, Nikos Spyropoulos. They all helped me in many ways and I can not thank them enough. Special thanks to Dimitris and Nikos for the help they provided with grid construction.

Besides my friends from the Laboratory I would like to thank all of friends for their unlimited support and faith. I know that I was not an easy friend.

At last, I would like to thank my family who is putting up with me for many many years. I deeply appreciate their support.

Finally I would like to thank Nefeli. The last 4 years I was encouraged, sustained, inspired and tolerated by her and I feel blessed that I have her in my life.

This page intentionally left blank.

Contents

List of Figures

viii

xi

This page intentionally left blank.

List of Tables

This page intentionally left blank.

Abstract

The interactional phenomena occurring when a helicopter hovers in proximity to the ground and to bluff bodies are addressed in this thesis. The work is motivated by the limited bibliography on this topic. Several surveys have been conducted both experimental and computational, however a systematic work that categorizes and classifies the interaction between the rotor and the ground/bluff bodies is missing. The present work takes into consideration several experimental campaigns, analyzes the results and then by using tools of different fidelity reproduces measured conditions. Through this process solid conclusions are extracted, substantiated both by experimental and computational evidence.

When a helicopter takes off or lands, its wake interferes with the ground and obstacles. This interaction, depending on the height-to-rotor diameter ratio, causes the altering of the rotor loading and performance as compared to the unconstrained case and gives rise to the development of a complex outwash flow in the surroundings of the helicopter. When a helicopter hovers outside the ground effect, the jet flow of the main rotor and the strong tip vortices of the wake travel without constrain below the rotor. As the rotor approaches the ground or an obstacle the jet flow and the vortices interact with the surrounding environment. This leads to the development of boundary layers on the surfaces of solid boundaries which eventually change the flow field. In these cases different shear layers interact with each other causing the formation of strong vortex structures that remain close to the helicopter.

The above phenomena are investigated by three different experimental campaigns conducted by Politecnico di Milano, the University of Glasgow, and ONERA. The test rigs resemble to each other but differ in certain parameters (rotor and obstacle dimensions, rotational speed, etc.). The helicopters that are used, are Mach scaled models leading to relatively low tip Re numbers (below 300000).

To complete the classification of the interactional phenomena, measurements are compared against numerical predictions. Two different tools have been used. The first is a medium fidelity potential solver in which solid boundaries are treated as inviscid surfaces and the wake is modeled by free vortex particles. The velocity field is obtained by solving with a particles mesh technique two Poisson equations. This solver is used for simulating the majority of the cases because of its computational efficiency. Comparison between the predictions of the potential solver against the experiments revealed the limitations of the solver due to its inherent inviscid character. However, these limitations confirmed the first conclusion from the experimental data, which dictates that viscous effects are dominating the flow, especially when the rotor is in close proximity to the ground and the obstacle.

In the direction of overcoming the above limitations and further elaborating the analysis of the interactional phenomena, a high fidelity hybrid solver is exploited. The hybrid solver couples a Lagrangian flow solver that covers the entire flow field with overlaid Eulerian solutions defined on confined regions around the contained solid boundaries. In this manner all boundary conditions are met (both on the solid and the far field boundaries). Simulations of the hybrid solver are performed in selective cases (those that the potential solver could not reproduce) as the computational cost of the model is significantly higher than that of the potential solver. Comparison of the hybrid model predictions to the experimental data, confirmed the original hypothesis and helped to dive into deeper analysis of the physical mechanisms that dominate the flow around a hovering helicopter in proximity to solid boundaries.

Chapter 1

Scope and Content

Chapter 1 provides an overview of the current state of art in helicopter-solid boundaries interactions and by that identifies the aspects of the problem that remain open, substantiates the significance of the thesis, justifies the selection of the aerodynamic tools for the analysis and outlines the novelties of the thesis.

1.1 State of the art in helicopter-ground- obstacle interaction

The physics of the flow around a helicopter is complicated and in many terms challenging to predict. The wake jet flow, which is proportional to the thrust exerted by the rotor, along with the strong vortices emitted at the tips of the blades, create a complex flow field downstream of its flight path. The navigation of the helicopter is achieved through the adjustment of several control angles handled by the pilot. By collectively pitching the blades more thrust is produced, while cyclic pitching affects the distribution of the thrust over the rotor disk. It creates an uneven force distribution that changes the moments of the helicopter. The entire flight envelop depends on the handling of the above angles, in order for the dynamic system to reach a flight equilibrium or to follow a desired flight path. The control of the helicopter by the pilots is performed by continuously trimming those angles. Assuming that the flow conditions are always changing (changes in wind velocity, turbulence, density of the air), the pilot must trim the helicopter in order to maintain the desired flight path.

When a helicopter executes hover flight during takeoff and landing, the flow field that is developed in the wake of its main rotor is affected by the blockage of the ground. The starting vortex ring of the rotor impinges on the ground and thereafter a so called "ground vortex" is formed that moves outwards forming an outwash flow. The formation and the intensity of the ground vortex depend on several parameters such as the helicopter distance from the ground, the wind

velocity and direction, if any, and the thickness of the boundary layer on the ground. The presence of the ground near the rotor has been known to alter the aerodynamics of the rotor In Ground Effect (IGE) as compared to Out of Ground Effect (OGE) and gives rise to performance benefits (reduced power consumption for given thrust) however there are also reports of operational and handling issues [1].

Helicopters are largely employed in missions within confined areas, in proximity to natural or man-made obstacles. Under such flights conditions, interactional phenomena take place that give rise to the development of an unsteady pressure field over the obstacle. Especially when referring to flight above residential areas, the transient behaviour of the helicopter may affect safety and noise emissions the comfort of the inhabitants. Moreover, helicopter rotor loads are affected with subsequent implications on handling qualities and pilot's workload.

These interactional phenomena, as well as the parameters of the problem that are important for the design of helicopters, have not been studied in detail by the helicopter community. The importance of such interactions on flight safety and public annoyance, as well as of the existing knowledge gap on the topic, led GARTEUR to form a specific action group, AG-22 [2] that started in 2014 and lasted four years. In this context the loading on the building, the stability and piloting quality of the helicopter along with the safety margins to be set on the distance between the helicopter and the building were investigated. The work presented in this thesis has been performed in the framework of the above joint action and shares measured data from experimental test campaigns conducted by the participating institutes within the group. Within the group, computational tools of varying fidelity and wind tunnel experiments were employed with the aim to unravel the complex flow field and characterize the loads of a helicopter rotor flying at low altitude, in close proximity to well shaped obstacles in addition to ground effect. A number of wind tunnel test campaigns were performed as part of this action group [3], [4], [5], while one of them, was conducted in the atmospheric flows test section of Polimi's wind tunnel, addressing the pure ground effect problem.

Within this action group and afterwards, measured data were used for the detailed/thorough validation of simulation tools of varying complexity and fidelity. Several studies were conducted using potential solvers such as [6], [7], [8] and [9]. Among them Tan et al. [6] used a vortex particle method [10] coupled with a viscous boundary model developed with the aim to investigate the interaction between the rotor and the obstacle/ground. Within this viscous boundary model [11], [12], [13] the non-slip and non-penetration boundary conditions are satisfied on the obstacle and the ground. Model predictions of loads compared well against measurements [4], although the model could not sufficiently resolve the flow field in the vicinity of the obstacle, due to limitations of the viscous boundary model. Another computational study took place at DLR. Schmid used an in-house panel code. It is a free wake panel code solving the potential flow equations and as-

suming the fluid incompressible and inviscid [14], [15], [16]. Predictions concerned the experimental test cases from Polimi wind tunnel campaign[3] and included simulation results with and without incoming wind (windy and non-windy conditions). Comparison to measurements indicated some deviations in the loads that were attributed due to the inviscid character of the model, even though the overall trend of the loads variation was well captured. The work done by Andronikos et al. [8] and [9] compared predictions of a potential free vortex particle wake model [17] coupled with a particle mesh solver [18] against experimental data of [3], [4], [5]. As in the work by Schmid, the trends of the load variations were captured well, while differences were again noted in cases viscous effects became dominant. The main advantage of the above two developments was their low computational cost despite the high number or rotor revolutions (at least 40) that were needed in order to obtain representative average rotor loads.

In addition, two numerical studies were conducted using standard URANS CFD models. Gibertini et al. [19] used ROSITA [20] an Eulerian grid-based method coupled with an unsteady Actuator Disk model. The results were in very good agreement with measurements concerning both the loading on the rotor hub and the flow field. Similar conclusions were also drawn from the work of Chirico et al. [21]. Chirico also combined a similar CFD with the Actuator Disk model (HMB) [22],[23] and experimented on superimposing the flow field of the obstacle on the hovering rotor. Even though the computational predictions of the above numerical methods were in line with measurements in all aspects, the computational cost was significantly higher than the one of potential method. The excessive time needed for such computations is a well known problem of URANS models, since the wall region must be well resolved. Because of that convergence is delayed.

Independent of the activities of GARTEUR, the rotor wake - ground interference problem had been addressed in certain experimental and numerical studies in the past.

On the experimental side, Curtiss et al. [24] conducted IGE experiments in an in-door test rig. An isolated rotor was towed in a long towing shed. They measured the loads of the rotor for different values of the advance ratio within the range 0-0.1 and for different flight height–to-rotor diameter ratios within the range 0.23-0.45. They distinguished two wake flow regions:

- the re-circulation flow in which the starting vortex rolls up ahead of the rotor disk and

- the ground vortex flow in which the starting vortex rolls up below the rotor disk

while, through extensive flow visualization, they identified the conditions that favor the development of each of them.

In the framework of the HELIFLOW project, Boer et al. [25] performed wind tunnel IGE tests during side-ward flight. The campaign took place in the large

3

low speed facility (LLF) of the German-Dutch wind tunnel (DNW). The rotor outwash and the position of the ground vortex were measured via particle image velocimetry (PIV). Smaller scale wind tunnel IGE tests were conducted by Ganesh and Komerath in the John J. Harper Low Speed Wind Tunnel of Georgia Institute of Technology [26] and by Nathan and Green in a low-speed, closed-return wind tunnel with a 2.7m wide x 2.10m high x 4m long, octagonal working section [27]. Ganesh and Komerath measured the velocity in the wake using hot-wire anemometry, which was combined with pulsed laser sheet flow visualizations and hub-load measurements. Their objective was to characterize the unsteadiness of the wake flow in ground effect. They measured fluctuations in the rotor inflow which were found 5-10% higher than the ones corresponding to OGE. They attributed the fluctuations to the ingestion of the re-circulation flow into the rotor near wake region. Nathan and Green mimicked the relative motion of the helicopter with respect to the ground when in forward flight, by adding a moving belt on the ground level instead of the tunnel wind flow. This suggests that the presence of the ground boundary layer is essential for the correct prediction of the interactional phenomena between the rotor wake and the ground.

More recently, Sugiura et al. [28] conducted IGE flight tests of the JAXA research helicopter. Velocity measurements were taken with a LIDAR system as well as ultra sonic anemometers and were combined with smoke visualizations. Light et al. [29] used the wide field shadowgraph method to photograph the tip vortices of a hovering helicopter rotor in ground effect at NASA Ames research centre. The campaign provided results regarding the correlation of the distance of the vortices from the rotor to the loading of the helicopter.

Tanner et al. [30] conducted an experimental survey at NASA Langley research centre regarding the outwash flow of a rotor-craft in ground effect. The measured data included outwash velocities and directions, rotor loads, fuselage loads, and ground pressures. The researchers observed a linear relationship between the rotor height and the percentage of download on the fuselage. Also, the peak mean outwash velocities occurred at radial stations between 1.7 and 1.8 r/R, regardless of the rotor height. In addition, measurements showed a dependence between the outwash profile and the azimuthal location of measurements. Comparisons to phase-locked PIV data showed similar contours but a more contracted wake boundary for the PIV data.

Regarding the modelling of the ground effect, one of the first attempts to characterise the influence of the ground on a helicopter was conducted in 1957 by Cheeseman and Bennett [31]. Their analysis was based on the method of images. Their results led to an equation that correlates the increase in thrust of a helicopter in IGE to its rotor radius and the flight distance from the ground as follow:

$$\frac{T_{IGE}}{T_{OGE}} = \frac{1}{1 - (\frac{R}{4Z})^2} \quad for \quad Z/R > 0.25 \tag{1.1}$$

where, R is the radius of the helicopter's main rotor and Z is the distance of the

rotor centre from the ground. Equation 1.1 refers only to the effect of the ground on a hovering rotor without wind and only concerns full scale helicopters.

Recently Conyers et al. [32] used this model in order to determine whether or not it can be applied to small scale propellers and multi-rotors. The results overall suggest that this model cannot accurately predict the ground effect on the performance of quad-rotors while for a model helicopter, predictions were quite good. Sugiura et al. [33] used these measured data and the HMB solver of Glasgow to validate their URANS simulations [34], [35]. Both solvers follow the Eulerian flow description and rely on overlapping CHIMERA grids in order to resolve simultaneously the moving blades and the ground. The focus of the comparison was in forward flight cases at low advance ratios. The results were in line with measurements however CHIMERA grids demand special care over the interface between the grids in order to secure interpolation accuracy. Thus, increase of computational cost is expected. Cavallo et al. [36] conducted a similar study on the rotor-ground interference using URANS simulations combined with an actuator disk model of the rotor. Similar to [33], the authors focused on forward flight conditions at low advance ratios and assessed the developed flow field around the helicopter. More recently Pasquali et al. [37] used a potential BEM solver ([38], [39]) in an investigation of the aerodynamics around a hovering rotor in ground effect. Two modeling concepts for the ground were used. The first mimics the ground as a infinite symmetry plane [40] (mirroring technique) and the second treats the ground as a body [41] (bounded domain method). The results in general are in good agreement with the experimental data. However, both methods, due to their inviscid character, showed some limitations. Although deviations were small, the need for incorporating in the simulation the ground induced viscous layer effects were noted in the comparisons.

Another investigation concerning ground effect on a hovering rotor was conducted by Kutz et al. [42], [43]. Motivated by the brownout and whiteout effect (debris and snow hinder the visibility of the pilot due to their interaction with the wake of the helicopter and the ground vortex) the authors investigated numerically the ground effect using the URANS solver of DLR with CHIMERA grid strategy for low speed forward flight cases and stationary hovering positions. Predictions were in very good agreement with experiments and revealed an unsteady development of the rotor wake in IGE which imprinted as oscillations in CT and FM measurements. Yin et al. [44] investigated the effect of the ground on both the main and the tail rotor of a helicopter using DLR's potential free wake solver. The blockage effect of the ground on the formation of the wake during hover flight was discussed. In a slightly different way, Brown et al. [45] conducted a numerical research on the effect of the ground on a hovering and slowly moving helicopter. In this study, the wake of the rotor was modeled as a time-dependent vorticity distribution in the space surrounding the rotor. Calculations using the above model were compared against earlier experimental data. The comparison suggested that the structure of the rotor wake in ground effect undergoes a transition between

5

several more-or-less well-defined flow regimes as the forward speed of the rotor was increased. Doligalski et al. [46] tried to categorize interactional phenomena between vortices and walls in general. The main goal was to capture the response of a viscous boundary layer to vortex motion. In brief, the conclusion was that a boundary layer eruption occurs in such circumstances in the form of a thin spiral containing significant amount of vorticity, which usually rolls up into one or more secondary vortices. The authors' opinion about resolving this problem with numerical tools was that possibly a Lagrangian type solver would be adequate.

With respect to the rotor - obstacle interaction problem, several independent experimental campaigns have been conducted. Among them, pioneering is Timm's [47] experimental work on the obstacle-ground-helicopter interaction problem. Timm produced visualizations of the flow recirculation induced by the obstacle and the ground. Qualitative information of the effect of the re-circulation on rotor performance and solutions to mitigate the above effect are presented in his paper. More recently, Luciak et al. [48] performed wind tunnel experiments of a rotor hovering next or above a side wall or over a well. In their paper measured data of the thrust and torque coefficients are presented for the various configurations that were tested. Iboshi et al. [49] experimentally investigated the effect of a single or a pair of vertically placed walls on the torque of a helicopter rotor hovering above the ground. Quinliven and Long [50] investigated the effect of a rotorcraft operating in the wake of a large upstream object in the Fluid Mechanics Laboratory (FLM) at NASA Ames Research Center. Experimental data showed that an upwind building tended to decrease induced velocities at the leading edge of the rotor disk which was due to the re-circulation formed between the rotor and the building.

Polsky and Wilkinson [51] performed field tests of a helicopter rotor flying next to a vertical wall of a hangar. They recorded the flow using sonic anemometers and they analyzed the downwash and outwash flow of the helicopter rotor versus height and distance from the rotor centre. Nacakli et al. [52] conducted wind tunnel tests of a helicopter interacting with the ship deck. They also investigated the interaction of the rotor wake with the ship wake through combined Particle Image Velocimetry (PIV) measurements and rotor thrust recordings. Taymourtash et al. [53] performed a series of wind tunnel tests in order to study the flow features on the flight deck of a ship without the presence of the helicopter. He conducted pressure measurements and captured the flow field using PIV. Next, they assessed the alteration on the flow field due to the atmospheric boundary layer. The database was then used to investigate the impact of such a flow field to the handling qualities of the helicopter. The spatially varying inflow fields were also measured on several experiments. Klotz [54] and Manolesos et al. [55] conducted experimental campaigns analyzing the flow field patterns and capture the pressure distribution of a flow around cubic obstacles.

On the simulation side, investigations of the problem are very limited. Some preliminary numerical studies have been presented in conjunction with the above

discussed experimental studies. Luciak et al. [48] performed limited simulations of a helicopter hovering above a well using actuator disk CFD analysis. In their work they present flow field descriptive characteristics (streamlines and velocity patterns). Quinliven and Long [50] performed simulations of their test using a Blade Element Vortex model based on a prescribed wake model and Biot-Savart's ground effect correction. Polsky and Wilkinson [51] compared their field test measurements against actuator disk CFD simulation results. They studied sensitivity of the predictions on mesh density and turbulence modeling and analyzed the effect of the atmospheric boundary layer.

Alpman et al. [56] developed a fully-coupled simulation tool to analyze the rotorcraft/ship dynamic interface problem. This was done by coupling a CFD code with a flight dynamics simulation model. In their paper they present simulation results of the UH-60A hovering behind an aircraft hangar and approaching an LHA class ship. They have shown that interactional phenomena between the rotor wake and the air-wake become strong when the rotor hovers in proximity to solid boundaries. Lim et al. [57] used an LES model in order to simulate the flow around a cube in a turbulent boundary layer. The results presented include a detailed comparison between measurements [58] and LES computations of both the inflow boundary layer and the flow field around a cube including the near wake. Xin in his study [59] for the effect of a ship airwake on a helicopter approaching on its deck, mimicked the ship with an obstacle. The helicopter was partially shaded by the obstacle recreating in this way the ship-helicopter interaction. The results obtained from a solver [60] for inviscid and incompressible flows and the correlation between measured data was fairly good.

1.2   Scope of the Thesis and Main objectives

The objective of this thesis is twofold; (a) to investigate and characterize the interactions of a helicopter's rotor wake with nearby obstacles and the ground; in the latter case emphasis is put on the analysis of the effect of the ground boundary layer on the spatial evolution of the wake, (b) to assess the capabilities of numerical methods of varying fidelity to correctly predict the flow field in the vicinity of the rotor and the obstacle, and the loads of the rotor.

The thesis systematically investigates, registers and analyzes the physics of the flow when a helicopter performs hover flight in confined areas. In this context, the hover flight of a helicopter directly above the ground and different hovering scenarios in proximity to obstacles have been included in the study. Previous research included experimental campaigns and computational analyses. However, a detailed and systematic characterization of the diverse interactional phenomena occurring in all possible relative positions of the rotor with respect to the obstacle is lacking. So, by taking into consideration three different experimental campaigns and the computational results obtained with tools of different fidelity, a consistent study of the phenomena is preformed. The experimental campaigns that are used, are those of Politecnico di Milano, University of Glasgow and ONERA. They were conducted in different wind tunnels with different model helicopters. Because the results concern similar configurations, the conclusions extracted from each experiment verify the others. Additionally, the extracted conclusions are confirmed by computations. Thus, at the end of the investigation a "book of reference" of helicopter hover flight cases in confined areas is compiled including specific guidelines on how this cases should be modelled within different computational environments as well as a survey of the limitations and the capabilities of the different modeling options.

The study primary focuses on five aspects of a helicopter's flight envelope. The first is the hovering case outside the ground effect. In this case the rotor is isolated from any other object and thus the flow below the rotor is unconstrained and uninterrupted. Even though this case has been examined in detailed in the past, it is crucial for determining how the produced jet flow in the wake of the main rotor affects the convergence of the hub loading. The second case is the hovering helicopter inside the ground effect. In contrast to OGE case, in IGE conditions the rotor is close to the ground and the development of the wake is confined in an area constrained by the ground. The investigation concerns the variation of the rotor loading with respect to the unconstrained case .The last three cases can be combined in one larger group and concern the effect of a well shaped rectangular obstacle on the flow field in the vicinity of the rotor, in combination with the ground effect. This group includes vertical and horizontal sweeps of the rotor centre next and above the top of the obstacle. Again the variations of the loads are examined and categorized and their correlation with the developed flow field is explained in detail. The difference between the present study and other studies in

the past is that besides the characterization of the phenomena occurring in each of the above cases separately, a unified discussion comparing all the above cases and the identification of the interactional phenomena that are more critical and eventually drive loads in each one of them is attempted. The above analysis also assesses the impact of this interaction on the surrounding environment such at the obstacle and the ground.

So far, for the investigation of the interaction problem between a helicopter and solid boundaries in the literature, both Eulerian CFD and potential solvers have been used. The following list summarizes the positive (+) and negative (-) aspects of these two numerical modelling methodologies:

Eulerian Solvers

+ Solid Boundary Conditions are accurately satisfied

+ Compressible and viscous phenomena can be easily reproduced in the near wall regions.

- The far-field must be truncated at a finite distance.

- Gradual grid coarsening increases numerical diffusion adds uncertainty in the wake development.

- For Multi-body simulations CHIMERA or sliding grids or actuators disk models are usually applied that complicate the numerics and delay convergence.

- The overall simulation cost id high especially when long realtime duration are required.

Lagrangian Solvers

+ They are mesh-free and self-adaptive.

+ They have nominally zero diffusion.

+ They satisfy exactly the farfield conditions.

+ They have low computational cost and can adapt to different hardware platforms (multi-CPU or GPU)

+ Multi-body simulations are easily handled.

- Solid Wall boundary conditions constitute a major challenge.

- Standard Lagrangian methods do not include viscous and compressibility effects.

The computational analyses in the present thesis consist of two steps. First, a low computational cost potential free wake vortex particle solver (GenUVP) [61] is evaluated. In summary, in the model i) a vortex particle approximation is followed along with the application of a particle mesh technique, ii) lifting bodies are simulated as thin lifting surfaces iii) obstacles are introduced as non-lifting bluff bodies, and iv) the ground is modeled by the mirroring technique. The capabilities of this solver to correctly predict the flow field in the rotor-obstacle vicinity (in particular the large vortex structures that affect loads) and the rotor loads is as-

sessed . Vortex particle methods have been widely used in simulating wind turbine [62] and helicopter [17] rotors. They are usually combined with boundary element methods for the modeling of lifting rotating blades. Even though these methods were originally formulated in an inviscid, incompressible context, several attempts have been made to introduce viscous effects as add on corrections [63, 64]. However, in problems where viscous interactions are dominant, limitations due to the inviscid character of these methods raise. Another important issue of simulating rotor-obstacle-ground conditions is that several rotor revolutions need to be simulated until a steady-state is reached. The simulated time should be long enough to let the wake impinge on the obstacle and eventually reach a periodic equilibrium state. The computational cost of the above discussed vortex methods gradually increases with time when convolution type velocity field computations (through application of Biot-Savart law) [65, 66] are performed. The above shortcoming is overcome through the introduction of particle mesh methods, which substantially reduce computational time [67, 68, 69, 70]. This allows for an extensive application of GenUVP especially for the detailed investigation of the effect of the interaction on the hub loads of a helicopter in several flight conditions (relative placement of the rotor with respect to the obstacle). The compromise made is the suppression of all viscous effects. The advantage of the above approach is that one may distinguish between the mirroring effect of the ground and the effect wall friction, which ends up to the displacement of the flow.

Regarding GenUVP simulations the following objectives have been set:

- Validation of the specific vortex particle model against measurements.

- Quantification of the effect of the rotor-obstacle interaction on the loads of a helicopter hovering in proximity to an obstacle in various configurations.

- Correlation of the characteristics of the developed inviscid flow field with the resulting rotor loads.

- Assessment of the cases where it can provide reliable results.

In the second step, a high fidelity CFD tool that inherently accounts for viscous effects is employed. Regarding the different implementations in CFD, many solvers include Finite Differences Methods (FDM) [71], Finite Volume Methods (FVM) [72], Discontinuous Galerkin Methods (DGM) [73], and finally Spectral Methods [74]. All these formulations combined with domain decomposition and parallel computing can be used in rotor-craft applications with affordable cost [75]. Application of local grid refinements offers higher accuracy and better gradient capturing [76]. Moreover, the addition of multi-grid based analyses lead to faster convergence [77] and the application of mixed grids allow handling boundary layers with higher accuracy [78].

Specifically, for problems that involve helicopter rotors, the solution is offered by over-set CHIMERA grids [79] and Sliding Grids [80]. These techniques, along

with the application of the Actuator Disk/Line method in the framework of standard URANS codes [36], have been exploited by the research community and offer a significant advantage against potential methodologies. The capability of resolving viscous phenomena on solid boundaries (boundary layer) is their main advantage in relation to the problems tackled in the present thesis. Despite the vast development of Eulerian grid based solvers, there are still issues related with the above methods that need to be addressed. When external flows are considered the far field must be truncated at some finite distance. Far field conditions could introduce errors that are sensed as reflections in the simulations [81]. Moreover, the usual grid coarsening as we more away from solid boundaries increases numerical diffusion.

In this context, the present work proposes a hybrid Eulerian-Lagrangian method that can accurately predict the formation of viscous boundary layers and simultaneously alleviates the problems of standard URANS codes related with the far field modeling. The corresponding solver (HoPFlow) was first introduced by [18] in 2014. The corresponding flow solver, couples a standard Eulerian finite volume solver with a Lagrangian particle based scheme [18, 82]. In the Eulerian part, separate grids of limited width are defined around every solid body, on which the flow equations are solved in their Eulerian form. In particular for the rotor-ground interaction problem different Eulerian grids are built around the rotating blades, and another grid is defined on the ground. In order to interconnect the independent domains defined by the various grids, the entire flow field is described in Lagrangian coordinates and the corresponding flow equations are solved via particle approximations in fully coupled mode with the solutions within the Eulerian grids. The Eulerian part solves the compressible flow equations in density-velocity-pressure formulation and uses pre-conditioning at low Mach while the Lagrangian part is based on the density-dilatation-vorticity-pressure formulation.

The main advantage of the hybrid model is that it can effectively deal with flow problems which involve several bodies, that move independently the one from the other and in close proximity. In addition, the numerical diffusion in the wake is significantly lower, and the conditions at infinity as well as the wall non-slip conditions are exactly met.

Regarding HoPFlow simulations, the following objectives have been set:

- Validation of the methodology for multiple independent moving bodies that include the main rotor of a helicopter and the fuselage.
  In [18] HoPFlow was validated for a two bladed rotor (Caradonna rotor), focusing on the compressible flow over the blades (shock wave), while in the present work the emphasis is on the flow field of the wake (interactional phenomena of shear layers).

- Assessment of the importance of viscous phenomena in the rotor-obstacle-ground interaction

- Conclusion of a robust solver that captures experimental measurements and consistently predicts rotor loads and the flow field.

In order to moderate the computational cost, the blades of the rotor are represented as actuator lines. In [18] comparisons against measurements revealed that the hybrid methodology can fully resolve the flow around a rotating blade (modelling the actual blade shape), also in cases of high Mach numbers where shock waves are present. Thus, this study focuses on analyzing far wake interactions driven by viscous phenomena (boundary layer development on the ground, flow separation over a cubic obstacle etc.) rather than resolving the flow in the vicinity of the rotor blades (flow characteristics in blade chord scale). In connection to the above, within the Eulerian domain, blades are modeled as lines exchanging momentum with the surrounding flow. This allows for larger time-steps in the unsteady simulations especially considering the large number of rotor revolutions needed to attain periodic-state conditions.

1.3   Novelties

Due to the limited bibliography on the subject the main focus of the present dissertation is to provide a consistent description of the relevant (interactional) flow phenomena:

- Firstly and most importantly, this thesis focuses on the deep understanding of the underlying physics of the rotor ground/obstacle interaction. This was possible by gathering and analyzing data of a variety of configurations.

- Expansion of the Particle Mesh solver.
  In order to perform simulations for problems such as the ground effect, the option of solving symmetric domains is added in the PM solver. This addition is used, in favor of the acceleration of simulations, in the potential free particle method $GenUVP$ and in $HoPFlow$.

- In this thesis, for the first time the hybrid solver HoPFlow is used for $3D$ simulations with multiple rotating and non-rotating bodies. This includes the rotating frame of the blades and the non-rotating frames of the fuselage the ground and the obstacle.

1.4 Thesis Outline

This thesis is divided in 4 chapters.

- Chapter 2 describes the theory of the different tools that have been used and the modifications that were needed in order to simulate simultaneously rotating bodies and standing still solid boundaries.

- Chapter 3 presents the results obtained by the present thesis. It describes the experimental campaigns that are used as reference and the computational configurations of the different solvers. Next, the underlying physics of different rotor-obstacle interaction problems are systematically analyzed and discussed. Computational predictions of different solvers are compared against measurements. Finally, predictions of the different tools are evaluated.

- Chapter 4 contains the conclusions drawn from the present work along with recommendations for future research.

This page intentionally left blank.

Chapter 2

Numerical analysis of the computational tools

In this chapter the theory and numerical tools used in this thesis are described.
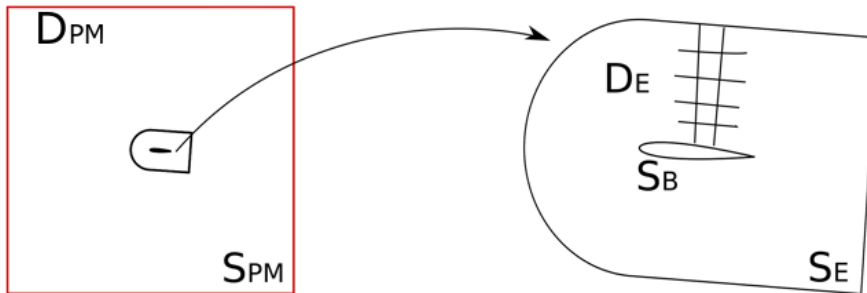
Figure 2.1: The Eulerian domain D_E contains the solid boundary S_B. The Lagrangian domain D_∞ includes D_{PM} and and D_E

The nature of the problem that involves rotating and non-rotating solid surfaces has led to selecting the material description of the flow. The corresponding equations are formulated in terms of density ρ, vorticity $\vec{\omega}$, dilatation θ and pressure p, that are attributed to compressible particles. Using Helmholtz's velocity decomposition theorem, the velocity field, is reconstructed by solving the Poisson equations for the two potentials. In order to reduce cost, a particle mesh technique is applied. In this process, the scattered space information is projected onto a uniform Cartesian grid (D_{PM}). Then the Poisson equations are solved over D_{PM} by properly applying the James-Lackner algorithm on sub-domains of D_{PM} and assigning correct boundary conditions on S_{PM}. Then, the RHS of the Lagrangian equations are calculated using finite differences on the PM grid. Finally, the new

flow properties are interpolated back at the positions of the particles.

In cases with solid boundaries S_B inside of the domain D, two options regarding the fulfilment of the corresponding wall boundary conditions have been considered. In the incompressible limit without viscous effects, the boundary condition is associated to the scalar potential and is numerically resolved by means of a panel method. In the more general case a separate overlapping domain D_E is deployed in which an Eulerian solver is utilized and thus wall boundary conditions on S_B are handled exactly, which particle methods have several difficulties to efficiently implement. On the outer boundary S_E the required conditions are provided by the Lagrangian solver. This is the one way the two solvers are coupled together, the other being the correction of the Lagrangian solution.

2.1 Flow equations in Lagrangian description

The cases that are analyzed in this work makes grid based Eulerian solvers not easy to use. Grid based CFD methods are proven to increase computational cost and implementation complexity of simulations, especially in cases that include rotating and non-rotating surfaces ([79]). Thus, the Lagrangian (material) description of the flow has been chosen because it is mesh free, self-adaptive, and therefore can easily handle multi-body simulations.

2.1.1 Density - Vorticity - Dilatation - Pressure formulation of flow equations

Continuity equation:

Let $\theta = \nabla \cdot \vec{u}$. Then, the continuity equation takes the following form:

$$\frac{\partial \rho}{\partial t} + \nabla \left(\rho \vec{u} \right) = 0 \Rightarrow$$

$$\frac{\partial \rho}{\partial t} + \left(\vec{u} \nabla \right) \rho = -\rho \nabla \vec{u} \Rightarrow$$

$$\frac{D\rho}{Dt} = -\rho \theta \tag{2.1}$$

Momentum equation in conservative form:

$$\frac{\partial(\rho \vec{u})}{\partial t} + \nabla \left(\vec{u} \otimes (\rho \vec{u}) \right) = \nabla \left(-p + \overleftrightarrow{\sigma} \right) \Rightarrow$$

$$\rho\frac{\partial \vec{u}}{\partial t} + \vec{u}\frac{\partial \rho}{\partial t} + (\vec{u}\cdot\nabla)\rho\vec{u} + (\rho\vec{u}\cdot\nabla)\vec{u} = \nabla\left(-p + \overleftrightarrow{\sigma}\right) \Rightarrow$$

$$\rho\left(\frac{\partial \vec{u}}{\partial t} + (\vec{u}\cdot\nabla)\,\vec{u}\right) + \vec{u}\underbrace{\left(\frac{\partial \rho}{\partial t} + \nabla\left(\rho\vec{u}\right)\right)}_{\textbf{Continuity equation}} = \nabla\left(-p + \overleftrightarrow{\sigma}\right) \Rightarrow$$

$$\frac{\partial \vec{u}}{\partial t} + (\vec{u}\cdot\nabla)\vec{u} = \frac{\nabla\left(-p + \overleftrightarrow{\sigma}\right)}{\rho} = 0 \Rightarrow$$

$$\frac{D\vec{u}}{Dt} = \frac{\nabla\left(-p + \overleftrightarrow{\sigma}\right)}{\rho} \tag{2.2}$$

Since,

$$(\vec{u}\cdot\nabla)\vec{u} = \nabla\frac{u^2}{2} - \vec{u}\times\vec{\omega}$$

then

$$\frac{\partial \vec{u}}{\partial t} + \nabla\frac{u^2}{2} - \vec{u}\times\vec{\omega} = \frac{\nabla\left(-p + \overleftrightarrow{\sigma}\right)}{\rho} \tag{2.3}$$

Taking the curl ($\nabla\times$) of 2.3 and introducing vorticity $\vec{\omega} = \nabla\times\vec{u}$:

$$\frac{\partial \nabla\times\vec{u}}{\partial t} + \nabla\times\left\{\nabla\frac{u^2}{2} - \vec{u}\times\vec{\omega}\right\} = \nabla\times\left(\frac{\nabla\left(-p + \overleftrightarrow{\sigma}\right)}{\rho}\right) \Leftrightarrow$$

$$\frac{\partial \vec{\omega}}{\partial t} - \nabla\times(\vec{u}\times\vec{\omega}) = \nabla\times\left(\frac{\nabla\left(-p + \overleftrightarrow{\sigma}\right)}{\rho}\right) \Leftrightarrow$$

$$\frac{\partial \vec{\omega}}{\partial t} - \{\vec{u}(\nabla\cdot\vec{\omega}) - \vec{\omega}(\nabla\cdot\vec{u}) + (\vec{\omega}\cdot\nabla)\vec{u} - (\vec{u}\cdot\nabla)\vec{\omega}\} = \nabla\times\left(\frac{\nabla\left(-p + \overleftrightarrow{\sigma}\right)}{\rho}\right) = 0$$

Since $\nabla\cdot\vec{\omega} = 0$ and $\nabla\cdot\vec{u} = \theta$:

$$\frac{\partial \vec{\omega}}{\partial t} + \vec{\omega}\theta - (\vec{\omega}\cdot\nabla)\vec{u} + (\vec{u}\cdot\nabla)\vec{\omega} = \nabla\times\left(\frac{\nabla\left(-p + \overleftrightarrow{\sigma}\right)}{\rho}\right) \Leftrightarrow$$

$$\underbrace{\frac{\partial \vec{\omega}}{\partial t} + (\vec{u}\cdot\nabla)\vec{\omega}}_{\textbf{Material Derivative}} + \vec{\omega}\theta - (\vec{\omega}\cdot\nabla)\vec{u} = \nabla\times\left(\frac{\nabla\left(-p + \overleftrightarrow{\sigma}\right)}{\rho}\right) \Leftrightarrow$$

$$\frac{D\vec{\omega}}{Dt} = -\vec{\omega}\theta + (\vec{\omega}\cdot\nabla)\vec{u} + \nabla\times\left(\frac{\nabla\left(-p + \overleftrightarrow{\sigma}\right)}{\rho}\right)$$

because,

$$\nabla\times\left(\frac{\nabla\left(-p + \overleftrightarrow{\sigma}\right)}{\rho}\right) = \frac{1}{\rho}\nabla\times\nabla\left(-p + \overleftrightarrow{\sigma}\right) + \nabla\frac{1}{\rho}\times\nabla\left(-p + \overleftrightarrow{\sigma}\right) \Leftrightarrow$$

$$= -\frac{1}{\rho^2}\nabla\rho\times\nabla\left(-p + \overleftrightarrow{\sigma}\right)$$

the vorticity equation takes the form:

$$\frac{D\vec{\omega}}{Dt} = -\vec{\omega}\theta + (\vec{\omega} \cdot \nabla)\vec{u} - \frac{1}{\rho^2}\nabla\rho \times \nabla\left(-p + \overleftrightarrow{\sigma}\right) \qquad (2.4)$$

By taking the divergence ($\nabla\cdot$) of 2.3 equation:

$$\nabla \cdot \left\{ \frac{\partial\vec{u}}{\partial t} + \nabla \cdot (\vec{u} \cdot \nabla)\vec{u} + \frac{\nabla\left(p - \overleftrightarrow{\sigma}\right)}{\rho} \right\} = 0 \Leftrightarrow$$

$$\frac{\partial\nabla \cdot \vec{u}}{\partial t} + \nabla \cdot (\vec{u} \cdot \nabla)\vec{u} + \nabla \cdot \frac{\nabla\left(p - \overleftrightarrow{\sigma}\right)}{\rho} = 0$$

$$\frac{\partial\theta}{\partial t} + \nabla \cdot (\vec{u} \cdot \nabla)\vec{u} + \nabla \cdot \frac{\nabla\left(p - \overleftrightarrow{\sigma}\right)}{\rho} = 0$$

By expanding the divergence of the advection term:

$$\nabla \cdot (\vec{u} \cdot \nabla)\vec{u} = (\vec{u} \cdot \nabla)(\nabla \cdot \vec{u}) + (\nabla \cdot \vec{u})^2 - 2\|\nabla\vec{u}\|$$
$$= (\vec{u} \cdot \nabla)\theta + \theta^2 - 2\|\nabla\vec{u}\|$$

where,

$$\nabla\vec{u} = \begin{bmatrix} \frac{\partial u}{\partial x} & \frac{\partial v}{\partial x} & \frac{\partial w}{\partial x} \\ \frac{\partial u}{\partial y} & \frac{\partial v}{\partial y} & \frac{\partial w}{\partial y} \\ \frac{\partial u}{\partial z} & \frac{\partial v}{\partial z} & \frac{\partial w}{\partial z} \end{bmatrix}$$

and

$$\|\nabla\vec{u}\| = det(\nabla\vec{u})$$

it follows that,

$$\underbrace{\frac{\partial\theta}{\partial t} + (\vec{u} \cdot \nabla)\theta}_{\textbf{Material Derivative}} + \theta^2 - 2\|\nabla\vec{u}\| + \nabla \cdot \frac{\nabla\left(p - \overleftrightarrow{\sigma}\right)}{\rho} = 0 \Leftrightarrow$$

$$\frac{D\theta}{Dt} = -\theta^2 + 2\|\nabla\vec{u}\| - \nabla \cdot \frac{\nabla\left(-p + \overleftrightarrow{\sigma}\right)}{\rho} \qquad (2.5)$$

The energy equation in conservative form,

$$\frac{\partial\rho E}{\partial t} + \nabla(\rho\vec{u}E) = \nabla\left(\vec{u} \cdot (-pI + \overleftrightarrow{\sigma})\right) = 0$$

it follows that,

$$\rho\frac{\partial E}{\partial t} + E\frac{\partial \rho}{\partial t} + (\rho\vec{u}\cdot\nabla)E + E\nabla(\rho\vec{u}) = \nabla\left(\vec{u}\cdot(-pI + \overleftrightarrow{\sigma})\right) \Leftrightarrow$$

$$\rho\left(\frac{\partial E}{\partial t} + (\vec{u}\cdot\nabla)E\right) + E\underbrace{\left(\frac{\partial\rho}{\partial t} + \nabla\rho\vec{u}\right)}_{\textbf{Continuity Equation}} = \nabla\left(\vec{u}\cdot(-pI + \overleftrightarrow{\sigma})\right) \Leftrightarrow$$

$$\rho\left(\frac{\partial E}{\partial t} + (\vec{u}\cdot\nabla)E\right) = \nabla\left(\vec{u}\cdot(-pI + \overleftrightarrow{\sigma})\right) \Leftrightarrow$$

$$\rho\frac{DE}{Dt} = \nabla\left(\vec{u}\cdot(-pI + \overleftrightarrow{\sigma})\right)$$

By introducing $\Pi = \rho V E$,

$$\frac{D\Pi}{Dt} = \frac{D\rho V E}{Dt} = \rho V\frac{DE}{Dt} + E\frac{D\rho V}{Dt} \Leftrightarrow$$

$$\frac{D\Pi}{Dt} = E\frac{DM}{Dt} + V\nabla\left(\vec{u}\cdot(-pI + \overleftrightarrow{\sigma})\right) \Leftrightarrow$$

$$\frac{D\Pi}{Dt} = V\nabla\left(\vec{u}\cdot(-pI + \overleftrightarrow{\sigma})\right) \tag{2.6}$$

So, collectively the set of Lagrangian equations in vorticity-dilatation formulation are given by equations 2.1, 2.4, 2.5, and 2.6. A way to solve the above system of equations is to use particles approximations. Particle approximations describe flows based on the assumption that the characteristics are distributed on a finite number of particles. Particles then carry mass M_p contained in a volume of $V_P(t)$ energy $M\rho E_p(t)$ and according to Helmholtz's decomposition theorem of the velocity, momentum is expressed through dilatation $\Theta_p(t)$ and vorticity $\vec{\Omega}_P(t)$ as is demonstrated next. Because particles have volume, flow properties can be expressed by volume integrals:

$$M_p = \int_{V_p(t)} \rho(\vec{x},t)dV_p(t) = \rho_p(t)\,V_p(t) \tag{2.7}$$

$$\Theta_p(t) = \int_{V_p(t)} \theta(\vec{x},t)dV_p(t) = \theta_p(t)\,V_p(t) \tag{2.8}$$

$$\vec{\Omega}_p(t) = \int_{V_p(t)} \vec{\omega}(\vec{x},t)dV_p(t) = \vec{\omega}_p(t)V_p(t) \tag{2.9}$$

$$\Pi_p(t) = \int_{V_p(t)} e(\vec{x},t)dV_p(t) = e_p(t)\,V_p(t) \tag{2.10}$$

in which, $\rho(\vec{x},t)$, $\theta(\vec{x},t)$, $\vec{\omega}(\vec{x},t)$, $e(\vec{x},t)$, correspond to the continuous field properties of the flow. Numerical particles act like flow markers approximating the flow field at discrete positions. Error analysis of particle methods indicates that numerical particles must overlap while the physical ones do not [83, 84]. This is

an important remark since it allows to recover the continuous flow properties by means of (one point) quadrature,

$$\rho(\vec{x}, t) = \sum_p \rho_p(t) V_p(t) \zeta_\epsilon(\vec{x} - \vec{Z}_p(t)) \tag{2.11}$$

$$\theta(\vec{x}, t) = \sum_p \theta_p(t) V_p(t) \zeta_\epsilon(\vec{x} - \vec{Z}_p(t)) \tag{2.12}$$

$$\vec{\omega}(\vec{x}, t) = \sum_p \vec{\omega_p}(t) V_p(t) \zeta_\epsilon(\vec{x} - \vec{Z}_p(t)) \tag{2.13}$$

$$e(\vec{x}, t) = \sum_p e_p(t) V_p(t) \zeta_\epsilon(\vec{x} - \vec{Z}_p(t)) \tag{2.14}$$

where ζ_ϵ represents a distribution function. In the original formulation of particle methods, the Dirac function was used in place of ζ_ϵ which corresponds to "point particles" [85]. Lack of smoothness and singularities in the field derivatives led to the introduction of smooth particle approximations [86, 87, 88]. In this respect, ζ_ϵ is considered as a smooth approximation of the Dirac function.

By introducing the volume δV in any property $\Phi = (\rho, \theta, \vec{\omega}, e)$ it follows that:

$$\frac{D(\Phi \delta V)}{Dt} = \delta V \frac{D\Phi}{Dt} + \Phi \frac{D\delta V}{Dt} = \delta V \left(\frac{D\Phi}{Dt} + \Phi\theta \right)$$

Therefore, when the viscous terms are excluded, equations take the following particle form:

Mass Conservation: $\quad \dfrac{DM_p}{Dt} = 0 \tag{2.15}$

Momentum Conservation: $\quad \dfrac{D\vec{\Omega}_p}{Dt} = V_p \left((\vec{\omega} \cdot \nabla)\vec{u} + \dfrac{1}{\rho^2} \nabla\rho \times \nabla p \right)_p \tag{2.16}$

$$\dfrac{D\Theta_p}{Dt} = V_p \left(2\|\nabla\vec{u}\| - \nabla \cdot \dfrac{\nabla p}{\rho} \right)_p \tag{2.17}$$

Energy Conservation: $\quad \dfrac{D\Pi_p}{Dt} = -V_p \nabla(\vec{u}p) \tag{2.18}$

where $(\cdot)_p$ denotes evaluation at the particle position $\vec{Z}_p$. Extension to viscous flows involves extra terms in the Θ, $\vec{\Omega}$ and Π equations. For the first two, the extra terms are derived from the divergence ($\nabla\cdot$) and curl ($\nabla\times$) of $\nabla\sigma/\rho$, while for the energy equation the extra term is $\nabla(\vec{u} \cdot \sigma)/\rho$. In these terms σ denotes the viscous stress tensor.

2.1.2 Helmholtz's velocity decomposition

In the ρ, $\vec{\omega}$, θ, p formulation the velocity $\vec{u}$ is a derived quantity. In this respect, Helmholtz's velocity decomposition states that $\vec{u}$ can be split, so:

$$\vec{u} = \vec{U}_\infty + \vec{u}_\phi + \vec{u}_\omega, \quad \vec{u}_\phi = \nabla\phi, \quad \vec{u}_\omega = \nabla \times \vec{\psi} \tag{2.19}$$

The irrotational part is defined through the scalar potential ϕ while the vortical one through the stream function $\vec{\psi}$ (also known as vector potential). By taking the divergence and curl of (2.19), gives:

$$\nabla^2 \phi = \nabla \cdot \vec{u} = \theta \tag{2.20}$$

$$\nabla^2 \vec{\psi} = -\nabla \times \nabla \times \vec{\psi} = -\nabla \times \vec{u} = -\vec{\omega} \tag{2.21}$$

Thus, the velocity field can be determined from ϕ and $\vec{\psi}$ after solving the above two Poisson equations, to which appropriate boundary conditions are assigned.
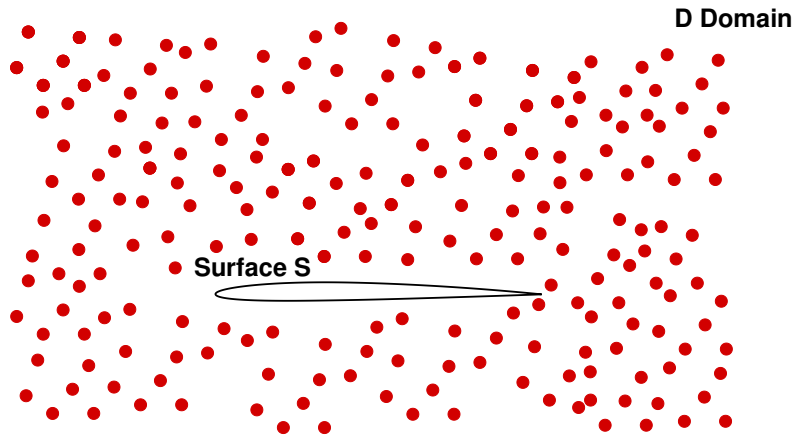
Figure 2.2: The flow domain in the case of an external flow around a solid body. Red circles denote the particles.

Let $S = \partial D$ denote the solid boundary of the flow field D. Making use of Green's theorem, integral representations for ϕ and $\vec{\psi}$ are obtained. Let $\vec{n}$, $\vec{\tau}_\alpha$, $\alpha = 1, 2$ denote the normal and tangent to S unit vectors, and $\partial_n(\cdot) = \vec{n} \cdot \nabla$, $\partial_\alpha(\cdot) = \vec{\tau}_\alpha \cdot \nabla$ the corresponding directional derivatives. Then,

$$\phi(\vec{x}) = \int_D \nabla^2 \phi(\vec{y}) \, G(\vec{r}) \, dD(\vec{y}) + \int_S \left(\partial_n \phi(\vec{y}) \, G(\vec{r}) - \phi(\vec{y}) \partial_n G(\vec{r}) \right) dS(\vec{y})$$

$$\psi_i(\vec{x}) = \int_D \nabla^2 \psi_i(\vec{y}) \, G(\vec{r}) \, dD(\vec{y}) + \int_S \left(\partial_n \psi_i(\vec{y}) \, G(\vec{r}) - \psi_i(\vec{y}) \partial_n G(\vec{r}) \right) dS(\vec{y}) \tag{2.22}$$

where $\vec{r} = \vec{x} - \vec{y}$ and G is the Green's function for the Laplace operator. Taking the $\nabla \cdot$ of the first and the $\nabla \times$ of the second, the integral representation of $\vec{u}$ is obtained:

$$\vec{u}(\vec{x}) = \vec{U}_\infty + \int_D \left(\theta(\vec{y}) \, \vec{K}(\vec{r}) + \vec{\omega}(\vec{y}) \times \vec{K}(\vec{r}) \right) dD(\vec{y}) +$$

$$\int_S \left(u_n(\vec{y}) \, \vec{K}(\vec{r}) + \vec{u_\tau}(\vec{y}) \times \vec{K}(\vec{r}) \right) dS(\vec{y}) \tag{2.23}$$

In the above expression, u_n, $\vec{u}_\tau$ denote the normal and tangential disturbance velocity components on S and $\vec{K}(\vec{r}) = \nabla G(\vec{r})$. The volume term in (2.23) is directly obtained from the volume integrals in (2.22). Also, the surface terms that are associated to ∂_n in (2.22) directly contribute their shares in $u_n, \vec{u}_\tau$. In order to recover the contribution of ϕ, ψ_i appearing in 2.22 into 2.23, integration by parts is carried out combined with Stokes' theorem applied to the second surface terms in (2.22) [89].

If there are no boundaries, the way to proceed is rather straightforward. For given initial conditions, the transport equations (2.15) are integrated in time and the particles are transported using the velocity field defined in (2.23). CPU cost is dominated by the convolution integral in (2.23). For N particles, the associated cost is proportional to N^2, which can easily explode as N becomes large and the intended duration of the simulation is long. When boundaries are present computational cost increases even more, since there are surface convolutions in (2.23) to be evaluated.

In (2.23), S is the boundary of D and therefore contains not only the solid boundaries S_B but also any other interface, as in the case of non-overlapping domain decomposition. On S_B, u_n along with $\vec{u}_\tau$ are determined so that $\vec{u}$ satisfies the solid boundary conditions. On interfaces, u_n and $\vec{u}_\tau$ are determined by the corresponding jump conditions. This involves the solution of two integral equations derived from (2.23) for $\vec{x} \in S$ [90, 91]. These equations will either determine u_n, $\vec{u}_\tau$ on S for given θ, ω or specify the production of dilatation and vorticity for given u_n, $\vec{u}_\tau$. However, solving these integral equations, can significantly penalize the cost and therefore should be avoided.

In the direction of avoiding the above integral calculations over the domain, the reconstruction of the velocity field can be determined by solving the Poisson equation for the scalar potential ϕ and the vector potential $\vec{\psi}$. Thus, instead of the integral representation of the velocity, four scalar Poisson equations are solved.

A way to reduce the number of equations to three (and accordingly the computational cost) is to solve for the velocity $\vec{u}$ directly:

$$\nabla^2 \vec{u} = -\nabla \times \vec{\omega} + \nabla \theta \tag{2.24}$$

However, in potential simulations the scalar potential is essential for the calculation of the pressure in Bernoulli's theorem. So, the following intermediate formulation is used in the present work:

$$\nabla^2 \vec{u}_\omega = -\nabla \times \vec{\omega} \tag{2.25}$$
$$\nabla^2 \phi = \theta \tag{2.26}$$

In addition, the above system of equations is proven to be suitable when symmetry boundary conditions are enforced (such as the simulations of the ground using the mirroring technique). The symmetry plane is determined as a surface where the normal velocity is equal to zero (no-penetration condition) while there

22

is no production of vorticity on it. The above boundary conditions are expressed as:

- $\frac{\partial \phi}{\partial n} = 0$

- $\vec{u}_\omega \cdot \vec{n} = 0$

- $\frac{\partial u_{\omega,x,y}}{\partial n} = 0$

where $\vec{n}$ is the normal vector to the symmetry plane.

2.2 The Particle-Mesh

Particle Mesh (PM) methods constitute an effective way to solve a Poisson equation. The idea is to solve the equation on a Cartesian grid using Fast Poisson solvers [92]. In this way, the expensive convolution terms of equation (2.23) are avoided. The cost reduces from N^2 to $N log N$ which for large N leads to almost linear increase. The particle mesh method consists of three discrete parts; a) the projection of the flow quantities of particles, b) the Poisson solver, and c) the interpolation back to particles. The PM solver was developed within the context of Papadakis' thesis [18]. So next, the modifications and enhancements that have been made in order to extend the solver to symmetric flows are detailed. The core of the solver is based on the James-Lackner algorithm which is first analyzed in order to set later on the principal ideas of the multi-domain symmetric capabilities of the Particle Mesh Method.

2.2.1 The Poisson Problem and the James-Lackner algorithm

Let D denote a compact subset of the full space (R^n) that well contains the support of the forcing f of a Poisson problem for w. Even though the forcing f is restricted inside D $(supp(f) \subset D)$ the generated field extends to infinity, where it is assumed to tend to zero. Therefore, the problem is formulated as:

$$\nabla^2 w = f(\vec{x}), \qquad \vec{x} \in R^n$$
$$\lim_{x \to \pm\infty} w = 0 \tag{2.27}$$

The solution on R^n is given using Green's function G in convolution form:

$$w(\vec{x}_o) = \int_{supp\{f\}} f(\vec{x}) \, G(\vec{x}_o - \vec{x}) dD(\vec{x}), \qquad \vec{x}_o \in R^n \tag{2.28}$$

23

In order to obtain the numerical solution of the above problem within the confined sub-domain D with boundary of ∂D of the full space R^n, the following problem is instead solved:

$$\nabla^2 w = f(\vec{x}), \qquad \vec{x} \in D$$
$$w = w_B, \qquad \vec{x} \in \partial D \tag{2.29}$$

in which, the boundary condition on ∂D translates the condition at infinity to an equivalent one at a finite distance. The unknown boundary conditions of 2.29 is directly obtained, using Green's function G:

$$w_B(\vec{x}_o) = \int_{supp\{f\}} f(\vec{x}) \, G(\vec{x}_o - \vec{x}) dD(\vec{x}) \tag{2.30}$$

Using equation (2.30) in order to calculate the boundary conditions remains extremely expensive for dense grids, even if tree algorithms were applied in this option. Thus, in the direction of mitigating cost, James and Lackner [93, 94] separated the space from the boundary forcing:

$$w = w_0 + w_1 \tag{2.31}$$

so that, the problem is split in two parts concerning the boundary conditions:

a)The Homogeneous Boundary Condition Problem

$$\nabla^2 w_0 = f(\vec{x}), \quad \vec{x} \in D$$
$$w_0 = 0, \qquad \vec{x} \in \partial D \tag{2.32}$$

b) The Surface Boundary Condition Problem

$$\nabla^2 w_1 = 0, \qquad \vec{x} \in D$$
$$w_1 = w_B, \quad \vec{x} \in \partial D \tag{2.33}$$

which can be given an explicit single layer (source) expression:

$$w_1(\vec{x}_o) = \int_{\partial D} \sigma(\vec{x}) \, G(\vec{x}_o - \vec{x}) dS(\vec{x}) \tag{2.34}$$

where,

$$\sigma = [\frac{\partial w_1}{\partial n}]$$

denotes the jump in the normal derivative on ∂D. By requiring continuity of w across ∂D,

$$\sigma = -[\frac{\partial w_0}{\partial n}] \tag{2.35}$$

In this expression, the costly space convolution integral (2.30) is substituted by a surface one (2.34). More specifically, depending on the position of the calculation point $\vec{x}$:

$$\vec{x} \in D, \quad w = w_0 + w_1 \tag{2.36}$$

$$\vec{x} \in R^n - D, \quad w = w_1 \tag{2.37}$$

In summary, for the full space problem, Poisson's equation is solved in two steps:

- First, the problem is solved applying zero boundary conditions on ∂D in order to obtain the solution w_0 on D.

- The next step is to determine the correct boundary condition w_1 on ∂D using equation 2.34.

2.2.2   Multi-block decomposition

A well known way to reduce computational time is to apply domain decomposition. In this manner a domain D is decomposed into N non-overlapping sub-domains. The solution in every sub-domain is used to reconstruct the solution over D. Let,
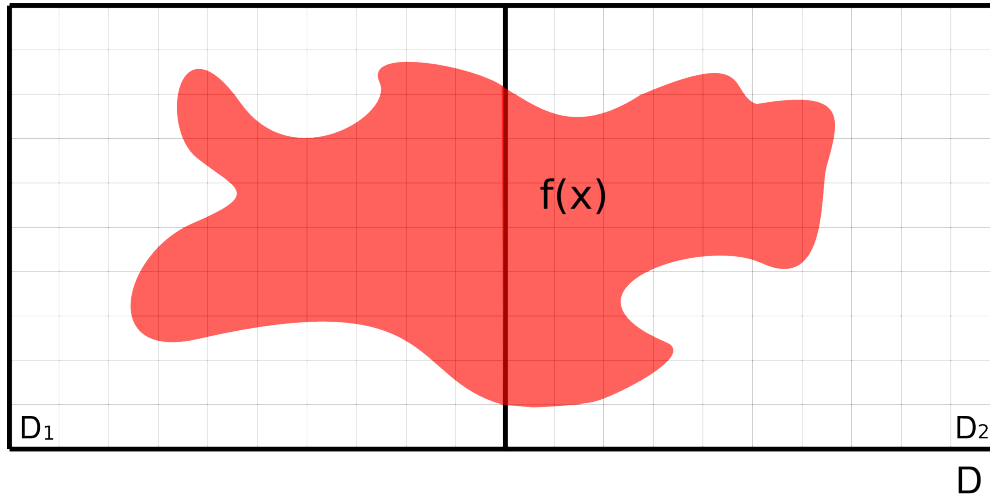
Figure 2.3: The full space problem split in two sub-domains.

$$D = \cup_{i=1}^{N} D_i$$

$$f(\vec{x}) = \sum_{i=1}^{N} f_i(\vec{x}) \tag{2.38}$$

$$w(\vec{x}) = \sum_{i=1}^{N} w_i(\vec{x})$$

where f_i, w_i denote the restrictions of f and w in $D_i \subset D$.

By considering f_i and w_i as zero extensions of restrictions in D_i, linear theory dictates that the problem is divided into N sub-problems:

$$\nabla^2 w_i = f_i(\vec{x}), \vec{x} \in D_i, i = 1, N \tag{2.39}$$

(a) Sub-domain 1   (b) Sub-domain 2
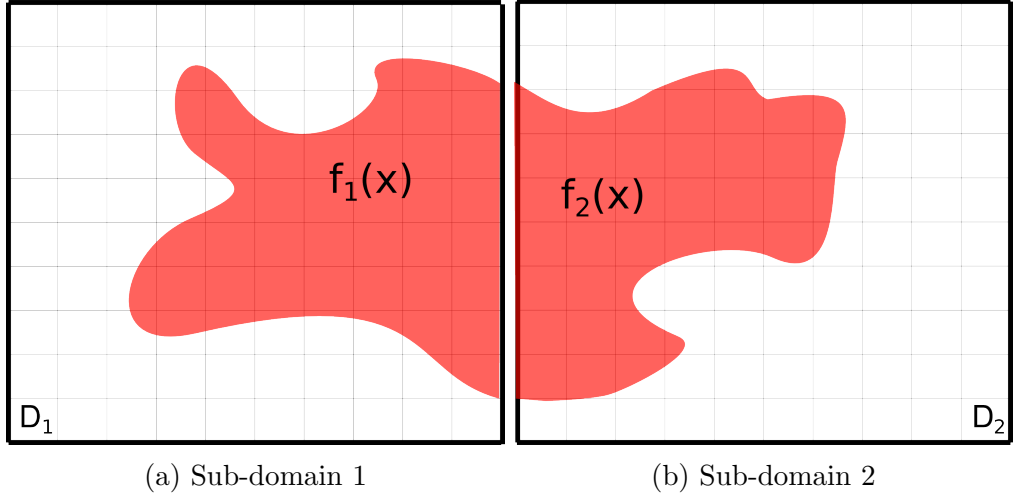
Figure 2.4: The decomposition of Domain D in two sub-domains D_1 and D_2.

In order to retain continuity across D and for w to be the exact solution with $w = \sum_{i=1}^{N} w_i(\vec{x})$, proper boundary conditions must be applied to ∂D_i.

While the free space problem over the full domain requires space data of compact support; for the sub-domains problem this may not hold. For this reason, all sub-domains D_i are extended to $D_{ei} \subset D_i$ as shown in Figure 2.5 .

So, for every D_i the homogeneous boundary condition problem becomes:

$$\begin{aligned} \nabla^2 w_{0i} &= f_i(\vec{x}), \quad \vec{x} \in D_{ei}, i = 1, N \\ w_{0i} &= 0, \qquad \vec{x} \in \partial D_{ei}, i = 1, N \end{aligned} \tag{2.40}$$

The solution of the above problem, determines the source distribution on ∂D_{ei}:

$$\sigma_i = \frac{\partial w_{0i}}{\partial \vec{n}}, \quad \vec{x} \in \partial D_{ei} \tag{2.41}$$

By combining w_{0i} and σ_i the solution $\tilde{w}_i$ in sub-domain D_i is calculated by solving the following problem:

$$\begin{aligned} \nabla^2 \tilde{w}_i &= f_i(\vec{x}), \quad \vec{x} \in D_{ei}, i = 1, N \\ \tilde{w}_i &= \sigma_i, \qquad \vec{x} \in \partial D_{ei}, i = 1, N \end{aligned} \tag{2.42}$$
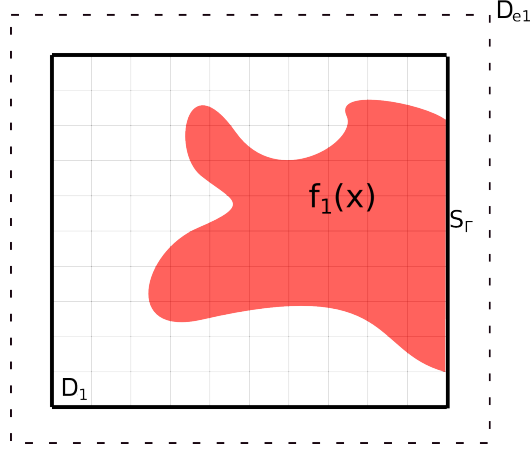
Figure 2.5: Illustration of the extended sub-domain.

In contrast, for the full space problem, the solution of equation 2.42 is not complete because the boundary conditions that determined 2.40 concern only the spatial forcing of the corresponding sub-domain and do not take into consideration the induced terms from the rest.

The completion of the boundary condition is accomplished by superimposing on ∂D_i all contributions that have not been previously calculated. In the example of the two sub-domains, for all x_0 on ∂D_1 that do not share common boundaries with subdomain 2, $w_{B1}(x_0)$ is given by:

$$w_{B1}(\vec{x}_0) = \tilde{w}_1 + \sum_{\vec{x} \notin \partial D_{e1}} G * \sigma(\vec{x}) \tag{2.43}$$

The first term of the above expression is the self contribution of sub-domain (1) on its own boundary ∂D_1, while the second term refers to the induction of sub-domain (2) on the boundary terms of (1).

At the interfacing boundary of the example, ∂D_{e1} and ∂D_{e2} (S_1 and S_2) the information given by the source distribution must be appropriately transferred, so the continuity holds across the interface S_Γ:

$$w_1 = w_2, \vec{x} \in S_\Gamma \tag{2.44}$$

$$[\frac{\partial w_1}{\partial n}] = -[\frac{\partial w_2}{\partial n}], \vec{x} \in S_\Gamma \tag{2.45}$$

Since the boundary conditions must be equal on both S_1 and S_2, the values of w on $x_0 \in S_\gamma$ should be:

$$w_{B1}(\vec{x}_0) = \tilde{w}_1 + \tilde{w}_2, \quad \vec{x}_0 \in S_\gamma \tag{2.46}$$

27

where, $\tilde{w}_2$ is the local solution in sub-domain (2). These two equations, complete the boundary conditions on sub-domain (1), on ∂D_1. For the second sub-domain, the same method is applied.

In general, the algorithm that is followed in order to obtain the correct boundary conditions in every sub-domain takes the following form:

$$\nabla^2 w_i = f_i, \qquad\qquad\qquad \vec{x} \in D_i,\ i = 1, N$$
$$w_i(\vec{x}) = \sum_{\vec{x} \in \partial D_k} \tilde{w}_k(\vec{x}) + \sum_{\vec{x}_m \notin \partial D_{ei}} G * \sigma_m(\vec{x}), \vec{x} \in \partial D_i,\ i = 1, N \qquad (2.47)$$

where, the first sum of $\tilde{w}$ includes the corresponding local (self-) solution of sub-domain i. If there are any interfacing boundaries, the neighboring sub-domains solutions are also added. The second term takes into consideration the contribution of the far-field boundaries of all the remaining sub-domains, which are not in direct contact with sub-domain (i).

Multi-domain formulation (2.47) contains a convolution term that remains expensive to calculate. In fact, as the number of sub-domains N increases, the cost of this calculation may become excessively high. The above problem can be avoided by applying the $Method\ of\ Local\ Corrections$ [95] (MLC).

The method is based on the far-field behavior of G, that allows using coarser approximations in order to account for the distant contributions. To this end, a coarser grid is introduced in which, the far-field term of equation (2.47) is approximated. Let w_c denote the coarse grid solution. Even if w_c will contain the distant term, it will also include the terms of the local and neighboring solutions that are already added in the first term. Thus, they must be subtracted. One method to avoid taking twice the contributions from the coarse grid, is to interpolate the already contained background information in $\tilde{w}_i$ on the coarse grid $\tilde{w}_{ck}$ and subtract it from the coarse solution. Then for the individual block i the convolution term takes the following expression:

$$\sum_{\vec{x}_m \notin \partial D_{ei}} G * \sigma_m(\vec{x}) = w_c - \sum_{\vec{x} \in \partial D_k} \tilde{w}_{ck}(\vec{x}) \qquad (2.48)$$

and the final form of the problem in every sub-domain is:

$$\nabla^2 w_i = f_i, \qquad\qquad\qquad \vec{x} \in D_i,\ i = 1, N$$
$$w_i(\vec{x}) = \sum_{\vec{x} \in \partial D_k} \tilde{w}_k(\vec{x}) + \left[w_c - \sum_{\vec{x} \in \partial D_k} \tilde{w}_{ck}(\vec{x}) \right], \qquad \vec{x} \in \partial D_i,\ i = 1, N \qquad (2.49)$$

For example, for the 3 points marked at the grid (Figure 2.6) the boundary values are given by:

$$w_A = \tilde{w}_2 + \left[w_c - \tilde{w}_{c2} \right] \qquad (2.50)$$
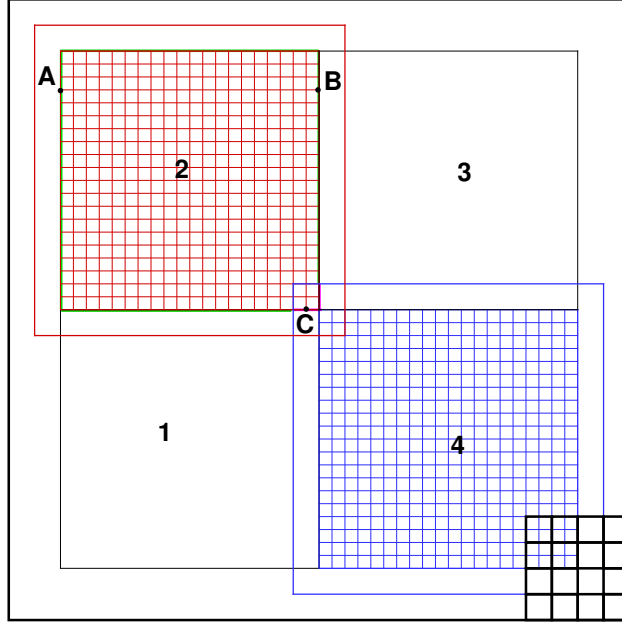
Figure 2.6: Two blocks are shown in red and blue together with their corresponding extensions marked by the same color line. In black a portion of the overlaid coarse grid that covers the complete domain is shown. Corresponding to the domains depicted, the green boundary is treated using the coarse grid while the purple boundary using the local solution.

$$w_B = \tilde{w}_2 + \tilde{w}_3 + \left[w_c - \tilde{w}_{c2} - \tilde{w}_{c3} \right] \tag{2.51}$$

$$w_C = \tilde{w}_2 + \tilde{w}_3 + \tilde{w}_1 + \tilde{w}_4 \tag{2.52}$$

Based on the above, the algorithm is split into four discrete steps:

- Step 1: Solve the homogeneous problem in every extended sub-domain D_{ei} and obtain w_{0i}, calculate σ_i on ∂D_{ei} and solve the boundary problem in D_{ei} in order to obtain the local solution $\tilde{w}_i$, i.e. (2.40) , (2.42).

- Step 2: Solve the full problem using a coarse grid (see Fig. 2.6) and obtain w_c.

- Step 3: Combine the local solutions $\tilde{w}_i$ and the coarse one w_c and define the correct Dirichlet boundary data w_i on ∂D_i for every sub-domain D_i.

- Step 4: Solve the Poisson Dirichlet problem in every sub-domain and obtain w_i, i.e. (2.49).

2.2.3 Symmetry conditions

In case the problem is symmetric over a plane, $\partial Dsym$, the forcing f may not be zero on $\partial Dsym$. Since the algorithm assumes forcing of compact support, boundary conditions on the symmetry plane may not be easy to satisfy. To overcome this difficulty, the boundary conditions on $\partial Dsym$ can be either Dirichlet or Neumann depending on the nature of the problem:

$$\nabla^2 w = f(\vec{x}), \qquad\qquad \vec{x} \in D$$

$$w = w_B, \qquad\qquad\qquad \vec{x} \in \partial D(Dirichlet) \tag{2.53}$$

$$w = w_D, or \frac{\partial w}{\partial n} = A, \qquad \vec{x} \in \partial D_{symmetry}(Dirichlet/Neumann) \tag{2.54}$$

where, n denotes the direction that is normal to the symmetry plane, w_D and A are case specific constants that can obtain any real number value.

Taking into consideration the above restrictions that arise in a symmetric problem, the algorithm is modified in order to determine the correct boundary conditions on every sub-domain. The steps that are followed in order to apply the algorithm to a symmetric problem and obtain the correct solution are:

- Step 1: Solve the free space problem in every extended sub-domain D_{ei} and obtain w_{0i}; calculate σ_i on ∂D_{ei} ; solve again the free space problem on D_{ei} in order to obtain the local solution $\tilde{w}_i$, i.e. (2.29) , (2.42).

- Step 2: Solve the symmetric problem in every sub-domain that is attached to the symmetry plane $\partial D_{symmetry}$ and obtain $w_{0symmetry,i}$, calculate σ_i on ∂D_{ei} and and solve again the problem in order to obtain the local solution $\tilde{w}_{symmetry,i}$, i.e. (2.29) , (2.42).

- Step 3: Solve the symmetric problem using a coarse grid (see Fig. 2.7) and obtain $w_{c,symmetry}$, i,e, (2.54).

- Step 4: Combine the local solutions $\tilde{w}_i$, $\tilde{w}_{symmetry,i}$ and the coarse one $w_{c,symmetry}$ and define the correct boundary data w_i on ∂D_i for every sub-domain D_i.

- Step 5: Solve the Poisson problem in every sub-domain and obtain w_i, i.e. (2.49).

In order to better illustrate the algorithm and how symmetry is handled, Figure 2.7 depicts a symmetric domain that is divided in 4 sub-domains. The first step of the algorithm is applied to all 4 extended sub-domains and then the local boundary conditions are obtained at ∂D_i. Moving to step two, the coarse grid is solved but is extended away of only the three faces; those not in contact with the symmetry plane. In the third step, the symmetric conditions are applied only for subdomains 1 and 4 because they are in contact with the symmetry plane.
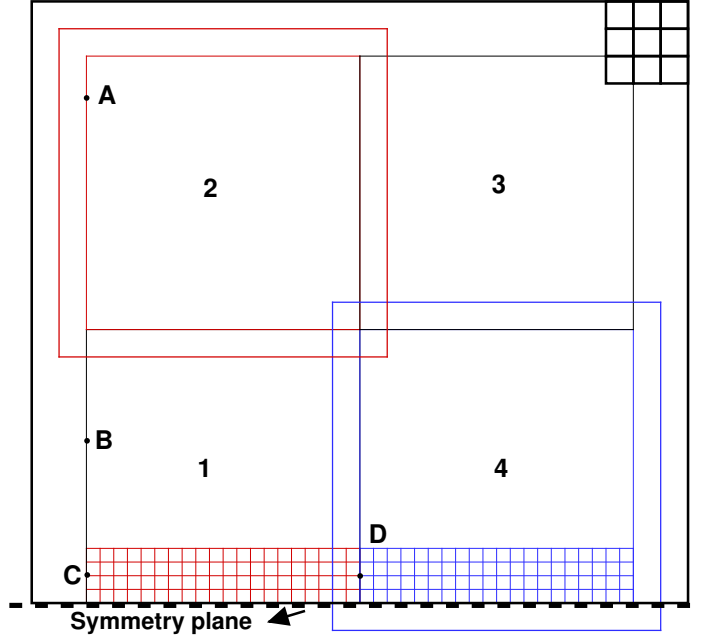
Figure 2.7: The symmetric problem grid is demonstrated is a problem that is divided in 4 sub domains. Sub-domains 1 and 4 are attached to the symmetry plane. the coarse grid (in black color is bounded on the symmetry plane. The red and blue colored grids represent the area where the error is significant, so the symmetric solution of the individual fine grid is used.

At this point, the algorithm has calculated the symmetric local solutions at the sub-domains near the symmetry by extending the domain away from only three faces, as for the coarse grid. The fourth step combines the previous calculated boundary conditions. For the four points (A, B, C, D) of Figure 2.7 the boundary conditions are defined as follows:

Point A:

$$w_A = \tilde{w}_2 + \left[w_{c,symmetry} - \tilde{w}_{c2} \right] \tag{2.55}$$

Because Block 1 solved the space problem without symmetry, the background information $\tilde{w}_2$ is interpolated and subtracted from the coarse solution. The symmetry is added to the solution only through the coarse grid.

Point B:

$$w_B = \tilde{w}_1 + \left[w_{c,symmetry} - \tilde{w}_{c1} \right] \tag{2.56}$$

While point B belongs to Block 2 and the symmetry problem is solved, the space solution is used because the distance of B from the symmetry plane is big. This happens because as explained before, Green's function decays fast and the error from the coarse grid becomes relatively small when the calculation points are not close to the symmetry plane.

On the contrary, at points adjacent to the symmetry plane, the symmetric solution is used. The threshold between using the one over the other solution had been defined for all blocks at about 4 cells of the coarse grid. The criterion was that the error of the solution at the end of the region where the symmetric contribution is used, to be relatively small. In this manner for points C and D:

Point C:

$$w_C = \tilde{w}_{symmetry,1} + \left[w_{c,symmetry} - \tilde{w}_{c1,symmetry} \right] \qquad (2.57)$$

Point D:

$$w_D = \tilde{w}_{symmetry,1} + \tilde{w}_{symmetry,4} + \left[w_{c,symmetry} - \tilde{w}_{c1,symmetry} - \tilde{w}_{c4,symmetry} \right]$$
$$(2.58)$$

Now that the boundary conditions have been determined for every sub-domain, the Poisson equation is solved and the correct solution is obtained both on the far-field and on the symmetry plane.

2.2.4 Projection and Remeshing

Particle approximations are defined as scattered data while the formulation of particle mesh methods assumes continuous distributions in space. Because PM methods solve the Poisson equations on a uniform Cartesian grid, space information must be projected onto the grid. In this direction, vorticity $\vec{\omega}$ and dilatation θ from the particles are projected onto the grid using a projection function. Once the velocity field $\vec{u}$ is obtained on the PM grid, the right hand side of the Lagrangian equations is calculated. Then both $\vec{u}$ and the RHS's of equations 2.15, 2.16, 2.17, 2.18 are transferred back (interpolated) to the particles. In this section, the required projection and interpolation operators are defined.

Let $Q_p = q_p \cdot V_p$ denote any flow quantity carried by the particles. Then on the grid the corresponding density is obtained by the following projection operation:

$$q_{i,j,k} \equiv \text{Proj}_{\text{PM}}(q_p; V_p) = \frac{\sum_p q_p V_p W(\vec{x}_{i,j,k} - \vec{Z}_p)}{\sum_p V_p W(\vec{x}_{i,j,k} - \vec{Z}_p)} \qquad (2.59)$$

where $\vec{x}_{i,j,k}$ denotes the position of the i, j, k grid node (also denoted as I),

$$W(\vec{r}) = W_1(r_x/h)W_1(r_y/h)W_1(r_z/h)$$
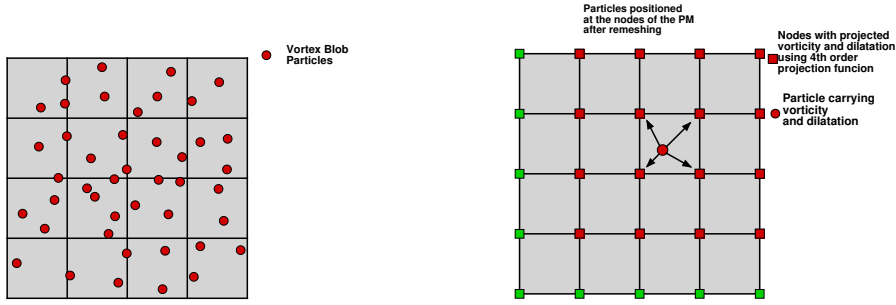
(a) Random particles position before remeshing (b) Particles positioned in a grid after remeshing

Figure 2.8: Schematic representation of the remeshing technique applied on a 2D Cartesian grid

$\vec{r} = (r_x, r_y, r_z)$, h denotes the grid spacing and W_1 the 1D interpolation function used. Inversely, any quantity defined on the grid, can be interpolated back to the particles positions using the same interpolation function:

$$q_p \equiv \text{Interp}(q_{i,j}) = \sum_{i,j,k} q_{i,j,k} W(\vec{x}_{i,j,k} - \vec{Z}_p) \qquad (2.60)$$

A well known problem in particle methods concerns the gradual loss of regularity in time. The spreading of particles can result in loss of accuracy while high particle concentration can lead to numerical instabilities [88].

This is analogous to grid irregularity or stretching in standard CFD solvers, which is corrected with grid refinement. Of course in principle the grid is generated so that there are no such issues. This is not always easy or guaranteed. In flow problems involving the evolution and/or propagation of steep gradients, the original grid may turn out to be inadequate. For this reason, grid refinement is needed. A similar procedure is also needed and applied in particle methods. Now the role of the grid is taken over by the particles themselves and grid refinement corresponds to the so called *remeshing*. Remeshing aims at recovering the conditions set by error analysis so that consistency and accuracy of the numerical solution is best served. In this respect, the particle volumes must cover the full space and be regularly re-distributed in space. In Particle Mesh methods these requirements are related to the size of the grid in combination with the interpolation function W that is used in (2.59) and (2.60).

Re-meshing is the action of re-positioning the particles at regularly ordered positions every N time steps (see fig. 2.8). The quantities carried by the relocated particles are interpolated from the PM grid at the new particle positions using (2.60). A point of concern in this respect, is that re-meshing adds numerical

diffusion. For example the support of $\vec{\omega}$ will spread out along its boundary and points that previously had zero vorticity will receive at least a small amount of $\vec{\omega}$. A way to limit numerical diffusion is to perform re-meshing on a denser grid than the PM one.

The volume assigned to the re-meshed particles is the *geometrical* volume (i.e. the volume of a PM cell, DV_{PM}) in order to keep the scheme conservative. Therefore special care is needed in order to ensure conservation of the flow properties carried by the particles. When changing the volume in the re-meshing procedure, any quantity Q carried by the particles must be conserved. Thus, when changing the volume of a particle V_i to the geometrical V_{ref}, conservation of quantities at particle level are ensured with the following scaling:

$$Q_{ref} = Q_i \Rightarrow \quad q_{ref}V_{ref} = q_iV_i \Rightarrow$$
$$q_i = \frac{Q_{ref}}{V_i} \quad \text{or} \quad q_{ref} = \frac{Q_i}{V_{ref}} \tag{2.61}$$

The above relation implies that the volume used in the projection operation (2.59) is the volume the particles will get after they are placed in their new (ordered) positions.

In case of symmetry problems, the projection on the grid and the interpolation back to the particles must be modified near the symmetry plane ∂D_{sym}. In order to retain a property Q of a particle inside D and at the same time include the contribution of the symmetric domain D' according to the mirroring technique, the following procedure is applied:

Let P be a particle carrying the fluid properties and P' be its symmetric one as seen in Figure 2.9. If $\vec{x}_p$ is within the 1st layer of PM cells above ∂D_{sym} part of Q carried by P will be projected onto the symmetry plane and underneath it. In order to be conservative the image P' of P is added so that any lost information is recovered.

$$f = Q_{proj}(P) + Q_{proj}(P') \tag{2.62}$$

The projected image properties of P' are defined by the symmetry conditions dictated by the mirroring technique as follows:

- $m_1 = m_{1'}$

- $V_1 = V_{1'}$

- $\Omega_{1,x} = -\Omega_{1',x}$

- $\Omega_{1,y} = -\Omega_{1',y}$

- $\Omega_{1,z} = \Omega_{1',z}$

- $\Theta_1 = \Theta_{1'}$
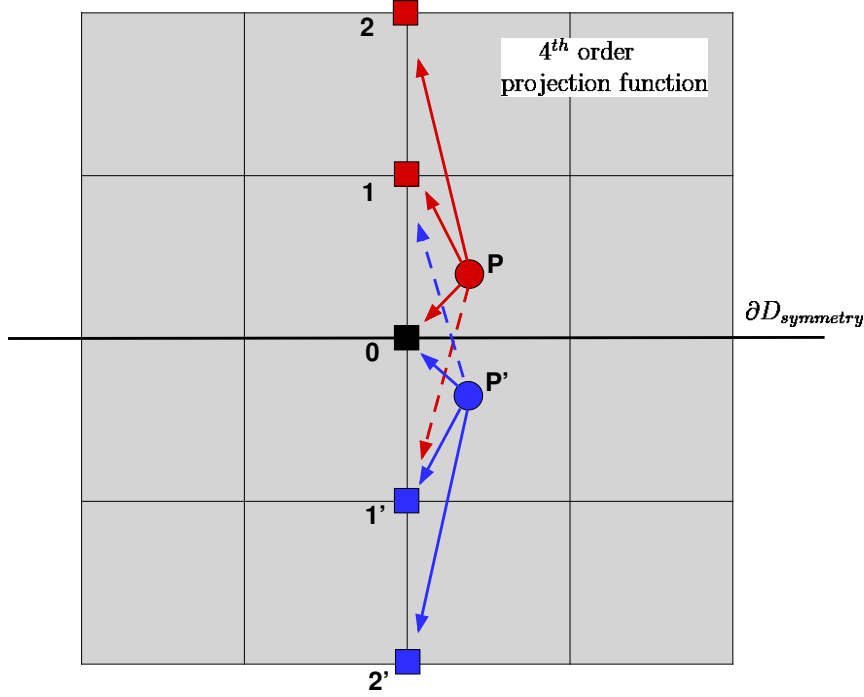
Figure 2.9: Projection near the symmetry plane

- $\Pi_1 = \Pi_{1'}$

In the opposite direction, when a property Q must be interpolated from the PM grid at the position of the particle P the corresponding image of the particle P' must be subtracted.

2.2.5 The Lagrangian Solver

For a given collection of Particles: $\{\vec{Z}_p^n,\, m_p^n,\, V_p^n,\, \vec{\Omega}_p^n,\, \Theta_p^n,\, \Pi_p^n\}$ at $t = n\Delta t$:

Step 1: Project $\{m_p^n,\, \Theta_p^n,\, \vec{\Omega}_p^n,\, \Pi_p^n\}$ on the PM grid
            and get: $\rho_{i,j}^n,\, \theta_{i,j}^n,\, \vec{\omega}_{i,j}^n,\, \varepsilon_{i,j}^n$.

Step 2: Calculate $-\nabla \times \vec{\omega}$ on the PM grid

Step 3: Solve $\nabla^2 \phi = \theta, \nabla^2 \vec{u_\omega} = -\nabla \times \vec{\omega}$,
            and obtain: $\phi_{i,j}^n,\, u_{\omega,i,j}^n,\, \vec{u}_{i,j}^n$

Step 4: Calculate on the PM grid the RHS of (2.15)

Step 5: Interpolate all grid based data q_{ij}^n at the particle positions:
            $q_p^n = \sum_{ij} q_{ij}^n\, W(\vec{x}_{i,j} - \vec{Z}_p)$

Step 6: Update all particle properties (integrate (2.15) in time)

Step 7: Re-mesh if needed

In Step 4, the Right Hand Side of (2.15) are obtained by means of central Finite Differences on the Particle Mesh grid. The time integration is performed using a 4th order Runge-Kutta scheme.

2.2.6   Acoustic wave damping

In the present formulation, acoustic waves are primary linked to dilatation variations. Hence, when a finite region is used, these waves can reflect at the outer boundary of the domain and create computational errors. A remedy to that is to add artificial damping in the dilatation equation:

$$\theta_{i,j,k}^{n+1} = \theta_{i,j,k}^n + \Delta t \cdot (RHS_{i,j,k} - \theta_{i,j,k}^n \cdot damp) \tag{2.63}$$

where,

$$damp = rate \cdot \sqrt{damp_x^2 + damp_y^2 + damp_z^2} \tag{2.64}$$

$rate$, is a case dependent constant, while $damp_x$, $damp_y$, $damp_z$ are the dumping functions and can take values within (0,1). Damping is activated over a specific region that ends at the outer boundary X_{outer} and starts at $X_{outer} - length_{damping}$.

$$damp_* = \min(1, \frac{x_{i,j,j} - (X_{outer} - length_{damping})}{length_{damping}}) \tag{2.65}$$

The $rate$ and $length_{damping}$ are chosen so that $\theta \equiv 0$ outside the PM domain.

2.3   The potential particle solver - GenUVP

Using Helmholtz's decomposition of the velocity field and taking into consideration equation (2.23), the flow problem is formulated in the context of lifting potential theory, assuming that the flow is incompressible and inviscid. So $\theta \equiv 0$, while free vorticity is concentrated on vortex sheets. In this context, Green's theorem gives:

$$\vec{u}_\phi(\vec{x}; t) = \int_{S(t)} (\sigma(\vec{y}, t) \cdot + \vec{\gamma}(\vec{y}, t) \times) \nabla G(r) \, dS(\vec{y}) \tag{2.66}$$

$$\vec{u}_\omega(\vec{x}; t) = \int_{D_\omega(t)} \vec{\omega}(\vec{y}; t) \times \nabla G(r) \, dD(\vec{y}) \tag{2.67}$$

where, $G(r) = -\frac{1}{4\pi r}$, $r = |\vec{r}|$, $\vec{r} = \vec{x} - \vec{y}$, $\nabla G(r) = \frac{\vec{r}}{4\pi r^3}$, $D_\omega(t)$ denotes the wake region which coincides with the support of $\vec{\omega}$ and $S(t)$ denotes collectively the solid boundaries.

2.3.1 Equations and conditions

GenUVP is a potential free vortex particle solver developed in the Laboratory of Aerodynamics of NTUA and has been used in a variety of problems, e.g. [96] and [97]. On solid surfaces S the non-penetration condition is imposed. By creating a surface grid on S, the geometry is divided into a finite number of panels. Every panel carries source and doublet distributions, σ and $\vec{\gamma}$ respectively. Surface distributions are defined by jump conditions for $\vec{u}$ in the normal and tangent to S directions:

$\sigma = [\vec{u}] \cdot \vec{n}$ and $\vec{\gamma} = [\vec{u}] \times \vec{n}$.

In potential theory the latter is associated to a dipole distribution

$\mu = [\phi]$: $\vec{\gamma} = \nabla\mu \times \vec{n}$.

A usual simplification, which is also here adopted, assumes that lifting bodies are thin. In such a case, S will only carry a dipole distribution μ and generate only surface vorticity $\vec{\gamma}$. In order to determine the unknown singularity distributions, the following conditions are applied:

a)The non-penetration condition on solid boundaries
The non-penetration boundary condition on S, is applied at the centres of the panels, which in the case of a surface S that moves with velocity $\vec{U}_S$ takes the form:

$$\vec{u}_{cp} \cdot \vec{n}_{cp} = \vec{U}_S \cdot \vec{n}_c p$$

where, $\vec{n}$ denotes the unit normal to S. In the general case $\vec{U}_S$ will include any rigid-body motion (e.g. rotation, pitch actuation) or deformation motion if flexibility is also accounted for.

b)The Kutta condition and Kelvin's Theorem
The vorticity emission condition, also known as Kutta condition, in the incompressible case, imposes zero pressure jump across the wake. It is applied along predefined emission lines of solid surfaces, such as the trailing edge or blade tips. This condition is connected to the generation of lift and defines the amount of emitted vorticity in the wake, that in the process of time builds up $\vec{\omega}$. Kelvin's theorem $\frac{D\Gamma}{Dt} = 0$ states that the total vorticity of the domain should remain zero at any given time.

c) Vorticity equation
The Helmholtz equation for vorticity transport, is derived from the momentum equation by taking its curl. This equation defines the evolution of $\vec{\omega}$ in the wake. Hence, at every time step, $\vec{\omega}$ is imported in equation 2.67 and the velocity field due to spacial vorticity is known.
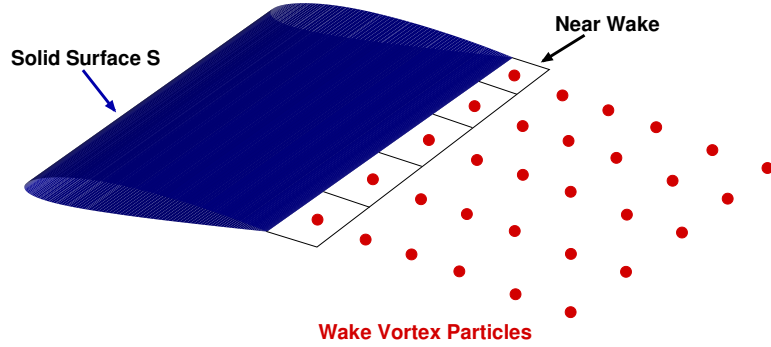
Figure 2.10: The flow domain in the case of an external flow around a solid body. Red circles denote the particles.

In potential theory, wake is introduced as a material surface that carries surface vorticity $\vec{\gamma}_W = \vec{n} \times [\vec{u}]$, where $[\vec{u}]$ denotes the velocity jump which is assumed to have zero normal component. Existing wake models differ on the choice of elements that describe the wake, but most importantly on whether or not the wake elements are connected. These requirements are by construction fulfilled when the wake is formed by vortex filaments or when the wake retains its structure as a surface. Connectivity however can generate numerical problems when wake deformation is excessive or when there is close interaction with solid bodies as in the present case. In order to bypass this shortcoming, free vorticity is represented by a collection of vortex blobs (see fig. 2.10). They are 3D point vortices equipped with a core and defined by their intensities $\vec{\Omega}_p$, their positions $\vec{Z}_p$ and their core size ϵ [98]:

$$\vec{\omega}(\vec{x};t) \cong \sum_p \vec{\Omega}_P(t)\, \zeta_\epsilon(\vec{x} - \vec{Z}_P(t)) \tag{2.68}$$

where ζ_ϵ is the cut-off or space distribution function. In the present work, the cubic exponential function is used which results in the following discrete velocity

representation:

$$\vec{u}_\omega(x;t) = \sum_p \vec{\Omega}_P(t) \times \nabla G(r_P)\,(1 - exp(r_p^3/\epsilon^3)), \;\; \vec{r}_p = \vec{x} - \vec{Z}_P \qquad (2.69)$$

where ϵ is $1.5 : 2$ times the length scale of the mean distance between neighboring particles in the wake. Vortex particles are generated at every time step in a two-step procedure. Firstly, the wake is released in the form of surface vorticity and keeps this form until the no-penetration and Kutta conditions are satisfied and $\vec{u}$ is determined. Then, in the convection step that follows, surface vorticity is integrated and transformed into vortex particles so that the zero and first moments of vorticity are conserved:

$$\vec{\Omega}_P(t) = \int_{D_\omega} \vec{\omega}(\vec{y};t)\,dD, \;\; \vec{\Omega}_p(t) \times \vec{Z}_P(t) = \int_{D_\omega} \vec{\omega}(\vec{y};t) \times \vec{y}\,dD \qquad (2.70)$$

while $\vec{\Omega}_P$ and $\vec{Z}_P$ are determined by integrating in time the corresponding evolution equations:

$$\frac{d\vec{Z}_P(t)}{dt} = \vec{u}(\vec{Z}_P;t), \; \frac{d\vec{\Omega}_P(t)}{dt} = (\vec{\Omega}_P(t) \cdot \nabla)\vec{u}(\vec{Z}_p;t) \qquad (2.71)$$

Even though in this section the term *vortex particles* is used, one should not be confused with the term particles that had been used previously in this chapter. The vortex particles that are used in potential theory and in $GenUVP$ do not reproduce the flow field. In inviscid potential theory, vorticity should only exist on body surfaces and the wake. So, vortex particles are an alternative representation of the shear layer that is emitted along the prescribed emission lines (trailing edge, etc).

Anyway, time evolution of vorticity can be a demanding process as the number of vortex particles increases. This increase is exponential in time and can penalize an efficient medium fidelity tool into an expensive one even if these calculations are performed in parallel using the MPI protocol. So in order to keep cost affordable, the particle mesh technique is employed as described in section 2.2.

2.3.2   Load calculation

Once σ and γ are obtained, $\vec{u}$ and ϕ can be calculated on the bodies. Hence, at the end of every time step pressure P on the surface of the solid boundary S is calculated using the momentum equation :

$$\nabla(\frac{\partial \phi}{\partial t} + \frac{\vec{u}^2}{2} + \frac{P}{\rho}) + \frac{\partial \vec{u}_\omega}{\partial t} + \vec{\omega} \times \vec{u} + \nabla(\frac{q}{\rho}) = 0 \qquad (2.72)$$

In order this equation to hold, the last two terms must be equal to the gradient of a scalar quantity q, which would represent the extra pressure due to the wake and

so:

$$P = P_{pot} + q \tag{2.73}$$

Then P_{pot} can be determined by the Bernoulli equation (2.74), while q is determined by taking the divergence of the remaining terms and taking into account that $\vec{u_\omega}$ is div free (2.75):

$$\nabla(\frac{\partial \phi}{\partial t} + \frac{\vec{u}^2}{2} + \frac{P_{pot}}{\rho}) = 0 \tag{2.74}$$

$$\frac{\nabla^2 q}{\rho} = -\nabla(\vec{\omega} \times \vec{u}) \tag{2.75}$$

In the presence of thin bodies carrying surface dipole distribution, the jump of pressure is calculated by introducing into (2.72) the jump of ϕ and $\vec{u}$ on the solid surfaces, $[\phi], [\vec{u}]$. By integrating the pressure over the body surface S the total body forces are obtained :

$$\vec{F} = \int_S -(P - P_\infty) \cdot \vec{n} ds \tag{2.76}$$

2.4 The Eulerian Solver - MaPFlow

The usual way to simulate flows in the presence of solid bodies, is to solve the Eulerian expression of the governing equations on a spatial grid. This ensures that the boundary conditions on surfaces are met correctly. In addition, CFD methods can include viscous and compressible effects (flow separation, formation of boundary layers, shock waves) that are essential components of a helicopter analysis. In this section the basic equations of the CFD solver as implemented in MaPFlow are described. MaPFlow is an in house software, developed in Papadakis' thesis ([18]).

2.4.1 Governing equations and implementation

Let D denote a volume of fluid and ∂D its boundary. By integrating the governing equations over D, the following integral form is obtained:

$$\int_D \frac{\partial \boldsymbol{U}}{\partial t} dD + \oint_{\partial D} (\boldsymbol{F_c} - \boldsymbol{F_v}) dS = \int_D \boldsymbol{Q} dD \tag{2.77}$$

In (2.77) $\boldsymbol{U}$, is the vector of the Conservative Flow Variables,

$$\boldsymbol{U} = \begin{pmatrix} \rho \\ \rho u \\ \rho v \\ \rho w \\ \rho E \end{pmatrix} \tag{2.78}$$

40

where ρ denotes the density, (u, v, w) the three components of the velocity field, and E the total energy, while $\boldsymbol{F_c}$ and $\boldsymbol{F_v}$ denote the Convective and Viscous Fluxes respectively,

$$\boldsymbol{F_c} = \begin{pmatrix} \rho V \\ \rho u V + n_x p \\ \rho v V + n_y p \\ \rho w V + n_z p \\ \rho(E + \frac{p}{\rho})V \end{pmatrix} \qquad (2.79)$$

$$\boldsymbol{F_v} = \begin{pmatrix} 0 \\ n_x \tau_x x + n_y \tau_x y + n_z \tau_x z \\ n_x \tau_y x + n_y \tau_y y + n_z \tau_y z \\ n_x \tau_z x + n_y \tau_z y + n_z \tau_z z \\ n_x \Theta_x + n_y \Theta_y + n_z \theta_z \end{pmatrix} \qquad (2.80)$$

In (2.80), V is the contravariant velocity, $V = \vec{u} \cdot \vec{n}$ and

$$\Theta_x = u\tau_{xx} + v\tau_{xy} + w\tau_{xz} + k\frac{\partial T}{\partial x}$$
$$\Theta_y = u\tau_{yx} + v\tau_{yy} + w\tau_{yz} + k\frac{\partial T}{\partial y}$$
$$\Theta_z = u\tau_{zx} + v\tau_{zy} + w\tau_{zz} + k\frac{\partial T}{\partial z} \qquad (2.81)$$

The above system is completed with the equation of state for perfect gases:

$$p = (\gamma - 1)\rho \left[E - \frac{u^2 + v^2 + w^2}{2} \right] \qquad (2.82)$$

In the present work (2.77) is solved with MaPFlow which is a compressible, cell centered CFD solver, which employs both structured and unstructured grids. The convective fluxes are discretized using the approximate Riemann solver of Roe [99] with Venkatakrishnan limiter [100], [101], while the viscous fluxes are discretized using a central 2nd order scheme. Turbulence closure includes several options; the one equation turbulence model of Spalart (SA) ([102]), as well as the two equation turbulence model of Menter ($k - \omega$ SST) [103]. MaPFlow can handle both steady and unsteady flows, the latter being an important requirement for aerodynamic tools employed for helicopter analysis. Time integration is achieved in an implicit manner permitting large CFL numbers. The unsteady calculations use a 2nd order time accurate scheme combined with the dual time-stepping technique(9) to facilitate convergence when complex unsteady flows with moving or deforming geometries are considered. Additionally, flows in the incompressible region are simulated using Low Mach Preconditioning [104].

Dual Time-Stepping

The Dual Step approach ([105]) adds an extra time-like derivative in the transport equation that refers to a different "time variable" τ, called "pseudo-time". The conservative variables in the pseudo-time problem are denoted by $U^\star$ because until convergence they do not satisfy the original unsteady problem.

Using this approach the unsteady problem is transformed into a steady one. In every true time-step the following problem is solved in the pseudo-time (τ) :

$$\frac{\partial(D^{n+1}\vec{U}^\star)}{\partial\tau} + \vec{R}^\star = 0 \tag{2.83}$$

Setting,

$$\vec{R}^\star = \frac{\partial(D\vec{U}^\star)}{\partial t} + R(\vec{U}^\star) \tag{2.84}$$

the following final form is obtained:

$$\frac{\partial(D^{n+1}\vec{U}^\star)}{\partial\tau} + \frac{\partial(D\vec{U}^\star)}{\partial t} = -R(\vec{U}^\star) \tag{2.85}$$

When (2.83) converges $R^\star = 0, \vec{U}^\star = \vec{U}$ which satisfies the original unsteady problem.

The discretized form of (2.85) can be written as:

$$\frac{D^{n+1}\Delta U^{\star k}}{\Delta\tau} + \frac{1}{\Delta t}\left[\phi_{n+1}\left(D\vec{U}^\star\right)^{n+1} + \phi_n\left(D\vec{U}\right)^n + \right.$$
$$\left. \phi_{n-1}\left(D\vec{U}\right)^{n-1}\right] = -R^{k+1} \tag{2.86}$$

or:

$$\frac{D^{n+1}\Delta U^{\star k}}{\Delta\tau} = -R^{\star k+1} \tag{2.87}$$

with $\Delta U^{\star k} = U^{\star k+1} - U^{\star k}$ and:

$$R^{\star k+1} = R^{k+1} - \frac{1}{\Delta t}\left[\phi_{n+1}\left(D\vec{U}^\star\right)^{n+1} + \phi_n\left(D\vec{U}\right)^n + \right.$$
$$\left. \phi_{n-1}\left(D\vec{U}\right)^{n-1}\right] \tag{2.88}$$

where k denotes the steady state problem sub-iteration.

In order to apply an Implicit Scheme in the Dual Time-Step procedure we must linearize the unsteady residual $R^{\star k+1}$:

$$\vec{R}^{\star k+1} \approx \vec{R}^{\star k} + \left(\frac{\partial \vec{R}}{\partial \vec{U}^{\star}}\right)_{k} \cdot \Delta \vec{U}^{\star k} \tag{2.89}$$

or,

$$\vec{R}^{\star k+1} \approx \vec{R}^{k} - \frac{1}{\Delta t}\left[\phi_{n+1}\left(D\vec{U}^{\star}\right)^{n+1} + \phi_{n}\left(D\vec{U}\right)^{n} + \right.$$
$$\left. \phi_{n-1}\left(D\vec{U}\right)^{n-1}\right] +$$
$$\frac{\partial \vec{R}}{\partial \vec{U}^{\star}}\Delta \vec{U}^{\star} - \phi_{n+1}\frac{D^{n+1}}{\Delta t}\Delta \vec{U}^{\star} \tag{2.90}$$

The correction $\Delta U^{\star}$ refers to the steady problem defined in pseudo-time. Thus, when the steady problem converges $\Delta U^{\star} = 0$. However, this does not mean $U^{n+1} - U^{n} = 0$ but $U^{k+1,n+1} - U^{k,n+1} = 0$. The ϕ coefficients change according to the time discretization scheme desired.

Substituting in (2.87) the final form is obtained:

$$\left[\frac{D^{n+1}}{\Delta \tau} + \phi_{n+1}\frac{D^{n+1}}{\Delta t} + \frac{\partial \vec{R}}{\partial \vec{U}^{\star}}\right]\Delta U^{\star k} = -R^{k} - Q^{k}_{dual} \tag{2.91}$$

where the dual step unsteady source-like terms Q^{k}_{dual} are given by:

$$Q^{k}_{dual} = \frac{1}{\Delta t}\left[\phi_{n+1}\left(D\vec{U}^{\star}\right)^{n+1} + \phi_{n}\left(D\vec{U}\right)^{n} + \right.$$
$$\left. \phi_{n-1}\left(D\vec{U}\right)^{n-1}\right] \tag{2.92}$$

It is noted here that the pseudo time step $\Delta \tau$ is defined as in the Steady state computations using local time-stepping.

2.5   Implementation of the Actuator line model

In the present work, rotor blades are modeled as actuator lines that contribute the corresponding body forces to the source term $\boldsymbol{Q}$ of equation 2.77. The loading is calculated on the basis of blade element analysis along the blade span and in conjunction with tabulated $2D$ polars [106]. The actuator line control points define the location of different blade elements that have specific lift and drag depending on their airfoil type, twist angle, chord length and incoming flow velocity. A resultant body force vector is then assigned to every actuator line control point. Lift and drag are calculated based on the local wind speed and angle of attack as shown in Figure 2.11, and detailed in the following equations:
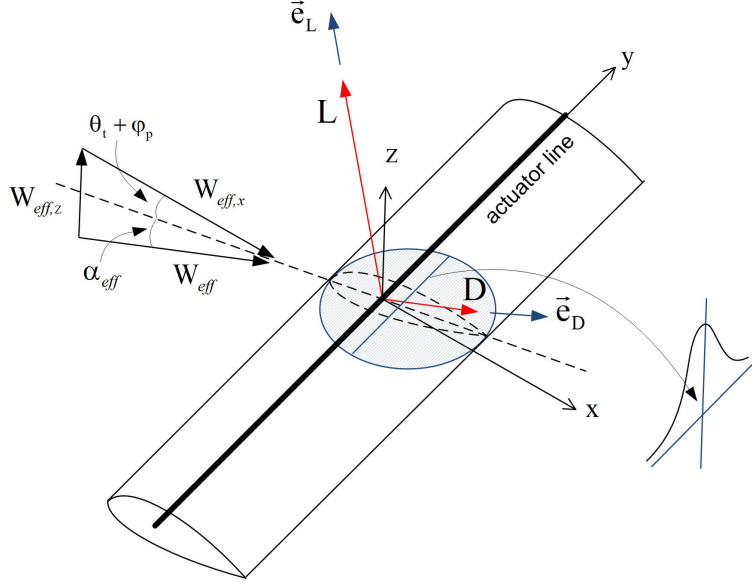
Figure 2.11: Blade element analysis

$$\phi = arctan\frac{W_{eff,z}}{W_{eff,x}} \tag{2.93}$$

$$a_{eff} = \phi - \theta_t - \phi_p \tag{2.94}$$

$$L = \frac{1}{2}\rho W_{eff}^2 C_L(a_{eff})c\Delta r, D = \frac{1}{2}\rho W_{eff}^2 C_D(a_{eff})c\Delta r \tag{2.95}$$

$$\vec{f_{cp}} = L\vec{e}_L + D\vec{e}_D \tag{2.96}$$

where, ϕ is the inflow angle, θ_t is the local twist angle, ϕ_p is the pitch angle of the blade, a_{eff} is the effective angle of attack, $C_L(a_{eff})$ and $C_D(a_{eff})$ are the lift and drag coefficient for the specific angle of attack, ρ is the density of the fluid, W_{eff} is the local two dimensional inflow velocity, c is the blade element characteristic chord, Δr is the width of the blade element, and $\vec{e}_L$, $\vec{e}_D$ are the unit vectors in the direction of lift and drag respectively.

The opposite of this body force and the corresponding energy are then imported as source terms in the momentum and energy equations of the cells that are swept by the blades during their rotation. In order to avoid singularities, the body forces and their corresponding work are numerically spread across a few cells using a $3D$ isotropic Gaussian distribution [107].

$$\vec{f_\epsilon} = \vec{f_{cp}}\eta_\epsilon \tag{2.97}$$

where, $\eta_\epsilon(d) = \frac{1}{\epsilon^3\sqrt{\pi^3}}e^{-\frac{d}{\epsilon}}$ is the regularization Gaussian kernel and $d = |\vec{x}_{cp} - \vec{x}_c|$ is the distance between a cell centered grid point and the control point of a blade element.

$$\vec{f_c} = -\sum_{i=1}^{N_{cp}} \vec{f}_{cp} \eta_\epsilon(cp_i, cell) \tag{2.98}$$

The freestream velocity vector is directly sampled at the release points of modified momentum of the actuator lines [108]. These emission points are also the mid points of the bound vorticity, where the blade local flow effects (upwash and down-wash created by the bound vortex) are negligible. Hence, a consistent estimation of the free-stream velocity is performed. The velocity at the emission points is estimated through a distance and volume weighted interpolation over the computed velocities of the neighboring cells using Radial Basis Functions (RBF) [107].

Even though recommended in [107], tip correction models are not used frequently, since the three-dimensional flow field containing tip and root vortices can be fully resolved, provided that the gird is adequately fine around the actuator lines. Using a small enough characteristic cell length Δx in the region of $\frac{c}{2} - \frac{c}{8}$, the standard blade force distribution suggested by [109] is sufficient to resolve the tip and root vortices. For this reason and in favor of simplicity, the cell sizing is usually preferred over more sophisticated projection techniques (e.g. [110], [111],[107]).

Both Cartesian and cylindrical grids can be treated by the code. However, Cartesian grids are considered more convenient when combining the rotor blades analysis in the same CFD context with a fully resolved 3D geometry (e.g. Main Rotor with Fuselage or Tail Rotor with Shroud). Both structured and unstructured grids can be employed, as long as the characteristic cell length is kept constant in the vicinity of the actuator lines. As a rule of thumb, in most AL implementations the time step has been chosen so that the tip of the actuator line sweeps no more than half cell per time step ($\Delta t \leq 0.5\frac{\Delta x}{V_{tip}}$). A total simulation time that completes no less than 5 rotations is necessary, in order for the initial aerodynamic and dynamic transients to fade out.

With respect to the radial resolution Δr, accuracy is maintained when it is chosen to be at most double the grid spacing $\Delta r \leq 2\Delta x$, so that the spherical regions around the body forces sufficiently overlap with each other in order to produce a continuous force distribution along the blade. Uniform spacing along the blade span has been utilized in most works. Geometric refinement towards the two edges (root and tip) has also been tested, but it turned out to make no difference, since the actuator line spacing ends up to be really fine.

Figure 2.12 illustrates wake vorticity iso-surfaces at the early stages of the wake development. The figure suggests that the actuator line model captures the trailed vorticity released by the tips and roots of the blades. In Figure 2.13 the wake vorticity after 10 revolutions is shown. Trailed vorticity can still be recognized near the blade tips. However, in this hover case, due to the low convection velocity, wake spirals remain closely packed and strongly interact with each other producing thus the contracting shear layer of the far wake and the torus shape starting vortex ring.
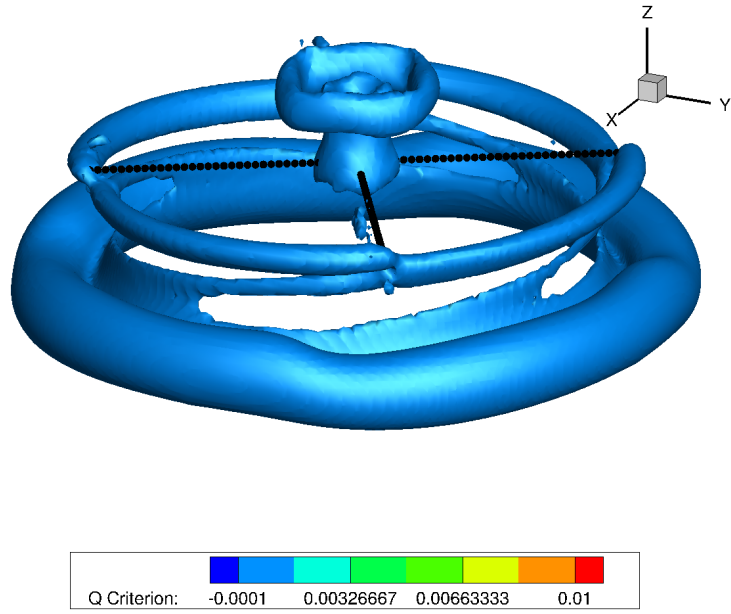
Figure 2.12: Trailing tip and root vortices at an early stage of the simulation.
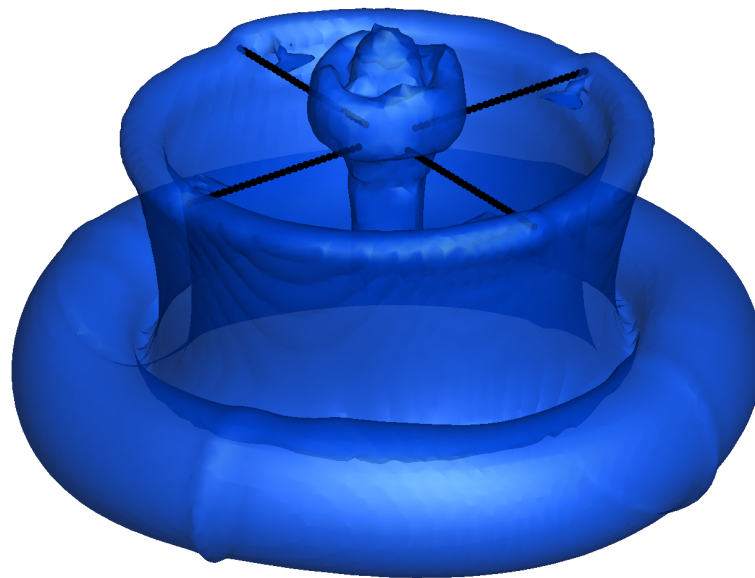
Figure 2.13: Trailing tip and root vortices after 10 rotor revolutions.

2.6   The Hybrid Solver - HoPFlow

The hybrid solver aims at combining the two expressions of the governing equations (Eulerian and Lagrangian) discussed in sections 2.1, 2.4 in a manner that both the far-field and solid boundary conditions are correctly imposed. In the specific formulation, the Lagrangian domain covers the entire space and therefore overlaps the Eulerian one. By choosing to use the PM method in the Lagrangian solver, the Lagrangian domain is divided in two parts: the PM domain D_{PM} and the pure particle one $D_P = R^n - D_{PM}$ under the understanding that D_{PM} will contain all solid boundaries. The foundations of how the hybrid solver (HoPFlow) couples the different solvers have been detailed in [18].
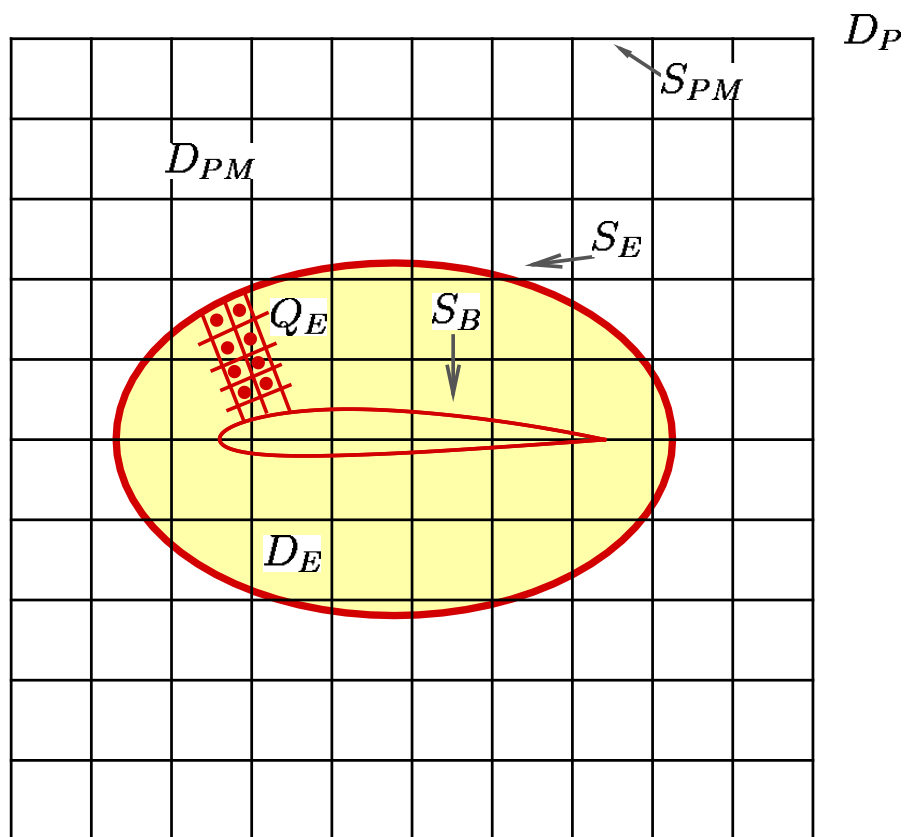
Figure 2.14:   The overlapping grids of the particle mesh and the CFD.

2.6.1 The coupling procedure

Figure 2.14 shows a typical numerical setup for the hybrid solver. The computational domain is decomposed in two overlapping parts; the Eulerian one, D_E, and the Lagrangian one D_{PM}. In D_E the MaPFlow solver is utilized and thus wall boundary conditions on S_B are handled efficiently. For the Eulerian part, boundary conditions are also needed on S_E. They are provided by the Lagrangian solver. In this way the two solvers are coupled. Because the two domains are independent and overlapping, a correct communication between them should provide a smooth transition from one solution to the other.

At a given time $t = n \cdot dt$, particles have the following properties: $\{\vec{Z}_p^n, m_p^n, V_p^n, \vec{\Omega}_p^n, \Theta_p^n, \Pi_p^n\}$. The unknown velocity field is obtained by means of the PM method and the projected properties of the particles onto the PM grid nodes allow the calculation of the Right Hand Side (RHS) of the Lagrange equations (2.15, 2.16, 2.17, 2.18). Then, the 4^{rth} order Runge-Kutta scheme convects the particles in time, leading to a new state of the particles: $\{\vec{Z}_p^{n+1}, m_p^{n+1}, V_p^{n+1}, \vec{\Omega}_p^{n+1}, \Theta_p^{n+1}, \Pi_p^{n+1}\}$

The PM solution near solid boundaries is wrong because the Lagrangian solver does not respect the exact geometry of the bodies. This error fades exponentially as we move away, and thus the need of a better representation of the field rises. Since the particle approach does not respect solid surfaces, particles can penetrate in bodies and the non-slip and non-penetration conditions may not be fully met.
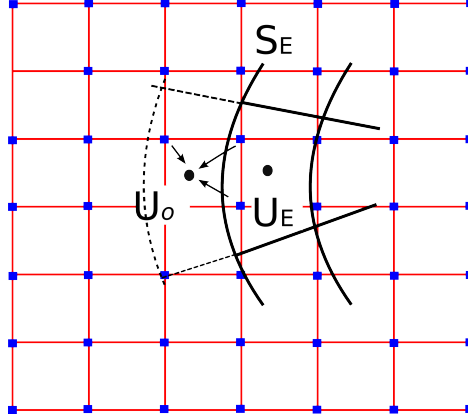
Figure 2.15: Definition of the boundary conditions on S_E. The state U_o at the center of the ghost cell (here marked by a dashed line) is obtained by interpolating the PM data defined at the nodes (here marked in blue).

In order for MaPFlow to solve the governing equations on a limited grid around the surfaces of the bodies, the solver must obtain the flow field variables on its outer-boundary. This is accomplished by interpolating the velocity vector and pressure from the particle mesh grid. With this procedure, the solver predicts correctly the flow field both on the far-field of D_{PM} and near solid boundaries

D_E. The combination of the two overlapping solutions, respecting the continuity and the conservation of the field is performed using an iterative scheme. The extension of the MaPFlow grid is case dependent but in most cases that involved airfoils the size was in the order of one chord length. The full analysis and grid independence investigation can be found in [18].

The coupling procedure involves a) the calculation of the correct far field conditions on S_E that MaPFlow uses, b) the substitution of the PM particles near S_B with the particles that are produced within D_E and c) the smooth transition between D_{PM} and D_E.

2.6.2 CFD boundary conditions on S_E

In order to solve the Eulerian equations, the correct boundary conditions on S_E must be defined. To this end, the Lagrangian solution that is defined at the nodes of the PM grid, is interpolated at the ghost nodes of the Eulerian grid, situated outside S_E. Next, the average over the surrounding ghost nodes provides the flow state at the center of each ghost cell. Finally the fluxes through S_E are determined from the Riemann invariants associated to the flow states on the two sides of S_E. A schematic representation of the above procedure is depicted in Figure 2.15. The red Cartesian grid represents the PM grid, while the black grid is the Eulerian one. It is important to notice that the scale of the two grids does not represent actual sizes.

2.6.3 CFD particles

Assuming that the Eulerian solution in D_E is correct if the solver is given appropriate conditions at S_E, then the modifications in vorticity and dilatation due to S_B are already contained in the Eulerian solution. Therefore, two steps are taken that define the coupling procedure between the Eulerian and Lagrangian parts of HoPFlow: (a) transform the Eulerian solution into particles and (b) replace the Lagrangian particles contained in D_E by those produced in step (a) (Figure 2.16). As the Eulerian solver is cell centered and does not use as primary quantities dilation and vorticity, step (a) includes: (i) use of Green–Gauss formula in order to obtain θ and $\vec{\omega}$ at the grid nodes, (ii) interpolation of ρ and p from cell centers at the Eulerian grid notes, and (iii) interpolation of the flow information from the Eulerian grid nodes at regular positions within every cell (in the schematic, there are four particles per cell). It is important to have good spatial density of particles, and so more than one Eulerian particles are defined per cell.

The ultimate goal after determining the correct boundary conditions, is to transfer the properties from the Eulerian particles to the Lagrangian ones. Thus, the properties of the Lagrangian particles that are inside the CFD mesh are substituted by the properties of the Eulerian. As seen in Figure 2.17, all the properties that are previously projected onto the Cartesian grid are deleted and then replaced

49
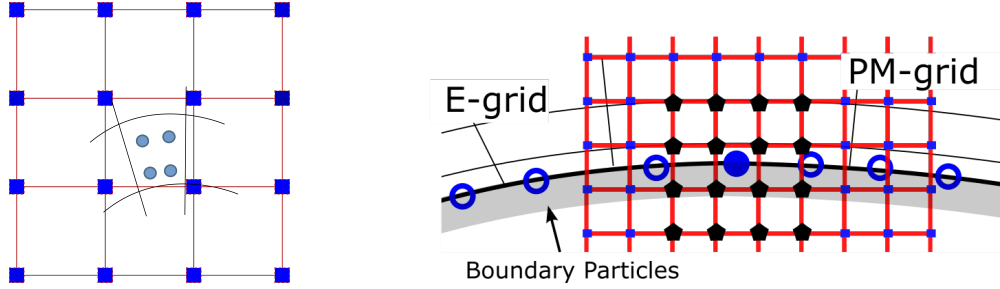
Figure 2.16: Spatial distribution of the E- particles. Left: One E-cell is shown within a 4x4 stencil of the PM grid corresponding to the $M4'$ projection function. There are four P_E particles in the E-cell marked as blue circles. Right: A part close to the solid boundary is shown. On S_B, surface particles are shown as blue open circles. The middle surface particle is embedded in the $M4'$ stencil activated for its projection.

by the projection of Q_E. This approach allows to correct the error of the PM solution that had been produced previously during the solution of the Lagrangian equations.

The procedure of substituting the already existing particles underlines the danger of including or excluding fluid properties on the grid because the two sets of particles have different positions and in cases of rotating CFD domains, their relative positions change in time. As seen in Figure 2.14 in general, the Lagrangian particles are remeshed in every time step at the center of the grid or at the nodes. On the contrary, CFD particles are always generated over the entire cell volume of the CFD grid. In most cases, the CFD grid does not have the same structure with the Lagrangian one. Hence, in order to avoid discontinuity across the grids, the CFD solver performs a number of iterations until the flow converges, and an error correction method is applied. In Figure 2.14 red dots, are the nodes inside the CFD domain that are activated when projecting the Lagrangian particles that are inside the CFD domain. Assuming that in the present example a second order projection function is used, some nodes outside the CFD domain are also activated (see the green nodes in Figure 2.14). When these particles are substituted by the Eulerian ones, the projection of Q_E will affect all the first in order nodes of the grid along the red line. In order for the above to happen, the projected Q_{PM} solution is interpolated back at the position of the CFD particles P_E and then again projected onto X_{PM}. This is called the error of the PM grid and represents the arithmetic error that is projected onto the PM nodes.

$$error\{Q_{PM}\}_{PM} = Projection\{Interpolation\{Q_{PM}\}_{P_E}\}_{PM} \qquad (2.99)$$

where, Q_{PM} are the projected values of a Lagrangian particle Q_P with volume V_P.

50

So the correct solution is readily obtained by subtracting *error* from Q_{PM} and adding the projected values of a CFD particle Q_{CFD} with volume V_{CFD}:

$$Q_{PM} = Projection\{Q_P\}_{PM} \tag{2.100}$$

$$Q_E = Projection\{Q_{CFD}\}_{PM} \tag{2.101}$$

$$correct\{Q_{PM}\} = Q_{PM} - error\{Q_{PM}\}_{PM} + Q_E \tag{2.102}$$
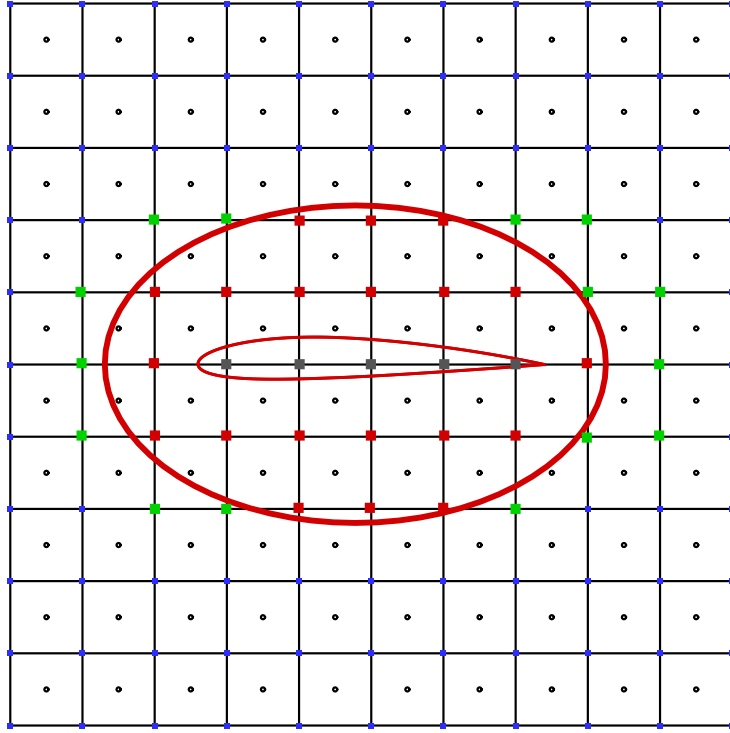
Figure 2.17: Projection of the particle values on the PM grid and the generation of the error due to the different positions between PM and CFD particles.

As seen in Figure (2.14), the *error* is expected to have significant values only in a strict region near S_E. Indeed, by applying equation (2.102) over the whole domain:

$$correct\{Q_{PM}\} = Q_{PM}, \qquad\qquad\qquad outside \quad S_E \tag{2.103}$$
$$correct\{Q_{PM}\} = Q_E, \qquad\qquad\qquad\quad inside \quad S_E \tag{2.104}$$
$$correct\{Q_{PM}\} = Q_{PM} - error\{Q_{PM}\}_{PM} + Q_E, \qquad near \quad S_E \tag{2.105}$$

Because projection of CFD particles engages only nodes that are in a confined area near the solid surfaces, moving outside the Eulerian grid the only projection that takes place concern the Lagrangian particles. Inside the CFD domain, all particles are substituted by the Eulerian ones, thus the CFD solution is the correct. In fact, this outcome proves the reason behind the coupling of the particle approach and the CFD method of the flow field.

A similar correction is applied for the nodes of the Cartesian grid that are inside solid bodies. In Figure (2.14) for the gray dots that are inside S_B, the projected values of Q_P along with the *error* are set to be zero considering that inside an airfoil there is no mass of fluid. Special treatment is also needed for the Lagrangian solver to understand the presence of solid bodies. In order to determine the correct motion of the particles, solid bodies are introduced as surfaces carrying particles. The corresponding surface terms are calculated similar to the CFD particles. Once the velocity field is obtained, the terms that are projected and participate in the solution procedure, are not retained, since they represent the bounded vorticity and must not be convected in time.
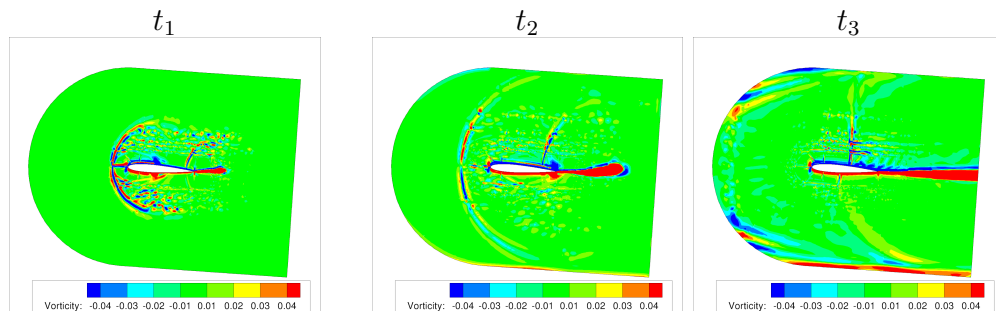
Figure 2.18: Impulsively started Flow around an airfoil. Snapshots of vorticity contours during the transient state of the convergence history show the development generation of a non physical entropy/vorticity close to the wall boundary that travels upstream($t_1 < t_2 < t_3$). Upon arrival at the S_E they are back reflected.

Another issue that needs to be addressed, concerns the onset of non-physical entropy waves during the early stages of the simulation. Since the initial conditions do not actually satisfy the boundary conditions, non-physical entropy/vorticity waves are generated which travel upstream of the flow. Figure 2.18 depicts a vorticity wave that travels upstream towards the inlet of the flow domain. In order to avoid such arithmetic errors, a buffer zone is defined around the CFD far-field S_E within which CFD particles are not generated. A buffer region of two PM cells is found to be sufficient for the correct calculation of the flow.

2.6.4   The HoPFlow algorithm

For a given collection of Particles: $\{\vec{Z}_p^n,\, m_p^n,\, V_p^n,\, \vec{\Omega}_p^n,\, \Theta_p^n,\, \Pi_p^n\}$ at $t = n\Delta t$,
in every time step of the hybrid solver the following sub-steps are performed:

Step 1:   Project $\{m_p^n,\, \Theta_p^n,\, \vec{\Omega}_p^n,\, \Pi_p^n\}$ on the PM grid and get:
$\rho_{ijk}^n,\, \theta_{ijk}^n,\, \vec{\omega}_{ijk}^n,\, \varepsilon_{ijk}^n.$

Step 2:   Solve $\nabla^2 \phi = \theta, \nabla^2 \vec{\psi} = -\vec{\omega}$ and obtain: $\phi_{ijk}^n,\, \vec{\psi}_{ijk}^n,\, \vec{u}_{ijk}^n,\, \vec{w}_{ijk}^n$

Step 4:   Provide Boundary Conditions for the CFD Solution in S_E

Step 5:   Update the CFD solution (dual step subiterations)

Step 6:   Update the flow information at the CFD particles.

Step 7:   If the dual step convergence is reached, continue; else go to 2

Step 8:   Calculate on the PM grid the terms in the RHS of (2.15),
e.g. $\nabla \rho_{ijk}^n,\, \nabla p_{ijk}^n,\, \nabla \vec{u}_{ijk}^n$

Step 9:   Interpolate all grid based data q_{ij}^n at the particle positions:
$q_p^n = \sum_{ijk} q_{ijk}^n W(\vec{x}_{ijk} - \vec{Z}_p)$

Step 10:   Integrate (2.15) in time using 4^{rth} order Runge-Kutta scheme
and obtain: $\{\vec{Z}_p^{n+1},\, m_p^{n+1},\, V_p^{n+1},\, \vec{\Omega}_p^{n+1},\, \Theta_p^{n+1},\, \Pi_p^{n+1}\}$

Step 11:   Re-mesh in order to retain mass coverage at the domain
and avoid overlapping particles that could lead in overlapping
in density

initialize HoPFlow

next dual step

Solve PM

next time step

Obtain the correct boundary conditions on CFD grid

Solve MaPFlow

convergence?

no

yes

Update the particles information with the correct from CFD

next RK step

Solve PM

Calculate the finite differences of the RHS on the PM grid and interpolate the values back to the particles

Solve the Lagrange equation using 4th order Runge-Kutta

Last Step of RK?

no

yes

Last time step?

no

yes

Finalize HoPFlow

Chapter 3

Analysis of the problem of Rotor-Ground/ Rotor-Obstacle interaction

This chapter analyzes in detail the interactional phenomena that occur when a rotor performs a hovering flight in close proximity to solid boundaries. The analysis includes the characterization and categorization of all the phenomena which take place when the vorticity emitted by a rotor and the jet produced by it, interact with solid surfaces such as the ground, walls and obstacles. In addition, a crucial step is to understand the mechanisms that lead these interactions in order to fully comprehend the problem and the handling implications. The above, also determine the computational tools that are best to reproduce the same mechanisms in a variety of problems that involve strong interactional phenomena and rotating frames.

The chapter starts with the description of the experimental rigs of the three campaigns that are used as reference. Then the details of the simulations set-up are provided. The results that are shown, are categorized in three sets depending on the conditions: OGE, IGE, interaction with obstacles. Direct comparisons to measurements are shown that concern on one hand the thrust and torque and on the other flow field patterns.

3.1 Experimental case Analysis and Computational Configuration

3.1.1 Experimental setup

In order to validate numerical results concerning the hovering flight of a helicopter in proximity to the ground and to an obstacle, three main experimental campaigns are employed. They were conducted in three different wind tunnels. All

three campaigns were performed in the context of Garteur AG22 Action Group. The first and the largest in scale test was conducted by the Politechnico di Milano (from hereon Polimi) and included experiments for the isolated rotor, the rotor in IGE conditions and the rotor hovering nearby an obstacle. The second campaign was performed at ONERA and measured the isolated rotor performance and the ground effect on the rotor in a confined area surrounded by walls. The third test campaign was conducted at the University of Glasgow and included results for the isolated rotor and the rotor obstacle interaction. The fact that simulations are compared to results from three different test campaigns, with different rotors and slightly altered obstacle shapes allows for more solid conclusions to be drawn concerning the underlying physics of the rotor obstacle interaction problem.

a) The Polimi experiment

The first experimental campaign was carried out at the Politechnico Di Milano (Polimi) [3]. The test was conducted at the Large atmospheric section of Polimi Wind Tunnel [112]. The relatively small dimensions of the helicopter model minimized the interference with the surrounding wind tunnel walls. The test concerned a helicopter hovering over a box-shaped obstacle, placed on the ground in various setups, corresponding to various horizontal and vertical locations of the rotor with respect to the obstacle (Figure 3.4). Rotor thrust and torque have been recorded along with detailed PIV wake flow measurements. In addition to the above, Polimi also tested the helicopter hovering above the ground without the presence of the obstacle (pure ground effect).
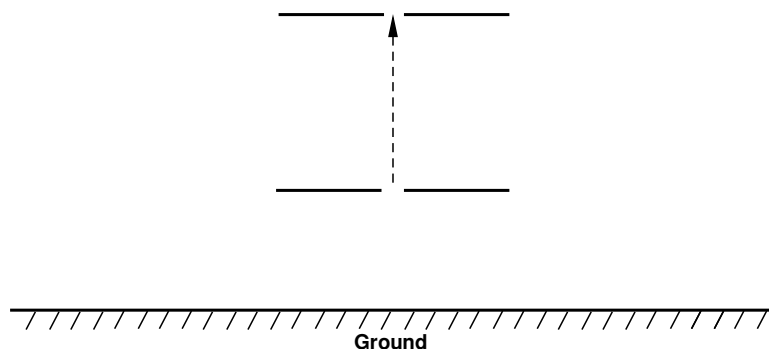
Figure 3.1: Schematic representation of Polimi's IGE. The rotor centre is placed at various heights from $Z/R = 1 - 4$.

The Mach number at the tip of the rotor was $M_{tip} = 0.3$ and the Reynolds number was $Re_{tip} = 220000$. Even though the Re_{tip} is relatively low as compared to full scale conditions ($\mathrm{Re}_{full\ scale} = 3.200.000$), the scope of the test campaign and of the following numerical analysis was not to reproduce exactly the full scale

conditions but to investigate the interactions of the wake shear layers with the boundary layers on the ground and the walls of the obstacle, even though these boundary layers have different characteristics from those in full scale. The results concern the rotor, the fuselage and the supporting mast.

Table 3.1: Wind tunnel model parameters (Polimi)

Characteristics	Polimi rotor
Obstacle height (z-dir)	0.45 m
Obstacle width (y-dir)	1 m
Obstacle width (x-dir)	0.8 m
Rotor diameter	0.75 m
Number of blades	4
Blade chord	32 mm
Airfoil type	NACA0012
Collective pitch	10°
Rotor speed	2580 RPM (39.25 Hz)

Figure 3.2: Schematic representation of Polimi's three cases that include the obstacle. Each color of the rotor represents one test case.

Table 3.2: Test Matrix Polimi experiment

Obstacle	Sweep	X/R	Y/R	Z/R	First Point	Last Point	Results
No	Z	0	0	-	Z/R= 1	Z/R= 4	Loads
Yes	X	-	0	3	X/R=-1	X/R= 4	Loads
Yes	Z	2	0	-	Z/R= 1	Z/R= 4	Loads
Yes	Z	-1	0	-	Z/R= 2	Z/R= 4	Loads & PIV

The experimental cases considered in the present thesis are the hover flight outside the ground effect, the sweep in the z axis (vertical axis) inside the ground effect and three cases with the presence of the obstacle as shown schematically in Figure 3.2. All the characteristics of the Polimi numerical cases are presented in Table 3.2. The measured results against which predictions are compared were averaged over time. Loads were averaged over 5 seconds; PIV measurements were averaged over a rotor revolution that contained 400 image samples.

b) The ONERA experiment

The ONERA test campaign (Table 3.4) concerned a two-bladed helicopter rotor executing hovering flight in proximity to the ground and to surrounding buildings (squared-courtyard). The helicopter was placed at the centre of a squared-courtyard (see Figure 3.3 in which the coordinate system defined for the test is given). The characteristics of the numerical cases of ONERA are given in Table 3.4. Rotor thrust, PIV and pressure measurements over the ground and on the walls were obtained. In Tables 3.4 and 3.3 the characteristics of the ONERA model and the test matrix are respectively provided. Load measurements acquired over a period of 15 seconds with a sampling frequency of 2kHz and PIV data are the result of 3500-5000 images obtained over a 10 minute interval. The results concern the rotor and the fuselage in addition to the supporting mast.

Table 3.3: Test Matrix ONERA experiment

Walls	Sweep	X/R	Y/R	Z/R	First Point	Last Point	Results
No (IGE)	Z	0	0	1	-	-	Loads
Yes	Z	0	0	1	-	-	PIV
Yes	Z	0	0	-	Z/R= 1	Z/R= 4	Loads

In contrast to the Polimi experiment, in the ONERA set up the main goal was to study how the hovering flight in IGE conditions is affected by the presence of surrounding vertical walls at a relatively small distance (the minimum distance

between the side walls and the rotor centre was 2R). The simulated cases were the OGE one, the IGE without the walls when the centre of the rotor is placed at $Z/R = 1$ and the sweep in z axis (vertical).

Table 3.4: Wind tunnel model parameters (ONERA)

Characteristics	ONERA rotor
Obstacle height (z-dir)	0.36 m
Obstacle width (y-dir)	0.3 m
Obstacle width (x-dir)	0.3 m
Rotor diameter	0.71 m
Number of blades	1
Blade chord	32 mm
Airfoil type	NACA0012
Collective pitch	8°
Rotor speed	2600 RPM (40.0 Hz)
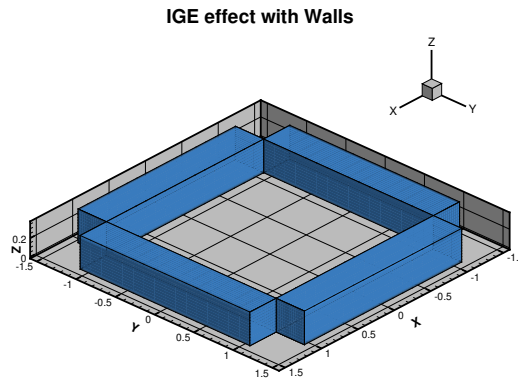
Figure 3.3: Overview of the courtyard setup of the ONERA experiment

c) The Glasgow experiment

University of Glasgow (Glasgow) performed a detailed experimental study of the interaction between a model helicopter rotor and a model obstacle [4]. The details of the experiment (dimensions, rotational speed, etc.) are shown in Table 3.5. In this campaign, two separate test rigs have been employed. The first, concerned a large rotor with a mach number at the tip $M_{tip} = 0.18$ and a tip Reynolds $Re_{tip} = 220000$. For the large rotor, load and induced velocity measurements over the rotor plane, using Laser Doppler Anemometry [3] have been

performed. The second rig concerned a small rotor for which Stereo PIV measurements were obtained in the region between the rotor and the obstacle. The small rotor had a Mach number equal to that of the large rotor, but a tip Reynolds of $Re_{tip} = 132000$. Rotor load data are averaged over 5 realizations of the test, each of 2.5 seconds duration. This test concerned only the rotor and the supporting mast (without the presence of a fuselage).

Table 3.5: Wind tunnel model parameters (Glasgow)

Characteristics	Glasgow Large rotor	Glasgow "Wee" rotor
Obstacle height (z-dir)	1 m	0.3 m
Obstacle width (y-dir)	1 m	0.3 m
Obstacle width (x-dir)	1 m	0.3 m
Rotor diameter	1 m	0.3 m
Number of blades	4	2
Blade chord	53 mm	31.7 mm
Airfoil type	NACA0012	NACA0012
Collective pitch	8°	8°
Rotor speed	1200 RPM (20 Hz)	4000 RPM (66 Hz)

Table 3.6: Test Matrix for Glasgow experiment

Obstacle	Sweep	X/R	Y/R	Z/R	First Point	Last Point	Results
Yes	X	-	0	2	X/R=-1	X/R= 1	Loads & PIV
Yes	Z	2	0	-	Z/R= 1	Z/R= 4	Loads & PIV
No	-	2	0	1.5	-	-	LDA
Yes	-	2	0	1.5	-	-	LDA

From all the test points measured in Glasgow, in this thesis two cases are analyzed, and predictions are compared to measured data-sets. These cases are shown in Figure 3.4. The two selected cases present similarities with certain configurations from the Polimi test campaign which are also addressed in this thesis. The first case concerns the sweep of the helicopter rotor in x axis while its z position remains the same (Z/R=3). In the second case the rotor is placed next to the obstacle at X/R=2 and the sweep is performed along z axis.
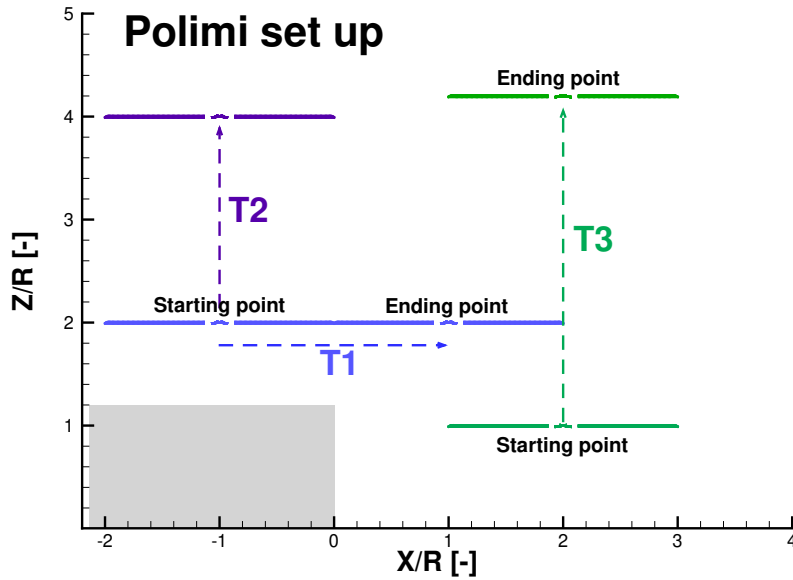
60
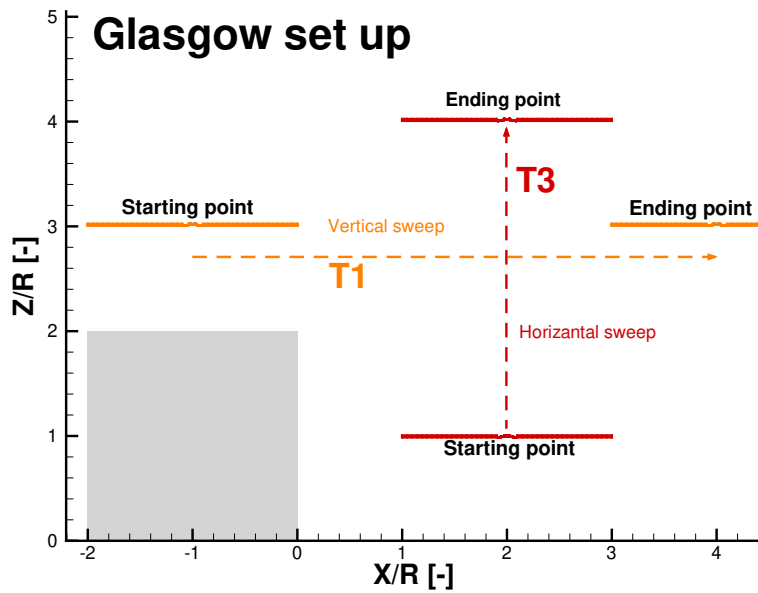
Figure 3.4: Schematic representation of Galsgow's two cases that include the obstacle. Each color of the rotor represents one test case.

Cases

In order to categorize the cases according to the set up and not to the wind tunnel where the experiment took place, code names have been defined according to the configuration examined.

- *OGE*: Hovering outside the ground effect

- *IGE*: Hovering inside the ground effect

- *T1*: Hovering above the obstacle performing a sweep in x axis

- *T2*: Hovering above the obstacle performing a sweep in z axis

- *T3*: Hovering next to the obstacle performing a sweep in z axis

61

3.1.2 Computational Configuration

The codes used in the simulations (GenUVP and HoPFlow) have been thoroughly validated in the past ([70],[113],[18],[61],[114],[17]) an thus, their pros and cons are known. Potential solvers are ideal for predicting the loading of a rotor with affordable computational cost. The hybrid solver is capable of reproducing the details of the flow field in particular when strong interactional and viscous phenomena dominate the flow. Computational mesh and time step independence analyses, for GenUVP and HoPFlow have been performed in previous studies [18], [106], [115]. The meshes and time steps in the simulations presented in this thesis, comply with the requirements set in order to have solutions independent to numerical parameters. In Table 3.7 the numerical tools that are exploited for each campaign and each case are shown.

Table 3.7: Specification of the numerical tools that have been used for each of the three experimental campaigns and cases.

Case	Method
OGE	GenUVP(Polimi, Onera, Glasgow) & HoPFlow(Polimi, Glasgow)
IGE	GenUVP(Polimi, Onera) & HoPFlow(Polimi)
T1	GenUVP(Polimi, Glasgow) & HoPFlow(Polimi)
T2	GenUVP(Polimi) & HoPFlow(Polimi)
T3	GenUVP(Polimi, Glasgow) & HoPFlow(Glasgow)

Potential solver (GenUVP) - Numerical configuration

In potential solvers, there is no need for space grids. The grid is fitted on the surface of the bodies. As stated in Chapter 2.3 in potential theory a lifting body can be represented either as a thick body (source and douplet distributions) or as a lifting surface (only douplet distributions). While thick bodies offer an exact representation of the actual blade shape and can predict the pressure distribution over the blade, thin lifting surfaces are significantly more cost effective. It is also important to note that when it comes to integrated loads (i.e. blade root moments, rotor hub loads etc.), both representations provide similar results because they both use the same final viscous corrections. In this connection, given that interactional simulations required a large number of rotations to be run, it is more effective to use lifting surfaces instead. An additional argument is that the available experimental results concerned only integrated loads on the hub and not sectional distributions. In all cases, the fuselage and the model support mast were not simulated. In Table 3.8 the computational details for the main rotor configuration are shown for all cases and test campaigns. The obstacles in the potential solver are modeled as thick source bodies as seen in Figure 3.5 and Figure 3.6.

Table 3.8: Computational details for the main rotor configuration using GenUVP

Case	Modeling	Grid	Time step
OGE (Polimi, Glasgow, ONERA)	Lifting Surface	9x21	4°
IGE (Polimi, ONERA)	Lifting Surface	9x21	4°
T1 (Polimi, Glasgow)	Lifting Surface	9x21	4°
T2 (Polimi)	Lifting Surface	9x21	4°
T3 (Polimi, Glasgow)	Lifting Surface	9x21	4°

Figure 3.5: Computational grid presentation for the Glasgow model. The blades are modeled as thin lifting surfaces carrying doublets and the obstacle is modeled as thick source body. A similar grid is used in Polimi computations.

Table 3.9: Computational details for the obstacle simulations using GenUVP

Case	Modeling	Grid	Time step
IGE (ONERA)	Thick source body	31x31x21	4°
T1 (Polimi, Glasgow)	Thick source body	31x31x21	4°
T2 (Polimi)	Thick source body	31x31x21	4°
T3 (Polimi, Glasgow)	Thick source body	31x31x21	4°

The effect of the ground can be introduced to potential solvers in two ways. The first, is to model the ground with panels carrying source distributions and satisfy the no-penetration condition at the centre of every panel. The second, is to apply mirroring of the douplet and source distributions along with the spatial vorticity so that the normal velocity to the mirroring plane is by construction cancelled. Both methods reproduce the effect of the ground considering it as a

slip wall. Because of the nature of the problems studied in this thesis, choosing the first method would imply that the extension of the area covered with ground panels would be very large and thus, the computational cost would be excessive. In addition, in order to avoid particles crossing the ground level, the density of the panels grid on the ground should be very high. This is mainly due to the fact that the non-entry condition is satisfied only on one point over every panel which implies that overall there will be non zero flow penetration through the ground panels. So, with some necessary adaptations to the code, the mirroring technique has been chosen.
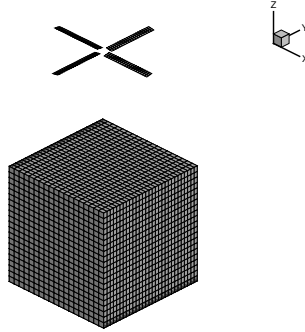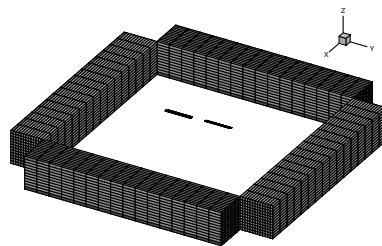

Figure 3.6: Computational grid of the ONERA model. The blades are modeled as thin lifting surfaces carrying doublets and the walls are modeled as thick source bodies.

With respect to cost, for an isolated hovering rotor, convergence to steady state is reached after 10 full revolutions. When the helicopter hovers in proximity to the ground or to an obstacle, convergence to a periodic state requires at least 40 rotor revolutions. In the results presented, such simulations extended up to 80 revolutions in order to ensure that the rotor wake which bounces on the ground and returns to the free flow (outwash flow) has fully evolved. Loads have been averaged over the azimuth during the second half of the simulation (from the 41st to 80th revolution). On the contrary, plotted flow contours are obtained through averaging over the last rotor revolution.

Because of the different sizes of the rotors and obstacles in the tests, all dimensions are normalized with the rotor radius. Loads in IGE and in proximity to the obstacle are normalized with the values obtained when the rotor hovers OGE.

Hybrid Solver (HoPFlow) - Numerical configuration

HoPFlow requires two sets of grids in order to solve the flow: A spatial grid surrounding the solid boundaries is needed in order to solve the flow in the vicinity of solid bodies using the URANS control volume model MaPFlow; and a structured uniform Cartesian grid that covers the whole computational domain on which the Particle Mesh method is applied.

In the present simulations, the blades are represented by actuator lines. In such a case, every blade is covered by a cylindrical cross grid that includes the lines of the actuator model and extends by 1.5× radius in the radial direction and by 0.5× radius around every cross section. In Figure 3.7 the setup and the grid that is used is shown for the Polimi experiment. A similar setup is also used in Glasgow computations. Each actuator line (each blade) is divided into 31 sections. As literature suggests and previous work at NTUA [106], a suitable grid spacing should range from $\frac{c}{2}$ to $\frac{c}{8}$, where c is the chord of the blade. In the present work, the spacing is set at $\frac{c}{5}$. The corresponding time-step needed for this spacing can be calculated as $\delta t = \frac{\delta x}{V_{tip}}$, where δx is the spacing of the grid and V_{tip} is the velocity at the tip of the blade. In this work, δt is equal to 0.2 which corresponds to an azimuth step of 1°. In this configuration, the CFD grid is moving along with the blades. Since the actual geometry of the blades is not resolved and the viscous effects are included in the process of calculating the loads, the flow around the blades is considered laminar.
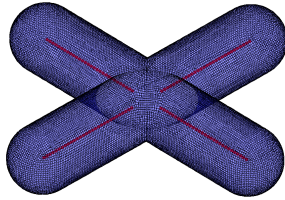
Figure 3.7: CFD mesh surrounding the rotor blades of Polimi's rotor. Red lines represent the blades.

Besides the CFD grids surrounding the blades (defined with respect to the blades' rotating frame) fixed CFD grids are deployed over the ground and around the obstacle (see Figure 3.8). As in the case of the blades, laminar flow is also assumed within these regions. This assumption is based on the fact that there is no wind inflow in the cases considered. So, any flow on the ground or around the obstacles is generated by the rotor wake. Taking into consideration that rotor induced velocities are low (3-6 m/s) and that characteristic lengths of the boundary layer development over the solid bodies of the problem extend from 1 - 2 radii at maximum, the corresponding Reynolds number varies between $Re_x = 263000 - 600000$. Since the overall Re_x number is relatively low and the phenomena investigated in the present thesis take place in the vicinity of the rotor disk, the decision to simulate laminar flow conditions is well substantiated. At the same time, any uncertainty derived from the turbulence modelling is eliminated. The extension of the grid is 0.5 times the radius of the corresponding experimental main rotor blade (Polimi and Glasgow) so the boundary layer on the ground and the obstacle

can be fully developed within the CFD domain. The first cell of the grid on the ground and the obstacle has a height of $2*10^{-4}$ m. The time-step of all HoPFlow simulations was 1° with respect to the rotational period of the main rotor.

In the few cases (IGE (Polimi) $Z/R = 1$ and T1 (Polimi) $Z/R = 2$) the fuselage has been added in the simulation. The corresponding CFD grid around the ground, the obstacle and the fuselage is 0.25 times the radius of the main rotor. Thinner grids are adopted in the above cases in order to avoid excessive overlapping (see Figure 3.9). In Table 3.10 the details of the grids used are presented.

Table 3.10: Computational details for the CFD grids used in HoPFlow

Case	Rotor (cells)	Walls (cells)	Fuselage (cells)
OGE (Polimi, Glasgow)	212.000	-	-
IGE (Polimi)	212.000	288.000	-
T1 (Polimi)	212.000	1.150.205	-
T2 (Polimi)	212.000	1.150.205	-
T3 (Glasgow)	212.000	602.596	
OGE (Polimi with fuselage)	1.005.802	-	120.690
IGE (Polimi with fuselage)	1.005.802	507.000	120.690
T1 (Polimi with fuselage)	1.005.802	1.150.705	120.690

The Particle Mesh grid extends at least 3 diameters away in all directions from the rotor and the obstacle so as to cover the entire flow domain and avoid abrupt interruption of the flow. The resolution of this grid is mainly dictated by the time-step of the rotating main rotor and the CFL number. Dilatation waves are propagating with the speed of $c \pm V_{inf}$ where c equals the speed of sound in the air and V_{inf} the un-disturbed free flow velocity. Taking the above into account, at every time-step, the distance that these waves are propagating must be within a range of $dx = 0.5 - 1.5 dx_{PM}$ where $dx = (c \pm V_{inf}) * t$. Thus, for the present work, the grid spacing of the PM is set to $\frac{c}{3}$.
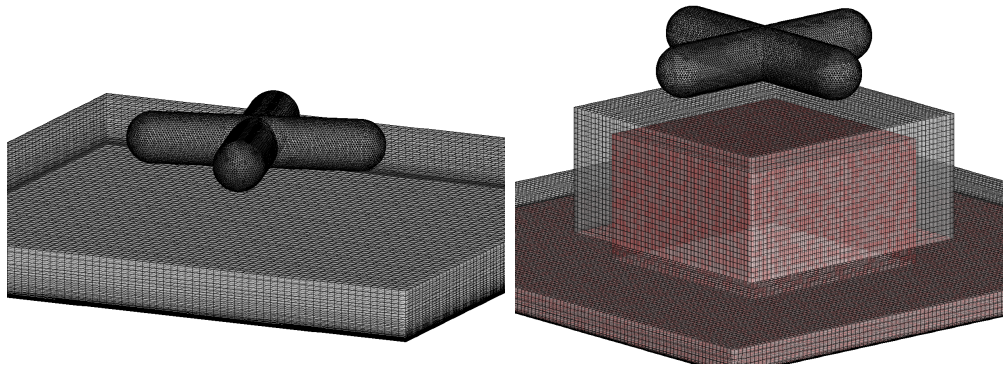
(b) CFD meshes surrounding the blades
(a) CFD meshes surrounding the blades of the rotor the ground and the obsta-
of the rotor and the ground.   cle.

Figure 3.8: Schematic representation of the grid that are used in HoPFlow simulations for the Polimi test campaign. The pure IGE case is shown on the left and the rotor/obstacle configuration on the right. The wall and ground are shown in red color. A similar grid is used in Glasgow computations.
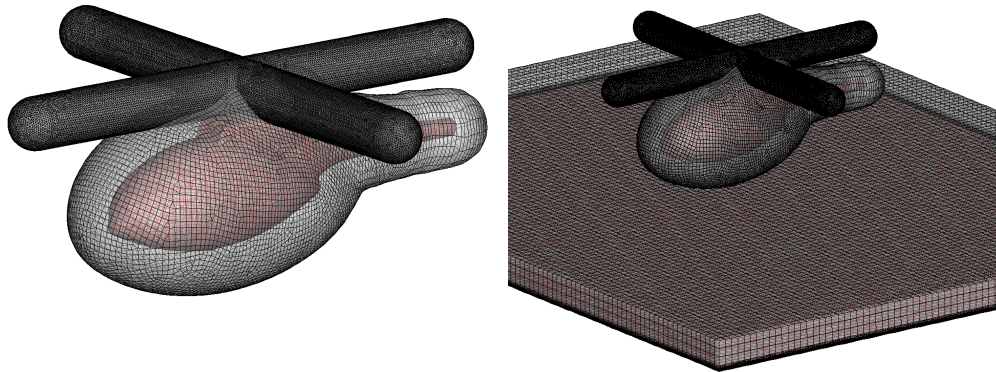
(a) CFD meshes surrounding the blades   (b) CFD meshes surrounding the blades
of the rotor and the fuselage.   of the rotor the ground and the fuselage.

Figure 3.9: Schematic representation of the grid that are used in HoPFlow simulations including the fuselage for the Polimi test campaign. The pure OGE case is shown on the left and the pure IGE rotor/fuselage/ground configuration on the right. The solid boundaries are presented with red color.

3.2 Hover flight simulations Outside the Ground Effect (OGE) using different methods

In all measurement campaigns (Polimi, Glasgow and ONERA) first the thrust of their corresponding model helicopter was measured OGE in order to determine the reference value of thrust against which the thrust of all interactional cases will be compared to. The results are shown in Table 3.11. The thrust coefficient of the three tests is different, given that the experimental setup and the rotors of the three test campaigns are different (see Tables 3.1, 3.4, 3.5).

$GenUVP$ simulations cover all the experiments considering only the main rotor in favor of computational cost. $HoPFlow$ simulations focus on the Polimi experiment in the attempt of validating the Actuator Line model and assessing the necessity of including the fuselage. In addition to loads, a detailed analysis of the flow field is performed using $HoPFlow$ data.

3.2.1 Main Rotor Load Results

The test data and the predicted values are given in Tables 3.11 and 3.12. They compare very well. The $GenUVP$ predictions deviate only by $\pm 0.3\%$ which is negligible. It is reminded that loads are calculated using viscous corrections of the blade element type based on the estimation of the angle of attack and 2D polars which in the present work were obtained with MaPFlow for different Mach numbers in the range 0-0.6 and the average local Reynolds number of the rotating blades (100000-200000). Given that the collective pitch is kept fixed in all OGE tests no unsteady effects (steady-state axi-symmetric conditions) on the performance of the rotor are expected. Pitch is also kept constant in the IGE and the interactional (presence of obstacle) cases but in those cases flow unsteadiness is triggered by the interaction of the wake with the solid boundaries which implies some unsteadiness in the loading.

Table 3.11: Measured Thrust Coefficient in OGE conditions for the three experimental campaigns

Experiment	Measured Thrust Coefficient
Polimi	0.00729
ONERA	0.00379
Glasgow	0.00736

Table 3.12: Predicted Thrust Coefficient in OGE conditions for the three experimental campaigns

Experiment	Predictions with GenUVP	Predictions with HoPFlow
Polimi	0.00731	0.00730
Polimi	-	0.00733 (with fuselage)
ONERA	0.00380	-
Glasgow	0.00735	0.007355

The collective pitch in the simulations was that of the experiments, so by conjecture good agreement in the loads means that the estimation of the angle of attack is also correct and so should be also the flow field. An OGE simulation of 10 full revolutions with *GenUVP* applying 90 steps per rev, lasts 2 hours on a 4-core laptop.

Excellent agreement is also obtained with *HoPFlow*. It is reminded that although the simulation solves the Navier Stokes equations, the fact that the blades are represented by actuator lines means that the loads are predicted similarly to *GenUVP*. However the way angles of attack are estimated is different and so in this respect good agreement implies that the two ways for estimating the angle of attack are in their final result equivalent.

The run time of the 10 full revolutions with *HoPFlow* in OGE conditions is substantially higher compared to that with *GenUVP*. Part of this increase is due to the much smaller time step needed leading to 360 steps per rev and approximately 24 hours run time. Moreover, the additional value from using high fidelity CFD in OGE conditions is definitely not linked to the prediction of the rotor wake field but with the details of the flow in the vicinity of the blade and with flow phenomena with length scales comparable in size to the scale of the blade chord. Since this study resolves the blades using the actuator line method coupled with the Dynamic Stall model, no added value is imported by using *HoPFlow* for OGE simulations. The value of *HoPFlow* emerges when interactions of the rotor wake with nearby walls is examined.

3.2.2   Flow field analysis in OGE

Wake evolution is closely connected to loading formation which renders vorticity calculations valuable. They are part of the solving procedure in vortex particle methods and therefore *GenUVP* and *HoPFlow* are definitely well suited for such a task. Figure 3.11 shows a snapshot of the OGE flow field of the hovering rotor as computed by *HoPFlow* after 10 rotor revolutions. Because the flow fields obtained by *GenUVP* and *HoPFlow* are similar only the results of the latter are shown. The results concern the rotor of Polimi and the simulation is performed without the presence of the fuselage. The magnitude of the flow velocity is illustrated in the plot, over a vertical plane that passes through the centre of the rotor (axi-

69

symmetry plane). It is worth noticing that flow field is smooth suggesting that the coupling of the Eulerian domain (CFD grid) with the Lagrangian one (far field) is performed in a consistent manner.

The typical for hovering rotors vortex ring travelling downstream at 3-4m/s, is clearly shown. The wake roll up that shapes the ring, is created at the very beginning of the simulation, as a result of the interaction of the starting vortices emitted by the different blades. Moreover, visible is the contracting jet flow that develops under the rotor disk. As expected, the rotor inflow velocity varies along the blade span and obtains its maximum value within the range 70-95% of the rotor radius. This is also the radial range within which local blade thrust obtains its maximum value. The absence of the fuselage, the hub and the rotor mast, explain the "hole" in the flow field close to the rotor centre. The absence of aerodynamic loading leads to a flow field that appears to be almost stagnant in the above region. The 1D distance of the starting vortex ring from the rotor plane and the convergence of the wake contracted shape indicate that after 10 revolutions the rotor loading has also converged. The above is also presented in Figure 3.10. In this figure, the velocity magnitude of the wake is presented as contour over the iso-surface of the wake (snapshot at the end of the 10th rotor revolution).
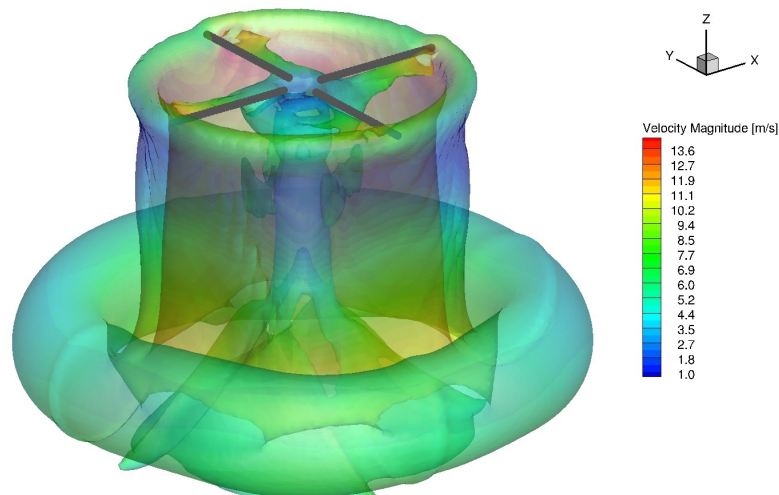
Figure 3.10: Wake iso-surface of the Polimi main rotor without the fuselage in OGE conditions. Over the iso-surface the velocity magnitude is depicted as it has been captured after the end of the 10th revolution.

70

Figure 3.11: Velocity magnitude contour and vectors of the OGE case of Polimi rotor without the fuselage, over an axi-symmetry plane at $r/R = 0$ (snapshot at the end of the 10th period).

An additional simulation of the same test case aiming at assessing the importance of the fuselage is also considered. The run concerns the Polimi rotor plus its fuselage and $HoPFlow$ results are shown in Figure 3.12. The overview of the wake (iso-surface of the vorticity magnitude) that is shown, clearly indicates that the wake is shaped differently. Instead of the symmetric shape obtained in the rotor-only simulation, the fuselage provokes asymmetry suggesting that also the loading will become asymmetric. The tail boom of the fuselage blocks the strong tip vortices of the blade when this passes from 0 degrees azimuth angle (blade parallel to flight path pointing downstream). This leads to decreased induced velocities at the downstream part of the rotor disk. As seen in the back view the starting vortex underneath the retreating and advancing sides are symmetrical. The above are more clearly illustrated in Figures 3.13,3.14 where the velocity magnitude of the flow field is shown, again at the end of the 10th revolution. In Figure 3.13, it is observed that the presence of the fuselage alters the position of the starting vortex ring. The vortex at the nose of the fuselage travels downwards faster after being deflected by the nose of the fuselage. On the other hand, the one at the back of the helicopter moves downwards at lower speed dictated by the blockage of the tail boom. Furthermore, a low velocity region is formed underneath the main body of the fuselage as a result of the wake jet flow separation (see also Figure 3.14).
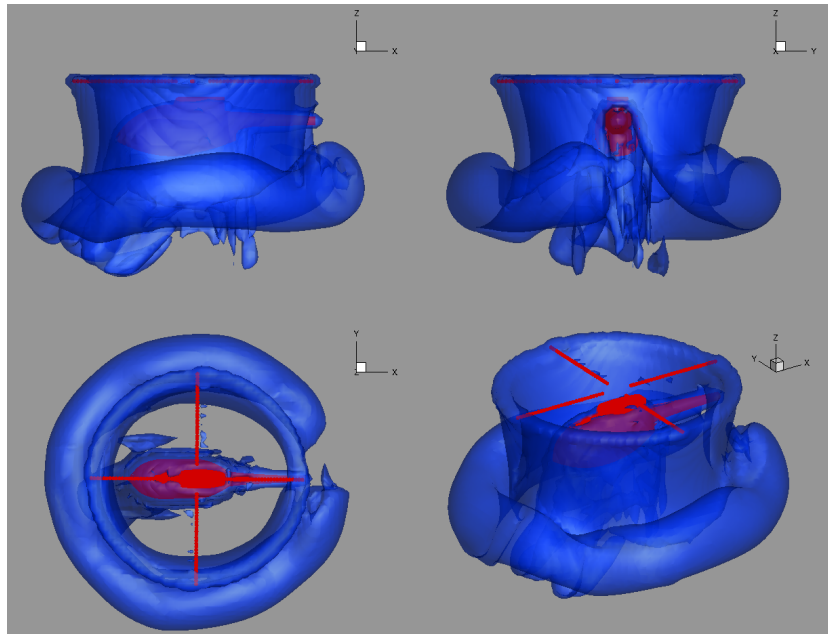
Figure 3.12: Overview of the wake for the case of the rotor-fuselage interaction.The case concerns the Polimi main rotor in addition with the fuselage. The wake is presented as the iso-surface of vorticity magnitude at the end of the $10^t h$ rotor revolution.

72

As discussed earlier an almost symmetric development of the wake is obtained with respect to the helicopter symmetry plane. This is noted on the vorticity plots of Figure 3.12 but also on the velocity field of Figure 3.14. As seen in the figure, two symmetrical ring vortices are formed below the fuselage. Comparing these results with the results of the stand-alone rotor, it is noted that reduced wake velocities are obtained in the full helicopter case. However, the wake jet flow in the case of the full helicopter is wider (reduced wake contraction). This leads to a more even loading of the rotor disk although the integrated overall thrust load of the rotor is not altered. A more illustrative, 3D flow pattern plot is shown in Figure 3.15. In this plot the magnitude of the flow velocity inside the wake is shown. Comparing this with the corresponding flow velocity pattern of the OGE case (see Figure 3.10) it is concluded that lower flow velocities are obtained in the wake of the full helicopter as compared to those of the single rotor. The region over which lower velocities are distributed is more extended.
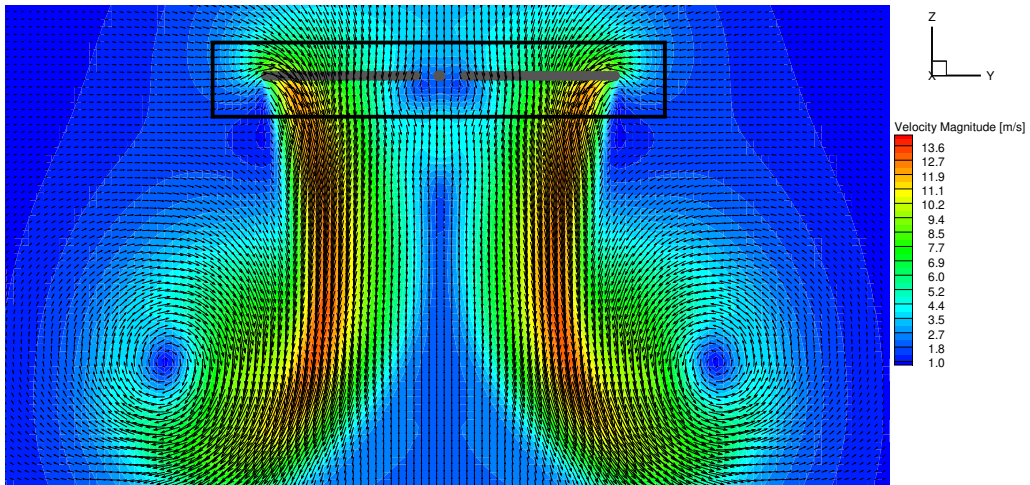

Figure 3.13: Velocity magnitude and vector contour of the OGE case of Polimi rotor with the fuselage, over an axi-symmetry plane at $r/R = 0$ (snapshot at the end of the 10th period, side view).

In the full helicopter simulation with $HoPFlow$ the pressure distributions and the streamlines of the flow over the surface of the fuselage have been recorded. In Figure 3.16 the pressure coefficient distribution on the fuselage and the stream-traces on the surface of the body are presented. It is observed that the presence of the fuselage, blocks the flow below the rotor disk. This is clearly depicted on the CP values which obtain higher values at the top of the fuselage roof due to the reduced flow velocities. The stagnation line is clearly identified on the helicopter roof, lying over the symmetry plane of the fuselage. Stream-traces on the roof of the fuselage, starting from the stagnation line, they split into two streams, one following the port side of the fuselage while the other the starboard side. The

73

streamtraces are abruptly interrupted when they reach the side edges of the fuse-lage as a result of the separation of the wake flow on the lower side of the fuselage.

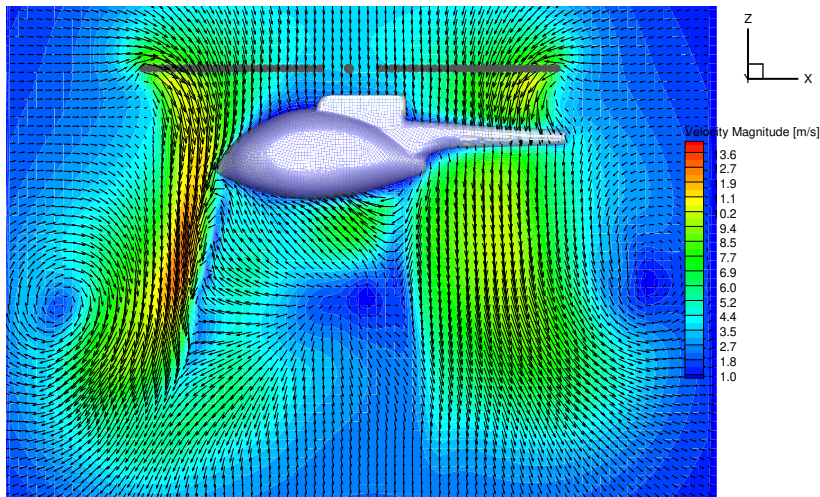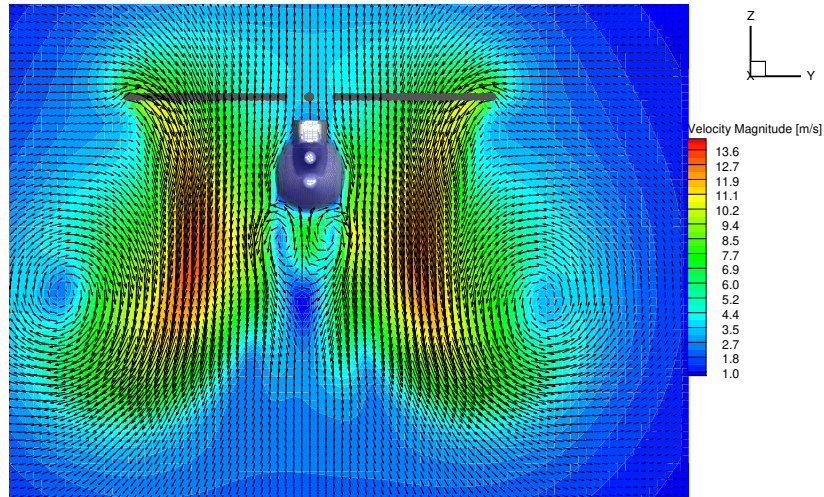Figure 3.14: Velocity magnitude and vector contour of the OGE case of Polimi rotor with the fuselage, over an axi-symmetry plane at $r/R = 0$ (snapshot at the end of the 10th period, side view).
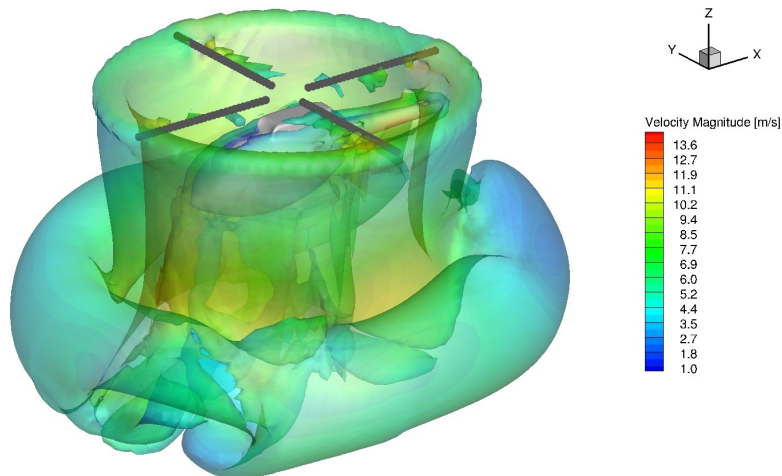
Figure 3.15: Wake iso-surface of the Polimi main rotor with the fuselage in OGE conditions. Over the iso-surface, the velocity magnitude is depicted as it has been captured after the end of the 10th revolution.
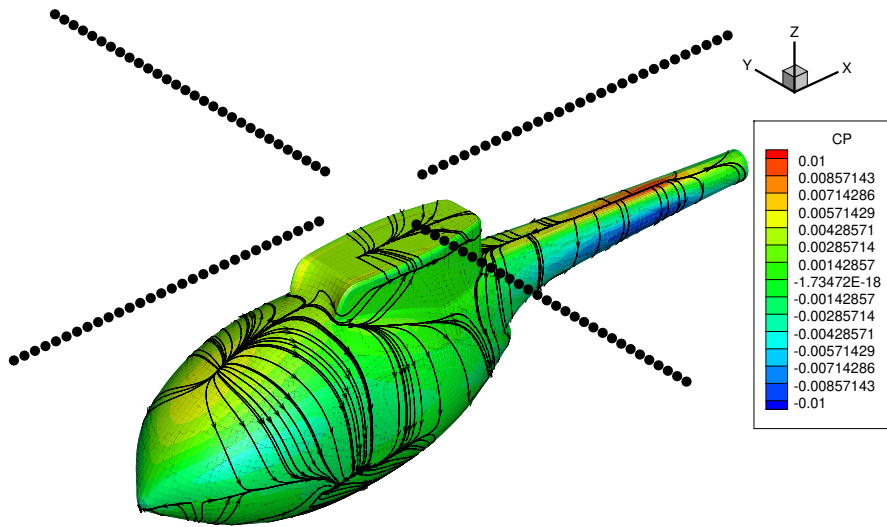
Figure 3.16: Pressure Coefficient distribution on the fuselage and stream-traces for the OGE hover case

In conclusion, OGE simulations with either method correctly predict loads and at the same time provide physically consistent flow fields as explained in [116]. The analysis showed that the presence of the fuselage in the simulations does not have a crucial effect on the loading of the main rotor, even though the wake changes shape. In OGE cases for zero values of the advance ratio, $GenUVP$ provides equally good predictions of the rotor loads and wake as high fidelity actuator line methods. Furthermore, vortex model is cost effective and provides robust predictions of loads. On the other hand, $HoPFlow$ can handle flows in which viscous effects are dominant (eg. presence of fuselage and occurrence of flow separation), although it is far more expensive than the vortex model, both in terms of computer time and memory requirements. Thus, it is more suitable for simulations in which modelling of the fuselage is imperative.

3.3 Performance of the rotor in ground effect

The first interactional case addresses helicopter hovering above the ground. There are tunnel results by Polimi for different distances from the ground and by ONERA with measurements at one point namely $Z/R = 1$. Simulations for all cases have been carried out with $GenUVP$ while with $HoPFlow$ the smallest distance has been considered.

Table 3.13: Cases and computational tools used

Data	GenUVP	HoPFlow (viscous case)	HoPFlow (inviscid case)
Loads	Z/R=1-4	Z/R=1	Z/R=1
Flow Field	-	Z/R=1	Z/R=1

In problems such as that of a rotor in close interaction with the ground, the latter has a significant contribution to the rotor loading. This effect is created by the jet of the helicopter in addition to the tip vortices emitted by the tip of the blades.

3.3.1 Experimental main rotor loads analysis in comparison to GenUVP and HoPFlow predictions

In Figure 3.17, $GenUVP$ predictions of the normalized thrust coefficient (black solid line) (CT) with respect to the distance from the ground Z/R are compared to the Polimi (black markers) and ONERA measurements and predictions respectively (red markers). In Polimi's experiment the maximum increase in CT with respect to OGE is about 15% and is recorded at the lowest measured station ($Z/R = 1$). At $Z/R = 4$ the effect of the ground almost vanishes. In the ONERA experiment, the maximum increase in CT is lower and goes up to 12%. This lower measurement is attributed to the deflections of the blades during the experiment. According to experimenters, the model helicopter showed deflections and deviations in the power of the motor leading to a higher standard deviations in measurements.

Predictions are in good agreement with the measurements. The increase in CT/CT_{OGE} as Z/R decreases, is correctly predict, however the recorded thrust variation does not exactly follow the analytically calculated exponential shape (ground effect of lifting wing calculated through application of Biot-Savart's law). At about $Z/R = 1.6$, CT values maintain a constant level forming thus a "knee" in the overall variation. $GenUVP$ captures well the thrust variation despite the absence of viscous effects. At heights $Z/R > 1.5$ predictions and measurements are almost identical. However, there is a small under-prediction of the ground effect

at lower heights $Z/R < 1.5$. The maximum deviation appears at $Z/R = 1$ and is ≈ 2.5 units lower than the measured increase of 15%.
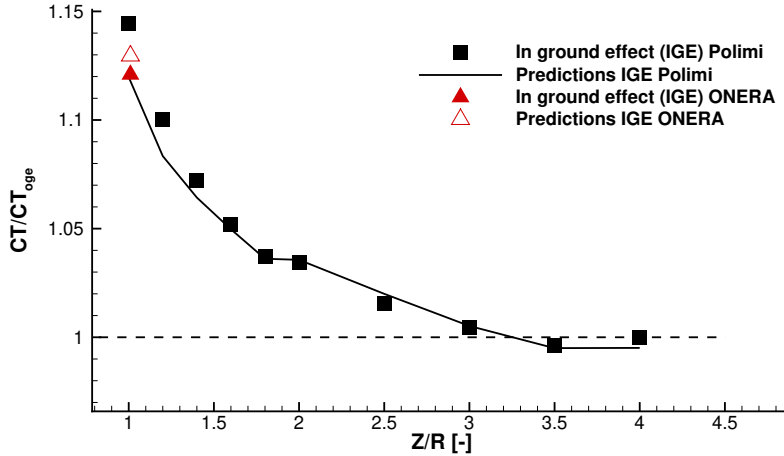
Figure 3.17: Rotor thrust variation in IGE for the Polimi and ONERA rotors. Comparison of measurements against prediction obtained with GenUVP

This difference in CT/CT_{OGE} of 15% is attributed to the displacement effect of the ground boundary layer which is not accounted for in $GenUVP$ simulations. Development of the boundary layer renders the active distance between the rotor disk and the ground smaller and, therefore, the increase in thrust is higher. In Figure 3.18 a contour plot of the velocity magnitude at an axi-symmetry plane centered at $X = 0$ is shown for the above $Z/R = 1$ case, obtained through a $HoPFlow$ simulation in which the ground is modelled as a slip wall. It is seen that in the absence of a boundary layer on the ground, the wake licks the ground while the magnitude of the velocity near the inviscid wall substantially increases leading to an outwash flow that moves fast away from the rotor.

Also, the Z/R value at which the "knee" of the CT variation occurs, is correctly predicted. As Z becomes smaller, wake vortices reach the ground and bounce back creating an outwash flow (see Figures 3.18 and 3.11 where the velocity magnitude of the OGE and IGE case at $Z/R = 1$ are shown). The wake-induced downwash depends strongly on the distance of the rotor from the ground, which affects the formation of the lateral flow. In particular, wake-induced downwash increases at lower heights. This is because wake vortices move outwards, parallel to the ground level (see Figure 3.18), while remaining closer to the rotor plane as compared to the OGE case. As a result, wake-induced velocities attain higher vertical component. At the same time the mirror vortices, that in theory account for the presence of the ground, also get closer and therefore their counteraction (induced upwash) becomes stronger. The above two opposing effects determine CT, which at some points eventually levels out. In this particular case, this occurs at $Z/R = 1.7 - 2.0$.

Comparing the experimental data of ONERA against $GenUVP$ predictions, a

good agreement is noted (less then 1%) in terms of absolute value. However, the $GenUVP$ prediction for the CT is greater than measurements. Considering the deflections in the experiment and that in simulations only the nominal rotational speed and pitch angle is used, this difference is justified.
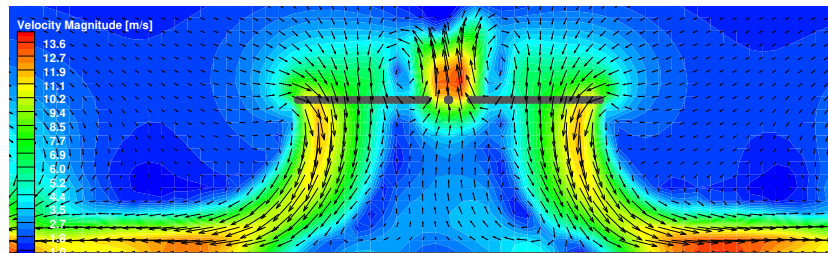
Figure 3.18: Velocity magnitude and vector contour of the IGE case of Polimi rotor at $Z/R = 1$ without the fuselage, over an axi-symmetry plane at $r/R = 0$ (snapshot at the end of the 6th period). The simulation is performed with HoPFlow with slippery conditions on the ground wall.

In conclusion, the trend of the IGE trust variation predicted by $GenUVP$ is in good agreement with experiments while computations are time efficient (16 hours on 20 cores for 40 revolutions of the main rotor) which indicates that $GenUVP$ is in every respect appropriate for industrial applications in which ground effect should be taken into account.

Unfortunately, inviscid methodologies cannot reproduce the displacement effect of the boundary layer. Thus, the increase in thrust when hovering within $Z/R = 1 - 1.5$ is smaller, regardless whether the method captures the overall trend. In order to investigate the importance of the ground boundary layer formation, the Polimi case for IGE conditions at $Z/R = 1$ has been revised.

Table 3.14: Comparison of measured thrust variation for the Polimi IGE case at Z/R=1 against predictions with HoPFlow

Predictions	HoPFlow (inviscid wall conditions)	HoPFlow (viscous wall conditions)
1.1441	1.149	1.1235

In Table 3.14 ,the increase in CT at $Z/R = 1$ with respect to the OGE case is shown. It is noted that prediction of $HoPFlow$ using viscous ground condition is in very good agreement with the measurements. The maximum thrust at $Z/R = 1$ is well captured at $\approx 15\%$. Thus, the formation of the boundary layer on the ground adds an extra effect that increases the thrust on the rotor for low hovering altitudes. The thrust value obtained with $HoPFlow$ by considering the ground as a slip (inviscid) wall is at the same level with that obtained with $GenUVP$.

The fact that $HoPFlow$ prediction of the thrust in the inviscid wall case is very close to that of $GenUVP$ but deviates by 3% from the case with viscous wall is a strong evidence that the effect of the boundary layer of the ground on rotor loads is by no means negligible at low altitude ($Z/R \approx 1$) hovering flights.
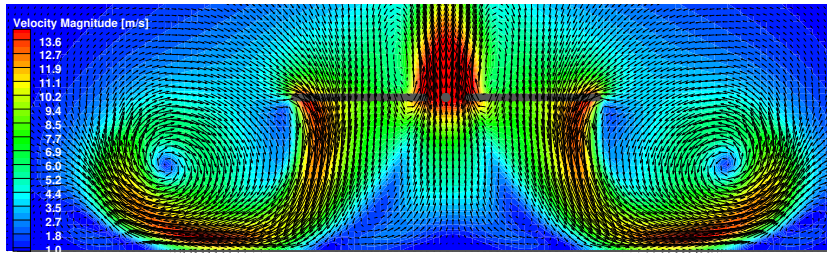
Figure 3.19: Velocity magnitude at a vertical plane at $X = 0$ for the Polimi case in IGE viscous conditions at height $Z/R = 1$. Snapshot at the end of the 6th period.
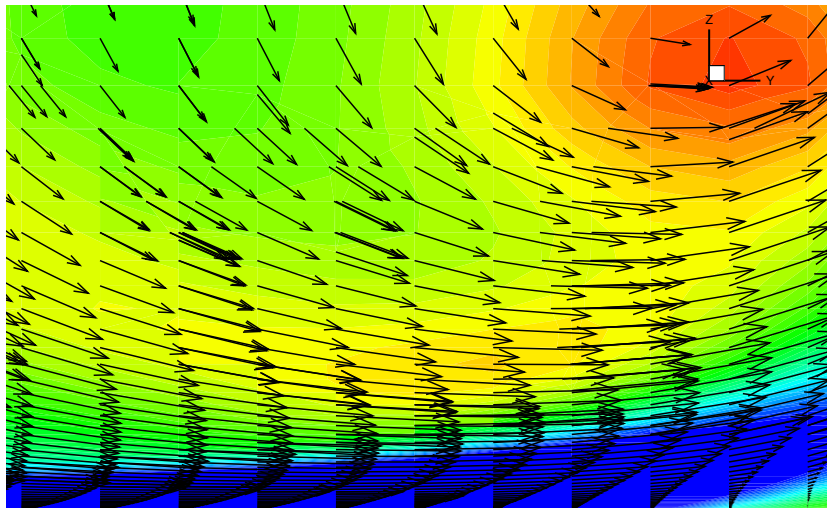
Figure 3.20: Boundary layer formation at a vertical plane at $X = 0$ for the Polimi case. Snapshot at the end of the 6th period.

The way that the formation of the boundary layer effects the loading on the rotor can be seen in Figure 3.19 and 3.20. The first shows the velocity field at an axi-symmetrical vertical plane $r/R1 = 0$ as it has developed after 6 periods on the particle mesh solver. The differences between viscous and inviscid simulations can be observed by comparing Figures 3.19 and 3.18. The key difference can be spotted at the position of the core of the tip vortex. In the viscous simulation, the vortex is higher and closer to the rotor. This is the result of the displacement effect

created by the boundary layer. In the particle mesh solution, the boundary layer is clearly identified by the decrease in the velocities close to the ground. Figure 3.20 shows the boundary layer region from the CFD (MaPFlow) solution.

Due to mass conservation, the velocity deficit near the ground generate an upwash flux that the forces the vortex to bounce. So, the vortex ring created by the rotor is pushed upwards, closer to the rotor level. When viscous effects are included, wake-induced velocities create a tangential to the ground flow that points away of the tip of the rotor. As a consequence, a boundary layer is formed outside the rotor disk as seen in Figure 3.19.

3.3.2 Investigation of the viscosity effect on the rotor loading and flow field characteristics with HoPFlow

Besides highlighting the effect of the ground boundary layer on the shape of the rotor developed wake, which implies a direct effect on the rotor loading, also interesting is to observe the effect of the ground boundary layer on the evolution of the starting rotor wake in hover. Figures 3.21 and 3.22 detail in terms of vorticity contours, the evolution of the wake that the two modeling options provide when $Z/R = 1$. The inviscid option is depicted in Figure 3.21, while the viscous option in Figure 3.22. From top to bottom, snapshots are shown at the end of the 1st, 2nd, 3rd, 4th, 6th, and 10th rotor revolution. At the end of the 1st period of the inviscid simulation (Figure 3.21), the starting vortex ring has formed below the edges of the rotor disk. At the end of the 2nd period, the ring moves downwards as a result of its self-induced velocity. At the end of the 3rd period, strong blade tip vortices are shaped that travel downstream. At this point, the core of the vortex ring is at $Z/R = 0.58$ above the ground level and at $r/R = 1.18$ away from the rotor center while the ring begins to roll up. At the end of the 4th period, delimited by the strong tip-vortices, the contracting rotor wake is now well shaped. The vortex ring moves further down and outwards and also starts to deform (the original circular cross section shape is now distorted) as it interacts with the ground. At the end of the 6th period, the vortex hits the ground at a radial distance of $r/R = 1.76$. The cross section of the ring is further distorted into an elliptical shape. Finally, at the end of the 10th period, the vortex travels outwards keeping the distance of its core from the ground constant at $Z/R = 0.22$.

(a) T= 1 Periods

(b) T= 2 Periods

(c) T= 3 Periods

(d) T= 4 Periods

(e) T= 6 Periods

(f) T= 10 Periods

VorMag: 0.0 0.0 0.1 0.1 0.1 0.1 0.1 0.2 0.2 0.2 0.2 0.2 0.3 0.3 0.3
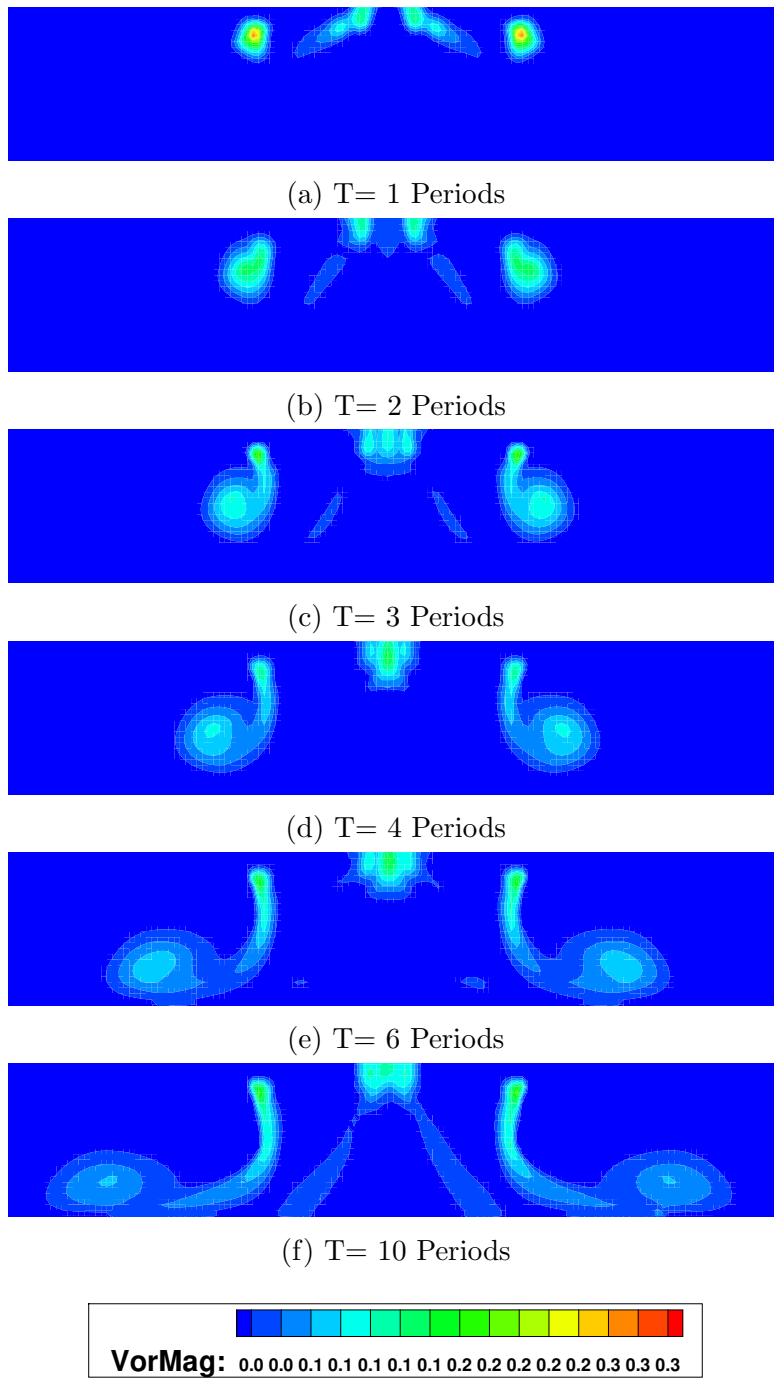
Figure 3.21: Vorticity pattern plots for IGE case at $Z/R = 1$ (snapshots taken at the end of the 1st, 2nd, 3rd, 4th, 6th and 10th rotor revolution). HoPFlow simulations with inviscid conditions on the wall.

Table 3.15: Tip vortex core position for the Polimi rotor at $Z/R = 1$ for inviscid wall condition

End of period	[Z/R] inviscid	[r/R] inviscid
1st	0.98	1.02
2nd	0.80	1.08
3rd	0.58	1.18
4th	0.45	1.34
6th	0.28	1.76
10th	0.22	2.14

In the viscous option (Figure 3.21), the shape obtained after the end of the first period (Figure 3.22a vs. Figure 3.21a) is very similar to that of the inviscid option. The predicted position of the vortex ring is almost identical in the two simulations (see also Table 3.15 and 3.16). However, the magnitude of the vorticity at the tip is higher in the viscous option and so is the loading. Higher circulation of the vortex ring implies that also higher down-wash will develop in the wake at the early stages of its generation.

In Figure 3.23, the down-wash and the in-plane velocity components over the rotor disk as obtained with the two modeling options are compared. Although the differences are small, the down-wash velocities (negative sign) over the rotor disk plane are higher in the viscous case (the extent of the blue pattern is greater in the viscous option results). Furthermore, the up-wash induced by the wake is higher outside the rotor disk area and the same holds for the in-plane velocities within the rotor disk area. This explains why in the viscous option, at the end of the 2nd period, both the vortex ring and the tip vortices of the blades have traveled a longer downwards distance as compared to the inviscid case. The same happens at the end of the 3rd revolution (longer downwards distance traveled by the wake) while in addition to the above, the ground boundary layer starts to develop. The shear in this boundary layer is caused by the wake jet flow that at the end of the 3rd revolution impinges on the ground. The development of the boundary layer creates a vertical displacement effect (an upwards transpiration velocity related to the displacement thickness of the boundary layer) which changes in shape of the vortex ring. The distortion of the vortex ring in the viscous modeling option begins earlier than in the inviscid one (already at the end of the 3rd revolution). The reason for that is twofold: (i) the ring in the viscous option travels downwards with a higher velocity due to higher loading and (ii) the ring interacts with the boundary layer of the ground. At the end of the 4th period, the thickness of the boundary layer has further increased while a stronger interaction with the vortex ring is observed. The cross section of the vortex ring obtains an elliptical shape. By getting closer to the ground, the interaction of the vortex ring with the boundary layer on the ground gets stronger. The outer edge of the ring is closer to the edge of a thicker boundary layer as compared to the inner edge.

(a) T= 1 Periods

(b) T= 2 Periods

(c) T= 3 Periods

(d) T= 4 Periods

(e) T= 6 Periods

(f) T= 10 Periods

VorMag: 0.0 0.0 0.1 0.1 0.1 0.1 0.1 0.2 0.2 0.2 0.2 0.2 0.3 0.3 0.3
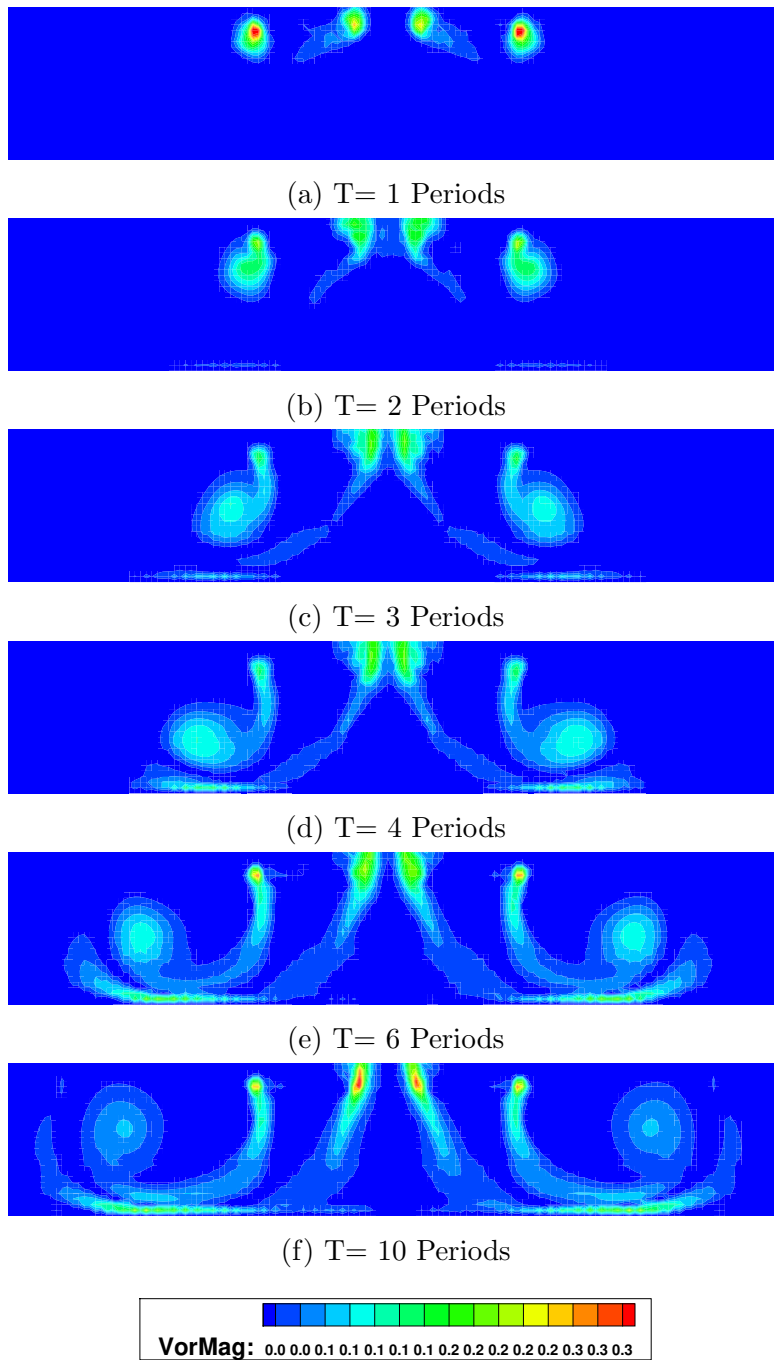
Figure 3.22: Vorticity pattern plots for IGE case at $Z/R = 1$ (snapshots taken at the end of the 1st, 2nd, 3rd, 4th, 6th and 10th rotor revolution). HoPFlow simulations with viscous conditions on the wall.

Transpiration velocities are therefore higher over the outer edge of the ring and the ring appears to rotate around its axis. At the end of 6th and 10th revolution, the vortex ring moves upwards and away from the ground as if it rebounds (at $Z/R = 0.51$ and $Z/R = 0.65$, respectively, see Tables 3.15, 3.16), while the wake tip-vortices start to interact with the boundary layer on the ground.

The above comparison has revealed that as the distance from the ground gets smaller, two features that can only be reproduced by taking into account viscosity, become decisive: First, the induced velocities in the wake are higher leading to higher loading and secondly, the vortex ring rebounds from the ground pushed by the displacement generated in the ground boundary layer.
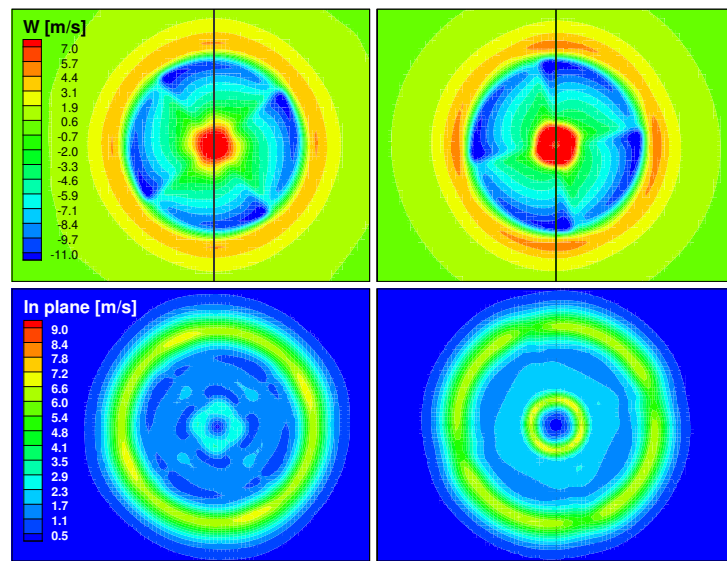
Figure 3.23: Comparison of the vertical and in plane velocity on the level of the rotor for the case with the viscous ground condition (right) and the inviscid ground (left). The rotor concerns the Polimi experiment, and the helicopter rotor is placed at $Z/R = 1$ in IGE conditions.

Table 3.16: Tip vortex core position for the Polimi rotor at $Z/R = 1$ with viscous wall conditions

End of period	[Z/R] viscous	[r/R] viscous
1	0.53	1.19
2	0.39	1.41
3	0.53	1.19
4	0.39	1.41
6	0.51	1.86
10	0.65	2.00

84
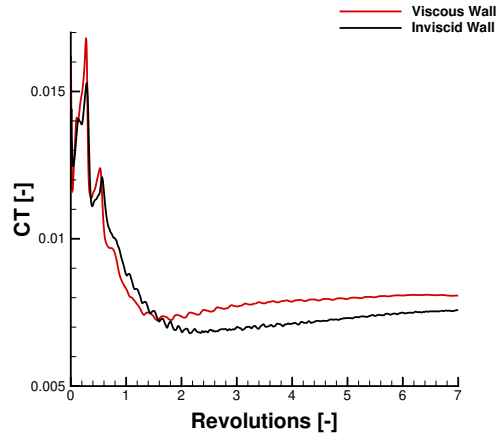
Figure 3.24: Comparison of the helicopters thrust coefficient from HoPFlow at IGE $Z/R = 1$ with inviscid and viscous wall conditions respectively.

Comparison of the predicted CT time series of the two HoPFlow simulation options is shown in Figure 3.24 for the case $Z/R = 1$. It indicates that the presence of a viscous wall gives rise to increased thrust of the rotor already from the very beginning of the simulation while after a number of revolutions CT converges to higher value.

3.3.3 Importance of the fuselage on the results of viscous simulations with HoPFlow

In the previous section, despite the good comparisons, the validation of the methods and the detailed discussion, simulations did not include the fuselage which was present in the measurements. So in order to complete the analysis an additional $HoPFlow$ simulation with the fuselage has been conducted. This simulation concerned the Polimi rotor at $Z/R = 1$. The Eulerian grid of the main rotor overlaps with the grid of the fuselage which in turn overlaps with the ground grid. In this respect, this case also verifies the ability of $HoPFlow$ to handle overlapping grids.

Adding the fuselage has negligible effect on the rotor thrust. The increase is again 15% ($CT/CT_{OGE} = 1.15$). However, as expected, the effect on the developed flow field is substantial.

As Figure 3.25 shows, the fuselage deflects the wake flow when it reaches its surface. The vortex formed over the upstream side of the rotor disk is diverted by the nose of the fuselage leading to high outwash flow. Furthermore, separation of the flow at the edge of the fuselage creates a re-circulation area underneath of it. Over the aft part of the fuselage, the tail boom, which extends downstream up to the rotor tip, blocks the wake flow leading to reduced velocities in the downstream part of the wake and smaller vortex structures in the resulting outwash flow. As a

85

result of the above the wake structure is no longer symmetric over the helicopter symmetry plane of Figure 3.25.

Figure 3.25: Velocity magnitude at a vertical plane at $Y = 0$ for the Polimi case in IGE viscous conditions at height $Z/R = 1$. Snapshot at the end of the 6th period.

However, looking the back view of the flow (Figure 3.26), there is resemblance to an only-rotor simulation. This is due to the size of the fuselage in the lateral direction. The effect of the fuselage on the formation of the wake is small since the wake vortices on the advancing and retreating sides of the rotor are not blocked by any surface. The only difference that can be spotted, concerns the region underneath the fuselage, where two counter rotating vortices are created due to flow separation. These vortices extend beyond the width of the fuselage and interact with the strong downwash flow induced by the rotor. Even though the fuselage interacts with the wake of the rotor and blocks part of the wake induced flow, it does not intervene in the way that the wake interacts with the ground. As in the case of the pure rotor a boundary layer develops on the ground as a result of the rotor downwash that pushes the rotor vortex ring upwards. Thus, a similar increase in CT/CT_{OGE} is again observed with respect to the inviscid ground case which lacks the displacement effect by the ground boundary layer.

As shown in Figure 3.27, the width of the boundary layer is smaller comparing to the simulation without the fuselage (Figure 3.20). This is due to a smaller mean jet velocity.

These differences at the level of the ground are also seen in the pressure distribution on the ground. In Figure 3.28 the pressure distribution on the ground is presented for the inviscid condition on the ground and for the viscous ground with and without the fuselage.
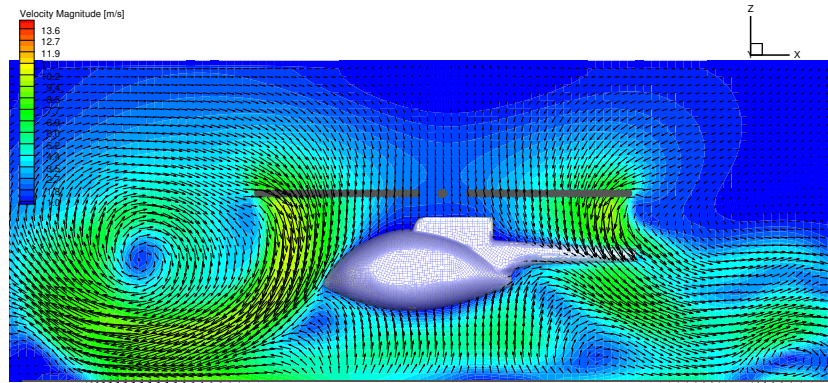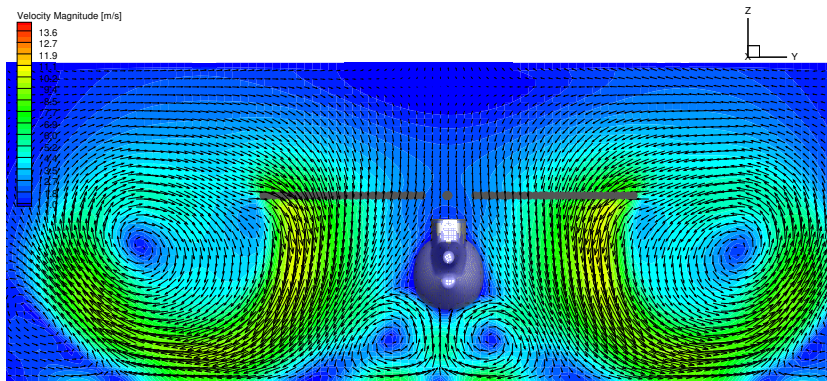
Figure 3.26: Velocity magnitude at a vertical plane at $X = 0$ for the Polimi case in IGE viscous conditions at height $Z/R = 1$. Snapshot at the end of the 6th period.
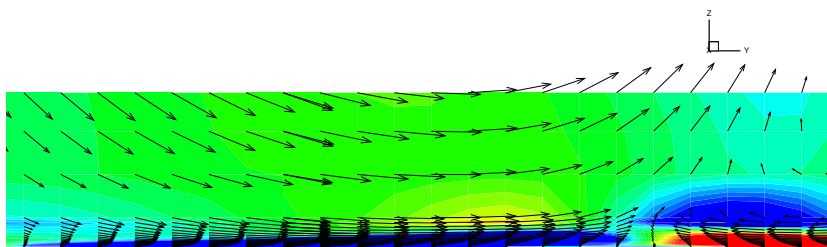
Figure 3.27: Boundary layer formation at a vertical plane at $X = 0$ for the Polimi case with the fuselage. Snapshot at the end of the 6th period.
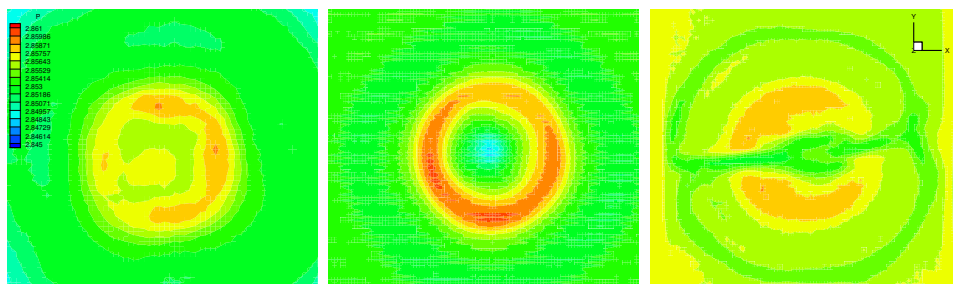
(a) Inviscid wall conditions

(b) Viscous wall conditions

(c) Viscous wall conditions and fuselage

Figure 3.28: Ground pressure distribution comparison between HoPFlow simulations for the single main rotor and the rotor-fuselage configuration.

87

3.4 Rotor Performance in IGE conditions with surrounding walls

ONERA examined the effect surrounding walls may have when combined with *IGE* as shown in Section 3.1.1 and specifically in Figure 3.3. Details about the configuration of the experimental rig can be found on Table 3.4 and Figure 3.3. For this case, the experimental data are compared with predictions obtained with *GenUVP*. Both loads measurements and flow field PIV data are reproduced using the potential solution.

3.4.1 Main Rotor Loads Results
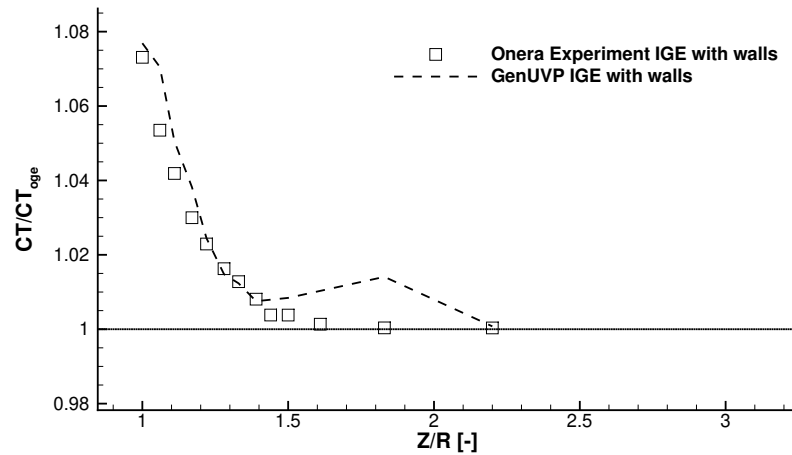
Figure 3.29: Rotor thrust variation in IGE with side walls. Comparisons of measurements against predictions obtained with GenUVP.

In Figure 3.29 the variation of the time averaged thrust with respect to the distance from the ground is shown. The thrust ratio with (IGE) and without (OGE) ground effect is plotted versus the dimensionless distance from the ground. According to measurements, when rotor is hovering IGE while there is a peripheral blockage, the thrust coefficient monotonically increases (almost exponentially) with respect to the *OGE* case as the distance from the ground decreases. At the lowest point, the highest increase in thrust is obtained, which is about 7%. The effect of the ground and of the surrounding buildings vanishes at Z/R values higher than 2.

Comparing the results of the previous chapter with the data from this experiment, it follows that the two campaigns are in line in terms of the tendency of the trust. The lower the height of the flight the greater the effect. On the other hand, there are two major differences. The first concerns the actual value of the increase. There is a 7% drop in the maximum thrust when the walls are added.

88

The second is that the height of flight after which the effect of the ground combined with peripheral walls vanishes, is lowered at $Z/R = 2$ compared to $Z/R = 4$ in the case of the only having the ground.

The comparison between measurements and the *GenUVP* predictions are in good agreement. The potential solver is capable of predicting the overall trend of the thrust increase as the rotor hovers closer to the ground. In quantitative terms the predict thrust values are very close to the measured ones with a maximum deviation of 1% at $Z/R = 1.8$. Such an overshoot was also seen in the tests as well as in the predictions of the Polimi *IGE* case (Section 3.3.3, Figure 3.17). In the case of this section, this is only seen in the predictions.

3.4.2 Flow field comparisons against ONERA PIV measurements

(a) ONERA Measurements   (b) GenUVP predictions
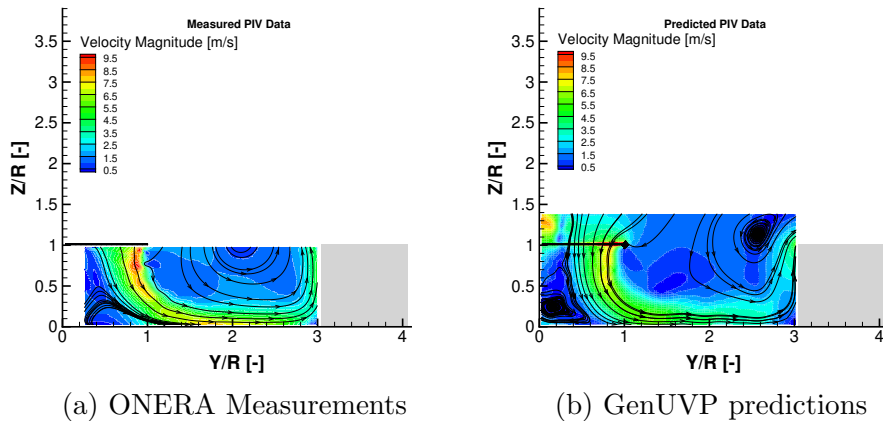
Figure 3.30: The velocity magnitude over a vertical plane placed at X/R=0 and flow patterns for the ONERA experiment when the rotor is placed at $Z/R = 1$ above the ground.

An effective way to explain the obtained reduction in thrust in the presence of the side walls as compared to the pure *IGE* case (for $Z/R = 1$), is to analyse the developed flow field. Figure 3.30(a) shows the measured pattern of the flow (velocity PIV measurements) in the region between the rotor and the ground/walls when the rotor is placed at $Z/R = 1$ above the ground. It can be seen that the wake of the rotor moves parallel to the ground and along the side wall before arriving at its top edge. It then rolls up forming a counter-clockwise vortex which remains within the court yard and stands in between the rotor and the side walls. The vortex core lies at a vertical position slightly higher than the rotor hub and induces downwash velocities over the rotor disc. This downwash contributes to

an opposite effect on the loads as compared to that of the ground, in which the position of the starting vortex ring is close but beneath the rotor hub and therefore increases the loading. In the absence of the side walls (and in the context of an inviscid simulation) the roll up of the wake that impinges on the ground would take place at a much larger distance from the rotor position and would therefore have minor effect on its performance.

In Figure 3.30 a similar flow pattern is obtained through simulations. While the streamlines follow the ground and the side walls as in the tests, there is flow leakage over the side walls along their edges. Also, the rolling up of the wake is stronger and takes place closer to the walls as compared to measurements. Both of these features are attributed to the essentially inviscid character of the model which in the present case neglects the interaction with the wall boundary layer. This also explains the slightly overestimated thrust. It is important to note that even though the averaged loads are in good agreement with measurements, the inviscid character of $GenUVP$ generates deficiencies in the flow field. However, it is important to consider that the effect of the surface roughness in simulations of flows between buildings is decisive even for the appearance of multiple or single vortices. In this context, the comparison of the flow patterns between measurements and inviscid predictions is satisfactory.

In the experiment, the low Reynolds number and the viscosity are responsible for trapping the vortex between the rotor and the wall and by that create a steady re-circulation region. Inviscid predictions on the other hand produce this vortex periodically. For instance, when the vortex ring of the IGE case impinges on the ground, it travels away from the rotor centre. When it reaches the side wall it is accelerated upwards licking the wall. Then, when the vortex reaches the upper edge of the wall, the induced velocities create an expansion zone that pushes the vortex beyond the walls. When the vortex moves far away from the rotor disk plane, in the absence of its induced velocities, the loading of the rotor decreases leading to the emission of a new ring type vortex. This unsteady phenomenon in the inviscid simulation is periodically repeated with a periodicity of 40 rotor revolutions.

3.5 Helicopter Hovering above an obstacle - Sweep in x axis (T1 case)

Next, the combined rotor-obstacle-ground interaction is addressed by varying the horizontal placement of the rotor center with respect to the obstacle (horizontal sweep defined in Figure 3.4). Predictions of the normalized CT and Figure of Merit (FM) with respect to the OGE case are compared against test data from Polimi and Glasgow test campaigns (Figure 3.31 and Figure 3.33 respectively). In all cases, the rotor center is at $Y/R = 0$, while the rotor plane is at 1R above the obstacle top. This means that in the Polimi test, $Z/R = 2$ and in the Glasgow

test $Z/R = 3$ with respect to the ground.

The T1 cases of the Polimi and Glasgow experiments have been simulated with *GenUVP* and *HoPFlow*. *GenUVP* simulations cover the whole range of points addressed in the experiments (see Table 3.2-3.6) while *HoPFlow* simulations focus on some points of the Polimi experiment ($X/R = -1, 0, 1$), where *GenUVP* fails to provide consistent load and flow field predictions.

3.5.1 Main Rotor Loads Results
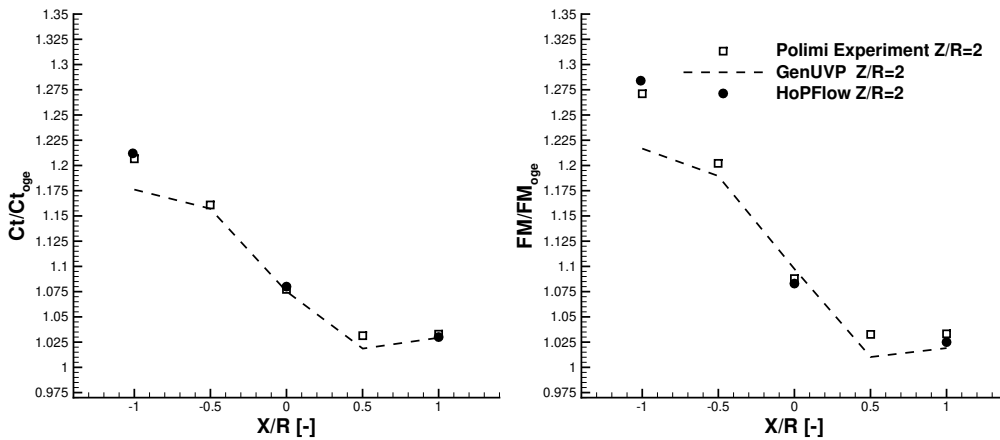
(a) Trust coefficient variations vs. x position

(b) Figure of Merit variations vs. x position

Figure 3.31: CT and FM variations against the distance from the centre of the obstacle (X/R=-1). Comparisons of measured data against *GenUVP* and *HoPFlow* predictions for the T2 Polimi case. The rotor has a constant distance of 2R from the ground.

Figure 3.31 depicts the variation in CT and FM of *Polimi* rotor with respect to the distance from the centre of the obstacle. At $X/R = -1$ the whole rotor disk is above the obstacle. The increase in thrust is even higher than that of the pure IGE conditions. CT/CT_{OGE} increases from about 15% when the rotor is $1R$ above the ground, in the pure ground effect case, to 21% when the rotor is $1R$ above the obstacle. It is noted that this 21% increase in thrust corresponds to a $2R$ distance from the ground in the Polimi test. This difference is due to the presence of the obstacle and is attributed to the different formation of the wake as compared to the IGE case. In the present case the tip and starting vortices are again constrained by the solid boundaries that introduce mirror vortices. In the presence of the obstacle and the ground, mirroring becomes more complicated. The different boundaries (horizontal and vertical walls) that need to be considered in the application of the mirror technique result in an infinite series of mirror vortices.

91
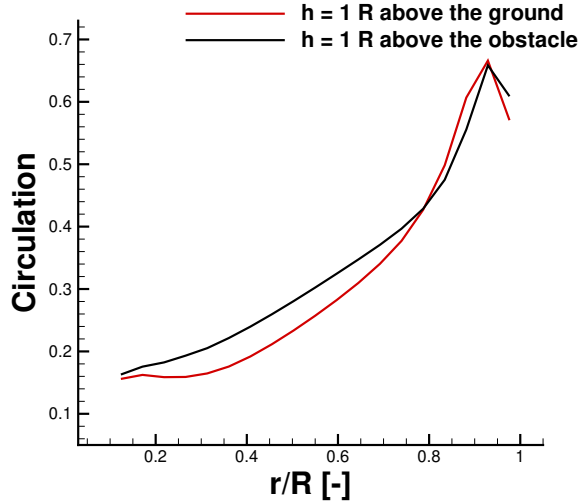
Figure 3.32: Comparison of the averaged circulation over the blade of the Polimi rotor of T2 case $Z/R = 2$ against the OGE case $Z/R = 1$.

Figure 3.32 shows the difference in circulation distribution along the blade span of the Polimi rotor with and without the obstacle as calculated with the potential solver $GenUVP$. In the two results the rotor is a) centered at $1R$ above the obstacle and b) placed $1R$ above the ground. Results correspond to time averaged circulation along the rotor blade over one period. For most of the blade length (80% of the span) circulation is higher when the rotor hovers above the obstacle, which explains the higher CT values predicted in this case. It is worth noticing that close to the tip the circulation distributions are very similar.

As the rotor centre is gradually moved away from the obstacle, the increase in both CT and FM becomes smaller. When the rotor disk is no longer shading the obstacle (this happens at $X/R = 1$), the thrust increase is 3.5%, which is almost the same as in the IGE case for $Z/R = 2$. This indicates that at this distance, the presence of the obstacle is no longer influencing the rotor loading.

Comparing predictions against measured data the following observations are made:

- The quality of the predictions is good, in both $GenUVP$ and $HoPFlow$. The same holds for the overall shape of the predicted CT and FM variations with X/R position. Despite its inviscid character, $GenUVP$ reproduces well the trend. The inclusion of the effect of the ground and the obstacle boundary layer through $HoPFlow$ simulations improves the level of agreement with measurements in quantitative terms.

- The maximum difference between $GenUVP$ predictions and measurements is noted at $X/R = -1$. The difference is about 2.5 % in CT and 5% in

FM. These differences are in line with the discussion of the IGE conditions, where it was also noted that as the distance of the rotor from the ground decreases, deviations between predictions and measurements increase, while the maximum difference was again obtained at $Z/R = 1$ and it was found to be of the same order of magnitude.

- $HoPFlow$ does not only correctly capture the shape of the variation, but also manages to predict well the maximum increase in CT and FM even at $X/R = -1$. This outcome is in accordance with the previous discussion on the importance of the viscous interactions that take place when a rotor hover in close proximity to solid boundaries.
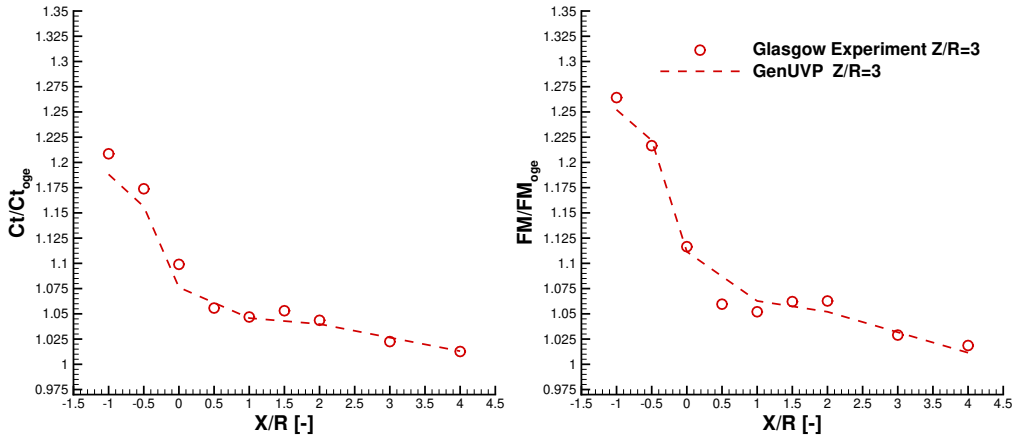
(a) Trust coefficient variations vs. x position

(b) Figure of Merit variations vs. x position

Figure 3.33: CT and FM variations against the distance from the centre of the obstacle (X/R=-1). Comparisons of measured data against $GenUVP$ predictions for the T2 Glasgow case. The rotor has a constant distance of 3R from the ground.

Similar to Polimi, the T2 case of Glasgow showcases the variation in CT and FM when the rotor undergoes a sweep in the $x-axis$. In contrast with the Polimi test, the rotor hovers at $Z/R = 3$ from the ground. Measurements by Glasgow (see Figure 3.33) depict the same trend in CT and FM variations as Polimi's. When the rotor centre is placed at $X/R = -1$ (the obstacle is shading the whole rotor), the maximum increase in CT is $\approx 21\%$, higher than the value at $Z/R = 1$ of the IGE case and slightly higher than that of the Polimi test.

The above indicates that the thrust increase is independent of the distance from the ground level, and is rather driven by the effect of the obstacle and the way the wake develops in this particular case. As the rotor centre moves away from the obstacle CT/CT_{OGE} decreases. At $X/R = 1$ (when the rotor is no longer

shaded by the obstacle) the increase in CT is 5%. In this test, the increase is slightly higher compared to the one of Polimi's test for the same position of the rotor. It is noted that in Glasgow's test, the distance of the rotor from the ground level is higher than in Polimi's test ($Z/R = 3$ in Glasgow's test against $Z/R = 2$ in Polimi's test) which indicates that at $X/R = 1$, the bigger obstacle in Glasgow's test, still influences the rotor inflow and the formation of its wake.

As the rotor centre moves further away from the edge of the obstacle, its effect gradually diminishes and at $X/R = 4$ practically vanishes, as the 1% increase in thrust obtained for the Glasgow configuration is in line with the recorded increase in IGE conditions. The two tests agree well in qualitative terms, although the two obstacles are not the same. The shapes of the measured CT and FM curves are very similar. The maximum difference is in the order of 2% comparing measurements against $GenUVP$ predictions and it is well justified by the difference in geometric characteristics (different shape and dimensions of obstacle and different rotor diameter).

Predictions for the Glasgow T1 case are only provided by $GenUVP$. The difference in thrust and Figure of merit is well captured by the model despite its inviscid character. As in the Polimi case, the overall shape and trend of the results are in good agreement with measurements. However, quantitative differences are observed when the rotor is shaded by the obstacle. This is attributed to the lack of the viscous interactional phenomena as discussed before.

3.5.2   Flow field comparisons against Polimi's PIV measurements

Polimi performed PIV measurements which are compared against predictions obtained with $GenUVP$ and $HoPFlow$. Contours of velocity magnitude and flow lines are shown on the vertical xz plane passing through the centre of the rotor $r/R = 0$.

When the hovering rotor is centered above the obstacle (at $X/R = -1$), flow measurements (Figure 3.34a) indicate that the slipstream of the rotor wake separates from the edges of the box roof. A re-circulation (clock-wise rotation) zone of low velocities is formed between the side wall of the obstacle and the wake shear layer. Hence, a low velocities region within the re-circulation zone is created. Because flow separation is not accounted for in $GenUVP$ (the wall and the ground are modeled only as non-penetrated surfaces), the predicted streamlines in Figure 3.34b, remain attached to the side wall of the obstacle. High downwash velocities are obtained over the side face of the obstacle. The counter-clockwise vortices appearing at $X/R = 0.5$, 1 and 2 are due to the roll up of the rotor wake, which once pushed downwards to the ground, then moves parallel to it as demonstrated in the pure IGE case.

The above qualitative difference between predictions and measurements, explains the increasing deviation in the obtained loads (see Figure 3.32) as the rotor

approaches the top of the obstacle. In the real flow, the downwash expands outside the bounds of the re-circulation zone and virtually increases the dimensions of the obstacle that the rotor "senses" and by that also increases the influence of the body on the rotor. These phenomena, which the inviscid code $GenUVP$ is not able to resolve, are well reproduced by $HoPFlow$. In Figures 3.32(c,d) the flow field recorded over the particle mesh grid of $HoPFlow$ simulation is shown. The contours depict the velocity magnitude and the stream-traces of the flow field with and without the presence of the fuselage.

(a) Polimi Measurements

(b) GenUVP Predictions

(c) HoPFlow Predictions without the fuselage
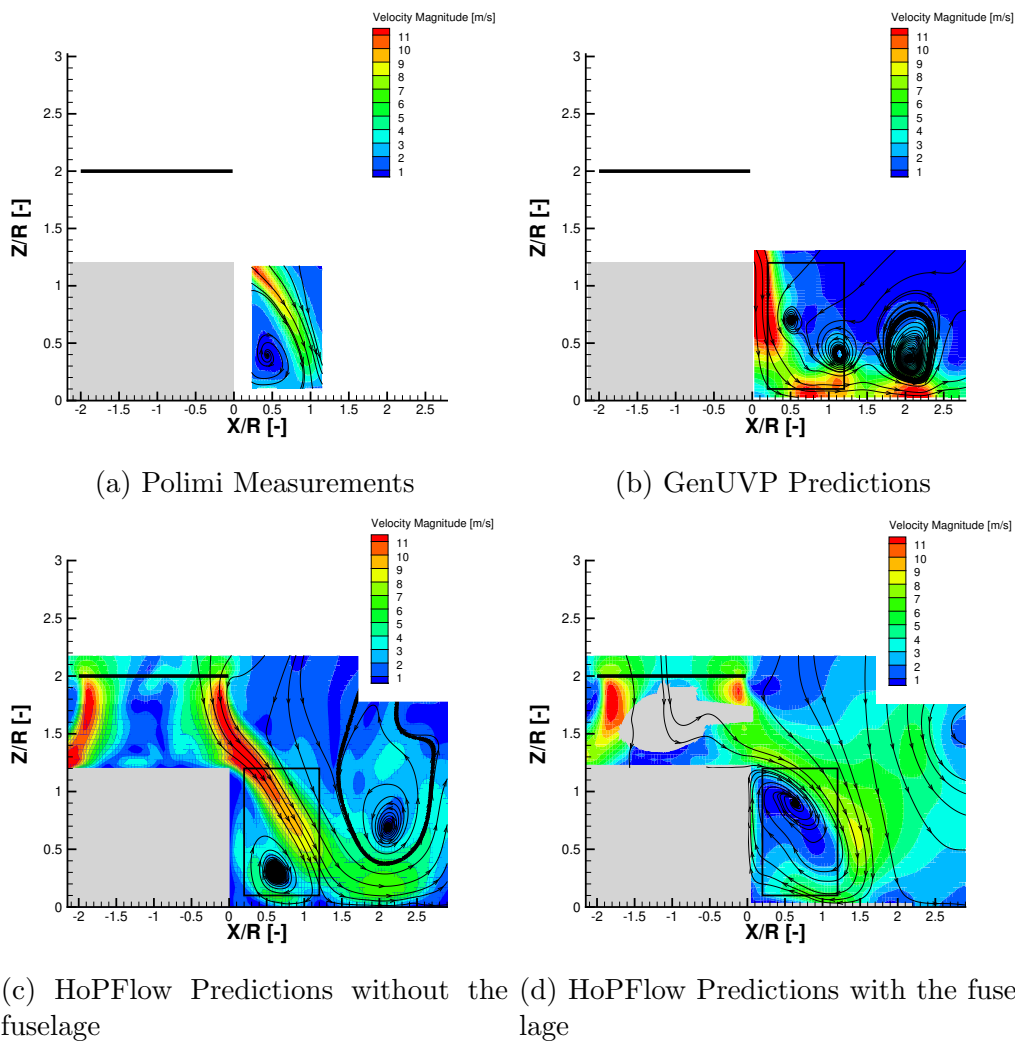
(d) HoPFlow Predictions with the fuselage

Figure 3.34: Flow field comparison for the Polimi experiment while the rotor is stationed at $X/R = -1$ and $Z/R = 2$.

In the case without the fuselage (Figure 3.32c), as the slipstream circumvents the obstacle over its edges, a re-circulation area is formed at the side wall of

the obstacle. Comparison with the test is good and *HoPFlow* reproduces the measured flow pattern. The extend of the re-circulation zone, the position on the ground where the wake jet flow impinges, the magnitude of the velocities in the wake slipstream are also in good correlation with the measurements. Only the velocities in the re-circulation zone are over-predicted. However, the deviation is small and does not affect the loads. It is worth noticing that similarly to the pure *IGE* case, as the wake of the main rotor approaches the ground, a boundary layer develops which pushes the vortex formed within the re-circulation zone upwards.

Then as regards the effect of the fuselage, the corresponding flow field for the same case is shown in Figure 3.32(d). When in proximity to the ground, the effect of the fuselage is to deflect the wake jet flow as a result of its blockage effect. When the helicopter is hovering above the obstacle, the same blockage effect is identified as well. Focusing on the region above the obstacle, two major differences are observed: (a) the jet flow produced by the main rotor has reduced velocities as compared to the only-rotor case. Therefore, the downwash that impinges on the obstacle and separates from its edges has lower velocities too. Switching to the window where measurements have been acquired, it is clear that a shear layer of reduced velocities and higher downstream extent is formed. The results are subjected to the assumption of laminar flow which eventually does not fit the conditions around and underneath the fuselage. So, besides the conclusion regarding the loads, the present simulation with the fuselage may be considered as a proof of concept step, requiring further investigation.

When the rotor centre is aligned with the edge of the obstacle (at $X/R = 0$), a re-circulation area of low velocities is again formed between the side face of the obstacle and the rotor downwash region (see Figure 3.35 (a) of the measured field). An anti-clockwise vortex is formed this time, which is pushed closer to the ground level as compared to the previous case (down-left side of the PIV window). In Figure 3.35a, the traces of both the retreating (downstream part of the rotor) and the advancing blade (upstream part of the rotor) wakes are distinguished. The downwash of the retreating blade as revealed, hits (not shown in the window) the roof of the obstacle and a stream of the wake flow exits from the downstream (right) side of the obstacle. Higher velocity magnitudes are noted in the wake of the retreating blade.

In the flow field predicted by *GenUVP* (Figure 3.35b) only the trace of the downstream (retreating) blade is detected over the simulation window, while the wake of the advancing blade (not shown in the plot) moves to the left (upstream). The above difference is caused once again by the inviscid wall condition. As in measurements, a low velocity zone is formed between the right wall of the obstacle and the wake slipstream. The flow mechanism that leads to the formation of this zone is different in measurements and in *GenUVP* results. In measurements, this zone is created by the combination of the two different shear layers. In *GenUVP* predictions this is caused by the lack of high downwash velocities underneath the hub of the main rotor.

(a) Polimi Measurements

(b) GenUVP Predictions

(c) HoPFlow Predictions without the fuselage
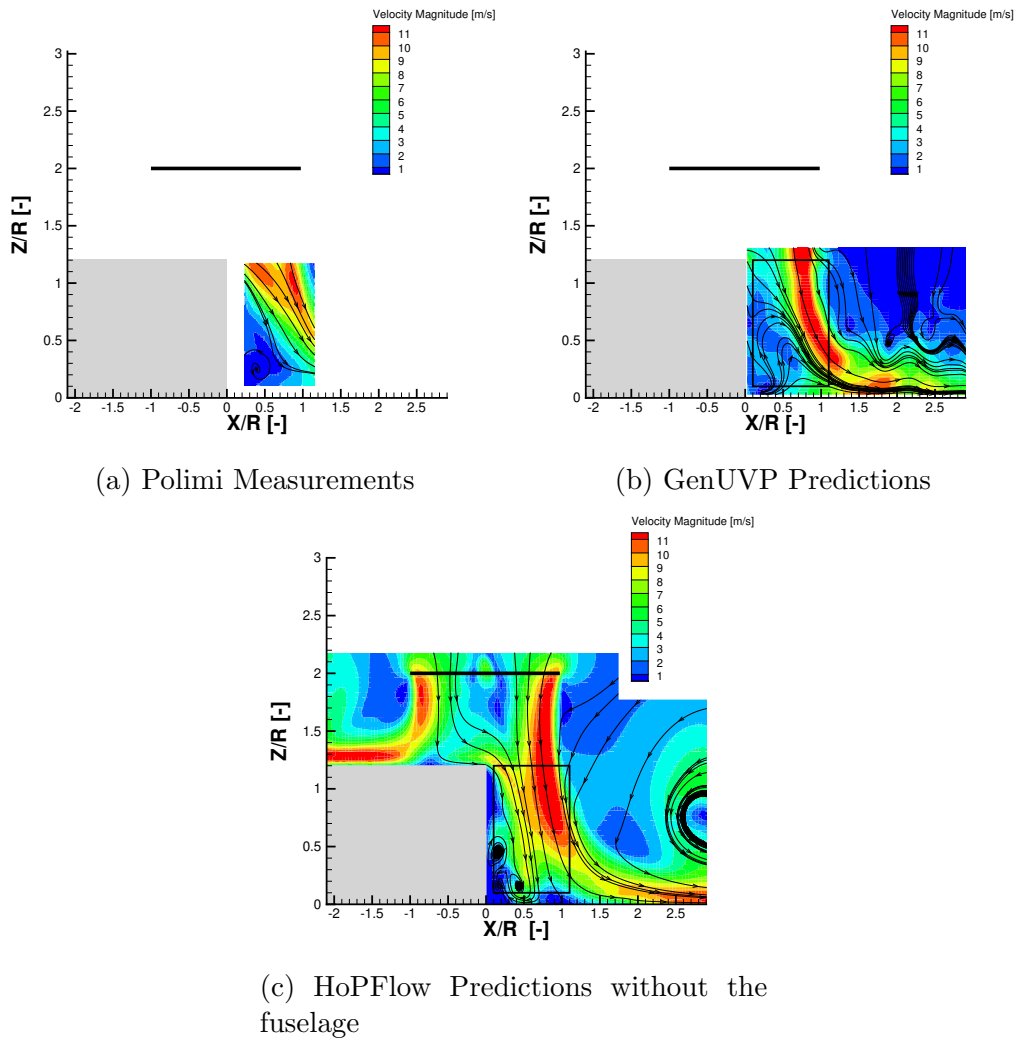
Figure 3.35: Flow field comparison for the Polimi experiment while the rotor is stationed at $X/R = 0$ and $Z/R = 2$.

Similarly to the experiment, the flow over the upstream part of the slipstream as predicted by $HoPFlow$, impinges on the box roof and moves upwind (Figure 3.35c). Over the downstream part, the predicted slipstream stream part of the rotor appears to have velocities higher than in the tests. The jet flow through the upstream half of the rotor splits in two; the very front part moves upstream while the rest after impinging on the roof top, separates and the shear layer continuous vertically downwards. There is indication in the measured window that at the roof edge there are two shear layers, suggesting that the upstream part of the jet flow altogether moves downstream (or the split favors the part moving downstream). As in measurements, a low velocity zone is formed between the right wall of the

obstacle and the wake slipstream. The above qualitative difference between predictions and measurements could be due to the effect of the fuselage which has been neglected in this simulation.

When the rotor centre is at $X/R = 0.5$, two weak counter-rotating vortices are formed within the PIV window at $Z/R = 0.9$ and $Z/R = 0.6$ which are predicted with $GenUVP$ but with an offset at $Z/R = 1.2$ and 0.4 respectively (Figure 3.36). In the larger simulation window, the slipstream of the left side is clearly formed, while that of the right side is barely detected at the left edge of the window.


(a) Polimi Measurements   (b) GenUVP Predictions

Figure 3.36: Flow field comparison for the Polimi experiment while the rotor is stationed at $X/R = 0.5$ and $Z/R = 2$.

When the rotor is further moved at $X/R = 1$ (Figure 3.37a), the slipstream of the advancing side starts to show up in the PIV window of the experiment. In the $GenUVP$ predictions-Figure 3.37b, a stronger slipstream is observed and further away from the side wall in comparison to the $X/R = 0.5$ case. Further, on the right of the PIV window, a counter rotating vortex is formed in a region of low velocities. A similar pattern is also seen in the simulations, although the recirculating zone is offset and smaller in size. On the right of this vortex the slipstream of the retreating side is seen as in the previous case.

Focusing on the corner between the side wall of the obstacle and the ground level, it is noted that downwash velocities in this region are slightly underestimated. Furthermore, the trace of the downwash flow is slightly shifted downstream as compared to the measured one. In the, larger than the measured, simulation window the trace of the slipstream of the retreating side is also detected.

In the $HoPFlow$ simulation, predictions of the flow field compare well to measurements. As seen in Figure 3.37(c), the upstream flow leads to a slipstream on the side wall of the obstacle. A re-circulation zone is created beneath the main rotor close the obstacle. Comparing $HoPFlow$ to the experiment, higher velocities

are noted in the PIV window. However, this increase could have been reduced by the presence of the fuselage.

(a) Polimi Measurements
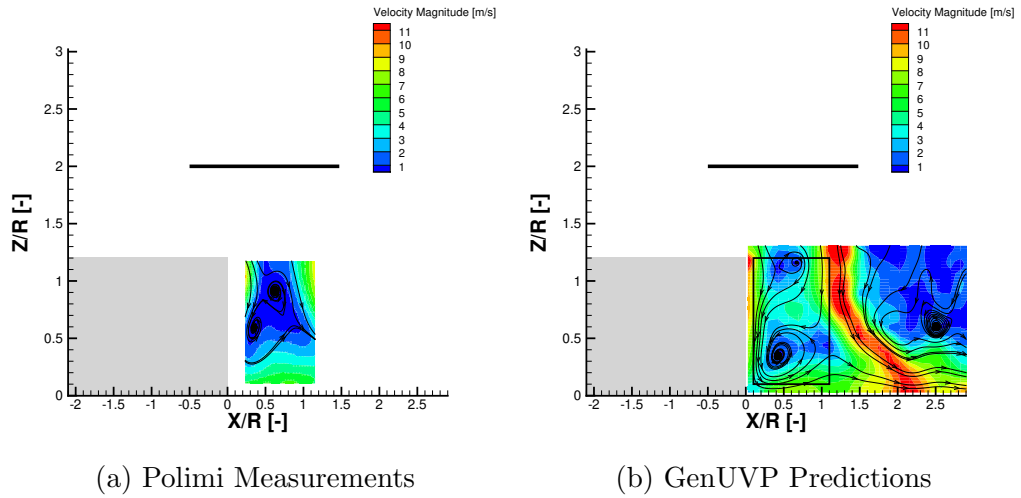

(b) GenUVP Predictions

(c) HoPFlow Predictions without the fuselage
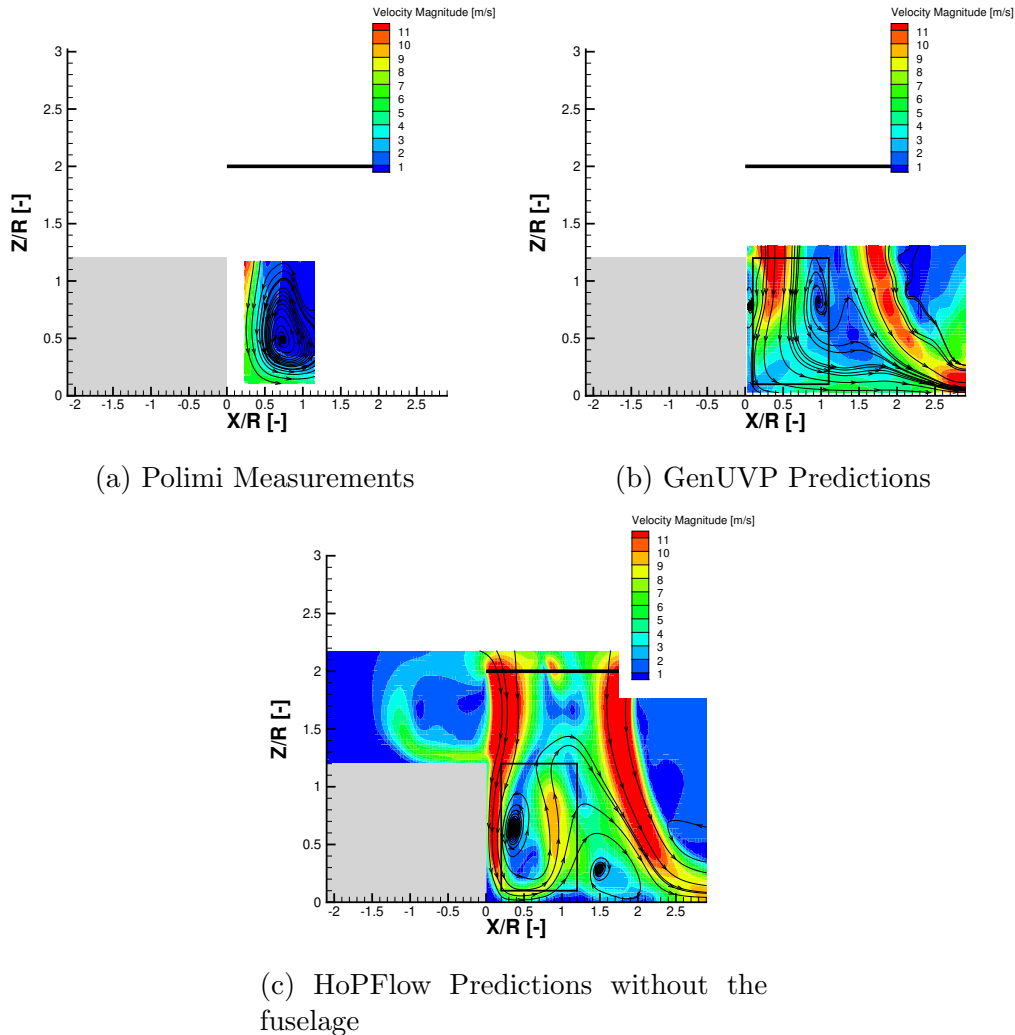
Figure 3.37: Flow field comparison for the Polimi experiment while the rotor is stationed at $X/R = 1$ and $Z/R = 2$.

Overall, better agreement between both sets of predictions and measurements is obtained when the rotor is less masked by the obstacle ($X/R = 0.5, 1.0$). At these test points, as depicted in the velocity magnitude contours, viscous phenomena are not dominating the flow field. However, when the rotor is fully shaded by the obstacle, only HoPFlow predictions are in good agreement with measurements and the reason is that the inclusion of viscous walls is the key element for the formation of the wake.

3.6 Helicopter Hovering above an Obstacle - sweep in z axis (T2 case)

In the present section the problem of a helicopter hovering above a rectangular obstacle is investigated. This problem is addressed by Polimi's test campaign. As explained in Section 3.1.1 the test matrix (Table 3.2 consists of a number of test points in which the rotor is placed at different vertical positions above a rectangular obstacle. At the first point of the test matrix, the rotor center is placed at $X/R = -1$ (the rotor is above the obstacle) and at $Z/R = 2$ (the rotor is 0.8 radii above the top of the obstacle). Then a vertical sweep along z axis is performed, the last measurement concerns the rotor placed at $Z/R = 4$, or 3.2 radii above the obstacle. On the simulation side, a full sweep performed using $GenUVP$ while $HoPFlow$ had been used to simulate three points of the test matrix $(Z/R = 1, 2, 4)$.

3.6.1 Main Rotor Loads Results
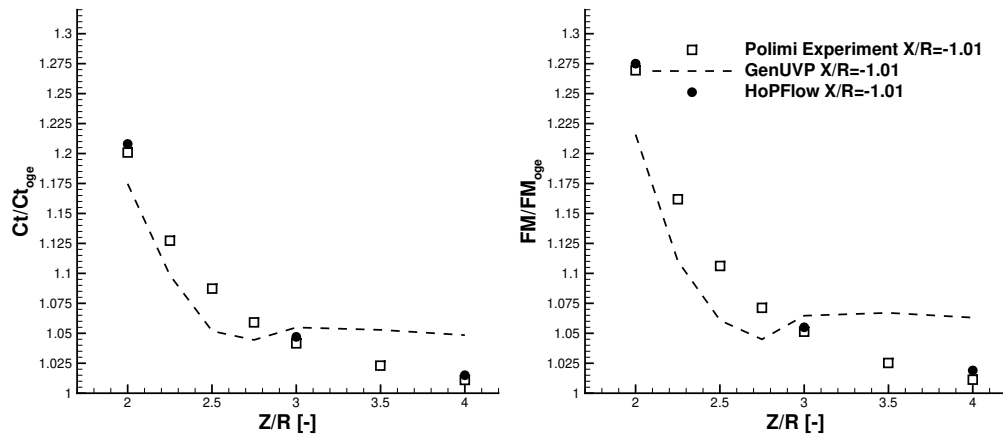
(a) Trust coefficient variations vs. z position

(b) Figure of Merit variations vs. z position

Figure 3.38: CT and FM variations against the distance from the ground (Z/R). Comparisons of measured data against $GenUVP$ and $HoPFlow$ predictions for the T1 Polimi case.

As in IGE case, measurements indicate that, the main effect of the obstacle on the helicopter rotor loads is to increase CT with respect to the OGE case (see Figure 3.38 (a). More specifically, the maximum increase appears at $Z/R = 2$ above the ground and it is equal to 20% (this position is the same test point of Polimi T1 case). As the helicopter rotor center vertical distance from the ground

is increased, a lower and lower increase in CT/CT_{OGE} is obtained. The rate of the variation of the load changes with the vertical position. A higher rate is noted in the range $Z/R = 2-3$. Above $Z/R = 3$ the rate of the load variation drops rapidly. The effect of the obstacle at $Z/R = 4$ (the rotor is placed at $Z/R = 3.2$ above the obstacle) is shown on rotor loading as an increase of almost 1%. Measurements suggest that, in comparison with the IGE case, the maximum increase obtained at $Z/R = 2$ ($Z/R \equiv 1$) is almost 7% higher than the maximum increase of the IGE case. This difference is the result of the different flow field that the obstacle creates. While in IGE case and at $Z/R = 1$ the jet of the helicopter is diverted by the ground leading to an expanded torus shape vortex (vortex ring), the obstacle creates a far more complex flow pattern that has as a result a further increase in CT. In Figure 3.38(b), the effect of the obstacle on the Figure of Merit is depicted. The Figure of Merit designates/determines the ability of the rotor to convert its rotational energy into thrust. Thus, measurements indicate that the effect of the obstacle on the torque of the rotor is the same as on thrust. On the other hand, the helicopter seems not to lose its ability to convert torque into thrust.

The comparison of the experimental data with predictions obtained by $GenUVP$, show that the inviscid methodology exhibits an offset with respect to measurements that ranges between 1-4%. Even though inviscid predictions capture the trend of the experiment and can give a first impression of how a helicopter will behave while hovering above and obstacle, however it cannot fully reproduce the effect in quantitative terms. For example, at $Z/R = 2$ the maximum increase predicted by $GenUVP$ is 16% (4% higher compared to the pure IGE case) while experiments suggest a 20% increase in thrust. This trend of under-predicting thrust continues until the rotor is hovering at $Z/R = 2.75$. Beyond $Z/R = 3$, $GenUVP$ predicts an almost constant level of thrust which is about 5% than that of the OGE case and therefore predictions deviate from measurements at increasing rate. This is explained by the fact that the wake jet flow that impinges on the "inviscid" obstacle (composed by inviscid walls) is excessively accelerated, leading to sources distribution over the obstacle that create a substantial upwash effect. This upwash destabilizes the structure of the wake and vortices start to move upwards and closer to the rotor. As a result in the inviscid methodology the effect of the obstacle does not fade beyond $Z/R = 3$ as done in measurements.

In the above analyses, the weaknesses of the potential model are recorded. These weaknesses are related to its inability to resolve viscous effects on the walls of the obstacle (boundary layer development on the ceiling and flow separation from the edges of the obstacle). To verify the effect of the above described viscous mechanisms, three simulations using $HoPFlow$ have been performed. These simulations not only confirm that the formation of a boundary layer and the separation of the flow have a critical impact on rotor loads when a helicopter hovers above the obstacle, but also verify the predictions of the hybrid solver . As seen in Figure 3.38, the three simulations concern the two extreme points of the vertical sweep test matrix (of maximum and lowest effect of the ground/obstacle) as well

as the mid point $Z/R = 3$. It is seen that HoPFlow model accurately predicts the increase in thrust in all the above three cases.

3.7 Helicopter Hovering next to an Obstacle - Sweep in z axis (T3 case)

In the present section, hovering at different vertical positions of the rotor centre next to the right wall of the obstacle is addressed (sweep in vertical direction – see Figure 3.4). Again, predictions of CT and FM are compared to measurements from the test campaigns of Polimi and Glasgow. Similar was the case discussed in Section 3.4.2. The difference between these cases is the greater rotor-to-side wall distance in the ONERA set-up, which allowed the rotor wake to travel a longer distance until it reaches the obstacle. In all cases the rotor is kept at $X/R = 2$ and $Y/R = 0$, which places the tip of the advancing blade (upstream side of the disk) $1R$ away from the edge of the obstacle. The sweep on Z/R starts at $Z/R = 1$ and ends at $Z/R = 4$. A distinct difference between the two tests is that $Z/R = 1$ in Glasgow's test corresponds to half the height of the obstacle, while in Polimi's test it is equal to the height of the obstacle. So, in Glasgow's test the rotor is blocked by the side wall on its left. $Z/R = 4$ is the height at which ground effect almost vanishes (see Figure 3.17).

Computations of the T3 cases have been performed using both $GenUVP$ and $HoPFlow$. $GenUVP$ simulations cover the whole range of points addressed in the experiments (see Table 3.2,3.6). $HoPFlow$ simulations are then focused on the cases of Glasgow experiment, where $GenUVP$ fails to provide consistent load and flow field predictions.

3.7.1 Main Rotor Loads Results

Comparisons between predictions and measurements are presented in Figure 3.39 and Figure 3.40 for the normalized CT and FM of Polimi's and Glasgow's experiments respectively. In the Polimi test (3.39), when the rotor is at $Z/R = 1$, the increase in CT is 3.5%. As the rotor moves upwards, CT decreases rapidly and obtains values less than 1. Beyond $Z/R = 1.5$ it starts to increase until $Z/R = 3.7$. At $Z/R = 4.25$ it exhibits a small decrease. It is worth highlighting that beyond $Z/R = 1.05$ the thrust coefficient and the Figure of Merit are both below the threshold of 1. This means that when the model helicopter hovers next to the wall of an obstacle, a loss of thrust and power efficiency compared to the OGE case is noted which can potentially compromise flight safety. The obstacle creates in this case a counter and stronger effect to that of the ground. It is notable that even at higher altitudes (Z/R=3-4), CT and FM do not fully recover their OGE values.

In the Glasgow test 3.40, when the rotor is at $Z/R = 1$, CT increases by 12% with respect to the OGE case. The increase in CT is dictated by the low distance
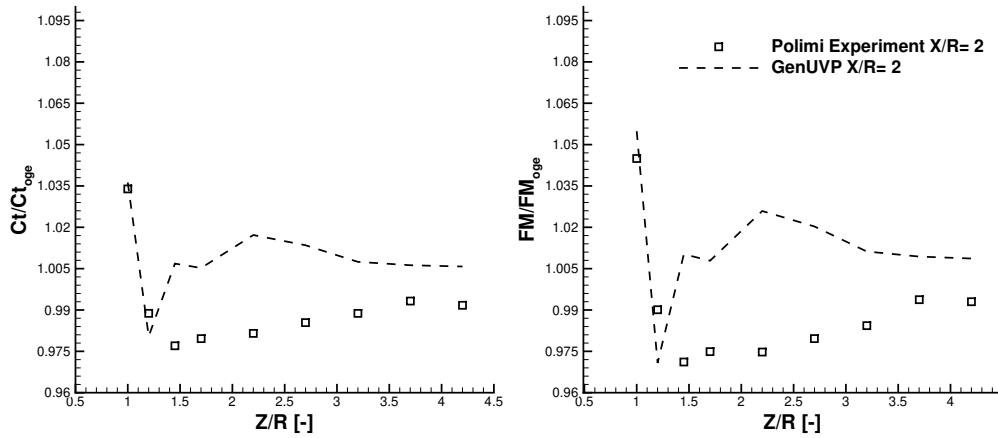
(a) Trust coefficient variations vs. z position

(b) Figure of Merit variations vs. z position

Figure 3.39: CT and FM variations against the distance from the ground ($Z/R = 0$). Comparisons of measured data against $GenUVP$ predictions for the T3 Polimi case. The rotor is placed at $X/R = 2$.
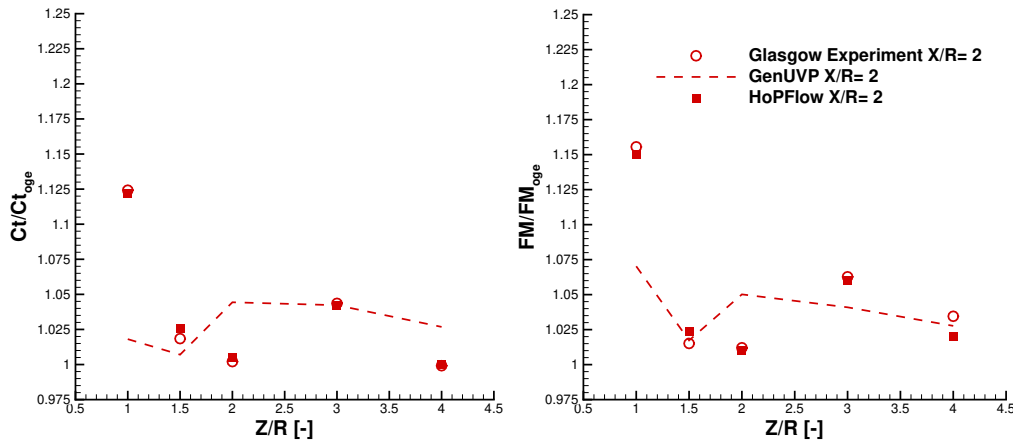
(a) Trust coefficient variations vs. z position

(b) Figure of Merit variations vs. z position

Figure 3.40: CT and FM variations against the distance from the ground ($Z/R = 0$). Comparisons of measured data against $GenUVP$ and $HoPFlow$ predictions for the T3 Glasgow case. The rotor is placed at $X/R = 2$.

from the ground. The increase in CT is 9% lower than that of the ground/obstacle effect when the rotor is placed at $1R$ above the obstacle and 2% lower than that of the IGE case. In this particular case, the rotor wake that impinges on the ground is afterwards pushed towards the side wall and is lifted up forming a flow

re-circulation zone in the region between the rotor and the side wall of the obstacle. The clockwise vortex formed between the obstacle and the rotor induces a downwash that decreases the effective angles of attack of the blades and thereby leads to lower increase in CT as compared to that of the pure IGE case. Similar trends are obtained at $Z/R = 1.5, 2$, where due to the same effect (of the wake licking the side wall and forming a clockwise vortex), the increase in CT is lower than that of the IGE case. At $Z/R = 4$, CT is equal to CT_{OGE} as in the IGE case. Only at $Z/R = 3$, CT abruptly increases and it appears to be 4% higher than CT_{OGE}. It is noted that in pure IGE the increase in CT at $Z/R = 3$ is less than 1%, thus the present CT difference is due to the obstacle that blocks the expansion of the wake.

Comparing predictions against measured data the following observations are made:

- The maximum difference between $GenUVP$ predictions and measurements in Glasgow's test, are noted at the lowest distance from the ground ($Z/R = 1$). This is in line with the results presented in the previous sections, and as explained in section 3.3.3, it is due to the inviscid character of the model which neglects boundary layer effects. The difference between predictions and measurements is somewhat higher in this case (about 7% in CT and 9% in FM), and this is because additional uncertainty is introduced in the potential flow predictions due to the effect of the obstacle side wall boundary layer. Predictions consistently reproduce the shape of the measured CT and FM variations with respect to the Glasgow test. Moreover, they capture the local increase in CT and FM at $Z/R = 3$. In fact $GenUVP$ predictions suggest that both CT and FM increase beyond $Z/R = 2$, following a local dip at $Z/R = 1.5$, while measurements indicate that at $Z/R = 2$ both CT and FM still remain low. It is noted that in Glasgow's test, $Z/R = 2$ is the height at which the rotor centre reaches the top side of the obstacle. Moreover, predictions overestimate CT at $Z/R = 4$. A 2 % increase in CT with respect to the CT_{OGE} is predicted, while as mentioned earlier, measurements suggest that at $Z/R = 4$ CT is equal to CT_{OGE}. The agreement in FM at this height is almost perfect.

- $HoPFlow$'s predictions are in very good agreement with measurements. HoPFlow correctly predicts the loading of the rotor even at heights where the obstacle fully shades the rotor ($Z/R = 1 - 2$). At $Z/R = 1$, a case where $GenUVP$ with the inviscid wall conditions underestimates thrust by almost 10%, the viscous wall conditions of HoPFlow drastically improves the predicted loading. Furthermore, changes in the slope of CT and FM variations with height between $Z/R = 2 - 4$ are well captured only with small deviations compared to measurements.

- In Polimi's test, $GenUVP$ simulations predict a slight increase in CT which is less than 2% and a similar slight increase in FM of the same order of

magnitude. Also in this case simulations predict a lower increase in CT and FM as compared to the IGE case. On the other hand, measurements indicate that both CT and FM drop below the levels of the OGE case. Only at $Z/R = 1$ predictions and measurements agree both in qualitative and quantitative terms.

- Overall the effect of the larger obstacle (of the Glasgow test) is more pronounced in this case and causes larger variations in thrust and torque. The above is equally seen in the predictions and in the measured data.

3.7.2 Flow field comparisons against Glasgow PIV measurements

The PIV measurements at Glasgow have been performed on the small scale "Wee" rotor. Besides being smaller in size than the rotor on which load measurements were recorded, the "Wee" rotor is also two-bladed instead of being four-bladed. Therefore, although the dimensionless parameters of the test are the same with those of the larger rotor, the measured flow field of the "Wee" rotor test can be only qualitatively correlated to the CT and FM measurements of the larger four bladed rotor presented in section (3.7).

When the hovering rotor is placed at the lowest vertical position ($Z/R = 1$), measurements in Figure 3.41(a) indicate that the slipstream on the rotor upstream side is curved by the presence of the ground. When the slipstream impinges on the ground, it moves parallel to it and then along the side wall. Finally, the slipstream exits at the edge of the side wall, where a clockwise vortex is formed at $Z/R = 2.2$. This vortex induces a downwash over the rotor disk which is responsible of reducing thrust as compared to pure IGE conditions discussed in Section 3.3.3. The predicted velocities by $GenUVP$ (see Figure 3.41(b)) are slightly higher than the measured ones (maximum levels are at 6.5 and 7m/s respectively). The clockwise vortex is also predicted, although misplaced with its centre at $Z/R = 0.6$ instead of $Z/R = 2.2$. The difference in the position of the vortex is due to the inviscid nature of the simulation which neglects the boundary layers developed over the ground and the walls of the obstacle.

On the contrary, predictions by $HoPFlow$ agree much better with the measured PIV results of Glasgow experiment. As depicted in Figure 3.41(c), the predicted velocity magnitude over the plane shows good agreement with the measured values and pattern. Moreover, the viscous wall conditions reproduce the physical phenomena correctly placing the vortex and the resulting re-circulation zone closer to the upper edge of the obstacle, as the experiment indicates. Even if a two-bladed rotor has been used instead of a four-bladed one, the correlation of the predicted flow field and predicted load results is reasonable. By taking into consideration the simulation of the T3 case of Polimi with $HoPFlow$ and $GenUVP$, it can be claimed that flights in close proximity to the ground have a

(a) Glasgow Measurements
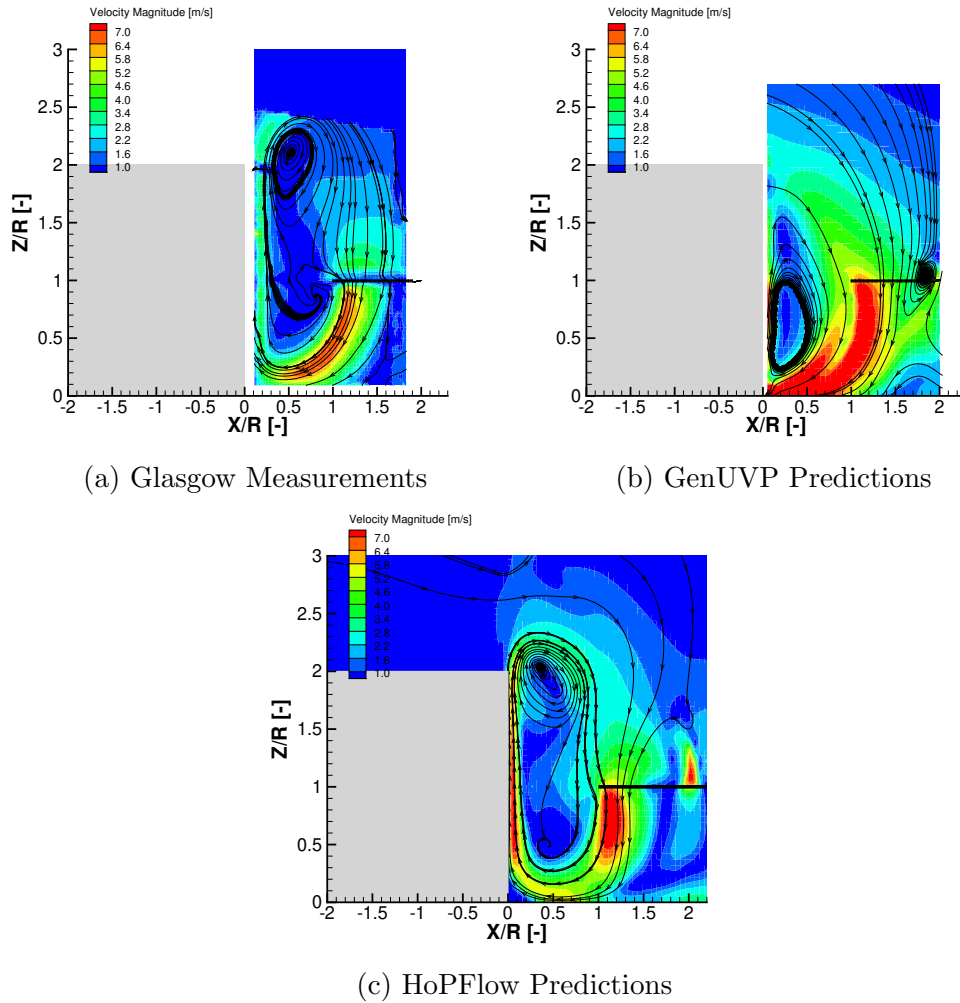

(b) GenUVP Predictions

(c) HoPFlow Predictions

Figure 3.41: Flow field comparison for the Glasgow experiment while the rotor is stationed at $X/R = 2$ and $Z/R = 1$.

similar effect on the rotor loading regardless of the main rotor design details.

When the rotor center is shifted upwards at $Z/R = 1.5$, the measured flow field is similar to that of the previous case (Figure 3.42a). The clock-wise vortex that induces a downwash to the rotor is again formed, but it is now situated under the disk close to the tip at $Z/R = 1.4$. The induced downwash results in a decrease in thrust. In the $GenUVP$ simulations, the vertical position of the centre of the vortex is lower, at $Z/R = 1.2$ as shown in Figure 3.42(b). Furthermore, the centre of the vortex is closer to the wall of the obstacle as compared to measurements. The boundary layer developing over the side wall is again responsible for pushing the vortex closer to the rotor in the measured data sets. As in the previous case wake velocities are overestimated, however wake expansion is again well captured. A

106

(a) Glasgow Measurements
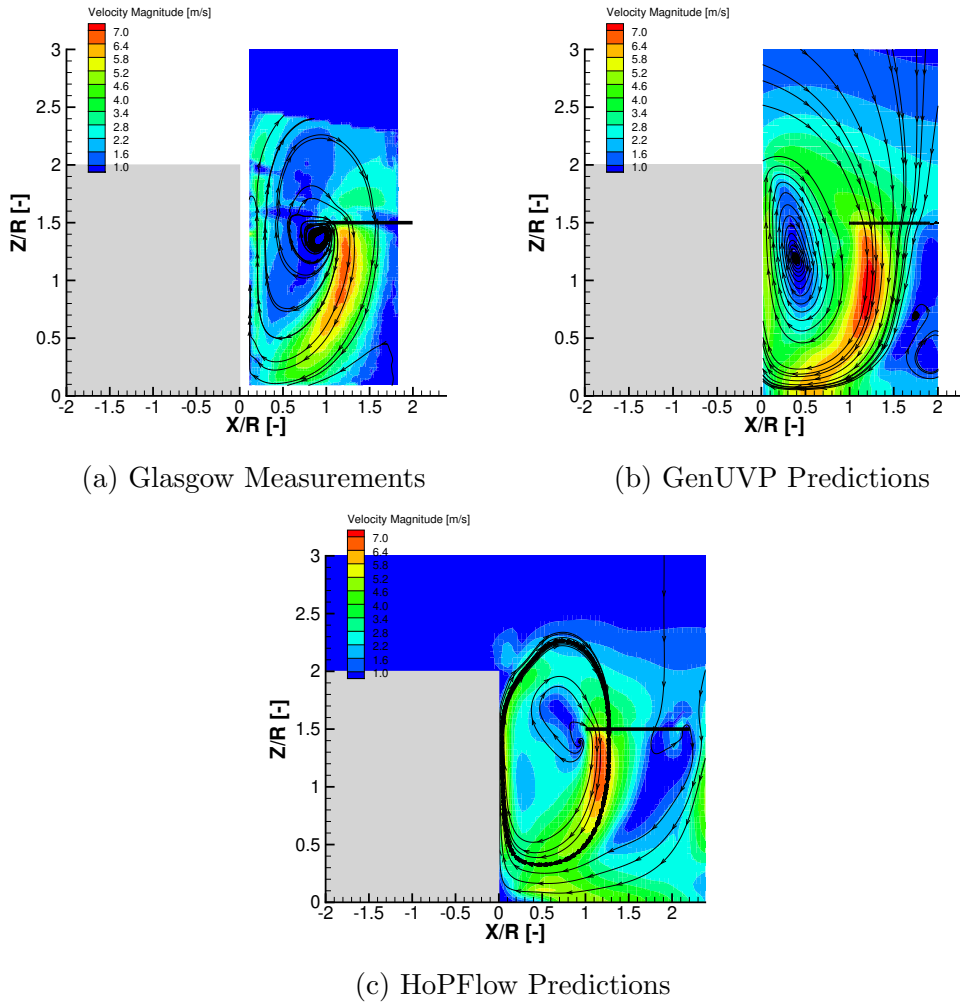
(b) GenUVP Predictions

(c) HoPFlow Predictions

Figure 3.42: Flow field comparison for the Glasgow experiment while the rotor is stationed at $X/R = 2$ and $Z/R = 1.5$.

more realistic representation of the flow field is observed in *HoPFlow*'s simulation (Figure 3.42c). The ability of the solver to account for the boundary layer that develops on the side wall of the obstacle allows the re-circulation flow vortex to move closer to the rotor tip as in the measurements. Moreover, the predicted magnitude of wake velocities is comparable to the measured values.

When the rotor is placed at $Z/R = 2$ (see Figure 3.43a), measurements suggest that the vortex remains close to the tip, now at $Z/R = 1.8$ .In *GenUVP*'s simulation, where the ground and the walls of the obstacle are inviscid (Figure 3.43b), the vortex appears between the tip and the side wall and at a lower height $Z/R = 1.2$. Again higher wake velocities are predicted, however the wake shape is well captured. It is noted that although the relative vortex-rotor position of the

cases $Z/R = 1.5$ and 2 is similar in the measurements, in the simulations the vortex centre appears closer to the rotor disk. This explains the sudden increase in CT observed in the $GenUVP$ predictions when moving the rotor centre upwards from $Z/R = 1.5$ to $Z/R = 2$. Apparently, the induced downwash that is responsible of reducing thrust, is weaker in the $Z/R = 2$ case as the vortex is further away from the rotor disk. Predictions of $HoPFlow$ (see Figure 3.43b) on the other hand are again in better agreement with measurements. Both the shape of the vortex and its position, match the experimental data. Also wake velocity magnitudes better match to measurements. Thus, $HoPFlow$ predictions of CT and FM for this test point are also in good agreement with the experimental values.

(a) Glasgow Measurements

(b) GenUVP Predictions
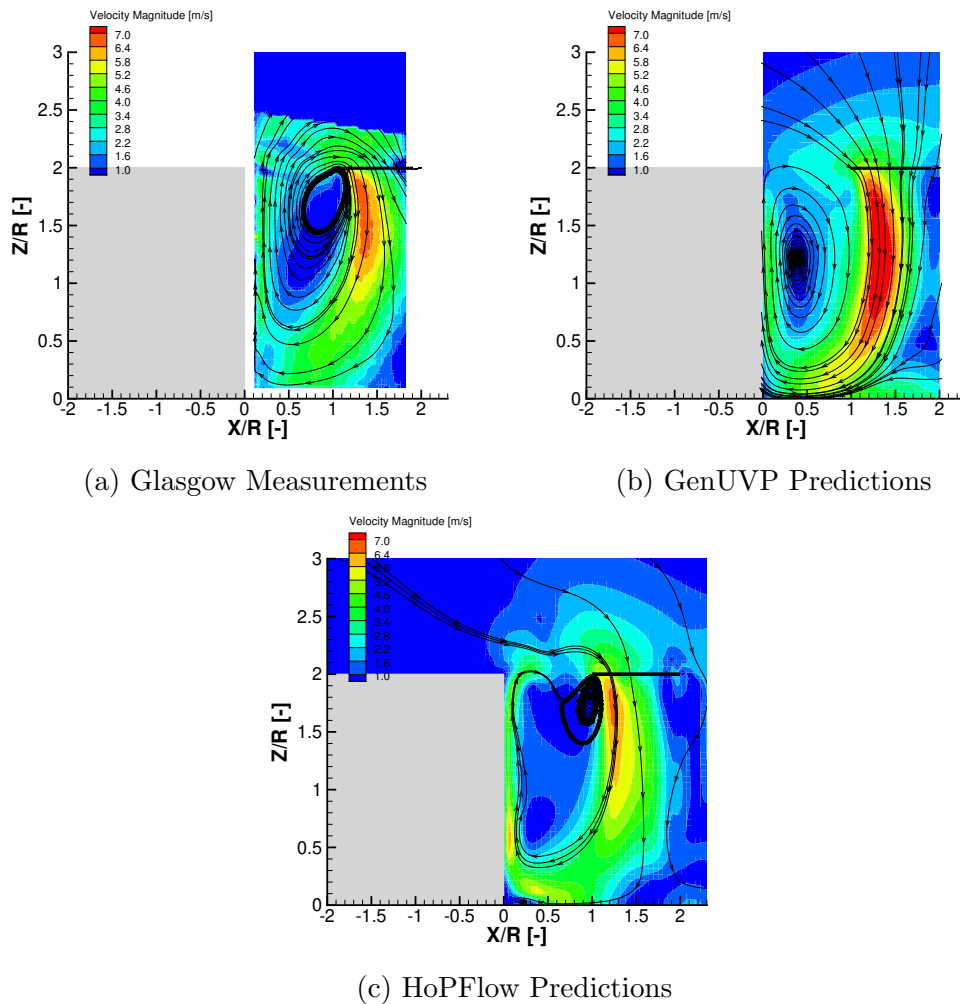

(c) HoPFlow Predictions

Figure 3.43: Flow field comparison for the Glasgow experiment while the rotor is stationed at $X/R = 2$ and $Z/R = 2$.

3.7.3 Rotor inflow velocity comparisons against Glasgow PIV measurements

In addition to the PIV data, rotor inflow velocity measurements using Laser Doppler Anemometry (LDA) are available from Glasgow's campaign on the large reference rotor (D=1m). Two configurations were considered. One without the obstacle and the rotor in IGE conditions at $Z/R = 1.5$, and a second one with the obstacle present. In the latter case, the rotor is at the same vertical position, $Z/R = 1$, but its centre is located at $X/R = 2$, thereby presenting an offset with respect to the obstacle. Rotor inflow velocities were measured at $0.04\,D$ above the rotor disk along two diameters, one in the X and one in the Y - direction. In Figures 3.44, 3.45 measured and predicted time averaged inflow velocities are compared along the two rotor diameters. In the pure IGE case, the measured
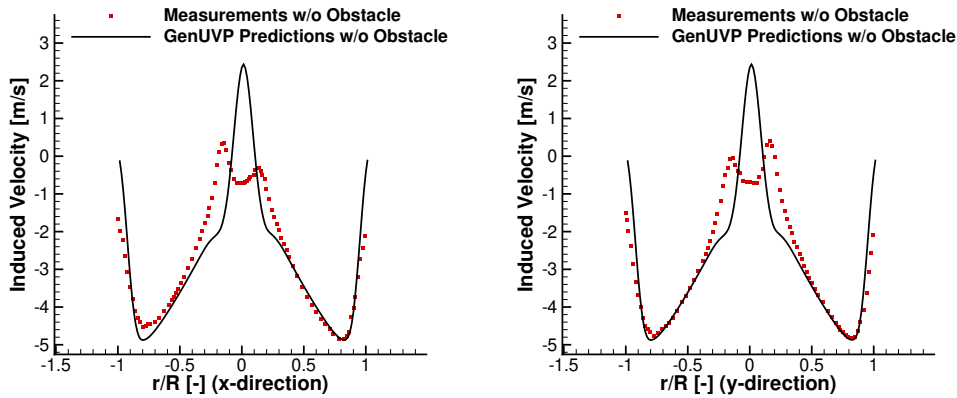
(a) Comparison against measured data along a diameter in X - direction   (b) Comparison against measured data along a diameter in Y - direction

Figure 3.44: Induced velocities on the rotor without the presence of the obstacle at distance $Z/R = 1.5$ from the ground

variation of the downwash along the X - direction is asymmetric (Figure 3.44a) which can be justified by the presence of the model support mast extending at positive X (and r/R) values. A smaller asymmetry is noted in the Y - direction, which is mainly concentrated at the two tips and is probably related to the asymmetric distribution of the measuring points over the two sides. Predictions provide symmetric inflow profiles in both directions, as the disturbance introduced to the flow by the model support is not taken into account. In the hub region, an upwash is noted which is due to the absence of the entire hub from the simulations.

Both predictions and measurements agree that maximum downwash is obtained at $r/R = 0.8$. This is where local thrust force along the blade is maximized. The overall agreement is good. The model slightly under-predicts the magnitude of

inflow velocity towards the tips. This can be explained by the strong tip vortices. The lack of physical diffusion in the inviscid simulations leads to over-predicted inflow velocities.
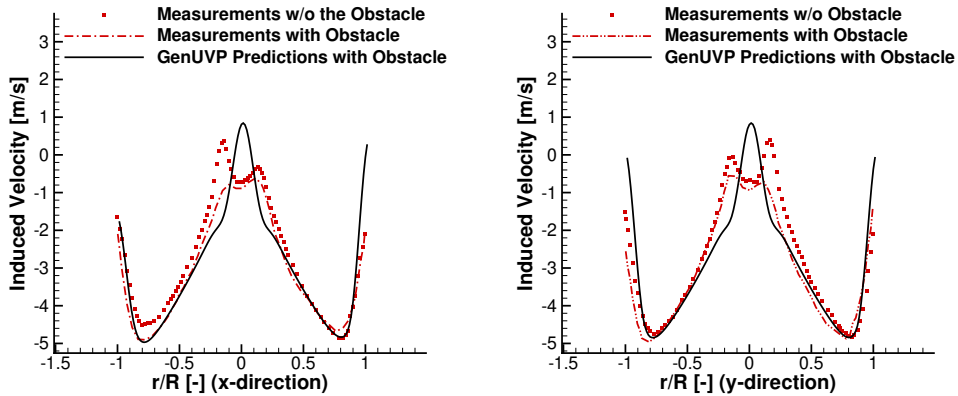

(a) Comparison against measured data along a diameter in X - direction.

(b) Comparison against measured data along a diameter in Y - direction

Figure 3.45: Induced velocities on the rotor in the presence of the obstacle at distance $Z/R = 1.5$ from the ground.

With the obstacle in place, good agreement with measurements is obtained while maximum differences are noted in the tip regions. The predicted profile along the X-direction is asymmetric, as expected, due to the effect of the downwash induced by the tip vortices that bounced on the solid boundary. As shown in Figure 3.37, the wake that hits on the ground rises up staying attached to the side wall of the obstacle. This results in additional downwash which increases the inflow velocities (in magnitude) on the rotor left side. The induced effect of the re-circulation area of the wake is clearly visible in Figure 3.45 (a). The predicted profile of the rotor in proximity to the obstacle is compared against the profile of the IGE case. The profile in the Y-direction is symmetric, as expected. In the presence of the obstacle higher induced velocities (in magnitude) are once again detected due to the effect of the additional downwash induced by the recirculating wake.

110

Chapter 4

Conclusions and Recommendations

The aim of the present work was (a) the investigation of the interactional phenomena that occur during the hover flight of a helicopter in confined areas and in proximity to the ground and obstacles, and (b) the validation of existing computational methods for predicting such interactions.

4.1 Conclusions

This thesis addresses the effect of the ground and obstacles on the main rotor of a hovering helicopter. When a rotor is hovering in proximity to the ground and in confined areas, the physical mechanisms that develop, lead to a two way interaction that influences the helicopter loading and stability.

In order to study the above described engineering problem a three step process has been followed. First, the experimental databases from three different wind tunnel experiments were collected and analyzed. Then, a medium fidelity free wake vortex particle solver (GenUVP) was used in order to simulate the majority of the cases and compare its results against measurements. Finally, a high fidelity hybrid CFD solver was used in order to handle and assess viscous effects. The fact that databases of more than one measurement campaigns and rotor/obstacle interaction configurations were made available, gave the opportunity to identify and categorize the physical mechanisms that, each time, and depending on the configuration examined, dominate the problem. Before proceeding with the comparison of predictions with measurements, similarities in flow and load variation patterns are sought in test campaigns of similar configurations, which are however conducted in different wind tunnels. The above configurations are then reproduced via simulations with the potential solver GenUVP. The low cost of the code led to multiple simulations covering the whole matrix of the test campaigns. Having

both measurements from wind tunnels and predictions proved to be essential in identifying the conditions where the viscous interactional phenomena are dominating the flow. Whether predictions agreed well with measurements or not, was an indication that viscous phenomena are important (given that GenUVP is an inviscid solver). Moreover, the above analyses revealed that deviations between potential predictions and measurements increased as the rotor comes closer to a solid boundary (either the ground or a side wall). The last step was to simulate the above cases in which GenUVP predictions were not satisfactory with HoPFlow and try to verify the experimental evidence. In this way, the conclusions extracted are a result of complementary exploitation of experimental and numerical tests.

Next, with respect to every case separately,

- **OGE:** The OGE case defines the reference CT and FM values of the undisturbed hover flight. These values are then used for the normalization of the corresponding thrust and figure of merit values of the interactional cases. In comparison to measurements, both the potential solver and HoPFlow were in very good agreement with all experimental data. In addition, through this process the development of the wake for the undisturbed case was investigated and captured.

- **IGE:** In the pure IGE case performed by Polimi, experiments indicate an exponential increase in CT as the rotor centre approaches the ground. Maximum increase of (12%) is obtained at $Z/R = 1$. The effect of the ground vanishes for $Z/R > 4$. The potential solver is in good agreement with measured data (good agreement in shape and values). However, deviations are noted for $Z/R < 1.7$ ($\approx 2.5\%$ smaller increase). This difference is attributed to the development of a boundary layer on the ground. The above argument is complemented by the predictions obtained with HoPFlow. Predictions by HoPFlow indicate that the boundary layer creates a displacement effect that pushes the vortex ring away from the ground at higher vertical distances. This creates an upwash over the rotor disk that increases the thrust on the rotor. The same exponential increase is also observed in the ONERA IGE data. Despite the presence of surrounding walls, the CT variation behaved similar to the pure IGE case. Two differences were observed: (a) maximum increase is now 7%, and (b) the effect of the ground and the surrounding walls vanished for heights higher than $Z/R = 1.7$. This happens because the vortex ring emitted by the tip of the rotor is trapped within the courtyard and it is pushed upwards when getting close to the walls. Thus, a re-circulation vortex is formed within the courtyard area and above the level of the rotor which induces downwash velocities that lead to a decrease of the overall thrust. The potential solver predicted well the experimental data and the comparison to measurements confirmed the mechanisms that decrease the thrust of the rotor.

112

- **T1:** In the horizontal sweep case, CT/CT_{OGE} and FM/FM_{OGE} curves vs. horizontal position of the rotor exhibit an abrupt drop as the rotor moves away from the obstacle. This is seen in both tests and it is well reproduced by the model in all cases. As indicated in Glasgow's tests, in which a larger horizontal distance is scanned, the effect of the obstacle on CT and FM remains high as the rotor remains close to the obstacle. A 5%-6% increase in CT and FM is obtained when the rotor is within the range $X/R = 0.5 - 2$ (for $Z/R = 3$) which is higher than the corresponding increase in the pure IGE case at $Z/R = 3$ (about 1% increase in CT). Pure IGE conditions are obtained for $X/R > 3$. In Polimi's horizontal sweep campaign, the minimum value of CT/CT_{OGE} (almost 1.03) is obtained at $X/R = 0.5$. The same behavior is also seen in GenUVP's predictions with a slight under prediction ($CT/CT_{OGE} = 1.02$). On the other hand, HoPFlow predictions of CT are in line with measurements. Also, the predicted flow fields correlate well with the measured ones, showcasing the same phenomena. The rotor downwash flow induces flow separation from the obstacle roof edges, which cannot be predicted by an inherently inviscid model but only with HoPFlow. As the horizontal distance of the rotor from the obstacle increases, the predicted flow fields by GenUVP agreed much better with those predicted by HoPFlow and the measured ones. Flow field measurements indicate that the reduced CT and FM values, when the rotor hovers next to the side wall of the obstacle, are due to the clockwise vortex that is formed between the rotor and the obstacle side wall, which induces strong downwash velocities over the rotor disk. This clockwise vortex is due to the rotor downwash flow, which first hits the ground and afterwards licks the ground and the side wall of the obstacle moving upwards

- **T2:** The pattern of the exponential increase in CT when a helicopter hovers above and close to a solid boundary is also observed in this experimental case by Polimi. The loading of the rotor obtains its maximum value at $Z/R = 1$ above the obstacle (21%). The effect of the obstacle is still present at $Z/R = 3$ above its top surface. At this station the distance from the ground is $Z/R = 4$ and the corresponding increase in CT is minimized in the pure IGE case. The 7% difference between the $Z/R = 1$ cases, the one above the ground and the other above the obstacle, was due to the different rotor wake development. In the pure IGE, the rotor slipstream generates a ground boundary layer that bounces back the rotor wake ring vortex resulting in an upwash. When there is an obstacle of limited size, the rotor slipstream instead of bouncing back the wake, the flow separates along the top edges of the obstacle and rolls up over its sides. This flow roll-up generated counter rotating vortices close to the obstacle and thus upwash induced velocities. GenUVP predictions fail to reproduced the effect due to the inviscid wall conditions; however the general trend and shape of the increase is captured. On the contrary, HoPFlow reproduces well the experiment as regards the

increase in CT as well as the predicted flow field.

- **T3:** The vertical sweep case, in which the rotor hovers next to the obstacle side wall turned out to be the most challenging. Even in this case maximum deviations between GenUVP results and measurements in the prediction of both CT and FM do not exceed 7%. Maximum difference is obtained again when the rotor approaches the ground (at $Z/R = 1$ - due to boundary layer displacement effect). At higher Z/R values differences between predictions and measurements do not exceed 5%. HoPFlow results are in very good agreement with measurements. This is attributed to the account of viscous effects that the hybrid method includes. Overall the models agree with both measured data sets in that the increase in CT and FM is lower in this case as compared to the pure IGE case. In Glasgow test, when the rotor exceeds the level of the obstacle top, the above effect weakens and the rotor loads are dominated by the combined obstacle/ground effect (mirroring effect). Predictions agree well with the above observation. Moreover, the predicted flow fields obtained by GenUVP in the vertical sweep case agree well with Glasgow flow measurements. There are only deviations in the position of the vortex, which as expected drive differences in CT of 4% and in FM of 5% results between predictions and measurements .

The above discussion summarizes the effect of the ground and an obstacle to a helicopter and the mechanisms that drive this influence. However, in order to understand the actual effect on the pilot of a helicopter these deviations must be quantified. Preliminary simulations indicate that by increasing the collective pitch of a rotor by 1 degree, thrust increases by $\approx 10\%$ (assuming that the attitudes of the helicopter remain the same). This suggests that even for the maximum increase in thrust and power that is noted at $Z/R = 1$ above the ground (T2 case) a pilot could easily adjust the collective pitch in order for the helicopter to retain its balance. Considering that in real-life flights, a helicopter cannot perform hovering or approach flight to a constant point in space or following a constant path, a 20% increase in thrust will be easily handled by the pilot. For a typical helicopter, fluctuations on the loading of the hub have a value of $\approx 5\%$. This means that in the majority of the cases, the deviations in CT/CT_{OGE} add only a small uncertainty. However, even a small increase in thrust could be proven a challenging task for a pilot when he cannot predict when the flow field would change. For example, in most cases examined the maximum increase is observed when the conditions of the flight and the flow field where symmetric (IGE, T2). This translates to uniform distribution of the forcing on the rotor plane. According to this, the moments of the rotor are fluctuating around 0 causing no significant handling issues. Even though the increase in CT in T1 and T3 cases is lower, the formation of the wake was blocked only in one direction causing the flow field to be asymmetric. Considering the above, the distribution of normal force on the rotor is asymmetrical too, creating an uneven loading and thus significant moments on

the hub. That could be catastrophic if a pilot is unaware of such phenomena. To conclude, the importance of this theoretical approach is the identification of the interactional phenomena in order to extend the existing bibliography on the topic.

The second achievement is the validation of two solvers of different fidelity in predicting these phenomena and evaluating the corresponding engineering implications.

- **GenUVP:** This solver is a medium fidelity potential solver. It treats the solid boundaries as inviscid surfaces (only non-penetration condition is applied on a surface grid) and in this connection it cannot predict viscous phenomena. The wake is modeled as blobs carrying vorticity and the velocity field is obtained by solving two Poisson's equations using the Particle Mesh technique. The evaluation of the solver is proven to be successful if some compromises are made. GenUVP delivers consistent predictions in all cases. Even if it cannot reproduce the exact experimental values in some cases, it predicts well the shape and trends of the results. In addition, this is happening in a timely manner. Its low computational cost permits multiple simulations in a variety of cases and across the whole test matrix allowing a thorough overview of the problem. The simulations can be performed even on a laptop and require small number of processors and ram capacity. Overall GenUVP is a suitable tool for preliminary predictions even in viscous dominated phenomena. In order to achieve the above, several modifications were made to the code: (a) GenUVP solver was coupled with the particle mesh solver in order to reduce the computational cost (from N^2 to $N \log N$) regarding the treatment of the particle to particle calculations (Biot-Savart), (b) GenUVP was parallelized in the framework of MPI for further reduction of the computing cost, (c) symmetry conditions through proper boundary conditions were introduced to the particle mesh solver in order to simulate the ground effect.

- **HoPFlow:** The hybrid solver is a combination of two sub-solvers; MaPFlow solves the Eulerian description of the Navier-Stokes equations and the Lagrangian solver which takes advantage of the particles approximation to describe the flow field and obtains the velocity vector via solving the Poisson equation using again the particle mesh technique. HoPFlow advantages over standard URANS codes are the significantly smaller spatial grids that are employed only near the solid boundaries and the fact that the method can handle complex multi body configurations with their members moving independently the one from the others. This is achieved through the introduction of the overlaid Lagrangian domain that communicates the information to the different CFD grids through a strongly coupled iterative scheme. In this manner, viscous and compressible phenomena are introduced into the field through MaPFlow, while the far wake is preserved as it is expressed via material vortex particles. The validation of the solver was successful in

115

every respect. In all cases that were simulated, the solver proved robust and consistent and in very good agreement with all experiments. Both the predictions of the rotor trust and torque but also the predicted flow fields agreed well with measurements. Having a numerical tool in hand, which reproduces well the experimental data in all tested cases also helps analyzing and understanding the phenomena in greater depth supplementing thus the experimental evidence. Within this framework, the rotor, the fuselage, the ground and the obstacle can be simultaneously accommodated within the simulation. The downside is that the solver is computationally demanding especially in comparison to GenUVP. For that reason it was used in selected cases and not in the whole range scanned by the experiments. It is worth noticing that the solver is fully parallel in the framework of MPI but only MaPFlow is fully scalable. The computational contribution of the present work in HoPFlow is twofold: (a) the symmetric particle mesh solver was coupled with the hybrid solver in order for the Lagrangian part to handle the effect of the ground, (b) many modifications were made in HoPFlow in order to be able to solve these engineering problems.

4.2   Recommendations

The recommendations discussed next concern at first short term possible improvements of the solver and then some longer term topics for future research.

Short term improvements:

- *Aeroelastic simulations:* In the context of the present thesis, only the aerodynamic effect of the rotor-ground/obstacle interaction is investigated. However, examining the aeroelastic behavior of a rotor under the influence of an unsteady flow field, is a crucial step in the design of a helicopter.

- *Full scale analysis:* In the present work, the results concern only model helicopters in low Re flows. Extension to full scale simulations that involve turbulent flow conditions is proposed. This may also improve the quality of the flow predictions with the fuselage.

- *Analysis of the descent flight scenario:* While hover flight at a stationary position is of critical importance to flight analysis, it is also essential to investigate the effect of the ground and obstacles on descending helicopters.

Long term research topics:

- *Non uniform Poisson Solver* In order to reduce even more the computational cost and at the same time be able to handle dense Particle Mesh grids wherever they are needed (close to solid boundaries), the Poisson solver should be reassessed. The algorithm allows only uniform structured grids.

This constrains the length of the computational domain and prohibits the increase of the density around bodies. Therefore, one possible option could be introducing two or more grid scaling.

- *Piloted simulations* In real-life flights the variations in the hub-loads of a helicopter may cause the helicopter to lose its stability and deviate from its path/position. So the focus should be in analyzing the response of a helicopter under such interactional flow conditions in piloted mode.

- *Wind in flight simulations* While the present thesis addressed the phenomena on a wind off scenario, in nature the cases where the is no wind present are extremely rare. Wind will cause the formation of a boundary layer upstream of the obstacle and the flow will separate on its way around it. This will eventually change the rotor/obstacle interaction.

4.3   Publications

- Theologos Andronikos, George Papadakis, Vasilis A. Riziotis, Spyros G. Voutsinas, "REVISING OF THE NEAR GROUND HELICOPTER HOVER: THE IMPORTANCE OF THE GROUND BOUNDARY LAYER DEVELOPMENT", MDPI, Appl. Sci. 2021, 11(21), 9935 https://doi.org/10.3390/app11219935

- Theologos Andronikos, George Papadakis, Vasilis A. Riziotis, John M. Prospathopoulos, Spyros G. Voutsinas, "Validation of a cost effective method for the rotor-obstacle interaction", Aerospace science and technology, Volume 113, June 2021, 106698

- Theologos Andronikos, Dimitris I. Manolas, Vasilis A. Riziotis, Spyros G. Voutsinas, "ROTORCRAFT FLIGHT IN INTERACTION WITH OBSTACLES", European Rotorcraft Forum, Conference paper, Milan, 2017

- Theologos Andronikos, George Papadakis, Vasilis A. Riziotis, "AERODYNAMIC ANALYSIS OF HELICOPTER IN INTERACTION WITH WIND TURBINE'S WAKE", European Rotorcraft Forum, Conference paper, Delft, 2018

This page intentionally left blank.

Appendix A

Naca0012 CL-CD polars

Table A.1: Naca0012 polars-Re 100000)

Angle	CL	CD	Angle	CL	CD
-3.500	-0.4957	0.01471	4.500	0.5761	0.01585
-3.000	-0.4545	0.01440	5.000	0.6141	0.01674
-2.500	-0.4137	0.01429	5.500	0.6503	0.01798
-2.000	-0.3737	0.01444	6.000	0.6862	0.01958
-1.500	-0.3320	0.01489	6.500	0.7235	0.02143
-1.000	-0.2578	0.01574	7.000	0.7631	0.02348
-0.500	-0.1345	0.01658	7.500	0.8050	0.02598
0.000	0.0000	0.01693	8.000	0.8471	0.02869
0.500	0.1344	0.01658	8.500	0.8884	0.03189
1.000	0.2578	0.01574	9.000	0.9246	0.03526
1.500	0.3320	0.01489	9.500	0.9524	0.04019
2.000	0.3737	0.01444	10.000	0.9661	0.04582
2.500	0.4136	0.01429	10.500	0.9913	0.05061
3.000	0.4544	0.01440	11.000	0.9845	0.05893
3.500	0.4957	0.01471	11.500	0.8378	0.07522
4.000	0.5365	0.01520	11.750	0.7898	0.08703

Table A.2: Naca0012 polars-Re 200000)

Angle	CL	CD	Angle	CL	CD
-3.500	-0.4915	0.01134	4.500	0.5782	0.01234
-3.000	-0.4463	0.01104	5.000	0.6195	0.01306
-2.500	-0.3942	0.01086	5.500	0.6591	0.01400
-2.000	-0.3085	0.01066	6.000	0.6971	0.01516
-1.500	-0.2255	0.01048	6.500	0.7351	0.01641
-1.000	-0.1454	0.01034	7.000	0.7725	0.01776
-0.500	-0.0700	0.01025	7.500	0.8096	0.01936
0.000	0.0000	0.01020	8.000	0.8481	0.02112
0.500	0.0700	0.01025	8.500	0.8890	0.02251
1.000	0.1454	0.01034	9.000	0.9291	0.02472
1.500	0.2255	0.01048	9.500	0.9693	0.02734
2.000	0.3085	0.01066	10.000	1.0067	0.02966
2.500	0.3942	0.01085	10.500	1.0445	0.03262
3.000	0.4462	0.01104	11.000	1.0681	0.03636
3.500	0.4915	0.01134	11.500	1.0860	0.04035
4.000	0.5357	0.01176	11.750	1.0969	0.04194

Table A.3: Naca0012 polars-Re 500000)

Angle	CL	CD	Angle	CL	CD
-3.500	-0.4066	0.00840	4.500	0.5530	0.00966
-3.000	-0.3306	0.00786	5.000	0.6275	0.01036
-2.500	-0.2655	0.00737	5.500	0.6796	0.01102
-2.000	-0.2089	0.00696	6.000	0.7215	0.01170
-1.500	-0.1552	0.00662	6.500	0.7632	0.01236
-1.000	-0.1034	0.00638	7.000	0.8036	0.01316
-0.500	-0.0517	0.00622	7.500	0.8439	0.01399
0.000	0.0000	0.00618	8.000	0.8851	0.01479
0.500	0.0517	0.00622	8.500	0.9250	0.01577
1.000	0.1034	0.00638	9.000	0.9632	0.01699
1.500	0.1552	0.00662	9.500	1.0054	0.01794
2.000	0.2089	0.00696	10.000	1.0417	0.01951
2.500	0.2655	0.00737	10.500	1.0817	0.02069
3.000	0.3307	0.00786	11.000	1.1128	0.02267
3.500	0.4066	0.00840	11.500	1.1474	0.02416
4.000	0.4798	0.00900	11.750	1.1626	0.02500

Bibliography

[1] D. Key, "Analysis of army helicopter pilot error mishap data and the implications for handling qualities," *25th European Rotorcraft Forum, Rome*, 199.

[2] A. Visingardi, F. De Gregorio, T. Schwarz, M. Schmid, R. Bakker, S. Voutsinas, Q. Gallas, R. Boisard, G. Gibertini, D. Zagaglia, G. Barakos, R. Green, G. Chirico, and M. Giuni, "Forces on obstacles in rotor wake – A GARTEUR action group," *43rd European Rotorcraft Forum, Milan*, 2017.

[3] G. Gibertini, D. Grassi, C. Parolini, D. Zagaglia, and A. Zanotti, "Experimental investigation on the aerodynamic interaction between a helicopter and ground obstacles," *Proceedings of the Institution of Mechanical Engineers, Part G: Journal of Aerospace Engineering*, vol. 229, no. 8, pp. 1395–1406, 2015.

[4] D. Zagaglia, M. Giuni, and R. B. Green, "Rotor-obstacle aerodynamic interaction in hovering flight: An experimental survey," *Annual Forum Proceedings - AHS International*, vol. 1, pp. 356–364, 2016.

[5] Q. Gallas, R. Boisard, J.-C. Monnier, J. Pruvost, and A. Gilliot, "Experimental and numerical investigation of the aerodynamic interactions between a hovering helicopter and surrounding obstacles," 2017.

[6] J. Tan, Y. Sun, T. Zhou, N. Barakos G, and R. Green, "Simulation of the aerodynamic interaction between rotor and ground obstacle using vortex method," *CEAS Aeronautical Journal*, 2019.

[7] M. Schmid, "Simulation of helicopter aerodynamics in the vicinity of an obstacle using a free wake panel method," *43rd European Rotorcraft Forum. CEAS, 12–15 September 2017, Milan, Italy*, 2017.

[8] T. Andronikos, D. Manolas, V. Riziotis, and S. Voutsinas, "Rotorcraft flight in interaction with obstacles," *43rd European Rotorcraft Forum. CEAS, 12–15 September 2017, Milan, Italy*, 2017.

[9] T. Andronikos, G. Papadakis, V. Riziotis, J. Prospathopoulos, and S. Voutsinas, "Validation of a cost effective method for the rotor-obstacle interaction," *Aerospace Science and Technology*, vol. 113, 2021.

[10] J.-f. Tan and H.-w. Wang, "Simulating unsteady aerodynamics of helicopter rotor with panel/viscous vortex particle method," *Aerospace Science and Technology*, vol. 30, no. 1, pp. 255–268, 2013.

[11] P. Koumoutsakos, A. Leonard, and F. Pepin, "Boundary conditions for viscous vortex methods," *Journal of Computational Physics*, vol. 113, no. 1, pp. 52–61, 1994.

[12] P. Ploumhans, G. Daeninck, and G. Winckelmans, "Simulation of three-dimensional bluff-body flows using the vortex particle and boundary element methods," *Flow, turbulence and combustion*, vol. 73, no. 2, pp. 117–131, 2004.

[13] P. Poncet, "Topological aspects of three-dimensional wakes behind rotary oscillating cylinders," *Journal of Fluid Mechanics*, vol. 517, pp. 27–53, 2004.

[14] J. Yin and S. Ahmed, "Helicopter main-rotor/tail-rotor interaction," *Journal of the American helicopter society*, vol. 45, no. 4, pp. 293–302, 2000.

[15] J. Yin, B. G. van der Wall, and G. A. Wilke, "Rotor aerodynamic and noise under influence of elastic blade motion and different fuselage modeling," in *40th European Rotorcraft Forum (ERF)*, pp. 2–5, 2014.

[16] J. Yin, B. G. van der Wall, and G. A. Wilke, "Investigation of a simplified aerodynamic modelling technique for noise predictions using fw–h propagation," *CEAS Aeronautical Journal*, vol. 7, no. 4, pp. 551–566, 2016.

[17] S. G. Voutsinas and D. G. Triantos, "Aeroacoustics of full helicopter configurations using vortex particle flow approximation," in *Proceedings of CEAS Forum on Aeracoustics of Rotors and Propellers, Rome, Italy*, pp. 175–91, DTIC Document, 1999.

[18] G. Papadakis, *Developement of a hybrid compressible vortex particle method and application to external problems including helicopter flows*. PhD thesis, National Techanical University of Athens, School of Mechanical Engineering, 2014.

[19] G. Gibertini, G. Droandi, D. Zagalia, P. Antoniazza, and A. Catelan, "CFD Assessment of the Helicopter and Ground Obstacles Aerodynamic Interference," *42nd European Rotorcraft Forum. ERF, Lille, France, pp. 553–556*, 2016.

[20] M. Biava, "Rans computations of rotor/fuselage unsteady interactional aero-dynamics," *Doctor of Philosophy Thesis, Politecnico di Milano, Milano, Italia*, 2007.

[21] G. Chirico, D. Szubert, L. Vigevano, and G. N. Barakos, "Numerical mod-elling of the aerodynamic interference between helicopter and ground obsta-cles," *CEAS Aeronautical Journal*, vol. 8, no. 4, pp. 589–611, 2017.

[22] G. Barakos, R. Steijl, K. Badcock, and A. Brocklehurst, "Development of cfd capability for full helicopter engineering analysis," in *31st European Ro-torcraft Forum*, vol. 2005, pp. 91–1, Council of European Aerospace Soc. Florence, Italy, 2005.

[23] R. Steijl, G. Barakos, and K. Badcock, "A framework for cfd analysis of helicopter rotors in hover and forward flight," *International journal for nu-merical methods in fluids*, vol. 51, no. 8, pp. 819–847, 2006.

[24] H. J. Curtiss, M. Sun, W. Putman, and E. J. Hanker, "Rotor aerodynamics in ground effect at low advance ratios," *Journal of the American Helicopter Society*, 1984.

[25] J. Boer, C. Hermans, and K. Pengel, "Helicopter ground vortex: comparison of numerical predictions with wind tunnel measurement," 2001.

[26] B. Ganesh and N. Komerath, "Unsteady aerodynamics of rotorcraft in ground effect," *Fluid Dynamics Meeting*, 2004.

[27] N. D. Nathan and R. Green, "The flow around a model helicopter main rotor in ground effect," *Exp Fluids*, vol. 52, pp. 151–166, 2012.

[28] Y. Sugiura, M.and Tanabe, H. Sugawara, N. Matayoshi, and H. Ishii, "Nu-merical simulations and measurements of the helicopter wake in ground ef-fect," *Journal of Aircraft*, 2016.

[29] J. S. Light, "Tip vortex geometry of a hovering helicopter rotor in ground effect," *Journal of the American helicopter society*, vol. 38, no. 2, pp. 34–42, 1993.

[30] P. E. Tanner, A. D. Overmeyer, L. N. Jenkins, C.-S. Yao, and S. M. Bar-tram, "Experimental investigation of rotorcraft outwash in ground effect," in *Proceedings of the 71th Annual Forum of the American Helicopter Society*, pp. 1–26, 2015.

[31] I. Cheeseman and W. Bennett, "The effect of the ground on a helicopter rotor in forward flight," 1955.

[32] S. A. Conyers, M. J. Rutherford, and K. P. Valavanis, "An empirical evaluation of ground effect for small-scale rotorcraft," in *2018 IEEE International Conference on Robotics and Automation (ICRA)*, pp. 1244–1250, IEEE, 2018.

[33] M. Sugiura, Y. Tanabe, H. Sugawara, G. Barakos, N. Matayoshi, and H. Ishii, "Validation of cfd codes for the helicopter wake in ground effect," *European Rotorcraft Forum*, 2017.

[34] Y. Wang, M. White, G. Barakos, P. Tormey, and P. Pantazopoulou, "Simulation of a light aircraft encountering a helicopter wake," *Journal of Aircraft*, vol. 52, no. 2, pp. 510–523, 2015.

[35] Y. Tanabe, S. Saito, and H. Sugawara, "Construction and validation of an analysis tool chain for rotorcraft active noise reduction," 2012.

[36] S. Cavallo, G. Ducci, G. Barakos, and G. Gibertini, "Cfd analysis of helicopter wakes in ground effect," *European Rotorcraft Forum*, 2018.

[37] C. Pasquali, J. Serafini, G. Bernardini, J. Milluzzo, and M. Gennaretti, "Numerical-experimental correlation of hovering rotor aerodynamics in ground effect," *Aerospace Science and Technology*, vol. 106, p. 106079, 2020.

[38] M. Gennaretti and G. Bernardini, "Novel boundary integral formulation for blade-vortex interaction aerodynamics of helicopter rotors," *AIAA journal*, vol. 45, no. 6, pp. 1169–1176, 2007.

[39] G. Bernardini, J. Serafini, M. M. Colella, and M. Gennaretti, "Analysis of a structural-aerodynamic fully-coupled formulation for aeroelastic response of rotorcraft," *Aerospace Science and Technology*, vol. 29, no. 1, pp. 175–184, 2013.

[40] W. R. M. Van Hoydonck, "Computation of rotorcraft wake geometry using nurbs," 2013.

[41] A. Filippone, R. Bakker, P. Basset, B. Rodriguez, R. Green, F. Bensing, and A. Visingardi, "Rotor wake modelling in ground effect conditions," 2011.

[42] B. Kutz, U. Kowarsch, M. Kessler, and E. Kraemer, "Numerical investigation of helicopter rotors in ground effect," in *30th AIAA Applied Aerodynamics Conference*, p. 2913, 2012.

[43] B. M. Kutz, M. Keßler, and E. Krämer, "Experimental and numerical examination of a helicopter hovering in ground effect," *CEAS Aeronautical Journal*, vol. 4, no. 4, pp. 397–408, 2013.

[44] J. Yin and J. Delfs, "Main/tail rotor interaction under ground effect using dlr 3d free wake code," 2003.

[45] R. E. Brown and G. R. Whitehouse, "Modelling rotor wakes in ground effect," *Journal of the American Helicopter Society*, vol. 49, no. 3, pp. 238–249, 2004.

[46] T. Doligalski, C. Smith, and J. Walker, "Vortex interactions with walls," *Annual Review of Fluid Mechanics*, vol. 26, no. 1, pp. 573–616, 1994.

[47] G. K. Timm, "Obstacle-induced flow recirculation," *J. Am. Helicopter Soc*, vol. 4, 1966.

[48] T. Lusiak, A. Dziubinski, and K. Szumanski, "Interference Between Helicopter and Its Surroundings, Experimental and Numerical Analysis," *Task Quarterly*, vol. 13, no. 4, 2009.

[49] N. Iboshi, N. Itoga, J. V. Prasad, and L. N. Sankar, "Ground effect of a rotor hovering above a confined area," *Annual Forum Proceedings - AHS International*, vol. 2, no. 1, pp. 1249–1262, 2008.

[50] K. Quinliven, T.A. amd Long, "Rotor performance in the wake of a large structure," *Presented at the American Helicopter Society 65th Annual Forum. AHS, Grapevine, Texas, pp: 447–475*, 2009.

[51] S. A. Polsky and C. H. Wilkinson, "A computational study of outwash for a helicopter operating near a vertical face with comparison to experimental data," *AIAA Modeling and Simulation Technologies Conference*, no. August, 2009.

[52] Y. Nacakli and D. Landman, "Helicopter downwash/frigate airwake interaction flowfield PIV surveys in a low speed wind tunnel," *Annual Forum Proceedings - AHS International*, vol. 4, no. May 2014, pp. 2988–2998, 2011.

[53] N. Taymourtash, D. Zagaglia, A. Zanotti, V. Muscarello, G. Gibertini, and G. Quaranta, "Experimental study of a helicopter model in shipboard operations," *Aerospace Science and Technology*, vol. 115, p. 106774, 2021.

[54] L. Klotz, S. Goujon-Durand, J. Rokicki, and J. Wesfreid, "Experimental investigation of flow behind a cube for moderate reynolds numbers," *Journal of fluid mechanics*, vol. 750, pp. 73–98, 2014.

[55] M. Manolesos, Z. Gao, and D. Bouris, "Experimental investigation of the atmospheric boundary layer flow past a building model with openings," *Building and Environment*, vol. 141, pp. 166–181, 2018.

[56] E. Alpman, L. N. Long, D. O. Bridges, and J. F. Horn, "Fully-coupled simulations of the rotorcraft / ship dynamic interface," *Annual Forum Proceedings - AHS International*, vol. 2, 2007.

[57] H. C. Lim, T. Thomas, and I. P. Castro, "Flow around a cube in a turbulent boundary layer: Les and experiment," *Journal of Wind Engineering and Industrial Aerodynamics*, vol. 97, no. 2, pp. 96–109, 2009.

[58] H. C. Lim, I. P. Castro, and R. P. Hoxey, "Bluff bodies in deep turbulent boundary layers: Reynolds-number issues," *Journal of Fluid Mechanics*, vol. 571, pp. 97–118, 2007.

[59] H. Xin, J. Prasad, and D. Peters, "An analysis of partial ground effect on the aerodynamics of a helicopter rotor," in *38th Aerospace Sciences Meeting and Exhibit*, p. 262, 2000.

[60] C. He, *Development and application of a generalized dynamic wake theory for lifting rotors*. PhD thesis, Georgia Institute of Technology, 1989.

[61] S. G. Voutsinas, "Vortex methods in aeronautics: How to make things work," *International Journal of Computational Fluid Dynamics*, vol. 20, no. 1, pp. 3–18, 2006.

[62] S. Voutsinas, M. Belessis, and K. Rados, "Investigation of the yawed operation of wind turbines by means of a vortex particle method," in *AGARD CONFERENCE PROCEEDINGS AGARD CP*, pp. 11–11, AGARD, 1995.

[63] A. J. Chorin, "Numerical study of slightly viscous flow," *Journal of Fluid Mechanics*, vol. 57, no. 04, pp. 785–796, 1973.

[64] E. Rivoalen and S. Huberson, "The particle strength exchange method applied to axisymmetric viscous flows," *Journal of Computational Physics*, vol. 168, no. 2, pp. 519–526, 2001.

[65] G. Batchelor, *An Introduction to Fluid Mechanics*. UK: Cambridge University Press, 1967.

[66] J. Katz and A. Plotkin, *Low speed aerodynamics*. UK: Cambridge University Press, 2001.

[67] S. Huberson and S. Voutsinas, "Particles and grids," *Computers and Fluids*, vol. 31, pp. 607–625, 2002.

[68] R. W. Hockney and J. W. Eastwood, *Computer Simulation Using Particles*. McGraw-Hill, 1981.

[69] B. Couet, O. Buneman, and A. Leonard, "Simulation of three-dimensional incompressible flows with a vortex in cell method," *J. Computational Physics*, vol. 39, pp. 305–328, 1981.

[70] G. Papadakis and S. G. Voutsinas, "In view of accelerating CFD simulations through coupling with vortex particle approximations," *Journal of Physics: Conference Series*, vol. 524, no. 1, 2014.

126

[71] C. Hirsch, *Numerical Computation of Internal and External Flows.* Wiley, 1990.

[72] R. J. LeVeque, *Finite volume methods for hyperbolic problems*, vol. 31. Cambridge university press, 2002.

[73] B. Cockburn and C.-W. Shu, "Runge–kutta discontinuous galerkin methods for convection-dominated problems," *Journal of scientific computing*, vol. 16, no. 3, pp. 173–261, 2001.

[74] T. A. Zang, C. L. Streett, and M. Y. Hussaini, "Spectral methods for cfd," 1989.

[75] A. Quarteroni and A. Valli, *Domain decomposition methods for partial differential equations.* Oxford Science Publications, 1999.

[76] G. Carey, *Computational Grids: Generation, Adaptation, and Solution Stategies.* Taylor & Francis, 1997.

[77] D. Mavriplis, "Accurate multigrid solution of the Euler equations on unstructured and adaptive meshes," *AIAA Journal*, vol. 28, pp. 213–221, 1990.

[78] A. Haselbacher and J. Blazek, "Accurate and efficient discretization of Navier-Stokes equations on mixed grids," *AIAA Journal*, vol. 38, pp. 2094–2102, 2000.

[79] Z. Wang, "A fully conservative interface algorithm for overlapped grids," *Journal of Computational Physics*, vol. 122, no. 1, pp. 96–106, 1995.

[80] R. Steijl and G. Barakos, "Sliding mesh algorithm for cfd analysis of helicopter rotor–fuselage aerodynamics," *International journal for numerical methods in fluids*, vol. 58, no. 5, pp. 527–549, 2008.

[81] T. J. Poinsot and S. Lelef, "Boundary conditions for direct simulations of compressible viscous flows," *Journal of computational physics*, vol. 101, no. 1, pp. 104–129, 1992.

[82] G. Papadakis and G. Voutsinas, Spyros, "A strongly coupled eulerian lagrangian method verified in 2d external compressible flows," *Computers & Fluids*, vol. 195, 2019.

[83] J. T. Beale and A. Majda, "Vortex methods. i. convergence in three dimensions," *Mathematics of Computation*, vol. 39, no. 159, pp. 1–27, 1982.

[84] J. T. Beale and A. Majda, "Vortex methods. ii. higher order accuracy in two and three dimensions," *Mathematics of Computation*, vol. 39, no. 159, pp. 29–52, 1982.

127

[85] L. Rosenhead, "The formation of vortices from a surface of discontinuity," *Proceedings of the Royal Society of London. Series A, Containing Papers of a Mathematical and Physical Character*, pp. 170–192, 1931.

[86] J. T. Beale and A. Majda, "High order accurate vortex methods with explicit velocity kernels," *Journal of Computational Physics*, vol. 58, no. 2, pp. 188–208, 1985.

[87] R. Krasny, "Desingularization of periodic vortex sheet roll-up," *Journal of Computational Physics*, vol. 65, no. 2, pp. 292–313, 1986.

[88] G.-H. Cottet and P. Koumoutsakos, *Vortex methods: Theory and Practice.* Cambridge University Press, 2000.

[89] S. Richardson and A. Cornish, "Solution of three dimensional incompressible flow problems," *J. of Fluid Mechanics*, vol. 82, pp. 309–319, 1977.

[90] J. Guermond, S. Huberson, and W. Shen, "Simulation of 2D external viscous flows by means of a domain decomposition method," *J. Computational Physics*, vol. 108, pp. 343–352, 1993.

[91] P. Plouhmans, G. Winckelmans, J. Salmon, A. Leonard, and M.S.Warren, "Vortex methods for direct numerical simulation of three-dimensional bluff body flows: Application to the sphere at Re=300, 500, and 1000," *J. Computational Physics*, vol. 178, pp. 427–436, 2002.

[92] R. Boisvert, "A fourth order accurate fast direct method for the Helmholtz equation," *Academic Press*, pp. 35–44, 1984.

[93] R. James, "The solution of poisson's equation for isolated source distributions," *Journal of Computational Physics*, vol. 25, no. 2, pp. 71–93, 1977.

[94] K. Lackner, "Computation of ideal mhd equilibria," *Computer Physics Communications*, vol. 12, no. 1, pp. 33–44, 1976.

[95] C. R. Anderson, "A method of local corrections for computing the velocity field due to a distribution of vortex blobs," *Journal of Computational Physics*, vol. 62, no. 1, pp. 111–123, 1986.

[96] S. Huberson, E. Rivoalen, and S. Voutsinas, "Vortex particle methods in aeroacoustic calculations," *Journal of Computational Physics*, vol. 227, no. 21, pp. 9216–9240, 2008.

[97] S. G. Huberson and S. G. Voutsinas, "Particles and grid," *Computers & fluids*, vol. 31, no. 4-7, pp. 607–625, 2002.

[98] J.-T. Beale and A. Majda, "High Order Accurate Vortex Methods with Explicit Velocity Kernels," *Computational Physics*, 1985.

[99] P. L. Roe, "Approximate riemann solvers, parameter vectors, and difference schemes," *Journal of computational physics*, vol. 43, no. 2, pp. 357–372, 1981.

[100] V. Venkatakrishnan, "On the Accuracy of Limiters and Convergence to Steady State Solutions," *AIAA paper 93-0880*, 1993.

[101] V. Venkatakrishnan, "Convergence to steady state solutions of the euler equations on unstructured grids with limiters," *Journal of computational physics*, vol. 118, no. 1, pp. 120–130, 1995.

[102] P. Spalart and S. Allmaras, "One-Equation Turbulence Model for Aerodynamic Flows," *Recherche Aerospatiale*, pp. 5–21, 1994.

[103] F. Menter, "Zonal Two Equation k-omega Turbulence Models for Aerodynamic Flows," *AIAA Paper 93-2906*, 1993.

[104] S. Ghosal, "An analysis of numerical errors in large-eddy simulations of turbulence," *Journal of Computational Physics*, vol. 125, no. 1, pp. 187–206, 1996.

[105] A. Jameson, "Time dependent calculations using multigrid, with applications to unsteady flows past airfoils and wings," *AIAA paper*, vol. 1596, p. 1991, 1991.

[106] N. Spyropoulos, J. Prospathopoulos, D. Manolas, G. Papadakis, and V. A. Riziotis, "Development of a fluid structure interaction tool based on an actuator line model," *Journal of Physics: Conference Series*, 2020.

[107] P. Jha and S. Schmitz, "Actuator curve embedding–an advanced actuator line model," *Journal of Fluid Mechanics*, vol. 834, 2018.

[108] L. Martinez-Tossas, M. Churchfield, and S. Leonardi, "Large eddy simulations of the flow past wind turbines: actuator line and disk modeling," *Wind Energy*, vol. 18, 2015.

[109] N. Troldborg, N. N. Sørensen, and J. Michelsen, "Numerical simulations of wake characteristics of a wind turbine in uniform inflow," *Wind Energy*, vol. 13, pp. 86–99, 2010.

[110] M. Shives and C. Crawford, "Mesh and load distribution requirements for actuator line cfd simulations," *Wind Energy*, vol. 16, 2013.

[111] P. Jha, M. Churchfield, P. Moriarty, and S. Schmitz, "Guidelines for volume force distributions within actuator line modeling of wind turbines on large-eddy simulation-type grids," *Journal of Solar Energy Engineering*, vol. 136, 2014.

[112] G. Lamberti, L. Amerio, G. Pomaranzi, A. Zasso, and C. Gorlé, "Comparison of high resolution pressure measurements on a high-rise building in a closed and open-section wind tunnel," *Journal of wind engineering and industrial aerodynamics*, vol. 204, p. 104247, 2020.

[113] G. Papadakis, D. Manolas, V. A. Riziotis, and S. G. Voutsinas, "A novel hybrid method for helicopter cost effective aeroelastic simulations," 2017.

[114] V. A. Riziotis and S. G. Voutsinas, "Modelling of wind tunnel interference on helicopter measurements and assessment of the currently used corrections based on the helinovi database," 2006.

[115] N. Spyropoulos, G. Papadakis, J. M. Prospathopoulos, and V. A. Riziotis, "Investigating the level of fidelity of an actuator line model in predicting loads and deflections of rotating blades under uniform free-stream flow," *Applied Sciences*, vol. 11, p. 12097, Dec 2021.

[116] A. J. Landgrebe, "Overview of helicopter wake and airloads technology," 1986.

ΕΘΝΙΚΟ ΜΕΤΣΟΒΙΟ ΠΟΛΥΤΕΧΝΕΙΟ

ΕΡΓΑΣΤΗΡΙΟ ΑΕΡΟΔΥΝΑΜΙΚΗΣ

ΔΙΔΑΚΤΟΡΙΚΗ ΔΙΑΤΡΙΒΗ

Αλληλεπίδραση αιωρούμενου ελικοπτέρου με το έδαφος και με εμπόδια. Υπολογιστική διερεύνηση.

Θεολόγος Ανδρόνικος

23 Φεβρουαρίου 2022

Αλληλεπίδραση αιωρούμενου ελικοπτέρου με το έδαφος και με εμπόδια. Υπολογιστική διερεύνηση.

ΔΙΔΑΚΤΟΡΙΚΗ ΔΙΑΤΡΙΒΗ

Θεολόγος Ανδρόνικος

Εξεταστική επιτροπή:

1. Κ. Μπελιμπασάκης, Καθηγητής, ΕΜΠ, Σχολή Ναυπηγών Μηχανικών

2. Δ. Μπούρης* Αν. Καθηγητής, ΕΜΠ, Σχολή Μηχανολόγων Μηχανικών

3. Κ. Γιαννάκογλου, Καθηγητής, ΕΜΠ, Σχολή Μηχανολόγων Μηχανικών

4. Ι. Νικολός, Καθηγητής, ΠΚ, Σχολή Μηχανικών Παραγωγής και Διοίκησης

5. Γ. Παπαδάκης, Αν. Καθηγητής, ΕΜΠ, Σχολή Ναυπηγών Μηχανικών

6. Β. Ριζιώτης (Επιβλέπων) *, Αν. Καθηγητής, ΕΜΠ, Σχολή Μηχανολόγων Μηχανικών

7. Σ. Βουτσινάς *, Καθηγητής, ΕΜΠ, Σχολή Μηχανολόγων Μηχανικών

 * Μέλος της Συμβουλευτικής (Τριμελούς) Επιτροπής

This page intentionally left blank.

Περιεχόμενα

Κατάλογος Σχημάτων

This page intentionally left blank.

Κατάλογος Πινάκων

This page intentionally left blank.

Περίληψη

Στην παρούσα διδακτορική διατριβή μελετάται η αλληλεπίδραση ενός αιωρούμενου ελικοπτέρου με το έδαφος και με εμπόδια. Η περιορισμένη βιβλιογραφία επί του φαινομένου τόσο σε υπολογιστικό όσο και σε πειραματικό πλαίσιο αποτέλεσε το κίνητρο της εργασίας. Στόχος της εργασίας είναι η διερεύνηση των επιπτώσεων αυτής της αλληλεπίδρασης στην πτήση αιώρησης του ελικοπτέρου καθώς και η ανάλυση και κατηγοριοποίηση των φυσικών φαινομένων που λαμβάνουν χώρα. Όταν ένα ελικόπτερο προσγειώνεται ή απογειώνεται ο ομόρρους του αλληλεπιδρά με το έδαφος και με παρακείμενα εμπόδια. Η παραπάνω κατάσταση οδηγεί σε μεταβολές των φορτίων και της απόδοσης του ελικοπτέρου, οι οποίες αποτελούν συνάρτηση του λόγου ύψους αιώρησης-διαμέτρου του κύριου δρομέα. Με αυτό τον τρόπο το πεδίο ροής διαφοροποιείται ουσιωδώς συγκριτικά με το αντίστοιχο της πτήσης αιώρησης μακριά από στερεά σύνορα.

Η πτήση αιώρησης ελικοπτέρου μακριά από το έδαφος χαρακτηρίζεται από τη δημιουργία μιας ροής δέσμης που εκπέμπεται από τον κύριο δρομέα, με τον ταυτόχρονο σχηματισμό ενός δακτυλίου στροβιλότητας. Προϊόντος του χρόνου, ο δακτύλιος αυτός απομακρύνεται με σταθερή ταχύτητα. Αντίθετα, όταν ένα ελικόπτερο αιωρείται κοντά στο έδαφος ή σε εμπόδια, παρατηρείται η δημιουργία οριακών στρωμάτων πάνω στις στερεές επιφάνειες, τα οποία αλληλεπιδρούν με τον δακτύλιο στροβιλότητας. Η αλληλεπίδραση των παραπάνω στρωμάτων διάτμησης οδηγεί στην δημιουργία ισχυρών δομών στροβιλότητας, διαμορφώνοντας με αυτό τον τρόπο ένα σύνθετο πεδίο ροής που επηρεάζει την φόρτιση του ελικοπτέρου.

Η ανάλυση της αλληλεπίδρασης περιλαβάνει πειραματικά αποτελέσματα και υπολογιστικές προσομοιώσεις για ένα μοντέλο ελικοπτέρου υπό κλίμακα. Οι διαστάσεις του ελικοπτέρου και των εμποδίων έχουν υποστεί ανάλογη μείωση ούτως ώστε να προσομοιάζουν την αλληλεπίδραση ελικοπτέρου με κτήριο. Η επιλογή των παραμέτρων λειτουργίας του υπό κλίμακα μοντέλου πραγματοποιήθηκε με τέτοιο τρόπο ώστε η ταχύτητα ακροπτερυγίου του κύριο δρομέα να διατηρηθεί σταθερή. Οι μετρήσεις πραγματοποιήθηκαν σε τρία διαφορετικά πανεπιστήμια και ερευνητικά κέντρα (Πολυτεχνείο του Μιλάνο, Πανεπιστήμιο της Γλασκόβης, ONERA) για σχετικά χαμηλούς αριθμούς Re (μικρότερους από 300000). Οι πειραματικές μετρήσεις αφορούν παρόμοιες διατάξεις με διαφορετικές παραμέτρους ωστόσο. Με αυτό τον τρόπο και αδιαστατοποιώντας τα αποτελέσματα, τα συμπεράσματα που εξάγονται μπορούν κατηγοριοποιηθούν βάσει των φυσικών φαινομένων και όχι ανάλογα με την εκάστοτε πειραματική διάταξη.

Για την επιβεβαίωση των πειραματικών μετρήσεων πραγματοποιήθηκαν υπολογιστικές προσομοιώσεις με εργαλεία μεσαίας και μεγάλης υπολογιστικής πιστότητας. Προκαταρκτικές προσομοιώσεις πιστοποίησαν την καλή λειτουργία των εργαλείων και ταυτόχρονα ανέδειξαν τους περιορισμούς της κάθε μεθοδολογίας. Το πρώτο εργαλείο, ένας ασυμπίεστος μη συνεκτικός κώδικας συνοριακών στοιχείων και στοιχείων

στροβιλότητας GenUVP, επιτρέπει την προσομοίωση μεγάλου αριθμού περιπτώσεων προλέγοντας ικανοποιητικά αποτελέσματα. Σε αυτή την κατεύθυνση, αναδείχθηκαν οι περιορισμοί των μη συνεκτικών μεθόδων αφού εγγενώς αδυνατούν να προλέξουν την δημιουργία οριακών στρωμάτων.

Για να ξεπεραστεί η παραπάνω αδυναμία, χρησιμοποιήθηκε επιλεκτικά μία υβριδική μέθοδος υψηλής ακρίβειας. Η μέθοδος αυτή συνδυάζει μέσω μίας επαναληπτικής διαδικασίας την Eulerian διατύπωση των εξισώσεων της μηχανικής των ρευστών με την Lagrangian εκδοχή. Με αυτό τον τρόπο επιτυγχάνεται η ικανοποίηση όλων των οριακών συνθηκών του πεδίου, και εισάγεται στις προσομοιώσεις η συνεκτικότητα του εδάφους και των εμποδίων. Τα αποτελέσματα που παρήχθησαν συγκρίνονται πολύ καλά με τις πειραματικές μετρήσεις.

Καταλήγοντας, κάνοντας χρήση τόσο πειραματικών δεδομένων από ανεξάρτητα πειράματα, όσο και υπολογιστικών αποτελεσμάτων διαφόρων μεθόδων, εξάγονται συμπεράσματα για το πρόβλημα της αλληλεπίδρασης ελικοπτέρου με το έδαφος και με εμπόδια.

Κεφάλαιο 1

Εισαγωγή

1.1 Ανασκόπηση του προβλήματος της αλληλεπίδρασης δρομέα ελικοπτέρου με το έδαφος και με εμπόδια

Η πτήση ενός ελικοπτέρου εν γένει χαρακτηρίζεται από περίπλοκους φυσικούς μηχανισμούς. Η μεγάλη ταχύτητα περιστροφής του κύριου δρομέα παράγει την απαραίτητη ώση έτσι ώστε να υπερνικηθεί η βαρύτητα του ελικοπτέρου και ταυτόχρονα να αναπτύξει ταχύτητα πτήσης. Η ροή δέσμης στον ομόρρου του δρομέα και οι στρόβιλοι ακροπτερυγίων που δημιουργούνται, ταξιδεύουν κατάντι του ελικοπτέρου, σχηματίζοντας ένα πολύπλοκο πεδίο ροής. Μέσα σε αυτό το πλαίσιο, η πλοήγηση πραγματοποιείται με την αλλαγή διαφόρων γεωμετρικών γωνιών στο επίπεδο του ελικοπτέρου και του δρομέα. Με αυτό τον τρόπο, καθίσταται δυνατή η αυξομείωση της ώσης αλλά και η αλλαγή της κατανομής των δυνάμεων πάνω στον δρομέα. Ως αποτέλεσμα οι ροπές που ασκούνται στο ελικόπτερο μεταβάλλονται. Για την ευστάθεια του ελικοπτέρου απαιτείται η συνεχής μεταβολή των παραπάνω χαρακτηριστικών με στόχο την εξισορρόπηση όλων των εξωτερικών δυνάμεων (βάρος, αντίσταση).

Σε αντίθεση με την κανονική πτήση του ελικοπτέρου, η διαδικασία προσγείωσης και απογείωσης διαφέρουν σημαντικά καθώς ο ομόρρους του κύριου δρομέα περιορίζεται από το έδαφος αλληλεπιδρώντας με αυτό και μεταβάλει σημαντικά το πεδίο ροής γύρω από το ελικόπτερο. Ο αρχικός δακτύλιος στροβιλότητας του δρομέα χτυπάει στο έδαφος και στην συνέχεια δημιουργείται ο ονομαζόμενος στρόβιλος εδάφους ο οποίος διογκώνεται με αποτέλεσμα να επάγεται ένα επιπλέον κατώρευμα. Ο σχηματισμός και η ένταση αυτού του στροβίλου εξαρτάται από πολλούς παράγοντες όπως η απόσταση του ελικοπτέρου από το έδαφος, η ταχύτητα του ανέμου (αν πνέει) και το πάχος του οριακού στρώματος. Επομένως, η παρουσία του εδάφους (IGE) μεταβάλει την αεροδυναμική συμπεριφορά του δρομέα συγκριτικά με την πτήση αιώρησης εκτός της επίδρασης του (OGE) βελτιώνοντας την απόδοση του στροφείου (μικρότερη καταναλισκόμενη ισχύς για την ίδια ώση). Ωστόσο έχουν αναφερθεί περιστατικά δυσκο-

λίας χειρισμού του ελικοπτέρου [1]. Δεδομένου πώς η πλειονότητα των απογειώσεων και προσγειώσεων πραγματοποιείται εντός κατοικημένων περιοχών, το πρόβλημα ε- νισχύεται με την αλληλεπίδραση του ομόρρου με κτήρια και άλλες κατασκευές στο ανθρωπογενές περιβάλλον. Αυτό έχει σαν αποτέλεσμα την δημιουργία ενός συνεχώς μεταβαλλόμενου πεδίου πιέσεων πάνω στις κατασκευές, εγείροντας ανησυχίες για την ασφάλεια των ενοίκων άλλα και την δυνατότητα των πιλότων να αντεπεξέλθουν σε αυτές τις απρόβλεπτες συνθήκες πτήσης.

Τα παραπάνω δεδομένα διαδραματίζουν σημαντικό ρόλο στο σχεδιασμό ενός ε- λικοπτέρου καθώς και στην κατάρτιση του φακέλου πτήσης. Να σημειωθεί πώς ο φάκελος πτήσης ενός ελικοπτέρου απαρτίζεται από διάφορα σενάρια πτήσης τα οποία προηγουμένως έχουν δοκιμασθεί και ελεγχθεί επιμελώς. Όλοι οι παραπάνω λόγοι και η έλλειψη εκτενούς βιβλιογραφίας οδήγησαν τον ευρωπαϊκό οργανισμό Garteur στον σχηματισμό μίας ομάδας δράσης AG-22 με σκοπό την αναλυτική διερεύνηση του φαινομένου και των επιπτώσεων στην φόρτιση των εμποδίων, στην ευστάθεια του ελικοπτέρου και στον χειρισμό του από τον πιλότο. Το πρόγραμμα ξεκίνησε το 2014, διήρκεσε 4 χρόνια και σε αυτό έλαβε μέρος και το Εργαστήριο Αεροδυναμικής του ΕΜΠ. Η εκτενής μελέτη [2] περιλαμβάνει υπολογιστικές προσομοιώσεις με εργαλεία διαφορετικής πιστότητας-ακρίβειας καθώς και πειραματικά δεδομένα [3], [4], [5] που αφορούν στην πτήση αιώρησης ελικοπτέρου κοντά στο έδαφος και σε εμπόδια. Με αυτό τον τρόπο αποτυπώθηκαν η επίδραση στην φόρτιση του δρομέα και του εμπο- δίου και η διαμόρφωση του πεδίου ταχύτητας σε διάφορες συνθήκες και περιπτώσεις. Μέρος των αποτελεσμάτων της παρούσας διατριβής παρουσιάστηκαν στα πλαίσια του συγκεκριμένου προγράμματος.

Κατά την διάρκεια του AG-22 αλλά και μετά το πέρας των δραστηριοτήτων του, οι πειραματικές μετρήσεις που προέκυψαν χρησιμοποιήθηκαν για την πιστοποίηση δια- φόρων μεθόδων καθώς και για την περαιτέρω διερεύνηση του προβλήματος από τους συμμετέχοντες στο πρόγραμμα. Η πλειοψηφία των μελετών πραγματοποιήθηκε με την μέθοδο των συνοριακών στοιχείων και τη μέθοδο της γραμμής άνωσης. Πρόκειται για μη συνεκτικές ασυμπίεστες μεθοδολογίες οι οποίες όμως απαιτούν μικρό υπολο- γιστικό χρόνο. Ο Tan στην δημοσίευση [6] χρησιμοποίησε μία μέθοδο στοιχείων στροβιλότητας [7] συζευγμένη με ένα μοντέλο οριακού στρώματος [8], [9], [10], προ- κειμένου να μελετήσει την αλληλεπίδραση του κύριου δρομέα του ελικοπτέρου με το έδαφος και το εμπόδιο. Οι προλέξεις συγκρίνονται καλά με τα πειραματικά δεδομένα [4], ωστόσο δεν είναι σε θέση να επιλύσουν με ακρίβεια το πεδίο ταχυτήτων αφο- ύ το μοντέλο για το οριακό στρώμα θέτει ορισμένους περιορισμούς. Μία παρόμοια υπολογιστική μελέτη πραγματοποιήθηκε από τον Schmid. Για τους υπολογισμούς χρησιμοποιήθηκε η μέθοδος συνοριακών στοιχείων σε σύζευξη με ένα μοντέλο ελε- ύθερου ομόρρου [11], [12], [13]. Οι προλέξεις συγκρίθηκαν με πειραματικά δεδομένα [3] και περιλαμβάνουν αποτελέσματα για την αλληλεπίδραση του δρομέα με το έδαφος και με εμπόδια σε περιπτώσεις με και χωρίς άνεμο. Οι συγκρίσεις με τα πειράματα ήταν σχετικά καλές καθώς προλέγουν σε μεγάλο βαθμό ικανοποιητικά τις μετρήσεις. Όμως η έλλειψή συνεκτικότητας στα στερεά σύνορα επηρεάζει σε μεγάλο βαθμό τα υπολογιστικά αποτελέσματα σε περιπτώσεις που ο δρομέας βρίσκεται πολύ κοντά στο

2

εμπόδιο και στις περιπτώσεις όπου υπάρχει άνεμος.

Η συνδρομή του εργαστηρίου αεροδυναμικής του ΕΜΠ σε υπολογιστικό πλαίσιο αποτελείται από δύο δημοσιεύσεις [14] και [15]. Οι παραπάνω μελέτες εξετάζουν την ικανότητα μίας μεθόδου συνοριακών στοιχείων (GenUVP) [16] συζευγμένης με τη μέθοδο στοιχείων στροβιλότητας να προλέγει ορθά το πρόβλημα της αλληλεπίδρασης χωρίς την παρουσία ανέμου. Τα αποτελέσματα συγκρίθηκαν με πειραματικά δεδομένα και από τις 3 διατάξεις. Οι συγκρίσεις κρίθηκαν καλές αν λάβει κανείς υπόψη και το μικρό υπολογιστικό κόστος. Παρόλα αυτά, μερικές περιπτώσεις παρουσίασαν σημαντικές αποκλίσεις σε σχέση με τα πειράματα. Το αποτέλεσμα αυτό είναι λογικό καθώς η μέθοδος στερείται της δυνατότητας προσομοίωσης συνεκτικών φαινομένων.

Η διαπίστωση πως τα συνεκτικά φαινόμενα διαδραματίζουν σημαντικό ρόλο στην πρόλεξη των φορτίων του δρομέα και του πεδίου ροής γύρω από αυτόν επιβεβαιώνεται και από τις δύο δημοσιεύσεις που πραγματοποιήθηκαν με Eulerian μεθοδολογίες. Ο Gibertini [17] χρησιμοποιώντας τον κώδικα ROSITA [18] ο οποίος συνδυάζει μία Eulerian διατύπωση σε συνδυασμό με ένα μοντέλο δίσκου ενέργειας αναπαρήγαγε αποτελέσματα που συγκρίνονται πάρα πολύ καλά με τις πειραματικές μετρήσεις. Οι συγκρίσεις αφορούν τόσο στα φορτία του δρομέα όσο και το πεδίο ροής. Παρόμοια μεθοδολογία εφαρμόστηκε και από τον Chirico [19],[20] στην δημοσίευσή του [21]. Οι προλέξεις συγκρίνονται πολύ καλά με τα πειραματικά αποτελέσματα όπως και στην προηγούμενη μελέτη. Η καλή σύγκριση αποδίδεται κατά κύριο λόγο στη συνεπή προσομοίωση του οριακού στρώματος που αναπτύσσονται στην επιφάνεια του εδάφους και του εμποδίου.

1.2   Σκοπός της εργασίας

Η παρούσα εργασία αποσκοπεί α) στην μελέτη του φαινομένου της αλληλεπίδρασης του ελικοπτέρου με στερεά σύνορα και β) στην πιστοποίηση και εκτίμηση της αξιοπιστίας δύο προϋπαρχόντων υπολογιστικών εργαλείων (μέθοδος συνοριακών στοιχείων, υβριδική μέθοδος).

Ο κύριος στόχος της διατριβής ήταν η συστηματική διερεύνηση του προβλήματος της αλληλεπίδρασης του ελικοπτέρου με το έδαφος και με εμπόδια. Αυτό περιλαμβάνει εκτός των άλλων την συστηματική ανάλυση και κατηγοριοποίηση των φυσικών μηχανισμών που λαμβάνουν χώρα σε τέτοια προβλήματα, την καταγραφή των επιπτώσεων της αλληλεπίδρασης στην φόρτιση του δρομέα και τη διαμόρφωση της ροής γύρω από αυτόν, καθώς και μία συγκριτική ποσοτική ανάλυση των επιδράσεων του εδάφους και του εμποδίου. Πρώτο βήμα σε αυτή την προσπάθεια ήταν η συγκέντρωση των πειραματικών δεδομένων που ήταν διαθέσιμα μέσω του προγράμματος Garteur AG-22 και η λεπτομερείς ανάλυση τους. Η ανάλυση βασίστηκε στην ομοιότητα των πειραματικών διατάξεων και είχε ως στόχο την καταρχήν κατανόηση του φαινομένου. Οι περιπτώσεις που εξετάστηκαν ήταν α) η πτήση αιώρησης του ελικοπτέρου σε εγγύτητα με το έδαφος ώστε να διαπιστωθεί η επίδραση του εδάφους στην ώση και την παραγόμενη από τον δρομέα ροπή στρέψης, β) η πτήση αιώρησης του ελικοπτέρου κοντά στο έδαφος με την ταυτόχρονη παρουσία κάποιου εμποδίου.

3

Οι περιπτώσεις που εξετάσθηκαν περιλαμβάνουν πέντε σενάρια πτήσης. Πρώτη εξετάσθηκε η πτήση αιώρησης εκτός της επίδρασης του εδάφους. Στην συνέχεια διερευνήθηκε η επίδραση του εδάφους στην πτήση αιώρησης χωρίς την παρουσία κάποιου εμποδίου. Με αυτό τον τρόπο ποσοτικοποιήθηκε η επίδραση αυτή ανάλογα με την απόσταση από το έδαφος και τα αποτελέσματα της παραπάνω ποσοτικοποίησης τέθηκαν ως βάση για την μετέπειτα ανάλυση. Η από κοινού επίδραση του εμποδίου και του εδάφους αποτιμάται στις άλλες τρεις περιπτώσεις όπου ο δρομέας μεταβάλει την κάθετη ή την οριζόντια θέση του σε σχέση με το έδαφος και το εμπόδιο.

Σε υπολογιστικό επίπεδο, όπως ειπώθηκε προηγουμένως, αντίστοιχες μελέτες έχουν πραγματοποιηθεί τόσο με μεθόδους συνοριακών στοιχείων όσο και με Eulerian μεθοδολογίες, τα θετικά και τα αρνητικά των οποίων συνοψίζονται παρακάτω:

Eulerian Μέθοδοι

+ Ακριβής ικανοποίηση των οριακών συνθηκών στα στερεά σύνορα

+ Επιλύουν συμπιεστές και συνεκτικές ροές

- Το υπολογιστικό χωρίο πρέπει να επεκταθεί αρκετά ώστε να ικανοποιούνται οι οριακές συνθήκες στο άπειρο

- Προοδευτική αραίωση του υπολογιστικού πλέγματος που οδηγεί και εκτεταμένη διάχυση

Μέθοδοι συνοριακών στοιχείων

+ Δεν απαιτούν χωρικό πλέγμα

+ Θεωρητικά παρουσιάζουν μηδενική διάχυση

+ Οι οριακές συνθήκες στο άπειρο ικανοποιούνται επακριβώς

+ Έχουν μικρό υπολογιστικό κόστος

- Είναι εγγενώς ασυμπίεστες και μη συνεκτικές μέθοδοι

- Δύσκολη ικανοποίηση των οριακών συνθηκών στα στερεά σύνορα

Η παρούσα εργασία χρησιμοποιεί δύο διαφορετικές μεθόδους για την προσομοίωση του προβλήματος. Πρώτα, χρησιμοποιείται η μέθοδος συνοριακών στοιχείων (GenUVP) [22]. Το μικρό υπολογιστικό κόστος της μεθόδου επιτρέπει την γρήγορη προσομοίωση όλων των περιπτώσεων. Με αυτό τον τρόπο, επιτυγχάνεται μία συνολική επισκόπηση του προβλήματος. Ταυτόχρονα, πιστοποιείται η ικανότητα τέτοιων μεθόδων να προλέγουν την αλληλεπίδραση ενός δρομέα ελικοπτέρου με το έδαφος και με εμπόδια. Η συγκεκριμένη μέθοδος έχει πιστοποιηθεί στο παρελθόν [23] [16] τόσο σε εφαρμογές για ανεμογεννήτριες όσο και σε ελικόπτερα. Τέλος, γίνονται αντιληπτοί οι περιορισμοί που θέτουν τέτοιες μέθοδοι για την αντιμετώπιση παρόμοιων περιπτώσεων. Διάφορες προσπάθειες έχουν πραγματοποιηθεί για την εισαγωγή συνεκτικών φαινομένων σε μη συνεκτικούς κώδικες [24, 25]. Ωστόσο, καθώς ο αριθμός Re αυξάνεται και τα συνεκτικά φαινόμενα γίνονται έντονα, τέτοιες μεθοδολογίες αδυνατούν να αποτυπώσουν με ακρίβεια το φαινόμενο. Όμως, η προκαταρκτική έρευνα που είναι απαραίτητη για την εξέταση του προβλήματος καθιστά τον (GenUVP) ένα

4

κατάλληλο εργαλείο ακόμα και αν δεν είναι ικανό να προλέγει την ανάπτυξη οριακού στρώματος.

Η συστηματική ωστόσο διερεύνηση του προβλήματος απαιτεί την χρήση μίας μεθόδου υψηλής ακρίβειας και δεν μπορεί να στηριχθεί εξ᾽ ολοκλήρου σε μεθόδους συνοριακών στοιχείων. Τέτοιες μέθοδοι βασίζονται στην Eulerian περιγραφή των εξισώσεων Navier-Stokes. Η επίλυση των εξισώσεων πραγματοποιείται με την χρήση Πεπερασμένων Διαφορών (FDM) [26], με Πεπερασμένους Όγκους (FVM) [27], με ασυνεχής μέθοδο Galerkin (DGM) [28] και τέλος με Spectral Methods [29]. Οι παραπάνω πλεγματικές μέθοδοι σε συνδυασμό με την μέθοδο διαχωρισμού πλεγμάτων [30] και με τεχνικές παράλληλου προγραμματισμού έχουν οδηγήσει σε μειωμένους χρόνους προσομοιώσεων, που όμως απαιτούν υπολογιστικές μονάδες με μεγάλο αριθμό επεξεργαστικών πυρήνων. Ακόμα μεγαλύτερη μείωση επιτυγχάνεται με την χρήση της μεθόδου multi-grid [31] η οποία οδηγεί σε ταχύτερες συγκλίσεις του προβλήματος.

Μία αδυναμία των πλεγματικών μεθόδων είναι η διαχείριση προβλημάτων στα οποία συνυπάρχουν περιστρεφόμενα και μη στερεά σύνορα. Το πρόβλημα αυτό αντιμετωπίζεται με τα ανεξαρτήτως κινούμενα πλέγματα (CHIMERA, over-set) [32] και Sliding Grids [33], που σε συνδυασμό με την θεωρεία του δίσκου ενέργειας [34], δίνουν καλά αποτελέσματα στην βιβλιογραφία για το πρόβλημα της αλληλεπίδρασης ενός δρομέα με στερεά σύνορα. Σε αντίθεση όμως με τα πλεονεκτήματα που φέρνουν έναντι των μεθόδων συνοριακών στοιχείων, στο σύνολο τους οι Eulerian μεθοδολογίες απαιτούν την χρήση εκτενών πλεγμάτων για να ικανοποιηθούν οι οριακές συνθήκες στο άπειρο [35]. Αυτό έχει σαν αποτέλεσμα την σταδιακή αραίωση των πλεγμάτων γεγονός που οδηγεί σε τεχνητή διάχυση.

Λαμβάνοντας υπόψιν όλα τα παραπάνω, η παρούσα εργασία προτείνει σαν λύση τη χρήση μίας υβριδικής μεθόδου. Η μέθοδος αυτή (HoPFlow) αναπτύχθηκε προγενέστερα από τον Δρ. Παπαδάκη [36] στα πλαίσια της διδακτορικής του διατριβής το 2014. Το υπολογιστικό αυτό εργαλείο συνδυάζει ένα κλασσικό εργαλείο πεπερασμένων όγκων και μία Lagrangian στοιχειακή προσέγγιση του πεδίου [36, 37]. Το Eulerian κομμάτι αποτελείται από χωρικά πλέγματα περιορισμένου εύρους τα οποία εκτείνονται γύρω από τα στερεά σύνορα. Συγκεκριμένα, για τα προβλήματα που εξετάζονται στην παρούσα διατριβή, ένα πλέγμα τοποθετείται πάνω από το έδαφος και το εμπόδιο, και ένα ακόμα γύρω από τα περιστρεφόμενα πτερύγια, το οποίο περιστρέφεται μαζί με αυτά. Για να μπορέσει η πληροφορία να μεταφερθεί από το ένα πλέγμα στο άλλο, το σύνολο του πεδίου ροής περιγράφεται από σημειακά στοιχεία (particles), για τα οποία επιλύεται η ροή σε Lagrangian συντεταγμένες, και στην συνέχεια μέσω ενός πλήρως συζευγμένου επαναληπτικού σχήματος επιτυγχάνεται συνέχεια όσον αφορά την λύση στα επιμέρους χωρικά πλέγματα. Στο Eulerian κομμάτι της μεθόδου επιλύονται οι συμπιεστές εξισώσεις της ροής έχοντας ως κύριες μεταβλητές την πυκνότητα-ταχύτητα-πίεση και χρησιμοποιεί προ-σταθεροποίηση για χαμηλούς αριθμούς Mach, ενώ στο Lagrangian κομμάτι οι κύριες μεταβλητές είναι η πυκνότητα-στροβιλότητα-συμπίεση. Με αυτό τον τρόπο εισάγεται στο υπολογιστικό εργαλείο τόσο ο υπερβολικός όσο και ο ελλειπτικός χαρακτήρας της ροής.

5

Τό συγκριτικό πλεονεκτήματα της μεθόδου σχετίζεται με την απουσία υπολογιστικού πλέγματος στο άπειρο σύνορο, που έχει ως αποτέλεσμα τη μείωση της διάχυσης στον ομόρρου δρομέων. Το παραπάνω συμβάλλει ουσιωδώς στη πιστότερη αναπαραγωγή φαινομένων αλληλεπίδρασης.

Οι στόχοι λοιπόν όσον αφορά το HoPFlow είναι:

- Η πιστοποίηση καταρχήν της μεθόδου στην επίλυση του προβλήματος της αλληλεπίδρασης ενός δρομέα με στερεά σύνορα.

- Η συγκριτική ανάλυση των προλέξεων με τις προλέξεις του GenUVP και των πειραματικών αποτελεσμάτων ως προς τη σημασία των συνεκτικών φαινομένων στο συγκεκριμένο πρόβλημα.

- Η δημιουργία ενός υπολογιστικού εργαλείου που μπορεί με συνέπεια να προλέγει ορθά περιπτώσεις όπου στρώματα διάτμησης και οριακά στρώματα αλληλεπιδρούν μεταξύ τους.

Στην παρούσα εργασία, η μοντελοποίηση των πτερύγων πραγματοποιείται με την θεωρεία της Γραμμής Ενέργειας στα πλαίσια του Eulerian τμήματος της προσομοίωσης. Οι λόγοι που οδήγησαν σε αυτή την επιλογή είναι α) η προσπάθεια μείωσης του υπολογιστικού κόστους, β) η καταγραφή στις μετρήσεις ολοκληρωμένων μεγεθών φόρτισης του δρομέα και όχι και λεπτόμερών κατανομών φόρτισης πάνω στα περύγια και γ) η επιλογή της μακροσκοπικής εστίασης της διερεύνησης στην επίδραση του εδάφους.

1.3 Δομή της διατριβής

Η παρούσα εργασία χωρίζεται σε 4 κεφάλαια:

- Στο Κεφάλαιο 1 παρουσιάζεται μία σύντομη βιβλιογραφική επισκόπηση και ο σκοπός της εργασίας.

- Στο Κεφάλαιο 2 γίνεται συνοπτική περιγραφή των υπολογιστικών εργαλείων που χρησιμοποιήθηκαν.

- Στο Κεφάλαιο 3 παρουσιάζεται η ανάλυση του προβλήματος. Αρχικά, περιγράφονται οι πειραματικές διατάξεις και οι υπολογιστικές παράμετροι των προσομοιώσεων. Στη συνέχεια παρουσιάζονται τα αποτελέσματα και συγκρίσεις μεταξύ μετρήσεων και προλέξεων των υπολογιστικών εργαλείων.

- Στο Κεφάλαιο 4 παρουσιάζονται τα συμπεράσματα και προτάσεις για μελλοντική έρευνα.

Κεφάλαιο 2

Περιγραφή υπολογιστικών εργαλείων

Σε αυτό το κεφάλαιο περιγράφονται συνοπτικά το θεωρητικό υπόβαθρο αλλά και οι υπολογιστικές λεπτομέρειες των εργαλείων που χρησιμοποιήθηκαν στην παρούσα εργασία. Όλες οι μέθοδοι έχουν απαπτυχθεί σε προγενέστερο χρόνο στο εργαστήριο Αεροδυναμικής του ΕΜΠ.

2.1 Οι πεδιακές εξισώσεις σε Lagrangian διατύπωση

2.1.1 Διατύπωση των εξισώσεων ως προς την Πυκνότητα-Στροβιλότητα-Διόγκωση

Η Lagrangian διατύπωση των εξισώσεων παίρνει την μορφή: *Εξίσωση συνέχειας:*

$$\frac{D\rho}{Dt} = -\rho\theta \tag{2.1}$$

Εξίσωση ορμής σε συντηρητική μορφή:

$$\frac{D\vec{\omega}}{Dt} = -\vec{\omega}\theta + (\vec{\omega}\cdot\nabla)\vec{u} - \frac{1}{\rho^2}\nabla\rho \times \nabla(-p + \overleftrightarrow{\sigma}) \tag{2.2}$$

$$\frac{D\theta}{Dt} = -\theta^2 + 2\|\nabla\vec{u}\| - \nabla\cdot\frac{\nabla(-p + \overleftrightarrow{\sigma})}{\rho} \tag{2.3}$$

Η εξίσωση ενέργειας σε συντηρητική μορφή:

$$\frac{D\Pi}{Dt} = V\nabla(\vec{u}\cdot(-pI + \overleftrightarrow{\sigma})) \tag{2.4}$$

7

Οι εξισώσεις 2.1, 2.2, 2.3, και 2.4 επιλύονται στην συνέχεια κάνοντας χρήση της στοιχειακής περιγραφής του πεδίου. Σύμφωνα με αυτή την λογική, το πεδίο περιγράφεται από σημειακά στοιχεία που έχουν μάζα M_p σε όγκο $V_P(t)$, και μεταφέρουν διόγκωση $\Theta_p(t)$ στροβιλότητα $\vec{\Omega}_P(t)$ και πίεση $e_P(t)$.

Εισάγοντας τον όγκο δV στις παραπάνω ιδιότητες $\Phi = (\rho, \theta, \vec{\omega}, e)$ και αφαιρώντας τους συνεκτικούς όρους, οι εξισώσεις σε Lagrangian διατύπωση παίρνουν την τελική μορφή:

$$\text{Διατήρηση Μάζας:} \quad \frac{DM_p}{Dt} = 0 \tag{2.5}$$

$$\text{Διατήρηση Ορμής:} \quad \frac{D\vec{\Omega}_p}{Dt} = V_p \left((\vec{\omega} \cdot \nabla)\vec{u} + \frac{1}{\rho^2} \nabla\rho \times \nabla p \right)_p \tag{2.6}$$

$$\frac{D\Theta_p}{Dt} = V_p \left(2\|\nabla\vec{u}\| - \nabla \cdot \frac{\nabla p}{\rho} \right)_p \tag{2.7}$$

$$\text{Διατήρηση Ενέργειας:} \quad \frac{D\Pi_p}{Dt} = -V_p \nabla(\vec{u}p) \tag{2.8}$$

2.1.2 Θεώρημα διαχωρισμού των ταχυτήτων του Helmholtz

Δεδομένου ότι το διάνυσμα της ταχύτητας Σύμφωνα με το θεώρημα του Helmholtz το διάνυσμα της ταχύτητα μπορεί να διαχωριστεί ως εξής:

$$\vec{u} = \vec{U}_\infty + \vec{u}_\phi + \vec{u}_\omega, \quad \vec{u}_\phi = \nabla\phi, \quad \vec{u}_\omega = \nabla \times \vec{\psi} \tag{2.9}$$

Υπό αυτό το πρίσμα, το πεδίο ταχύτητας προκύπτει από την επίλυση δύο Poisson εξισώσεων για το βαθμωτό δυναμικό ϕ και για το διανυσματικό δυναμικό $\vec{\psi}$.

Για την επίλυση των Poisson εξισώσεων χρησιμοποιείται η τεχνική του Particle Mesh (PM)

2.2 Τεχνική Particle-Mesh

Οι Particle Mesh (PM) μέθοδοι χρησιμοποιούνται για την επίλυση μίας Poisson εξίσωσης. Η διαδικασία επίλυσης αποτελείται από τρία στάδια.

Πρώτον η χωρική πληροφορία η οποία είναι διανεμημένη σε στοιχειακή μορφή προβάλλεται μέσω της συνάρτησης προβολής σε ένα καρτεσιανό ομοιόμορφο πλέγμα. Αν με $Q_p = q_p \cdot V_p$ συμβολίζεται το μέγεθος που μεταφέρεται από τα στοιχεία στροβιλότητας, χρησιμοποιώντας τις συναρτήσεις προβολής:

$$q_{i,j,k} \equiv \text{Proj}_{\text{PM}}(q_p; V_p) = \frac{\sum_p q_p V_p W(\vec{x}_{i,j,k} - \vec{Z}_p)}{\sum_p V_p W(\vec{x}_{i,j,k} - \vec{Z}_p)} \tag{2.10}$$

όπου με $\vec{x}_{i,j,k}$ συμβολίζεται το διάνυσμα θέσης των i, j, k κόμβων του πλέγματος. Η συνάρτηση παρεμβολής ορίζεται ως:

$$W(\vec{r}) = W_1(r_x/h)W_1(r_y/h)W_1(r_z/h)$$

όπου h συμβολίζει την απόσταση μεταξύ δύο κόμβων του πλέγματος.
Στην συνέχεια, η εξίσωση

$$\nabla^2 w = f(\vec{x}), \qquad \vec{x} \in D$$
$$w = w_B, \qquad \vec{x} \in \partial D \qquad\qquad (2.11)$$

λύνεται με την μέθοδο Fast Fourier Transform (FFT).

Τέλος,η πληροφορία μεταφέρεται από το πλέγμα στα στοιχεία στροβιλότητας χρησιμοποιώντας τις ίδιες συναρτήσεις παρεμβολής:

$$q_p \equiv \text{Interp}(q_{i,j}) = \sum_{i,j,k} q_{i,j,k} W(\vec{x}_{i,j,k} - \vec{Z}_p) \qquad\qquad (2.12)$$

2.2.1   Αλγόριθμος Lagrangian επιλυτή

Τα βήματα για την λύση των Lagrangian εξισώσεων μπορούν να συνοψιστούν στα εξής:

Για δεδομένα στοιχεία στροβιλότητας: $\{\vec{Z}_p^n, m_p^n, V_p^n, \vec{\Omega}_p^n, \Theta_p^n, \Pi_p^n\}$ ατ $t = n\Delta t$:

Βήμα 1:   Προβολή των $\{m_p^n, \Theta_p^n, \vec{\Omega}_p^n, \Pi_p^n\}$ στο PM πλέγμα:
$\rho_{i,j}^n, \theta_{i,j}^n, \vec{\omega}_{i,j}^n, \varepsilon_{i,j}^n$.

Βήμα 2:   Επίλυση $\nabla^2 \phi = \theta, \nabla^2 \vec{\psi} = -\vec{\omega}$ και υπολογισμός των
$\phi_{i,j}^n, \psi_{i,j}^n, \vec{u}_{i,j}^n, \vec{w}_{i,j}^n$ με χρήση πεπερασμένων διαφορών

Βήμα 3:   Υπολογισμός στο PM πλέγμα των όρων των εξισώσεων εξέλιξης
(2.5), π.χ. $\nabla\rho_{ij}^n, \nabla p_{ij}^n, \nabla\vec{u}_{ij}^n$

Βήμα 4:   Παρεμβολή των ποσοτήτων στο πλέγμα q_{ij}^n στις θέσεις των
στοιχείων στροβιλότητας: $q_p^n = \sum_{ij} q_{ij}^n W(\vec{x}_{i,j} - \vec{Z}_p)$.

Βήμα 5:   Ανανέωση των ποσοτήτων που μεταφέρουν τα στοιχεία
στροβιλότητας.

Βήμα 6:   Επαναπλεγματοποίηση εφόσον χρειάζεται.

2.3   Μέθοδος Συνοριακών Στοιχείων

Το θεώρημα του Helmholtz μπορεί να αναπαραστήσει το πεδίο ταχύτητας της ροής σε προβλήματα ασυμπίεστων ($\theta \equiv 0$) μη συνεκτικών ροών. Σε αυτή την περίπτωση η ελεύθερη στροβιλότητα είναι διανεμημένη πάνω σε φύλλα στροβιλότητας (επιφανειακή) που αναπαριστούν τον ομόρρου του εκάστοτε ανωστικού σώματος.

Σύμφωνα με το θεώρημα του Green:

$$\vec{u}_\phi(\vec{x};t) = \int_{S(t)} (\sigma(\vec{y},t) \cdot + \vec{\gamma}(\vec{y},t) \times) \nabla G(r) \, dS(\vec{y}) \qquad (2.13)$$

$$\vec{u}_\omega(\vec{x};t) = \int_{D_\omega(t)} \vec{\omega}(\vec{y};t) \times \nabla G(r) \, dD(\vec{y}) \qquad (2.14)$$

όπου, $G(r) = -\frac{1}{4\pi r}$, $r = |\vec{r}|$, $\vec{r} = \vec{x} - \vec{y}$, $\nabla G(r) = \frac{\vec{r}}{4\pi r^3}$ ενώ $D_\omega(t)$ υποδηλώνει το χωρίο του ομόρρου στο οποίο συγκεντρώνεται η στροβιλότητα $\vec{\omega}$. Η καμπύλη $S(t)$ αναπαριστά τα στερεά σύνορα.

2.3.1 Υλοποίηση

Το υπολογιστικό εργαλείο GenUVP αναπτύχθηκε στο εργαστήριο Αεροδυναμικής του ΕΜΠ και είναι βασισμένο στη μέθοδο των συνοριακών στοιχείων συζευγμένη με ένα μοντέλο ομόρρου ελεύθερων στοιχείων στροβιλότητας. Λεπτομερής περιγραφή του εργαλείου μπορεί να βρεθεί στα [38] και [39]. Συνοπτικά αναφέρεται πως για την επίλυση του πεδίου εφαρμόζονται οι συνθήκες μη εισχώρησης στα στερεά σύνορα, η συνθήκη Kutta στην ακμή εκφυγής των ανωστικών σωμάτων, το θεώρημα του Kelvin και η εξίσωση μεταφοράς της στροβιλότητας.

Η πρώτη, εφαρμόζεται σε σημεία ελέγχου πάνω στα τμήματα στα οποία διακριτοποιούνται τα στερεά σύνορα (επιφανειακό πλέγμα) και εξασφαλίζει πως η κάθετη ταχύτητα της σχετικής ροής σε αυτά είναι ίση με το 0. Η μη γραμμική συνθήκη Kutta εξασφαλίζει πώς το πήδημα πίεσης στην ακμή εκφυγής είναι ίσο με το μηδέν και επιλύεται μέσω μιας επαναληπτικής διαδικασίας, ενώ το θεώρημα Kelvin υποδεικνύει την στροβιλότητα (ένταση και διάνυσμα) που αποβάλλεται στον ομόρρου. Τέλος, βάσει της εξίσωσης μεταφοράς της στροβιλότητας, εξασφαλίζεται η εξέλιξη του ομόρρου.

2.4 Ο Eulerian Επιλυτής - MaPFlow

2.4.1 Εξισώσεις Navier-Stokes

Το σύστημα εξισώσεων ολοκληρωμένο σε όγκο Ω με σύνορο $\partial\Omega$ έχει τη μορφή :

$$\frac{\partial}{\partial t} \int_\Omega \vec{U} d\Omega + \oint_{\partial\Omega} (\vec{F}_c dS - \vec{F}_v) dS = \int_\Omega \vec{Q} d\Omega \qquad (2.15)$$

όπου $\vec{U}$,

$$\vec{U} = \begin{pmatrix} \rho \\ \rho u \\ \rho v \\ \rho w \\ \rho E \end{pmatrix} \qquad (2.16)$$

10

το διάνυσμα των συντηρητικών μεταβλητών,
$\vec{F}_c$,

$$\vec{F}_c = \begin{pmatrix} \rho V \\ \rho u V + n_x p \\ \rho v V + n_y p \\ \rho w V + n_z p \\ \rho(E + \frac{p}{\rho})V \end{pmatrix} \tag{2.17}$$

το διάνυσμα των συντηρητικών γενικευμένων παροχών (Convective Fluxes) και $V = \vec{u} \cdot \vec{n}$,
$\vec{F}_v$,

$$\vec{F}_v = \begin{pmatrix} 0 \\ n_x \tau_x x + n_y \tau_x y + n_z \tau_x z \\ n_x \tau_y x + n_y \tau_y y + n_z \tau_y z \\ n_x \tau_z x + n_y \tau_z y + n_z \tau_z z \\ n_x \Theta_x + n_y \Theta_y + n_z \theta_z \end{pmatrix} \tag{2.18}$$

το διάνυσμα των συνεκτικών παροχών (Viscous fluxes) και :

$$\Theta_x = u\tau_{xx} + v\tau_{xy} + w\tau_{xz} + k\frac{\partial T}{\partial x}$$
$$\Theta_y = u\tau_{yx} + v\tau_{yy} + w\tau_{yz} + k\frac{\partial T}{\partial y}$$
$$\Theta_z = u\tau_{zx} + v\tau_{zy} + w\tau_{zz} + k\frac{\partial T}{\partial z}$$

Το σύστημα των εξισώσεων κλείνει με την καταστατική εξίσωση για ιδανικό αέριο:

$$p = (\gamma - 1)\rho[E - \frac{u^2 + v^2 + w^2}{2}] \tag{2.19}$$

Στην παρούσα εργασία, οι παραπάνω εξισώσεις επιλύονται με το MaPFlow. Ο MaPFlow λύνει συμπιεστές ροές στα κέντρα των κελιών ενώ το χωρικό πλέγμα μπορεί να είναι είτε δομημένο είτε μη δομημένο. Οι όροι μεταφοράς διακριτοποιούνται βάσει του προσεγγιστικού επιλύτη Riemann του Roe [40] ενώ χρησιμοποιεί Venkatakrishnan limiter [41],[42]. Οι συνεκτικοί όροι διακριτοποιούνται με ένα κεντρικό σχήμα $2^{ης}$ τάξης. Για την μοντελοποίηση της τύρβης είναι διαθέσιμα δύο μοντέλα. Το πρώτο είναι το μοντέλο του Spalart (SA) [43] καθώς και το μοντέλο δύο εξισώσεων του Menter ($k - \omega$ SST) [44].

Το εργαλείο είναι ικανό να διαχειρίζεται μόνιμες και μη μόνιμες ροές, με τις τελευταίες να αποτελούν απαραίτητη προϋπόθεση για την επίλυση προβλημάτων που περιλαμβάνουν την αεροδυναμική ανάλυση ελικοπτέρων. Η ολοκλήρωση στον χρόνο πραγματοποιείται με ένα άρρητο σχήμα που επιτρέπει μεγαλύτερα χρονικά βήματα. Για τις μη μόνιμες ροές χρησιμοποιείται ένα σχήμα δεύτερης τάξης στον χρόνο σε συνδυασμό με την τεχνική του dual time-stepping [45] για να διασφαλιστεί η ταχύτερη σύγκλιση όταν περιλαμβάνονται περιστρεφόμενες γεωμετρίες και πλεγματικές παραμορφώσεις που δημιουργούν ένα σύνθετο πεδίο ροής. Για την αντιμετώπιση ροών που

11

είναι ασυμπίεστες χρησιμοποιείται ένας πρ-σταθεροποιητής [46] για χαμηλούς αριθμούς Mach. Το εργαλείο περιγράφεται αναλυτικά και με λεπτομέρεια στην διδακτορική διατριβή [36].

2.5 Θεωρεία Γραμμής Δράσης - Υλοποίηση στο MaPFlow

Για την επιτάχυνση των υπολογισμών, τα πτερύγια του ελικοπτέρου στην παρούσα εργασία μοντελοποιούνται ως γραμμές δράσης στο πλαίσιο του MaPFlow οι οποίες συνεισφέρουν με αντίστοιχες δυνάμεις στους όρους πηγής $\boldsymbol{Q}$ της εξίσωσης 2.15. Τα φορτία υπολογίζονται μέσω μίας ανάλυσης στοιχείων πτερύγωσης που εφαρμόζεται κατά μήκος των πτερυγίων και σε συνδυασμό με $2D$ καμπύλες άνωσης-αντλίστασης-ροπής [47]. Τα σημεία ελέγχου πάνω στα πτερύγια καθορίζουν σημεία, τα οποία παράγουν άνωση και αντίσταση ανάλογα με το είδος της αεροτομής, την γωνία στρέψης, το μέγεθος της χορδής και την επαγόμενη ταχύτητα. Με αυτό τον τρόπο σε κάθε σημείο ελέγχου αντιστοιχίζεται ένα διάνυσμα δύναμης. Στην συνέχεια, η άνωση και η αντίσταση υπολογίζονται βάσει της τοπικής ταχύτητας ανέμου και της γωνίας πρόσπτωσης της ροής όπως φαίνεται σχήμα 2.1 και περιγράφεται απο τις ακόλουθες εξισώσεις:
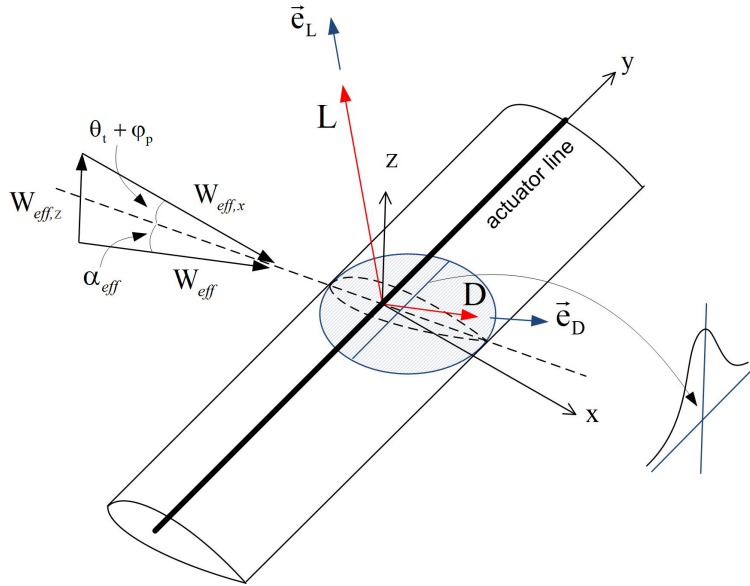
Σχήμα 2.1: Blade element analysis

$$\phi = arctan\frac{W_{eff,z}}{W_{eff,x}} \tag{2.20}$$

12

$$a_{eff} = \phi - \theta_t - \phi_p \tag{2.21}$$

$$L = \frac{1}{2}\rho W_{eff}^2 C_L(a_{eff})c\Delta r, D = \frac{1}{2}\rho W_{eff}^2 C_D(a_{eff})c\Delta r \tag{2.22}$$

$$\vec{f}_{cp} = L\vec{e}_L + D\vec{e}_D \tag{2.23}$$

όπου, ϕ είναι η γωνία της επερχόμενης στο στοιχείο ροής, θ_t είναι η γωνία συστροφής, ϕ_p είναι η γωνία pitch το πτερυγίου, a_{eff} είναι η φαινόμενη γωνία πρόσπτωσης, $C_L(a_{eff})$ και $C_D(a_{eff})$ είναι οι συντελεστές άνωσης και αντίστασης, ρ είναι η πυκνότητα του ρευστού, W_{eff} είναι η τοπική διδιάσταση επαγόμενη ταχύτητα, c είναι η μέση χορδή του στοιχείου, Δr είναι το μήκος του στοιχείου, και $\vec{e}_L$, $\vec{e}_D$ είναι τα διανύσματα βάσης στην κατεύθυνση της άνωσης και της αντίστασης αντίστοιχα.

Οι παραπάνω δυνάμεις μεταφέρονται στο MaPFlow σαν όροι πηγής στην εξίσωση διατήρησης της ορμής και της ενέργειας στα κελιά του πλέγματος τα οποία σαρώνει το κάθε πτερύγιο στην διάρκεια της περιστροφής του και κατανέμονται στον χώρο χρησιμοποιώντας μια $3D$ Gaussian κατανομή [48].

2.6   Ο Υβριδικός επιλυτής - HoPFlow

Ο υβριδικός επιλυτής HoPFlow βασίζεται στην σύζευξη της Lagrangian διατύπωσηω των πεδιακών εξισώσεων με την Eulerian. Η μέθοδος αναπτύχθηκε στο εργαστήριο Αεροδυναμικής του ΕΜΠ στα πλαίσια προηγούμενης διδακτορικής διατριβής [36] ,όπου και υπάρχει η αναλυτική περιγραφή της μεθόδου.
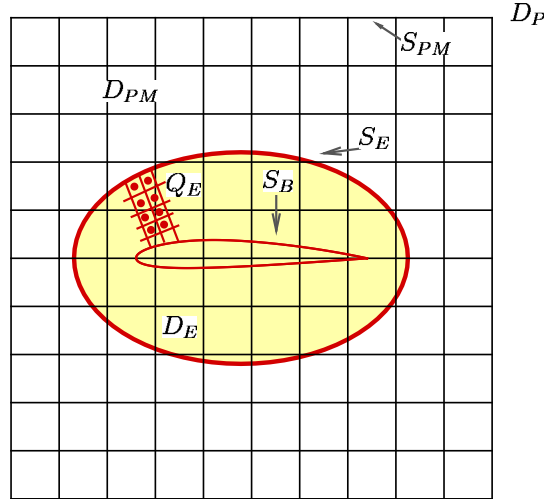
Σχήμα 2.2:   Σχηματική αναπαράσταση των επικαλυπτόμενων χωρίων D_{PM} του Particle Mesh και D_E του MaPFlow.

2.6.1 Η διαδικασία της σύζευξης

Στο Σχήμα 2.2 φαίνεται η γενική ιδέα πίσω από την υπολογιστική διαδικασία της με-
θόδου. Το υπολογιστικό χωρίο D_P έχει διαχωριστεί σε δύο επικαλυπτόμενα υποχωρία
α) το Eulerian D_E και β) το Lagrangian D_{PM}. Στο D_E εφαρμόζεται το εργαλείο
MaPFlow και με αυτό τον τρόπο οι οριακές συνθήκες στο όριο του σώματος S_B
ικανοποιούνται με ακρίβεια. Λόγω της περιορισμένης έκτασης του χωρικού πλέγμα-
τος του χωρίου D_E, οι οριακές συνθήκες στο εξωτερικό σύνορο S_E δεν μπορούν να
ταυτίζονται πλέον με τις συνθήκες του απείρου. Για αυτό τον λόγο η πληροφορία
στην S_E προκύπτει έπειτα από παρεμβολή της λύσης του Particle Mesh στην S_E.
Με αυτό τον τρόπο επιτυγχάνεται η σύζευξη των δύο εργαλείων. Ωστόσο, επειδή τα
δύο χωρία είναι ανεξάρτητα μεταξύ τους, πρέπει να οριστεί ορθά η επικοινωνία μεταξύ
τους ώστε οι λύσεις που προκύπτουν να είναι συνεχείς.

Για μία δεδομένη χρονική στιγμή $t = n \cdot dt$, τα στοιχεία έχουν τις εξής ιδιότητες:
$\{\vec{Z}_p^n, m_p^n, V_p^n, \vec{\Omega}_p^n, \Theta_p^n, \Pi_p^n\}$

Με την χρήση του Particle Mesh και την επίλυση της Poisson υπολογίζεται το
πεδίο ταχύτητας. Με το διάνυσμα της ταχύτητας γνωστό και με τις τιμές των στοι-
χείων προβεβλημένες στο πλέγμα του PM, μπορεί να υπολογιστεί στο PM το δεξί
μέλος των Lagrange εξισώσεων (2.5, 2.6, 2.7, 2.8). Έπειτα, με ένα σχήμα Runge-
Kutta τέταρτης τάξης τα particles εξελίσσονται στον χρόνο οδηγώντας σε μία νέα
κατάσταση:
$\{\vec{Z}_p^{n+1}, m_p^{n+1}, V_p^{n+1}, \vec{\Omega}_p^{n+1}, \Theta_p^{n+1}, \Pi_p^{n+1}\}$

Δεδομένου πως οι Particle Mesh μέθοδοι παρουσιάζουν αδυναμία στον υπολογι-
σμό της λύσης κοντά στα στερεά σύνορα καθώς δεν σέβονται την ακριβή γεωμετρία
των σωμάτων, το σφάλμα κοντά στην S_B είναι αρκετά μεγάλο. Επομένως, ένα τέτοιος
υπολογισμός δεν είναι σίγουρο πως θα ικανοποιεί τις συνθήκες μη εισχώρησης και μη
ολίσθησης. Για αυτό το λόγο, η επίλυση της ροής κοντά στα στερεά σύνορα πραγμα-
τοποιείται με το MaPFlow. Επειδή το σφάλμα μειώνεται εκθετικά με την απόσταση
από την S_B, η έκταση του χωρικού πλέγματος ορίζεται με τέτοιο τρόπο ώστε κοντά
στην S_E το σφάλμα να είναι πολύ μικρό.

Η διαδικασία της σύζευξης περιλαμβάνει α) τον σωστό υπολογισμό των οριακών
συνθηκών στο εξωτερικό σύνορο S_E του D_E, β) την αντικατάσταση των στοιχείων
του PM εντός της D_E και συνεπώς της λύσης με την λύση που έχει υπολογιστεί από
το MaPFlow και γ) με την ομαλή μετάβαση των λύσεων μεταξύ του D_{PM} και D_E.
Για την επίτευξή των παραπάνω χρησιμοποιείται ένα επαναληπτικό σχήμα.
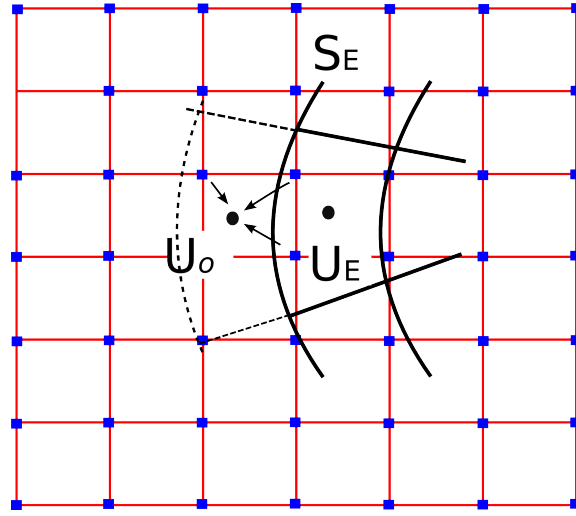
Σχήμα 2.3: Αναπαράσταση υπολογισμού των οριακών συνθηκών στην S_E. Η κατάσταση U_o στο κέντρο του ghost cell (εδώ φαίνεται με την μαύρη διακεκομμένη γραμμή) προκύπτει από την παρεμβολή των τιμών που έχει το PM στους κόμβους (μπλε σημεία).

2.6.2 Υπολογισμός οριακών συνθηκών του CFD στην S_E

Δεδομένου ότι τα πλέγματα του D_{PM} και D_E είναι επικαλυπτόμενα άλλα δεν έχουν κατά ανάγκη κοινούς κόμβους, οι σωστές οριακές συνθήκες στην S_E προκύπτουν με παρεμβολή της λύσης του PM στους κόμβους των εικονικών κελιών του πλέγματος του MaPFlow που τοποθετούνται εκτός της S_E. Στην συνέχεια, η μέση τιμή των κόμβων των ghost cells, καθορίζει την κατάσταση της ροής στα κέντρα των κελιών. Τέλος, οι παροχές διαμέσου της S_E υπολογίζονται μέσω των αναλλοίωτων Riemann που σχετίζονται με το πεδίο εντός και εκτός της S_E. Η παραπάνω διαδικασία περιγράφεται σχηματικά στο Σχήμα 2.3.

2.6.3 CFD *particles*

Η ανανέωση της λύσης του PM εντός της D_E πραγματοποιείται με την αντικατάσταση των PM στοιχείων με τα στοιχεία που προκύπτουν από την λύση του MaPFlow. Αν υποτεθεί πως η λύση του MaPFlow είναι σωστή αν οι οριακές συνθήκες στην S_E είναι σωστές, τότε η επίδραση του σώματος S_B εμπεριέχεται στην λύση του και εν συνεχεία στην στροβιλότητα και συμπιεστότητα του χωρίου. Η σύζευξη επομένως των δύο χωρίων που περιλαμβάνει την αντικατάσταση των PM particles ακολουθεί τα εξής βήματα: α) τον μετασχηματισμό της Eulerian λύσης σε particles, β) την αντικατάσταση όσων particles εμπεριέχονται στο χωρίο D_E με αυτά που δημιουργήθηκαν

15

στο πρώτο βήμα (Σχήμα 2.4). Επειδή το MaPFLow είναι δομημένο με τρόπο ώστε οι μεταβλητές του προβλήματος να υπολογίζονται στα κέντρα των κελιών, το πρώτο βήμα περιλαμβάνει: την χρήση το θεωρήματος Green–Gauss για τον υπολογισμό των θ και $\vec{\omega}$ στους κόμβους του πλέγματος, την παρεμβολή των ρ και p από τα κέντρα των κελιών του CFD στους κόμβους και τέλος τον διαμοιρασμό της πεδιακής πληροφορίας από τους κόμβους των κελιών σε σταθερές θέσεις εντός κάθε κελιού όπως φαίνεται στο Σχήμα 2.4. Είναι πολύ σημαντικό για την υπολογιστική ευστάθεια του σχήματος να υπάρχει καλή χωρική κατανομή της πληροφορίας και για αυτό τον λόγο παραπάνω από ένα partcles δημιουργούνται σε κάθε κελί του CFD.
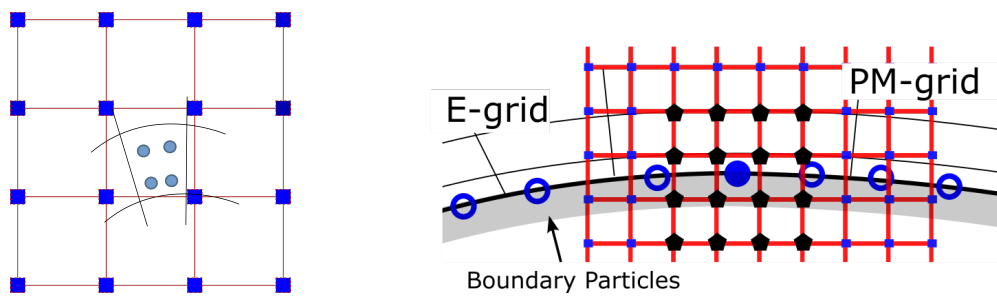

Figure 2.4:   Χωρική κατανομή των Eulerian E- particles. Αριστερά: Ένα Eulerian κελί εντός του πλέγματος του PM έκτασης 4x4 κελιών. Υπάρχουν τέσσερα P_E particles μέσα στο E-cell που φαίνονται με μπλε χρώμα. Δεξιά: Φαίνεται ένα κομμάτι των πλεγμάτων κοντά στο στερεό σύνορο. Πάνω στην S_B, παράγονται επιφανειακά particles που έχουν μπλε χρώμα. Οι μαύροι κόμβοι αντιπροσωπεύουν τους κόμβους του PM που προβάλλεται το επιφανειακό particle του σχήματος.

Ο τελικός στόχος όπως αναφέρθηκε είναι η αντικατάσταση της λύσης του PM με την λύση του CFD. Για αυτό τον λόγο, τα particles του PM που βρίσκονται εντός της D_E πρέπει να αντικατασταθούν με αυτά που δημιουργήθηκαν από την προηγούμενη διαδικασία που περιλαμβάνουν την σωστή πληροφορία για το πεδίο ροής κοντά στο στερεό. Αυτό προϋποθέτει την διαγραφή της προβεβλημένης πληροφορίας που προϋπάρχει στους κόμβους του PM. Στην συνέχεια προβάλλεται στους κόμβους η πληροφορία από τα E-particles στους κόμβους του PM (2.5). Η διαδικασία αυτή ωστόσο, ενέχει τον κίνδυνο να συμπεριληφθεί επιπλέον πληροφορία του πεδίου στους κόμβους για δύο βασικούς λόγους. Πρώτον, όπως αναφέρθηκε και προηγουμένως, τα δύο πλέγματα δεν είναι κατ΄ ανάγκη όμοια και δεύτερον, η επαναληπτική διαδικασία που ακολουθείται μέχρι να υπάρξει σύγκλιση της λύσης του CFD δημιουργούν ένα σφάλμα που πρέπει να εξαλειφθεί.

Όπως φαίνεται στο Σχήμα 2.2 στην πλειονότητα των περιπτώσεων, στο τέλος κάθε χρονικού βήματος, τα Lagrangian particles αναδιανέμονται στα κέντρα ή στους κόμβου του καρτεσιανού πλέγματος του PM. Αντίθετα, τα CFD particles σχηματίζονται

16

σε όλο τον όγκο των κελιών του Eulerian πλέγματος και μάλιστα, τα δύο αυτά πλέγματα δεν έχουν την ίδια δομή. Επιπλέον σε περιπτώσεις περιστρεφόμενων σωμάτων, οι σχετικές θέσεις διαρκώς αλλάζουν. Για να αποφευχθεί η ασυνέχεια της λύσης των διαφορετικών πλεγμάτων, μία μέθοδος διορθώσεις του σφάλματος πραγματοποιείται κατά την διάρκεια των εσωτερικών επαναλήψεων του MaPFlow. Στο Σχήμα 2.2, οι κόκκινες τελείες αντιπροσωπεύουν τους κόμβους του PM που βρίσκονται εντός του D_E που περιγράφεται από την κόκκινη καμπύλη. Ωστόσο, για τα particles τα οποία βρίσκονται κοντά στο σύνορο και εάν υποτεθεί πως χρησιμοποιείται συνάρτηση προβολής δεύτερης τάξης, πληροφορία θα προβληθεί και εκτός του Eulerian χωρίου (βλέπε τους κόμβους με το πράσινο χρώμα στο Σχήμα 2.2). Κατά την διαδικασία της αντικατάστασης επομένως, η προβολή στο πλέγμα του συνόλου των Eulerian particles Q_E Θα δημιουργήσει μία ασυνέχεια που θα αφορά την περιοχή που βρίσκεται κοντά στο σύνορο του Eulerian χωρίου. Η διόρθωση αυτής της παράβασης επιτυγχάνεται με το εξής τρόπο. Η ήδη προβεβλημένη πληροφορία Q_{PM} των Lagrangian particles, παρεμβάλλεται στις θέσεις των CFD particles P_E και στην συνέχεια ξανά προβάλλεται στο PM στις θέσεις X_{PM}. Η διαδικασία αυτή ονομάζεται error του PM και αναπαριστά το αριθμητικό σφάλμα στους κόμβους.

Οι παρακάτω εξισώσεις περιγράφουν με ακρίβεια το σχήμα το οποίο ακολουθείται:

$$error\{Q_{PM}\}_{PM} = Projection\{Interpolation\{Q_{PM}\}_{P_E}\}_{PM} \qquad (2.24)$$

όπου, Q_{PM} είναι η προβεβλημένη πληροφορία των Lagrangian particle Q_P με όγκο V_P.

Επομένως, η σωστή πληροφορία στους κόμβους λαμβάνεται εάν αφαιρεθεί το $error$ από το Q_{PM} και προστεθεί η προβεβλημένη πληροφορία των CFD particle Q_{CFD} με όγκο V_{CFD}:

$$Q_{PM} = Projection\{Q_P\}_{PM} \qquad (2.25)$$

$$Q_E = Projection\{Q_{CFD}\}_{PM} \qquad (2.26)$$

$$correct\{Q_{PM}\} = Q_{PM} - error\{Q_{PM}\}_{PM} + Q_E \qquad (2.27)$$

17
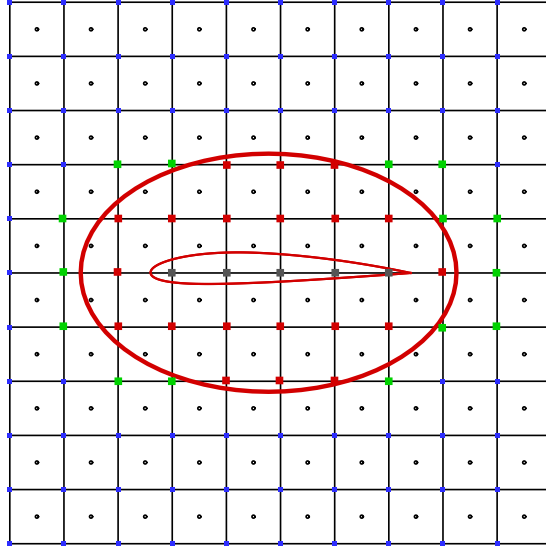
Σχήμα 2.5: Σχηματική περιγραφή της διαδικασίας προβολής στο πλέγμα του PM και της γέννεσης του error στους κόμβους.

Όπως παρατηρείται στο Σχήμα 2.2, το *error* αναμένεται να παρουσιάζει τιμές στα όρια της S_E. Πράγματι, η εφαρμογή της εξίσωσης 2.27 κατά μήκος όλου του υπολογιστικού χωρίου δίνει:

$$correct\{Q_{PM}\} = Q_{PM}, \qquad \text{έξω από την} \quad S_E \qquad (2.28)$$

$$correct\{Q_{PM}\} = Q_E, \qquad \text{μέσα από την} \quad S_E \qquad (2.29)$$

$$correct\{Q_{PM}\} = Q_{PM} - error\{Q_{PM}\}_{PM} + Q_E, \qquad \text{κοντά στην} \quad S_E \qquad (2.30)$$

Επειδή η προβεβλημένη πληροφορία σε κόμβους του PM οι οποίοι βρίσκονται εντός των στερεών συνόρων δεν έχει κάποιο φυσικό νόημα, μία παρόμοια διαδικασία χρησιμοποιείται για την διόρθωση της λύσης. Στο Σχήμα 2.2 στους κόμβους με το γκρι χρώμα δίνεται μηδενική τιμή τόσο για τα Q_P όσο και για το *error*. Μία ακόμα υπολογιστική λεπτομέρεια έγκειται στον τρόπο με τον οποίο υπεισέρχεται η παρουσία των σωμάτων στον Lagrangia επιλυτή. Στις particle μεθόδους, η παρουσία των σωμάτων αναπαρίσταται από επιφανειακά particles τα οποία τοποθετούνται όπως δηλώνει και η ονομασία τους στην επιφάνεια του σώματος. Οι επιφανειακοί όροι υπολογίζονται στα πλαίσια του MaPFlow με όμοιο τρόπο όπως και τα χωρικά particles. Όταν το πεδίο ταχύτητας έχει υπολογισθεί μέσω του PM τότε, αυτοί οι όροι αφαιρούνται από το πλέγμα του PM καθώς αναπαριστούν την προσδεδεμένη στροβιλότητα και δεν πρέπει να εξελιχθούν στον χρόνο.

2.6.4   Ο αλγόριθμος του HoPFlow

Για ένα δεδομένο σύνολο Particles: $\{\vec{Z}_p^n, m_p^n, V_p^n, \vec{\Omega}_p^n, \Theta_p^n, \Pi_p^n\}$ την χρονική στιγμή $t = n\Delta t$, ο επιλυτής ακολουθεί τα επόμενα στάδια:

Βήμα 1:   Προβολή των $\{m_p^n, \Theta_p^n, \vec{\Omega}_p^n, \Pi_p^n\}$ στο PM πλέγμα:
$\rho_{ijk}^n, \theta_{ijk}^n, \vec{\omega}_{ijk}^n, \varepsilon_{ijk}^n$.

Βήμα 2:   Λύση των $\nabla^2\phi = \theta, \nabla^2\vec{\psi} = -\vec{\omega}$ και υπολογισμός των:
$\phi_{ijk}^n, \vec{\psi}_{ijk}^n, \vec{u}_{ijk}^n, \vec{w}_{ijk}^n$

Βήμα 3:   Καθορισμός των οριακών συνθηκών του CFD στην S_E

Βήμα 4:   Ανανέωση της CFD λύσης (dual step επαναλήψεις)

Βήμα 5:   Αντικατάσταση των PM particles με τα CFD με την μέθοδο
του *error*.

Βήμα 6:   Αν το CFD έχει συγκλίνει συνέχισε, αλλιώς πήγαινε στο βήμα 2

Βήμα 7:   Υπολογισμός του δεξιού μέλους των εξισώσεων (2.5)
στο πλέγμα του PM, $\nabla\rho_{ijk}^n, \nabla p_{ijk}^n, \nabla\vec{u}_{ijk}^n$

Βήμα 8:   Παρεμβολή της υπολογισμένης πληροφορίας στο πλέγμα q_{ij}^n πίσω
στις θέσεις των particles: $q_p^n = \sum_{ijk} q_{ijk}^n W(\vec{x}_{ijk} - \vec{Z}_p)$

Βήμα 9:   Ολοκλήρωση της εξίσωσης(2.5) στον χρόνο με $4^{\eta\varsigma}$ τάξης
Runge-Kutta: $\{\vec{Z}_p^{n+1}, m_p^{n+1}, V_p^{n+1}, \vec{\Omega}_p^{n+1}, \Theta_p^{n+1}, \Pi_p^{n+1}\}$

Βήμα 10:   Re-mesh για να υπάρξει αλληλοεπικάλυψη particles
που θα οδηγήσει σε αλληλοεπικάλυψη πυκνότητας και μάζας

This page intentionally left blank.

Κεφάλαιο 3

Ανάλυση του προβλήματος της αλληλεπίδρασης δρομέα ελικοπτέρου με το έδαφος και με εμπόδιο

Σε αυτό το κεφάλαιο πραγματοποιείται η ανάλυση της αλληλεπίδρασης ενός ελικοπτέρου με το έδαφος και με εμπόδια. Αρχικά, παρουσιάζονται οι πειραματικές διατάξεις που μελετήθηκαν υπολογιστικά καθώς και οι υπολογιστικές λεπτομέρειες της προσομοίωσής τους από τα εργαλεία που αναπτύχθηκαν. Στην συνέχεια, η κάθε περίπτωση αναλύεται ξεχωριστά και εξάγονται συμπεράσματα για το εκάστοτε πρόβλημα.

3.1   Πειραματικές διατάξεις και υπολογιστικές λεπτομέρειες

Η μελέτη της αλληλεπίδρασής ελικοπτέρου και στερεών συνόρων βασίστηκε τόσο σε πειραματικές μετρήσεις που διεξήχθησαν σε διάφορα πανεπιστήμια και ερευνητικά κέντρα όσο και σε υπολογιστικές προσομοιώσεις με τα εργαλεία GenUVP και HoPFlow. Σε αυτή την παράγραφο περιγράφονται οι πειραματικές διατάξεις και παρουσιάζονται λεπτομέρειες που αφορούν τις προσομοιώσεις. Για την καλύτερη κατηγοριοποίηση του προβλήματος, οι περιπτώσεις που εξετάστηκαν χωρίζονται ως εξής:

Εξεταζόμενες Περιπτώσεις

- *OGE*: Πτήση αιώρησης εκτός της επίδρασης του εδάφους

- *IGE*: Πτήση αιώρησης υπό την επίδραση του εδάφους

- *T1*: Πτήση αιώρησης πάνω από το εμπόδιο μεταβάλλοντας την θέση του δρομέα κατά τον x άξονα

- *T2*: Πτήση αιώρησης πάνω από το εμπόδιο μεταβάλλοντας την θέση του δρομέα κατά τον z άξονα

- *T3*: Πτήση αιώρησης δίπλα από το εμπόδιο μεταβάλλοντας την θέση του δρομέα κατά τον z άξονα

3.1.1 Ανάλυση πειραματικών διατάξεων

Τα πειράματα που παρουσιάζονται διεξήχθησαν στο πλαίσιο του προγράμματος Garteur από το Πανεπιστήμιο του Μιλάνο (Polimi) [3], από το Πανεπιστήμιο της Γλασκόβης (Gasgow) και από το ερευνητικό κέντρο ONERA της Γαλλίας. Οι μετρήσεις πραγματοποιήθηκαν στις αντίστοιχες σήραγγες και αφορούν δρομείς και εμπόδια που παρουσιάζουν πολλές ομοιότητες όμως είναι διαφορετικά προκειμένου να ελεγχθεί η συνέπεια των συμπερασμάτων που προκύπτουν.

α) Το πείραμα του Polimi

Το πείραμα αφορά σε πτήση αιώρησης ελικοπτέρου κοντά σε εμπόδιο το οποίο έχει τοποθετηθεί στο έδαφος, ενώ η θέση του δρομέα μεταβάλλεται κάθετα ή οριζόντια σε σχέση με το εμπόδιο (βλέπε Σχήμα 3.2. Επίσης, πραγματοποιήθηκαν μετρήσεις που αφορούν μόνο την επίδραση του εδάφους στην απόδοση του δρομέα όπως φαίνεται στο Σχήμα 3.1. Τα αποτελέσματα που παρουσιάζονται (μεταβολές στην ώση και την ροπή και πεδίο ταχυτήτων) αφορούν τις περιπτώσεις που δεν υπήρχε άνεμος. Στο πίνακα 3.1 παρουσιάζονται τα χαρακτηριστικά του δρομέα και του εμποδίου.

Πίνακας 3.1: Παράμετροι του πειραματικού μοντέλου (Polimi)

Χαρακτηριστικά	Δρομέας Polimi
Ύψος εμποδίου (z-άξονας)	0.45 m
Πλάτος εμποδίου (y-άξονας)	1 m
Μήκος εμποδίου (x-άξονας)	0.8 m
Διάμετρος δρομέα	0.75 m
Αριθμός πτερυγίων	4
Χορδή	32 mm
Αεροτομή	NACA0012
Γωνία	10°
Ταχύτητα περιστροφής	2580 RPM (39.25 Hz)
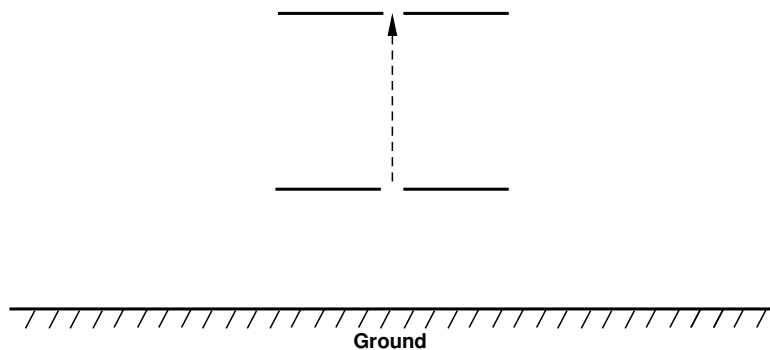
Σχήμα 3.1: Αναπαράσταση της περίπτωσης IGE για τον δρομέα του Polimi. Το κέντρο του δρομέα μεταβάλει την θέση του μεταξύ $Z/R = 1 - 4$.
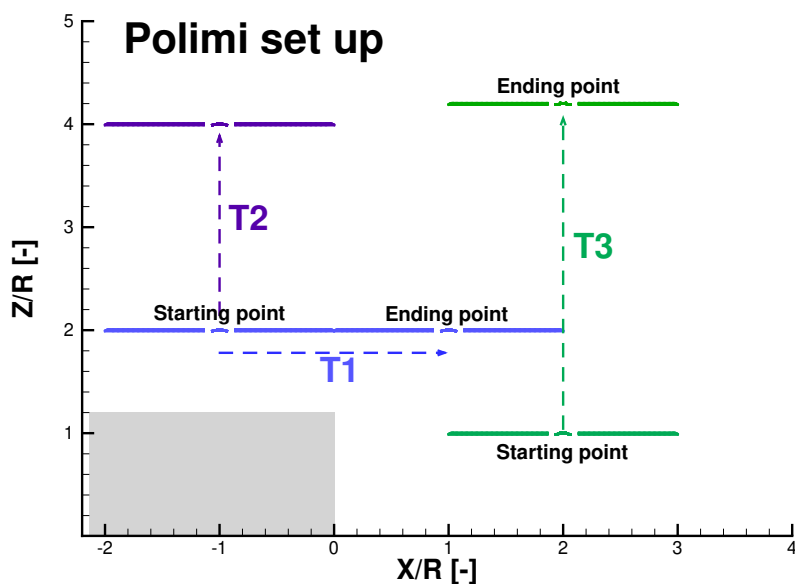
Σχήμα 3.2: Αναπαράσταση των περιπτώσεων T1 (μπλε), T2 (μοβ) και T3 (πράσινο) του Polimi

Τα αποτελέσματα των μετρήσεων έχουν προκύψει παίρνοντας την μέση τιμή της χρονοσειράς κατά τα 5 τελευταία δευτερόλεπτα της προσομοίωσης. Οι μετρήσεις των πεδίων ταχύτητας (PIV) είναι ο μέσος όρος από 400 εικόνες που καταγράφηκαν κατά την τελευταία περίοδο των πειραμάτων.

23

β)Το πείραμα της ONERA

Η ONERA πραγματοποίησε μετρήσεις για έναν δίπτερο δρομέα 3.2 που πραγματοποιεί πτήση αιώρησης κοντά στο έδαφος σε μία περιοχή που περιβάλλεται περιμετρικά από τοίχους όπως φαίνεται στο Σχήμα 3.3. Το ελικόπτερο τοποθετήθηκε στο κέντρο μεταξύ των τοίχων και μετρήθηκε το κατά πόσο επηρεάζει η συγκεκριμένη διάταξη την πτήση του ελικοπτέρου σε συνάρτηση με την απόστασή του από το έδαφος. Οι λεπτομέρειες της διάταξης φαίνονται στον Πίνακα 3.2

Πίνακας 3.2: Παράμετροι του πειραματικού μοντέλου (ONERA)

| Χαρακτηριστικά	Δρομέας ONERA
Ύψος εμποδίου (z-άξονας)	0.36 m
Πλάτος εμποδίου (y-άξονας)	0.3 m
Μήκος εμποδίου (x-άξονας)	0.3 m
Διάμετρος δρομέα	0.71 m
Αριθμός πτερυγίων	2
Χορδή	32 mm
Αεροτομή	NACA0012
Γωνία	8°
Ταχύτητα περιστροφής	2600 RPM (40 Hz)
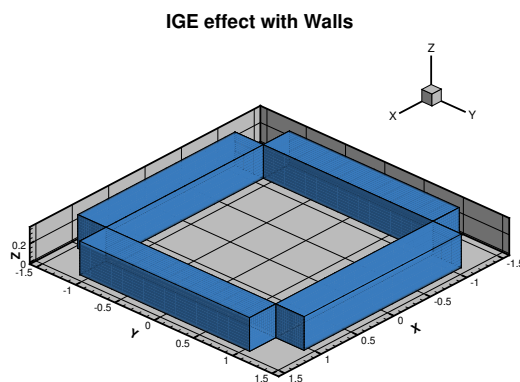
Σχήμα 3.3: Αναπαράσταση της πειραματικής διάταξης της ONERA

Οι μετρήσεις των φορτίων πραγματοποιήθηκαν σε μία περίοδο 15 δευτερολέπτων με συχνότητά δειγματοληψίας 2kHz ενώ οι μετρήσεις PIV είναι αποτέλεσμα μέσου όρου περίπου 5000 εικόνων που καταγράφηκαν σε διάστημα 10 λεπτών.

γ)Το πείραμα του Πανεπιστημίου της Γλασκώβης

Πίνακας 3.3: Παράμετροι του πειραματικού μοντέλου Glasgow

Χαρακτηριστικά	Μεγάλος δρομέας	"Wee" δρομέας
Ύψος εμποδίου (z-άξονας)	1 m	0.3 m
Πλάτος εμποδίου (y-άξονας)	1 m	0.3 μ
Μήκος εμποδίου (x-άξονας)	1 m	0.3 m
Διάμετρος δρομέα	1 m	0.3 m
Αριθμός πτερυγίων	4	2
Χορδή	53 mm	31.7 mm
Αεροτομή	NACA0012	NACA0012
Γωνία	8°	8°
Ταχύτητα περιστροφής	1200 RPM (20 Hz)	4000 RPM (66 Hz)
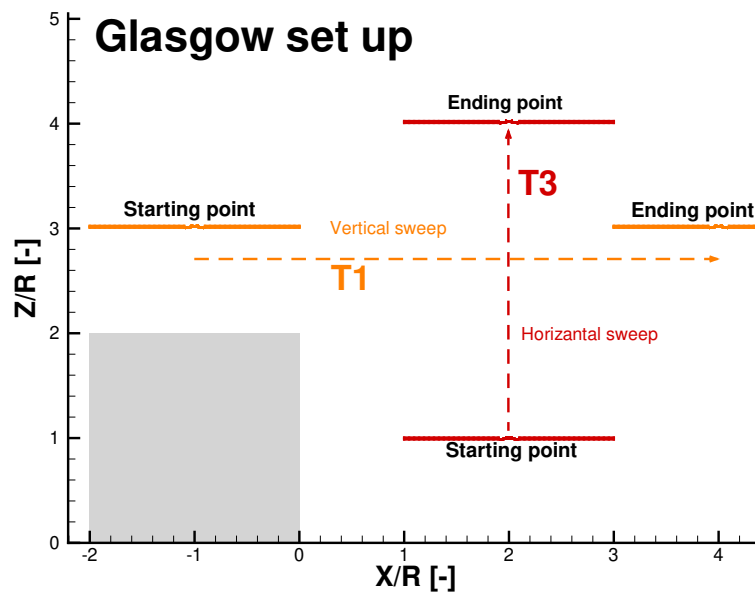
Σχήμα 3.4: Αναπαράσταση των περιπτώσεων T1 (πορτοκαλί) και T3 (κόκκινο) του Glasgow

Το πανεπιστήμιο της Γλασκώβης πραγματοποίησε μία εκτεταμένη διερεύνηση της αλληλεπίδρασης ελικοπτέρου με το έδαφος και με εμπόδιο [4]. Οι λεπτομέρειες της πειραματικής διάταξης παρουσιάζονται στον Πίνακα 3.3. Κατά την διάρκεια του πειράματος μετρήθηκαν οι διακυμάνσεις στα φορτία και οι επαγόμενες ταχύτητες στο

επίπεδο του δρομέα , με την τεχνική του Laser Doppler Anemometry [3] και χρησι-
μοποιώντας τον μεγάλο δρομέα. Ο δρομέας Wee χρησιμοποιήθηκε για την αποτύπωση
του πεδίου ταχύτητας. Τα αποτελέσματα του συγκεκριμένου πειράματος αφορούν τι-
μές που προέκυψαν από τον μέσο όρο 5 επαναλήψεων, 2.5 δευτερολέπτων η κάθε
μία. Στο Σχήμα 3.4 παρουσιάζονται οι περιπτώσεις που εξετάστηκαν στην παρούσα
εργασία.

3.1.2 Υπολογιστικές λεπτομέρειες

Στην παρούσα εργασία, η ανάλυση του προβλήματος, πραγματοποιήθηκε εκτός των
άλλων και με αποτελέσματα υπολογιστικών προσομοιώσεων δύο διαφορετικών ερ-
γαλείων, του GenUVP και του HoPFLow. Στον Πίνακα 3.4 παρουσιάζονται τα
υπολογιστικά εργαλεία που χρησιμοποιήθηκαν στην εκάστοτε περίπτωση.

Πίνακας 3.4: Εργαλεία που χρησιμοποιήθηκαν για την προσομοίωση των πει-
ραμάτων

Περίπτωση	Υπολογιστικό εργαλείο	Πείραμα
OGE	GenUVP	Polimi, Onera, Glasgow
	HoPFlow	Polimi, Glasgow
IGE	GenUVP	Polimi, Onera
	HoPFlow	Polimi
T1	GenUVP	Polimi, Glasgow
	HoPFlow	Polimi
T2	GenUVP	Polimi
	HoPFlow	Polimi
T3	GenUVP	Polimi, Glasgow
	HoPFlow	Glasgow

Υπολογιστικές λεπτομέρειες στον GenUVP

Οι μέθοδος των συνοριακών στοιχείων, δεν απαιτεί την δημιουργία χωρικού πλέγμα-
τος, αντίθετα το πλέγμα τοποθετείται στις επιφάνειες των σωμάτων. Στην παρούσα
διατριβή, τα πτερύγια προσομοιώνονται σαν λεπτές ανωστικές επιφάνειες με επιφα-
νειακές κατανομές διπόλων. Τα εμπόδια προσομοιώθηκαν σαν μη ανωστικά σώμα-
τα με πάχος, με επιφανειακές κατανομές πηγών. Στον πίνακα 3.5 παρουσιάζονται
η επιφανειακή διακριτοποίηση των σωμάτων για κάθε πείραμα καθώς και η χρονική
διακριτοποίηση. Τα Σχήματα 3.5 και 3.6 δείχνουν την διακριτοποίηση για δύο τυπι-
κές περιπτώσεις. Η προσομοίωση του εδάφους πραγματοποιείται με την μέθοδο του
αντικατοπτρισμού.

Πίνακας 3.5: Υπολογιστική διακριτοποίηση των πτερυγίων με τον GenUVP

Περίπτωση	Πλέγμα	Χρονικό βήμα
OGE (Polimi, Glasgow, Onera)	9x21	4°
IGE (Polimi, Onera)	9x21	4°
T1 (Polimi, Glasgow)	9x21	4°
T2 (Polimi)	9x21	4°
T3 (Polimi, Glasgow)	9x21	4°
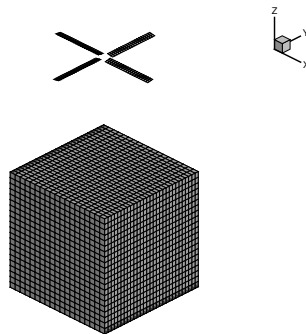
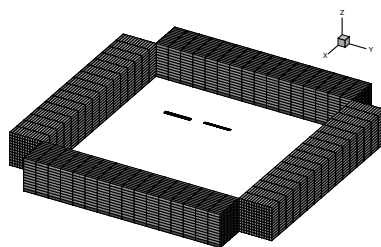

Σχήμα 3.5: Παράδειγμα επιφανειακής διακριτοποίησης των πτερύγων και του εμποδίου για τις περιπτώσεις του Polimi, Glasgow

Πίνακας 3.6: Υπολογιστική διακριτοποίηση των εμποδίων με τον GenUVP

Περίπτωση	Πλέγμα	Χρονικό βήμα
IGE (Onera)	31x31x21	4°
T1 (Polimi, Glasgow)	31x31x21	4°
T2 (Polimi)	31x31x21	4°
T3 (Polimi, Glasgow)	31x31x21	4°

Λαμβάνοντας υπόψιν το υπολογιστικό κόστος, ο χρόνος των προσομοιώσεων για τις περιπτώσεις OGE ήταν 10 περιστροφές του δρομέα όπου και παρατηρήθηκε η σύγκλιση των φορτίων. Για τις υπόλοιπες περιπτώσεις, ο χρόνος δεν ήταν ο ίδιος και παρατηρήθηκε ότι για την σύγκλιση των φορτίων σε μία περιοδική λύση απαιτούνται τουλάχιστον 40 περιστροφές του δρομέα. Στην πράξη, και για την σωστή πρόλεξη του πεδίου ταχυτήτων, πραγματοποιήθηκαν 80 περιστροφές. Τα αποτελέσματα που παρουσιάζονται αφορούν τον μέσο όρο των τιμών κατά το διάστημα από την $41^η$ έως την $80^η$ περιστροφή.

27

Σχήμα 3.6: Παράδειγμα επιφανειακής διακριτοποίησης των πτερύγων και του εμποδίου για την περίπτωση της ONERA

Υπολογιστικές λεπτομέρεις στο HoPFlow

Στις προσομοιώσεις με το HoPFlow, τα πτερύγια αναπαρίστανται με την μέθοδο της γραμμής δράσης για την μείωση του υπολογιστικό κόστους. Σε αυτή την κατεύθυνση, ένα χωρικό κυλινδρικό πλέγμα σε σχήμα σταυρού αναπτύσσεται γύρω από τα πτερύγια. Το πλέγμα αυτό έχει μέγεθος 1.5 φορές την ακτίνα του πτερυγίου στην ακτινική κατεύθυνση, ενώ στις άλλες δύο εκτείνεται 0.5 φορές την ακτίνα. Στο Σχήμα 3.7 φαίνεται το παραπάνω πλέγμα το οποίο χρησιμοποιήθηκε για τα πειράματα του Polimi και της Γλασκώβης. Οι κόκκινες γραμμές αναπαριστούν τις γραμμές δράσεις οι οποίες έχουν διακριτοποιηθεί με 31 σημεία η κάθε μία.
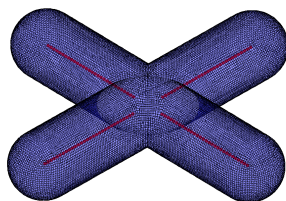
Σχήμα 3.7: Το πλέγμα του CFD για το πτερύγια. Με κόκκινες γραμμές φαίνονται οι θέσεις των πτερυγίων.

Εκτός του περιστρεφόμενου πλέγματος που περικλείει τα πτερύγια, στις περιπτώσεις που υπάρχει το έδαφος και το εμπόδιο, αναπτύσσεται και ένα χωρικό πλέγμα πάνω από τα στερεά σύνορα αυτών (Σχήμα 3.8. Το πλέγμα εκτείνεται 0.5 φορές την ακτίνα του δρομέα έτσι ώστε το οριακό στρώμα που αναπτύσσεται να περιλαμβάνεται πλήρως μέσα στο χωρίο του CFD. Το πρώτο κελί έχει ύψος $2 * 10^{-4}$ μέτρα και η ροή θεωρείται στρωτή. Σε κάποιες από τις προσομοιώσεις, συμπεριλήφθηκε και η άτρακτος του ελικοπτέρου, επομένως αναπτύχθηκε και ένα τρίτο ανεξάρτητο πλέγμα γύρω από αυτή (Σχήμα 3.9. Λεπτομέρειες σχετικά με τον αριθμό των κελιών φαίνονται στον Πίνακα 3.7.
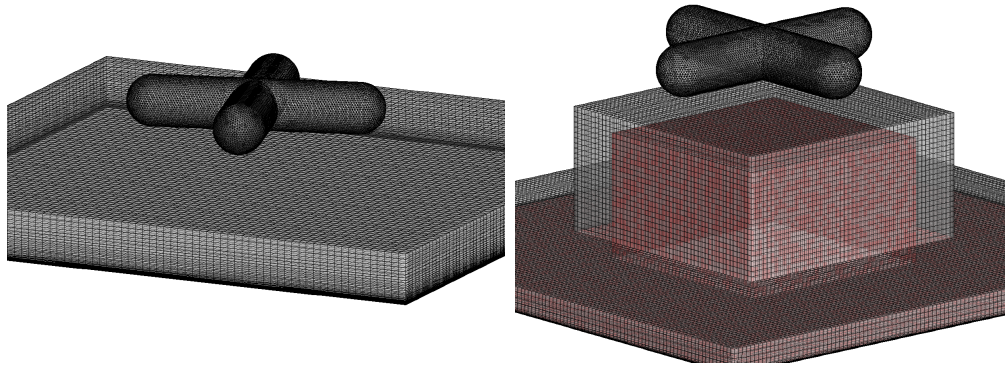
(α΄) Το πλέγμα CFD στην περίπτωση (β΄) Το πλέγμα CFD στην περίπτωση
IGE.   T1,T2,T3.

Σχήμα 3.8: Απεικόνιση του χωρικού πλέγματος που αναπτύσσεται γύρω από
τα πτερύγια του δρομέα και πάνω από τα στερεά σύνορα στις προσομοιώσεις με
HoPFlow χωρίς την παρουσία της ατράκτου.
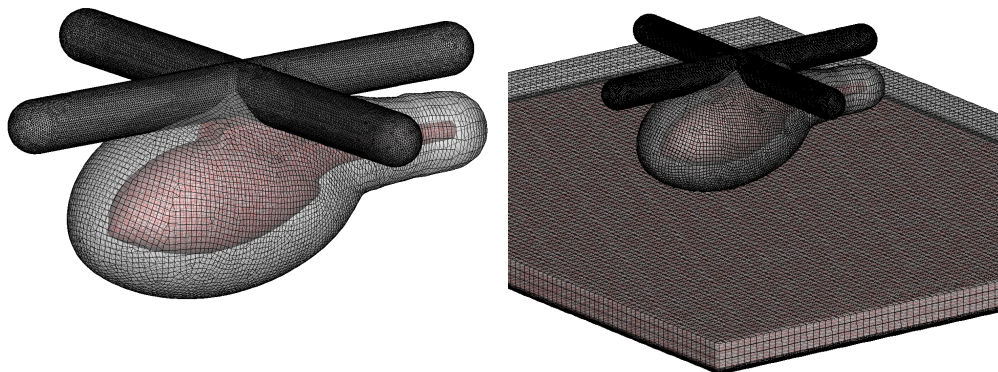
(α΄) Το πλέγμα CFD γύρω από τα πτε- (β΄) Το πλέγμα CFD γύρω από τα πτε-
ρύγια και την άτρακτο του ελικοπτέρου   ρύγια και την άτρακτο του ελικοπτέρου
στην περίπτωση OGE.   στην περίπτωση IGE.

Σχήμα 3.9: Απεικόνιση του χωρικού πλέγματος που αναπτύσσεται γύρω από
τα πτερύγια του δρομέα και πάνω από τα στερεά σύνορα στις προσομοιώσεις με
HoPFlow με την προσθήκη της ατράκτου.

Πίνακας 3.7: Διακριτοποίηση των πλεγμάτων του HoPFlow

Περίπτωση	Δρομέας (κελιά)	Τοίχοι (κελιά)	Άτρακτος (κελιά)
OGE (Polimi, Glasgow)	212000	-	
IGE (Polimi)	212.000	288.000	-
T1 (Polimi)	212.000	1.150.205	-
T2 (Polimi)	212.000	1.150.205	-
T3 (Glasgow)	212.000	602.596	-
OGE (Polimi with fuselage)	1.005.802	-	120.690
IGE (Polimi with fuselage)	1.005.802	507.000	120.690
T1 (Polimi with fuselage)	1.005.802	1.150.705	120.690

3.2 Πτήση αιώρησης εκτός της επίδρασης του εδάφους

Η ανάλυση του προβλήματος της αλληλεπίδρασης δρομέα ελικοπτέρου με στερεά σύνο-ρα εστιάζεται στη καταγραφή των φορτίων του δρομέα ως μεταβολών του συντελεστή ώσης σε σύγκριση με τον αντίστοιχο συντελεστή ώσης που καταγράφηκε σε συνθήκες OGE. Με αυτό τον τρόπο αξιολογείται η επίδραση του εδάφους και του εμποδίου στο δρομέα ως αύξηση η μείωση σε σχέση με την απόδοση του στροφείου μακρυά από το έδαφος. Για αυτό τον λόγο, στις μετρήσεις των πειραμάτων συμπεριλαμβάνονται απο-τελέσματά για τον συντελεστή ώσης εκτός επίδρασης του εδάφους (CT_{OGE}) σύμφωνα με τον οποίο αδιαστατοποιούνται τα υπόλοιπα αποτελέσματα.

Πίνακας 3.8: Πειραματικές μετρήσεις του συντελεστή ώσης σε συνθήκες OGE για τα τρία πειράματα

Πείραμα	Συντελεστής ώσης
Polimi	0.00729
ONERA	0.00379
Glasgow	0.00736

Στον Πίνακα 3.8 παρουσιάζονται οι πειραματικές μετρήσεις. Είναι φανερό πώς ο συντελεστής ώσης του κάθε δρομέα είναι διαφορετικός ως απότοκο των διαφορών που παρουσιάζουν οι δρομείς μεταξύ τους.

Πίνακας 3.9: Υπολογιστικές προλέξεις του συντελεστή ώσης (CT) σε συνθήκες OGE για τα τρία πειράματα

Πείραμα	GenUVP	HoPFlow
Polimi	0.00731	0.00730
Polimi	-	0.00733 (προσομοίωση με την άτρακτο)
ONERA	0.00380	-
Glasgow	0.00735	0.007355

Αντίστοιχα με τα πειράματα, πραγματοποιήθηκαν προσομοιώσεις για την καταγραφή του συντελεστή ώσης. Στο Πίνακα 3.9 φαίνονται οι προλέξεις του GenUVP και του HoPFlow. Μετρήσεις και προλέξεις παρουσιάζουν πολύ μικρές αποκλίσεις και βρίσκονται σε πολύ καλή σύγκριση. Αξίζει να σημειωθεί πως οι προλέξεις του GenUVP και του HoPFlow παρουσιάζουν καλή συμφωνία καθώς ο τρόπος υπολογισμού των φορτίων είναι κοινός και στις δύο μεθόδους. Ακόμα, δεν παρατηρείται ιδιαίτερη διαφορά όταν στην προσομοίωση συμπεριλαμβάνεται και η άτρακτος του ελικοπτέρου για πείραμα του Polimi. Παρατηρείται μόνο μία πτώση της τάξης του 0.4% η οποία ωστόσο κρίνεται ασήμαντη.

3.2.1 Ανάλυση του ροϊκού πεδίου

Στις στροβιλές μεθοδολογίες όπως είναι αυτές που χρησιμοποιούνται στην παρούσα μελέτη, υπάρχει άμεση συσχέτιση μεταξύ του φορτίου που προλέγεται και του ομόρρου που διαμορφώνεται κατά την επίλυση. Για αυτό το λόγο πραγματοποιείται μία διερεύνηση του πεδίου ροής κάτω από τον δρομέα για να τονισθούν οι μηχανισμοί που οδηγούν στην σύγκλιση των φορτίων. Το Σχήμα 3.10 δείχνει ένα στιγμιότυπο όπως αυτό καταγράφηκε από το HoPFlow μετά από 10 περιστροφές για τον δρομέα του Polimi σε OGE συνθήκες χωρίς την άτρακτο. Το σχήμα αποτυπώνει το μέτρο της ταχύτητας σε ένα κατακόρυφο επίπεδο του αξονοσυμμετρικού πεδίου που διέρχεται από το κέντρο του δρομέα. Όπως φαίνεται, σε μία τυπική πτήση αιώρησης σχηματίζεται ένας δακτύλιος στροβιλότητας ο οποίος μετακινείται προς τα κάτω με μία μέση ταχύτητα $3\text{-}4m/s$. Ο δακτύλιος είναι αποτέλεσμα της αλληλεπίδρασης των αρχικών στροβίλων των ακροπτερυγίων. Επιπλέον δημιουργείται μια δέσμη αέρα κάτω από τον δρομέα. Οι ταχύτητες μεταβάλλονται κατά την ακτινική κατεύθυνση και αποκτούν την μέγιστη τιμή τους στο 75-90% την ακτίνας του δρομέα, θέση στην οποία εντοπίζεται και η μεγαλύτερη φόρτιση στο πτερύγιο. Η έλλειψη της ατράκτου οδηγεί στον σχηματισμό μίας περιοχής μηδενικών ταχυτήτων κοντά στην ρίζα των πτερυγίων λόγω της απουσίας αεροδυναμικής φόρτισης σε αυτή την περιοχή. Όταν ο δακτύλιος στροβιλότητας έχει φτάσει περίπου μία διάμετρο κάτω από τον δρομέα, το πεδίο ταχύτητας συγκλίνει στην περιοχή του δρομέα και κατά συνέπεια συγκλίνουν και τα φορτία του δρομέα.
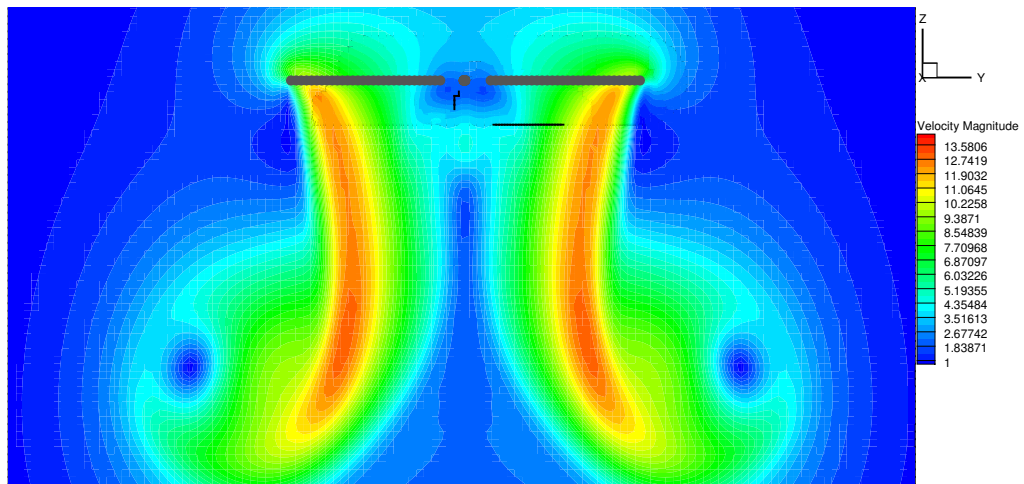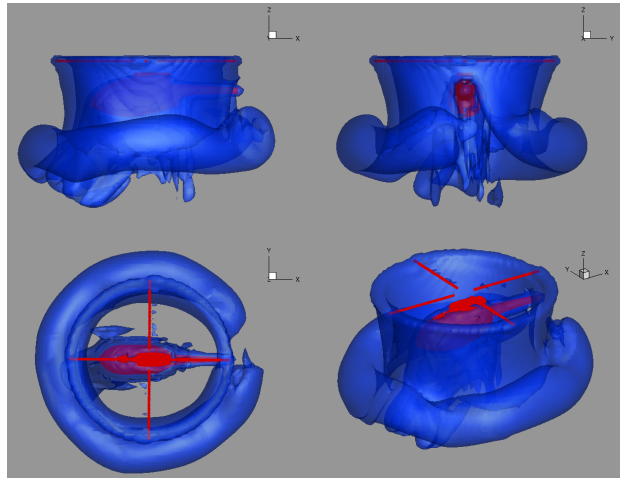
Σχήμα 3.10: Το μέτρο της ταχύτητας (m/s) για συνθήκες OGE όπως αυτό καταγράφηκε από το $HoPFlow$ σε μία αξονο-συμμετρική πλάκα στο $r/R = 0$ για τον δρομέα του $Polimi$ χωρίς την παρουσία της ατράκτου (στιγμιότυπο στο τέλος της 10ης περιόδου).

Αντίστοιχη προσομοίωση πραγματοποιήθηκε με το HoPFlow και για την περίπτω-ση όπου περιλαμβάνεται και η άτρακτος του ελικοπτέρου. Σχήμα 3.11 απεικονίζεται ομόρρους του ελικοπτέρου σε στιγμιότυπο κατά το πέρας της 10ης περιόδου. όπως καταγράφτηκε με το HoPFlow. Σε αντίθεση με την προηγούμενη περίπτωση όπου ο ομόρρους του δρομέα και το πεδίο ταχύτητας παρουσιάζουν αξονο-συμμετρικό χαρα-κτήρα, η παρουσία της ατράκτου μεταβάλλει αυτό το χαρακτηριστικό καθώς εμποδίζει την διαμόρφωση της ροής. Αυτό περιγράφεται καλύτερα και από το πεδίο ταχύτη-τας (μέτρο και διανύσματα) όπως αυτό καταγράφηκε την ίδια χρονική στιγμή σε δύο κατακόρυφα επίπεδα που περνούν από το κέντρο του δρομέα (Σχήμα 3.12 και 3.13.

Η μη συμμετρική ανάπτυξη του ομόρρου αποτυπώνεται στο Σχήμα 3.12. Καθώς η ροή συναντάει το ρύγχος της ατράκτου, επιταχύνεται ανάντι του δρομέα. Αντίθετα, όταν συναντάει την ουραία δοκό παρεμποδίζεται από την παρουσία της. Αυτό έχει σαν αποτέλεσμα ο δακτύλιος που δημιουργείται να μην μετατοπίζεται με την ίδια ταχύτητα και για αυτό το λόγο κατάντι της ροής παραμένει πιο κοντά στον δρομέα. Αντίθετα, στο Σχήμα 3.13 ενώ η ροή εμποδίζεται από την άτρακτο, η συμμετρία της γεωμετρίας σε αυτό τον άξονα οδηγεί σε συμμετρική ροή.

Η αλληλεπίδραση του δρομέα με την άτρακτο όπως φάνηκε και προηγουμένως εμποδίζει την ανάπτυξη αξονο-συμμετρικής ροής. Παράλληλα, η ροή που αναπτύσ-σεται γύρω από την άτρακτο οδηγείται σε αποκόλληση δημιουργώντας ένα διαρκώς μεταβαλλόμενο πεδία στο κάτω μέρος της. Το μέτρο των ταχυτήτων έδειξε πως συ-νολικά η ροή έχει επιβραδυνθεί (μείωση στην μέγιστη τιμή) ωστόσο, η κατανομή των ταχυτήτων στο ακτινικό επίπεδο έχει διευρυνθεί. Αυτός είναι και ο λόγος που ενώ η παρουσία της ατράκτου αλλοιώνει το πεδίο ροής, το ολοκληρωμένο φορτίο του δρομέα δεν μεταβάλλεται ουσιαστικά.

Σχήμα 3.11: Ο ομόρρους του δρομέα του *Polimi* σε συνθήκες *OGE* με την παρουσία της ατράκτου όπως καταγράφτηκε από το *HoPFlow*(ισο-παραμετρική επιφάνεια του μέτρου της στροβιλότητας στο τέλος της 10ης περιόδου).
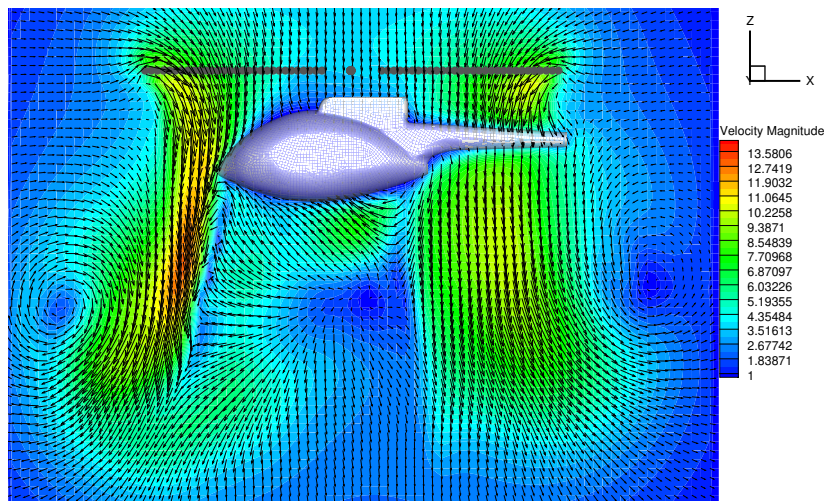
Σχήμα 3.12: Το μέτρο και το διάνυσμα της ταχύτητας (m/s) για συνθήκες *OGE* όπως αυτό καταγράφηκε από το *HoPFlow* σε μία αξονο-συμμετρική πλάκα στο $r/R = 0$ για τον δρομέα του *Polimi* με την παρουσία της ατράκτου (στιγμιότυπο στο τέλος της 10ης περιόδου, πλάγια όψη).
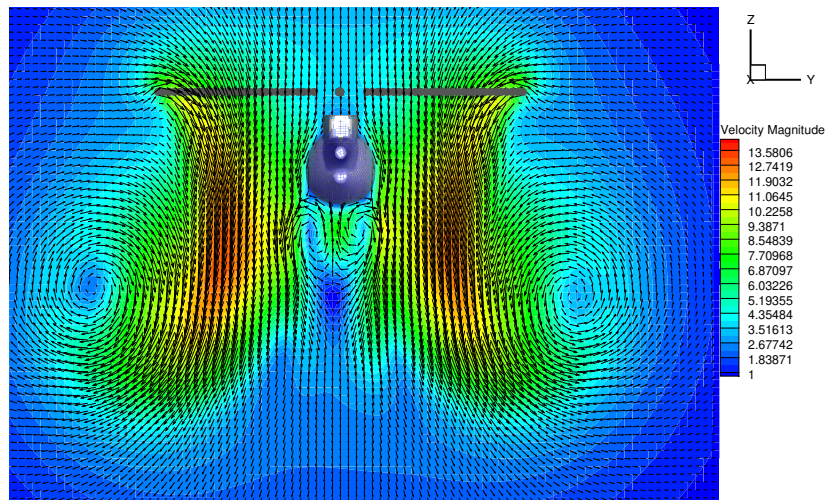
Σχήμα 3.13: Το μέτρο και το διάνυσμα της ταχύτητας (m/s) για συνθήκες OGE όπως αυτό καταγράφηκε από το $HoPFlow$ σε μία αξονο-συμμετρική πλάκα στο $r/R = 0$ για τον δρομέα του $Polimi$ με την παρουσία της ατράκτου (στιγμιότυπο στο τέλος της 10ης περιόδου, πίσω όψη).

Συνοψίζοντας, η πτήση αιώρησης ενός ελικοπτέρου μακρυά από το έδαφος χαρακτηρίζεται από την γρήγορη σύγκλιση των φορτίων καθώς ο ομόρρους του απομακρύνεται ενομπόδιστα από το επίπεδο του δρομέα οδηγώντας σε σύγκλιση του πεδίου ταχυτήτων κοντά σε αυτόν. Οι πειραματικές μετρήσεις από τις 3 διατάξεις συμφωνούν με τις υπολογιστικές προλέξεις του $GenUVP$ και του $HoPFlow$ με πολύ μικρές διαφορές. Ακόμη, διαπιστώθηκε πως η παρουσία της ατράκτου δεν επηρεάζει ουσιωδώς την φόρτιση του δρομέα.

3.3 Απόδοση δρομέα ελικοπτέρου σε συν-θήκες επίδρασης του εδάφους

Η πρώτη περίπτωση αλληλεπίδρασης δρομέα ελικοπτέρου με στερεά σύνορα εντοπίζε-ται στην πτήση αιώρησης κοντά στο έδαφος. Για αυτή την περίπτωση εξετάζεται η επίδραση του εδάφους στον συντελεστή ώσης του δρομέα με σύγκριση πειραματικών δεδομένων και υπολογιστικών προλέξεων του $GenUVP$. Στην συνέχεια εξετάζε-ται η επίδραση της συνεκτικότητας του εδάφους στα αποτελέσματα. Η περίπτωση IGE περιλαμβάνει μετρήσεις του $Polimi$ για την μεταβολή του φορτίου για ύψη από $Z/R = 1 - 4$ και μετρήσεις της $ONERA$ για το σημείο $Z/R = 1$.

3.3.1 Ανάλυση των πειραματικών μετρήσεων και συγκρίσεις με τον GenUVP

Στο Σχήμα 3.14 προλέξεις του κανονικοποιημένου συντελεστή ώσης (CT/CT_{OGE}) σε συνάρτηση με το ύψος της πτήσης αιώρησης από το έδαφος συγκρίνονται με πει-ραματικά δεδομένα. Οι μετρήσεις υποδεικνύουν αύξηση από 12-14.5% στην ώση του δρομέα όταν η πτήση πραγματοποιείται σε ύψος $Z/R = 1$ από το έδαφος. Οι μετρήσεις του $Polimi$ (μαύρα στίγματα) καταγράφουν μία συνεχόμενη μείωση αυτής της αύξη-σης καθώς ο δρομέας απομακρύνεται από το έδαφος ενώ η επίδραση του εδάφους στην φόρτιση αρχίζει να είναι αμελητέα μετά το ύψος $Z/R = 3$ και φθίνει τελείως στο $Z/R = 4$.
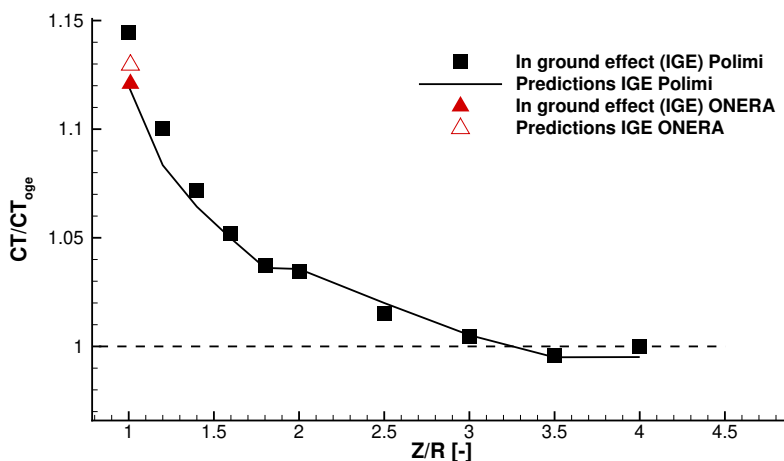
Σχήμα 3.14: Μεταβολές στην ώση του δρομέα σε συνθήκες IGE για τους δρομείς του $Polimi$ και της $ONERA$. Συγκρίσεις μετρήσεων με προλέξεις του $GenUVP$.

Οι προλέξεις του $GenUVP$ βρίσκονται σε πολύ καλή σύγκριση με τις μετρήσεις. Η μαύρη καμπύλη (προλέξεις) αναπαράγει σε ικανοποιητικό βαθμό το φαινόμενο τόσο

σε σχήμα όσο και σε απόλυτες τιμές. Ωστόσο, μετρήσεις και προλέξεις δεν ακολουθούν επακριβώς την αναλυτική λύση για την επίδραση του εδάφους που υποστηρίζει μια μονότονη, εκθετική μείωση της για την πτήση μίας ανωστικής πτέρυγας κοντά στο έδαφος. Περίπου στο ύψος $Z/R = 1.6$ το CT παρουσιάζει μία τοπική επιπεδοποίηση σχηματίζοντας ένα ¨γόνατο¨. Από αυτό το σημείο και για μεγαλύτερα ύψη, οι προλέξεις σχεδόν ταυτίζονται με τις μετρήσεις παρόλο που το υπολογιστικό μοντέλο δεν περιλαμβάνει στις προσομοιώσεις την συνεκτικότητα του εδάφους. Για ύψη μικρότερα από $Z/R = 1.6$ όμως, παρατηρείται μία υπο-εκτίμηση της παραγόμενης ώσης η οποία αυξάνεται καθώς ο δρομέας πλησιάζει το $Z/R = 1$ όπου και αποκτά την μέγιστη τιμή της (περίπου 2.5%). Η διαφορά αυτή αποδίδεται στην έλλειψη συνεκτικών φαινομένων στο έδαφος. Το οριακό στρώμα το οποίο αναπόφευκτα αναπτύσσεται από τις επαγόμενες ταχύτητες του δρομέα, μετατοπίζει την ροή προς τα πάνω μειώνοντας το σχετικό ύψος της αιώρησης. Η παραπάνω αδυναμία της παρούσας μεθόδου αποτυπώνεται στο Σχήμα 3.15 όπου παρουσιάζονται το μέτρο και τα διανύσματα της ταχύτητας σε ένα επίπεδο της αξονοσυμμετρικής ροής στο r/R=0. Η κατανομή της ταχύτητας στο σχήμα αυτό δείχνει πως η ροή κινείται επιταχυνόμενη καθώς πλησιάζει το έδαφος και με αυτό τον τρόπο, οι στρόβιλοι των ακροπτερυγίων απομακρύνονται από τον δρομέα οδηγώντας σε σύγκλιση του φορτίου σε μικρότερα επίπεδα.
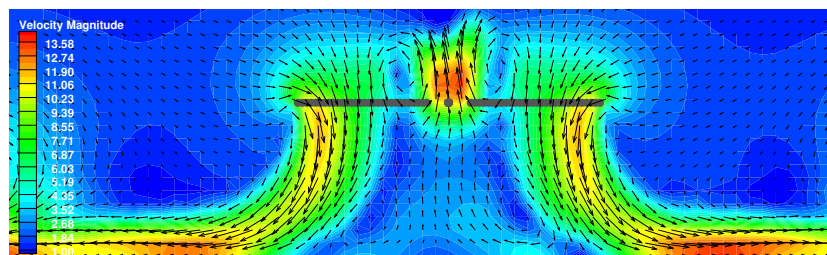
Σχήμα 3.15: Το μέτρο και το διάνυσμα της ταχύτητας (m/s) για συνθήκες IGE όπως αυτό καταγράφηκε από το $HoPFlow$ σε μία αξονοσυμμετρική πλάκα στο $r/R = 0$ για τον δρομέα του $Polimi$ στην θέση $Z/R = 1$ χωρίς την παρουσία της ατράκτου (στιγμιότυπο στο τέλος της 6ης περιόδου, συνθήκη ολίσθησης στο έδαφος).

3.3.2 Διερεύνησή των επιπτώσεων της συνεκτικότητας του εδάφους στα φορτία του δρομέα και την διαμόρφωση του πεδίου

Για την διερεύνηση της σημασίας της προσομοίωσης της συνεκτικότητας στο έδαφος πραγματοποιήθηκαν δύο προσομοιώσεις με το $HoPFlow$ για τον δρομέα του $Polimi$ στην θέση $Z/R = 1$. Η πρώτη επέβαλε στο έδαφος μόνο τη συνθήκη μη εισχώρησης ενώ η δεύτερη επιπλέον και τη συνθήκη μη ολίσθησης. Στην πράξη η πρώτη προσομο-

ίωση δεν επιτρέπει να αναπτυχθούν συνεκτικά φαινόμενα στον τοίχο και ουσιαστικά παραπέμπει στην προσομοίωση με τον $GenUVP$.

Πίνακας 3.10: Σύγκριση πειραματικών μετρήσεων του CT στην θέση $Z/R = 1$ για τον δρομέα του $Polimi$ με προλέξεις του $HoPFlow$

Μετρήσεις	$HoPFlow$ (συνθήκη μη ολίσθησης)	$HoPFlow$ (συνθήκη ολίσθησης)
1.1441	1.149	1.1235

Όπως φαίνεται στον Πίνακα 3.10 όταν δεν εφαρμόζεται η συνθήκη μη ολίσθησης στο έδαφος, τα αποτελέσματα για το CT είναι όμοια με τις προλέξεις του $GenUVP$ και παρουσιάζουν απόκλιση περίπου 2%. Αντίθετα, με την εισαγωγή των συνεκτικών φαινομένων στην προσομοίωση, η απόκλιση μειώνεται ουσιωδώς (περίπου 0.4%). Με αυτό τον τρόπο επιβεβαιώνεται η προηγούμενη εκτίμηση πως η αδυναμία του $GenUVP$ να αναπαραγάγει τα πειραματικά αποτελέσματα σε ύψη αιώρησης μικρότερα του $Z/R =$ 1.7 έγκειται στον μη συνεκτικό χαρακτήρα της μεθόδου.

Ο τρόπος με τον οποίο το οριακό στρώμα που αναπτύσσεται στο έδαφος επηρεάζει την φόρτιση του δρομέα φαίνεται στο Σχήμα 3.16 και 3.17. Το πρώτο παρουσιάζει το πεδίο ταχύτητας σε μία αξονοσυμμετρική πλάκα (στο επίπεδο του PM) που διέρχεται από το κέντρο του δρομέα ($r/R1 = 0$) όπως αυτό έχει αναπτυχθεί μετά από 6 περιστροφές του δρομέα. Η ουσιαστική διαφορά μεταξύ της συνεκτικής και μη συνεκτικής προσομοίωσης (Σχήμα 3.15) εντοπίζεται στην θέση και το σχήμα των στροβίλων των ακροπτερυγίων. Στην προσομοίωση με συνεκτικό έδαφος ο δακτύλιος στροβιλότητας βρίσκεται σε υψηλότερη θέση και σε μεγαλύτερη εγγύτητα με τον δρομέα. Το φαινόμενο της μετατόπισης είναι αποτέλεσμα της δημιουργίας του οριακού στρώματος το οποίο αλληλεπιδρά με την στροβιλότητα του δακτυλίου. Επειδή η στροβιλότητα του δακτυλίου έχει αντίθετο πρόσημο από την στροβιλότητα του οριακού στρώματος, η αλληλεπίδραση οδηγεί στην διαπλάτυνση του δακτυλίου. Στο σχήμα 3.17, το οριακό στρώμα (καταγεγραμμένο στο επίπεδο του $MaPFlow$) οδηγεί τους στροβίλους των ακροπτερυγίων να κατευθυνθούν προς τα επάνω, καθώς το έλλειμμα ταχυτήτων μεταφράζεται σαν παροχή ρευστού στην αντίθετη κατεύθυνση. Με αυτό τον τρόπο, ο δακτύλιος αναπηδάει και η θέση του συγκλίνει κοντά στον δρομέα οδηγώντας σε μεγαλύτερα φορτία.

3.3.3 Διερεύνηση της επίδρασης της ατράκτου του ελικοπτέρου στα αποτελέσματα

Όπως διαπιστώθηκε, η συνεκτικότητα του εδάφους διαδραματίζει σημαντικό ρόλο στην σωστή πρόλεξη των φορτίων ενός ελικοπτέρου σε πτήση πολύ κοντά στο έδαφος. Το οριακό στρώμα που διαμορφώνεται στο έδαφος μεταβάλλει σε μεγάλο βαθμό το πεδίο ταχυτήτων. Υπό αυτό το πρίσμα, πραγματοποιήθηκε άλλη μία προσομοίωση με το
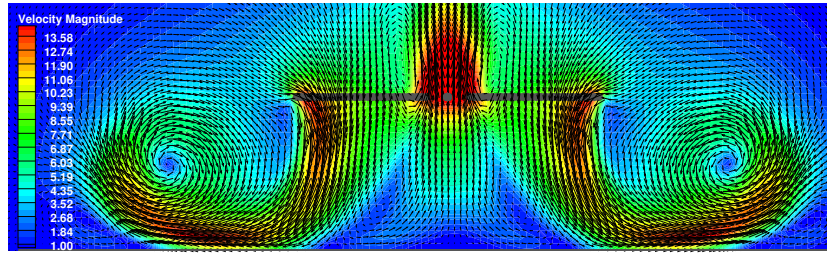
Σχήμα 3.16: Το μέτρο και το διάνυσμα της ταχύτητας (m/s) για συνθήκες IGE όπως αυτό καταγράφηκε από το $HoPFlow$ σε μία αξονοσυμμετρική πλάκα στο $r/R = 0$ για τον δρομέα του $Polimi$ στην θέση $Z/R = 1$ χωρίς την παρουσία της ατράκτου (στιγμιότυπο στο τέλος της 6ης περιόδου, συνθήκη μη ολίσθησης στο έδαφος).
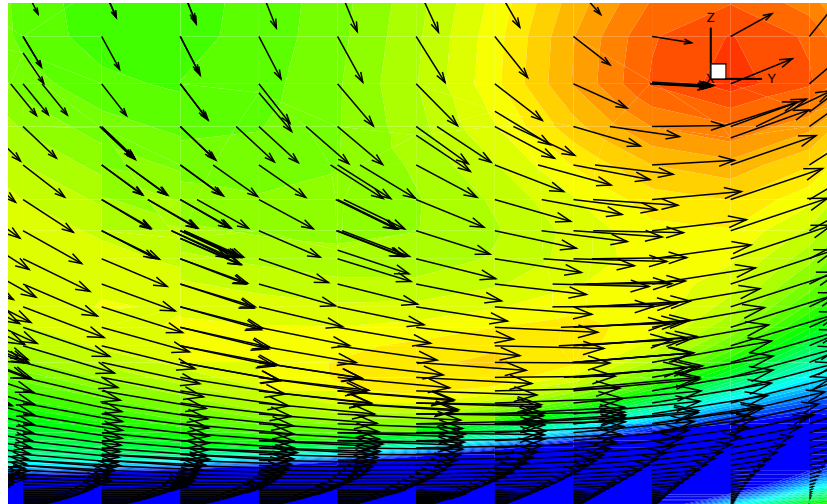
Σχήμα 3.17: Σχηματισμός του οριακού στρώματος του εδάφους για συνθήκες IGE όπως αυτό καταγράφηκε από το $HoPFlow$ σε μία αξονοσυμμετρική πλάκα στο $r/R = 0$ για τον δρομέα του $Polimi$ στην θέση $Z/R = 1$ χωρίς την παρουσία της ατράκτου (στιγμιότυπο στο τέλος της 6ης περιόδου, συνθήκη μη ολίσθησης στο έδαφος).

$HoPFlow$ και αυτή την φορά προστέθηκε και η άτρακτος, η οποία από μόνη της προσδίδει ένα ακόμα επίπεδο αλληλεπιδράσεων.

Στην περίπτωση λοιπόν που ο δρομέας πραγματοποιεί πτήση αιώρησης κοντά στο έδαφος και συγκεκριμένα στην θέση $Z/R = 1$ η μεταβολή του CT είναι πολύ μικρή και συγκεκριμένα της τάξεως του 0.5% συγκριτικά με την απουσία της ατράκτου $(CT/CT_{OGE} = 1.15)$. Το συγκεκριμένο αποτέλεσμα δείχνει πως παρ' όλη την αλληλεπίδραση του ομόρρου του δρομέα με την άτρακτο, η κύρια αιτία της επιπρόσθετης

αύξησης του φορτίου είναι η συνεκτικότητα του εδάφους.

Στο Σχήμα 3.18 και 3.19 παρουσιάζεται το μέτρο και το διάνυσμα του πεδίου ταχύτητας σε δύο κάθετες πλάκες που περνάνε από το κέντρο του δρομέα ($r/R = 0$). Αυτό που παρατηρείται είναι πρακτικά μία υπέρθεση των πεδίων που προκύπτουν από την πτήση αιώρησης με την άτρακτο μακρυά από το έδαφος και από την πτήση στο έδαφος με την ανάπτυξη του οριακού στρώματος. Η παρουσία της ατράκτου όπως και προηγουμένως έχει μειώσει την μέγιστη ταχύτητα της ροής δέσμης που δημιουργείται από τον δρομέα και δημιουργεί περιοχές ανακυκλοφορίας στο κάτω μέρος της και κοντά στο έδαφος. Κινούμενοι μακρυά από την άτρακτο, ο δακτύλιος στροβιλότητας που δημιουργείται δεν απομακρύνεται από τον δρομέα, αλλά αναπηδάει στο οριακό στρώμα και τοποθετείται σε κοντινότερη ως προς τον δρομέα θέση. Επίσης επισημαίνεται πως λόγω της ύπαρξης της ατράκτου, ο δακτύλιος έχει διογκωθεί συγκριτικά, ωστόσο αυτό δεν επηρεάζει σε μεγάλο βαθμό το φορτίο.

Σχήμα 3.18: Το μέτρο και το διάνυσμα της ταχύτητας (m/s) για συνθήκες IGE όπως αυτό καταγράφηκε από το $HoPFlow$ σε μία αξονοσυμμετρική πλάκα στο $r/R = 0$ για τον δρομέα του $Polimi$ στην θέση $Z/R = 1$ με την παρουσία της ατράκτου (στιγμιότυπο στο τέλος της 6ης περιόδου, συνθήκη μη ολίσθησης στο έδαφος, πλάγια όψη).
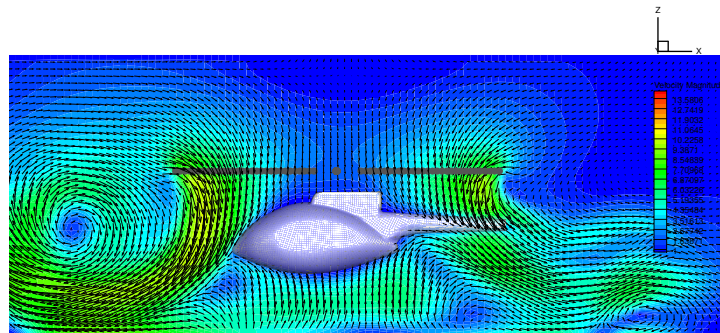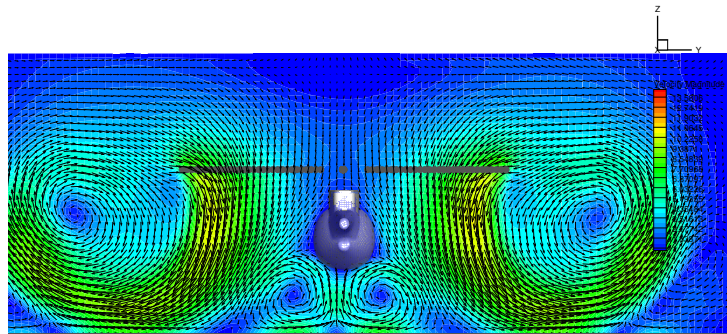
Σχήμα 3.19: Το μέτρο και το διάνυσμα της ταχύτητας (m/s) για συνθήκες IGE όπως αυτό καταγράφηκε από το $HoPFlow$ σε μία αξονοσυμμετρική πλάκα στο $r/R = 0$ για τον δρομέα του $Polimi$ στην θέση $Z/R = 1$ με την παρουσία της ατράκτου (στιγμιότυπο στο τέλος της 6ης περιόδου, συνθήκη μη ολίσθησης στο έδαφος, πίσω όψη).

3.4 Πτήση αιώρησης ελικοπτέρου πάνω α- πό εμπόδιο - μεταβολή της θέσης του δρομέα στον x άξονα $T1$ περίπτωση

Μία ακόμα περίπτωση που αναλύεται είναι η πτήση αιώρησης ελικοπτέρου πάνω από εμπόδιο, μεταβάλλοντας αυτή την φορά όχι το ύψος της αιώρησης αλλά την θέση του άξονα του δρομέα σε σχέση με το κέντρο του εμποδίου. Η ανάλυση περιλαμβάνει συγκρίσεις πειραματικών μετρήσεων για τη φόρτιση του δρομέα και το πεδίο ταχύτητας με προλέξεις του $GenUVP$ και του $HoPFlow$. Για την συγκεκριμένη περίπτωση χρησιμοποιήθηκαν δεδομένα της πειραματικής διάταξης του $Polimi$, κατά την οποία ο δρομέας αρχικά τοποθετείται πάνω από το κέντρο του εμποδίου $X/R = -1.01$ και στην συνέχεια μεταβάλλεται η θέση του κατά τον x-άξονα μέχρι και την θέση $X/R = 1$, όπου ο δρομέας πλέον βρίσκεται εξ ολοκλήρου εκτός της σκίασης του εμποδίου. Το ύψος της αιώρησης παραμένει σταθερό στο $Z/R = 2$ ενώ οι προλέξεις των φορτίων αφορούν προσομοιώσεις μόνο του κύριου δρομέα, χωρίς την ύπαρξη της ατράκτου.

Το Σχήμα 3.20 παρουσιάζει τις μεταβολές στο CT και του βαθμού απόδοσης FM του δρομέα του ελικοπτέρου συναρτήσει της απόστασης του από το κέντρο του εμποδίου για δεδομένο ύψος αιώρησης. Όταν ο δρομέας βρίσκεται στο $X/R = -1.01$ σκιάζεται πλήρως από το εμπόδιο. Η αύξηση στην ώση είναι της τάξεως του 21% όταν βρίσκεται περίπου $1R$ πάνω από το εμπόδιο ($2R$ πάνω από το έδαφος) σε αντίθεση με τη 15% αύξησης για ύψος αιώρησης $1R$ πάνω από το έδαφος. Ίδια μεταβολή καταγράφεται και για την περίπτωση του FM.
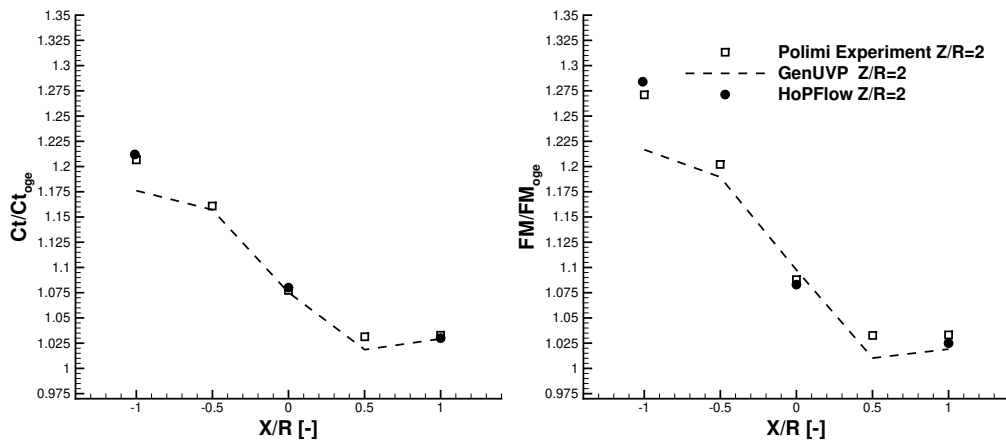
(α΄) Μεταβολές του συντελεστή ώσης συ- (β΄) Μεταβολές του συντελεστή FM συ-
ναρτήσει της θέσης του δρομέα στον x- ναρτήσει της θέσης του δρομέα στον x-
άξονα   άξονα

Σχήμα 3.20: Η επίδραση του εμποδίου στο CT και FM του δρομέα σε συνάρτηση με την απόσταση του δρομέα από το κέντρο του εμποδίου (X/R). Συγκρίσεις πειραματικών δεδομένων με προλέξεις του $GenUVP$ και $HoPFlow$ για την περίπτωση $T2$ του $Polimi$.
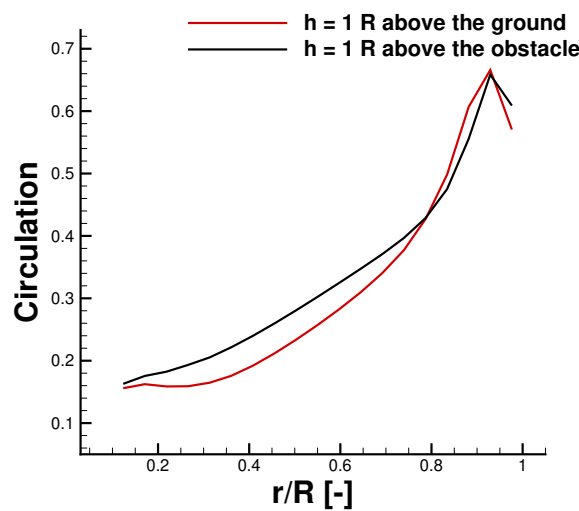
Σχήμα 3.21: Σύγκριση του χρονικού μέσου όρου της κατανομής της κυκλοφορίας στο πτερύγιο του δρομέα του $Polimi$ για τις περιπτώσεις $T2\ Z/R = 2$ και $IGE\ Z/R = 1$.

41

Όπως φαίνεται και στο Σχήμα 3.21 η διαφορά στην ώση προκύπτει από την αυ-
ξημένη κυκλοφορία στα πτερύγια του δρομέα. Η σύγκριση αφορά τη μέση τιμή στο
χρόνο της κατανομής της κυκλοφορίας πάνω στο πτερύγιο στην περίπτωση που ο
δρομέας τοποθετηθεί στο $Z/R = 1$ πάνω από το εμπόδιο (μαύρη καμπύλη) και πάνω
από το έδαφος (κόκκινη καμπύλη) αντίστοιχα.

Όσο απομακρύνεται σταδιακά ο δρομέας από το εμπόδιο, η αύξηση τόσο στο CT
όσο και στο FM μειώνεται. Όταν πλέον το ελικόπτερο παύει να βρίσκεται πάνω από
το εμπόδιο (αυτό συμβαίνει στο $X/R = 1$), η ώση παρουσιάζει αύξηση 3.5%, που είναι
σχεδόν η ίδια με την περίπτωση που το ελικόπτερο αιωρείται στο $Z/R = 2$ χωρίς την
παρουσία κάποιου εμποδίου. Συμπεραίνεται λοιπόν πως από αυτή την απόσταση και
έπειτα, το εμπόδιο δεν έχει κάποια επίδραση στην φόρτιση του ελικοπτέρου.

Συγκρίνοντας τις πειραματικές μετρήσεις με τις υπολογιστικές προλέξεις, εξάγο-
νται τα ακόλουθα συμπεράσματα:

- Η ποιότητα των συγκρίσεων είναι καλή, τόσο για τον $GenUVP$ όσο και για
  το $HoPFlow$. Το ίδιο ισχύει και για την μορφή των μεταβολών των CT και
  FM συναρτήσει της απόστασης X/R. Παρ'όλο το μη συνεκτικό χαρακτήρα
  του, ο $GenUVP$ αναπαράγει ικανοποιητικά τα πειράματα. Ωστόσο, η εισαγωγή
  συνεκτικών φαινομένων με το $HoPFlow$, βελτιώνει σημαντικά τις απόλυτες
  τιμές των φορτίων κυρίως στο $X/R = -1.01$.

- Η μέγιστη διαφορά των προλέξεων του $GenUVP$ εντοπίζεται στο $X/R = -1$
  (2.5 % στο CT και 5% στο FM όταν οι τοίχοι έχουν μη συνεκτικές συνθήκες).
  Το αποτέλεσμα αυτό ωστόσο είναι απόλυτα σύμφωνο με τις προλέξεις σε IGE
  συνθήκες, όπου επίσης καταγράφηκε εξάρτηση του σφάλματος με το ύψος της
  αιώρησης του ελικοπτέρου.

- Οι προλέξεις του $HoPFlow$ αναπαράγουν τόσο το CT όσο και το FM στο
  $X/R = -1.01$ όπως ακριβώς συνέβη και στην περίπτωση του IGE. Με αυτό
  τον τρόπο επιβεβαιώνεται πως η συνεκτικότητα διαδραματίζει σημαντικό ρόλο
  κυρίως όταν το ελικόπτερο βρίσκεται σε μικρή απόσταση από το σύνορο.

3.4.1 Συγκρίσεις του πεδίου ταχύτητας

Οι παραπάνω διαπιστώσεις για την επίδραση του εμποδίου στα φορτία, επιβεβαιώνονται
και από το πεδίο ταχύτητας το οποίο καταγράφεται σε ένα επίπεδο που διέρχεται από
το κέντρο του δρομέα $r/R = 0$ και αποτυπώνει το μέτρο της ταχύτητας καθώς και τις
γραμμές ροής. Οι πειραματικές μετρήσεις του πεδίου (PIV) συγκρίνονται με προλέξεις
του $GenUVP$ και του $HoPFlow$.

Όταν ο δρομέας βρίσκεται πάνω από το κέντρο του εμποδίου στο $X/R = -1.01$
οι μετρήσεις του πεδίου (Σχήμα 3.22α΄) δείχνουν πως το πεδίο δέσμης του δρομέα
του ελικοπτέρου προσκρούει στην οροφή του εμποδίου, διαχωρίζεται σε δύο εφα-
πτομενικές στο εμπόδιο δέσμες, οι οποίες αποκολλώνται στην συνέχεια στην άκρη
του. Δημιουργείται επομένως μία περιοχή ανακυκλοφορίας (ωρολογιακή περιστροφή)
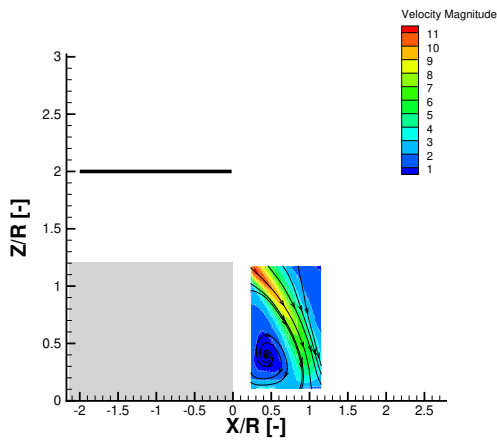
(α΄) Πειραματικές μετρήσεις
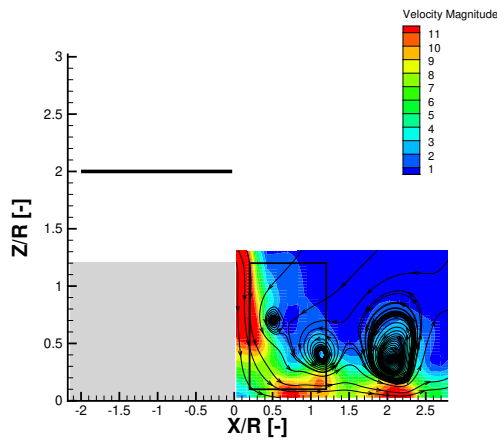
(β΄) Προλέξεις *GenUVP*

(γ΄) Προλέξεις *HoPFlow* χωρίς την παρουσία της ατράκτου
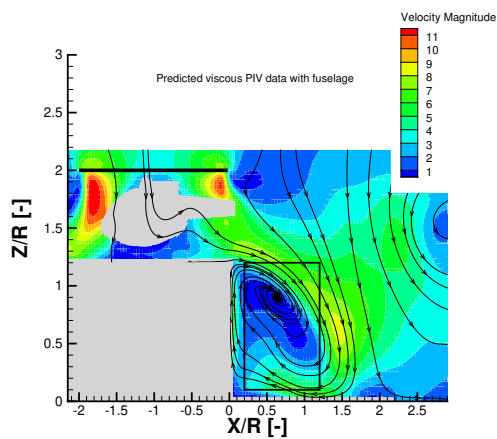
(δ΄) Προλέξεις *HoPFlow* με την παρουσία της ατράκτου

Σχήμα 3.22: Συγκρίσεις του πεδίου ταχύτητας (m/s) όπως καταγράφτηκε σε μία κάθετη αξονο-συμμετρική πλάκα για το πείραμα του *Polimi* όταν ο δρομέας πραγματοποιεί πτήση αιώρησης στην θέση $X/R = -1.01$ και $Z/R = 2$.
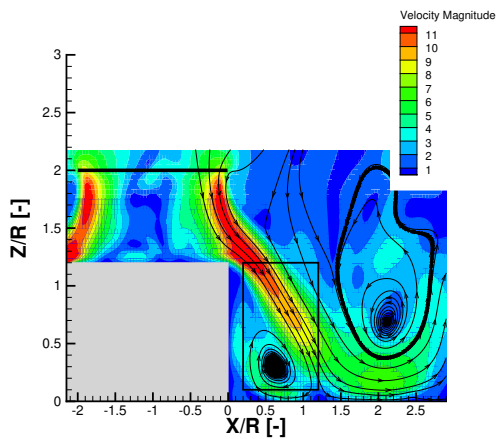
χαμηλών ταχυτήτων μεταξύ των κάθετων τοίχων του εμποδίου και του στρώματος διάτμησης του ομόρρου του ελικοπτέρου.

Το πεδίο ροής όπως αυτό διαμορφώνεται με τον *GenUVP* αποτυπώνεται στο Σχήμα 3.22β΄. Δεδομένου ότι οι τοίχοι του εμποδίου είναι επιφάνειες στις οποίες ικανοποιείται μόνο η συνθήκη μη εισχώρησης, η μέθοδος αδυνατεί να προλέξει την αποκόλληση της ροής. Ως αποτέλεσμα η ροή παραμένει προσκολλημένη στο εμπόδιο, όπως δείχνουν και οι καταγεγραμμένες γραμμές ροής. Παράλληλα, η ροή επιταχύνεται στους κάθετους τοίχους και οι στρόβιλοι των ακροπτερυγίων που εμφανίζονται στις θέσεις $X/R = 0.5$, 1 και 2 απομακρύνονται από το εμπόδιο. Η παραπάνω ποιοτική

διαφορά μεταξύ των μετρήσεων και των προλέξεων εξηγούν και την διαφορά στην φόρτιση του δρομέα (βλέπε Σχήμα 3.21, σημείο $X/R = -1.01$). Η παρουσία της ζώνης ανακυκλοφορίας περιμετρικά του εμποδίου στις μετρήσεις διευρύνει τα όρια στα οποία ο ομόρρους του ελικοπτέρου έρχεται σε επαφή με ένα φυσικό ή ιδεατό σύνορο με αποτέλεσμα οι διαστάσεις του εμποδίου να ¨μεγαλώνουν' φαινομενικά για τον δρομέα. Με αυτό τον τρόπο αυξάνει και η επιρροή που έχει στην φόρτιση.

Σε αντίθεση με τον μη συνεκτικό $GenUVP$, το $HoPFLow$ επιβάλλοντας στους τοίχους και το έδαφος και τη συνθήκη μη εισχώρησης αλλά και τη συνθήκη μη ο- λίσθησης είναι σε θέση να προλέξει σωστά το πεδίο, αναπαράγοντας τη φυσική του φαινομένου. Όπως φαίνεται και στο Σχήμα 3.22γ΄, η μέθοδος είναι ικανή να προλέξει την αποκόλληση της ροής στο άκρο του εμποδίου δημιουργώντας την περιοχή ανακυ- κλοφορίας. Ακόμη, το σημείο πάνω στο έδαφος όπου προσκρούει η ροή αποτυπώνεται όπως και στο πείραμα στο σημείο $X/R = 1$. Μόνο μικρές διαφοροποιήσεις παρατηρού- νται οι οποίες αφορούν στο μέτρο της ταχύτητας εντός της περιοχής ανακυκλοφορίας και το μέγεθος των ταχυτήτων του στρώματος διάτμησης. Ωστόσο, η υπερεκτίμηση της ταχύτητας δεν έχει μεγάλη επιρροή στην φόρτιση του δρομέα, η οποία προλέγεται με απόκλιση μικρότερη του 0.5% συγκριτικά με το πείραμα.

Επειδή η προηγούμενη προσομοίωση δεν περιλαμβάνει την άτρακτο του ελικο- πτέρου καθώς και τον υποστηρικτικό βραχίωνα, για την καλύτερη διερεύνηση του προβλήματος πραγματοποιήθηκε και μία προσομοίωση στην οποία συμπεριλαμβάνεται η άτρακτος. Τα αποτελέσματα που φαίνονται στο Σχήμα 3.22δ΄ παρουσιάζουν αρκετές ομοιότητες όσον αφορά την προσομοίωση με το $HoPFlow$ χωρίς την άτρακτο. Η φυ- σική των προλέξεων περιλαμβάνει την αποκόλληση της ροής αλλά και την δημιουργία της ζώνης ανακυκλοφορίας. Λαμβάνοντας υπόψιν και την αντίστοιχη προσομοίωση με την άτρακτο σε συνθήκες IGE, παρατηρείται πως και στην συγκεκριμένη περίπτωση, η ύπαρξη της ατράκτου διαχέει τη ροή κάτω από τον δρομέα μειώνοντας το μέτρο της ταχύτητας. Αυτό έχει ως αποτέλεσμα από τη μία να προλέγονται ταχύτητες στην ζώνη ανακυκλοφορίας όμοιου μέτρου με αυτές του πειράματος, από την άλλη όμως η ζώνη ανακυκλοφορίας έχει μεγαλώσει μετατοπίζοντας κατάντι και την περιοχή όπου το στρώμα διάτμησης έρχεται σε επαφή με το έδαφος.

Μετατοπίζοντας το κέντρο του δρομέα στο $X/R = 0$ τα αποτελέσματα των με- τρήσεων παρουσιάζουν την ίδια φυσική με προηγουμένως. Η ροή που προσπίπτει στο πάνω μέρος του εμποδίου διαχωρίζεται, οδηγώντας την ροή που κινείται κατάντι του εμποδίου να αποκολληθεί. Ως αποτέλεσμα δημιουργείται μία ζώνη ανακυκλοφορίας η οποία όμως εντοπίζεται αυτή τη φορά μικρότερη και μετατοπισμένη προς τον κάθετο τοίχο του εμποδίου (Σχήμα 3.23α΄). Η φορά του εξασθενημένου στροβίλου στην ζώνη ανακυκλοφορίας έχει αλλάξει (ανθωρολογιακή φορά), ωστόσο οι ταχύτητες μέσα στην ζώνη έχουν πολύ μικρό μέτρο. Έχει σημασία να αναφερθεί πως στην πάνω αριστερή γωνία του παραθύρου των μετρήσεων παρατηρούνται τα δύο στρώματα διάτμησης να ενώνονται. Η εφαπτομενική στην οροφή ροή, που ερχέται ανάντι του εμποδίου, εμ- φανίζεται εξασθενιμένη (μικρότερο μέτρο ταχύτητας). Αυτό έχει σαν αποτέλεσμα να αλλάξει κατεύθυνση από την αδιατάραχτη ροή του δρομέα η οποία είναι εμφανώς πιο ισχυρή.
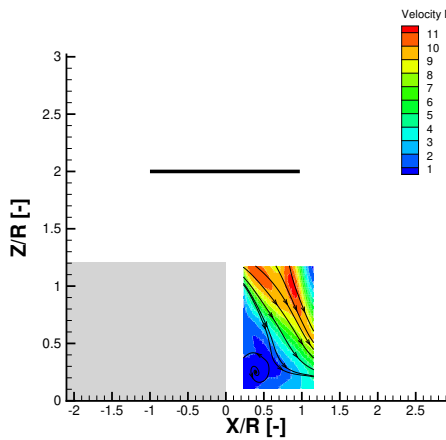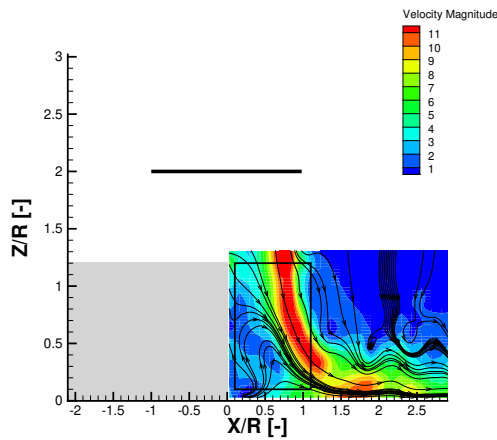
(α΄) Πειραματικές μετρήσεις

(β΄) Προλέξεις $GenUVP$
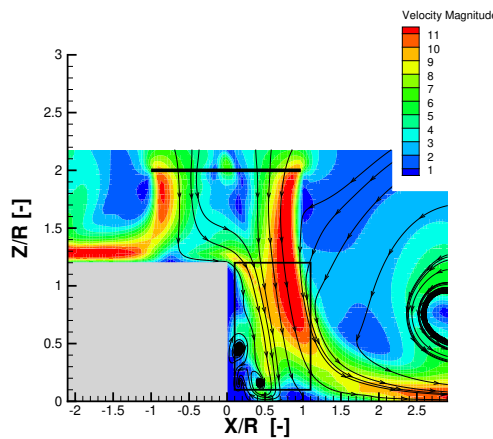
(γ΄) Προλέξεις $HoPFlow$ χωρίς την πα-
ρουσία της ατράκτου

Σχήμα 3.23: Συγκρίσεις του πεδίου ταχύτητας (m/s) όπως καταγράφτηκε σε
μία κάθετη αξονο-συμμετρική πλάκα για το πείραμα του $Polimi$ όταν ο δρομέας
πραγματοποιεί πτήση αιώρησης στην θέση $X/R = 0$ και $Z/R = 2$.

Το πεδίο όπως καταγράφεται από τον $GenUVP$ φαίνεται στο Σχήμα 3.23(β΄) και
λόγω του μη συνεκτικού χαρακτήρα του, αδυνατεί να αναπαράγει το φαινόμενο. Σε
αντίθεση με το πείραμα, η ροή που προσπίπτει στην οροφή του εμποδίου δεν διαχωρίζε-
ται, αντίθετα κατευθύνεται ανάντι του εμποδίου. Με αυτό τον τρόπο ο ομόρρους του
δρομέα προσκρούει στο έδαφος και κατευθύνεται κατάντι του εμποδίου δημιουργώντας
έτσι μία περιοχή χαμηλών ταχυτήτων κοντά στην περιοχή του εμποδίου. Αντίθετα,
τα αποτελέσματα του $HoPFlow$ είναι σε πολύ καλή συμφωνία με τις πειραματικές
μετρήσεις. Η φυσική της αλληλεπίδρασης αναπαράγεται πλήρως και μόνο ποσοτικές
διαφορές εντοπίζονται (Σχήμα 3.23γ΄). Στην περίπτωση της προσομοίωσης η ροή που

45

έρχεται από την οροφή παρουσιάζει σημαντική εξασθένιση και σε συνδυασμό με την υπερεκτίμηση του κατωρεύματος του δρομέα, η ζώνη ανακυκλοφορίας περιορίζεται δραστικά και μετατοπίζεται πολύ καλά στο εμπόδιο. Οι ποσοτικές αυτές διαφορές πιθανόν να περιορίζονταν στην περίπτωση που προσομοιωνόταν και η άτρακτος, που όπως επισημάνθηκε προηγουμένως διαχέει την ροή.

(α΄) Πειραματικές μετρήσεις
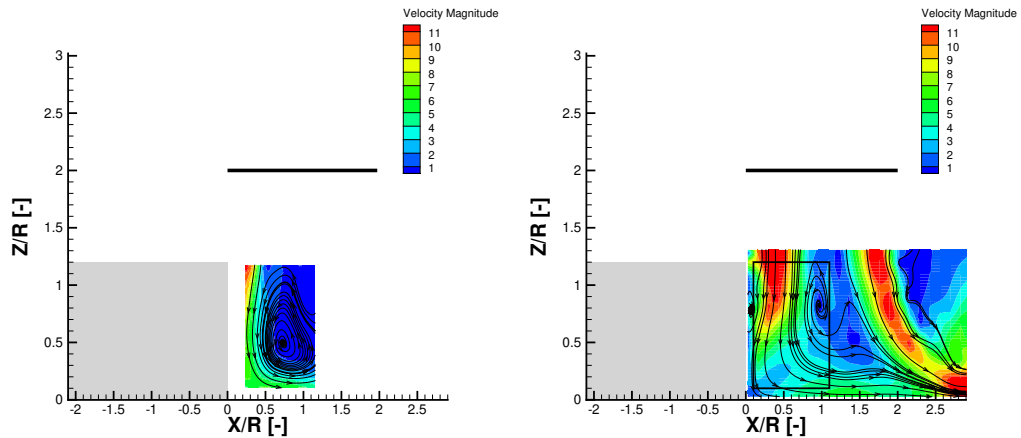
(β΄) Προλέξεις $GenUVP$
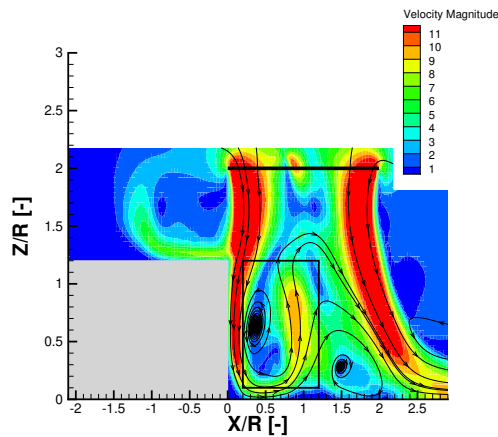
(γ΄) Προλέξεις $HoPFlow$ χωρίς την πα-
ρουσία της ατράκτου

Σχήμα 3.24: Συγκρίσεις του πεδίου ταχύτητας (m/s) όπως καταγράφτηκε σε μία κάθετη αξονο-συμμετρική πλάκα για το πείραμα του $Polimi$ όταν ο δρομέας πραγματοποιεί πτήση αιώρησης στην θέση $X/R = 1$ και $Z/R = 2$.

Όταν ο δρομέας έχει απομακρυνθεί ακόμα περισσότερο από το εμπόδιο στο $X/R = 1$ (Σχήμα 3.24α΄) κανένα μέρος του δίσκου δεν σκιάζεται πλέον, με αποτέλεσμα η ροή να διαχωρίζεται στην άκρη του εμποδίου οδηγώντας σε ένα κατακόρυφο στρώμα δι-άτμησης που κινείται προς το έδαφος και ένα άλλο στην οροφή του εμποδίου κινούμενο

ανάντι του δρομέα. Έτσι, όπως φαίνεται και στο παράθυρο των μετρήσεων, δημιουργείται μία ζώνη ανακυκλοφορίας χαμηλών ταχυτήτων. Παρόμοιο μοτίβο έχουν και τα υπολογιστικά αποτελέσματα (Σχήμα 3.24β΄,γ΄). Στην προσομοίωση με τον $GenUVP$ η ζώνη ανακυκλοφορίας έχει μετατοπισθεί υψηλότερα και προς το κέντρο του δρομέα, αφού όπως φαίνεται, λόγω του μη συνεκτικού χαρακτήρα της μεθόδου ο ομόρρους δεν διαχωρίζεται αλλά κατευθύνεται παράλληλα προς στον κάθετο τοίχο. Αντίθετα, τα αποτελέσματα του $HoPFlow$ αναπαράγουν ορθά το φαινόμενο εμφανίζοντας όμως τις ίδιες ποσοτικές διαφοροποιήσεις με πριν.

Συνολικά, για τον $GenUVP$ οι συγκρίσεις είναι ικανοποιητικές, αναλογιζόμενοι τον μη συνεκτικό χαρακτήρα της μεθόδου. Παρόλα αυτά, καλύτερες προλέξεις αναμένονται τόσο στο πεδίο όσο και στα φορτία όταν ο δρομέας απομακρύνεται από το εμπόδιο. Αντίθετα, τα αποτελέσματα του $HoPFlow$ συγκρίνονται πολύ καλά με τις μετρήσεις καθώς αναπαράγουν σε μεγάλο βαθμό τα φυσικά φαινόμενα που παρατηρούνται στο πείραμα.

3.5 Πτήση αιώρησης ελικοπτέρου πάνω από εμπόδιο - μεταβολή της θέσης του δρομέα στον z άξονα $T2$ περίπτωση

Σε αυτή την παράγραφο αναλύεται η αλληλεπίδραση ενός ελικοπτέρου με ένα εμπόδιο όταν ο δρομέας τοποθετείται πάνω από το κέντρο του εμποδίου (περίπτωση $T1$). Για αυτή την περίπτωση, θα παρουσιαστούν αποτελέσματα που αφορούν συγκρίσεις πειραματικών δεδομένων με υπολογιστικές προλέξεις του $GenUVP$ και του $HoPFlow$. Για την συγκεκριμένη πειραματική διάταξη, υπάρχουν μετρήσεις από το $Polimi$ και αφορούν τετράπτερο δρομέα που πραγματοποιεί πτήση αιώρησης σε σταθερές θέσεις κάθε φορά πάνω από το εμπόδιο, μεταβάλλοντας το ύψος πτήσης στον $z-$άξονα. Το πρώτο σημείο τοποθετείται στο $Z/R = 2$ από το έδαφος (περίπου $Z/R = 0.8$ από την πάνω επιφάνεια του εμποδίου, ενώ το τελευταίο σημείο των μετρήσεων βρίσκεται στο $Z/R = 4$ πάνω από το έδαφος. Οι προσομοιώσεις λαμβάνουν υπόψιν μόνο τον κύριο δρομέα και όχι της άτρακτο του ελικοπτέρου.

Τα αποτελέσματα των πειραματικών μετρήσεων παρουσιάζουν αρκετές ομοιότητες στην επίδραση του εμποδίου στα φορτία του κύριου δρομέα με την περίπτωση IGE (βλέπε Σχήμα 3.25). Ο συντελεστής CT/CT_{OGE} παρουσιάζει μία εκθετική μεταβολή συναρτήσει του ύψους αιώρησης από το έδαφος. Η μεγαλύτερη αύξηση παρατηρείται όταν το $Z/R = 2$ και είναι ίση με 21.5%. Καθώς το ύψος αυξάνει, η αύξηση του CT/CT_{OGE} μειώνεται και στο ύψος $Z/R = 4$ η επίδραση του εμποδίου πρακτικά μηδενίζεται. Συγκρίνοντας τα αποτελέσματα με την περίπτωση IGE είναι ορατό πώς όταν το ελικόπτερο πραγματοποιεί πτήση αιώρησης πάνω από το εμπόδιο και ο δρομέας είναι πλήρως σκιασμένος από αυτό, η επίδραση του μοιάζει σε μεγάλο βαθμό με την επίδραση του εδάφους. Η σημαντικότερη διαφορά ωστόσο, είναι πως η αύξηση της ώσης είναι κατά 7% μεγαλύτερη. Η διαφορά αυτή οφείλεται κυρίως στο διαφορετικό

47
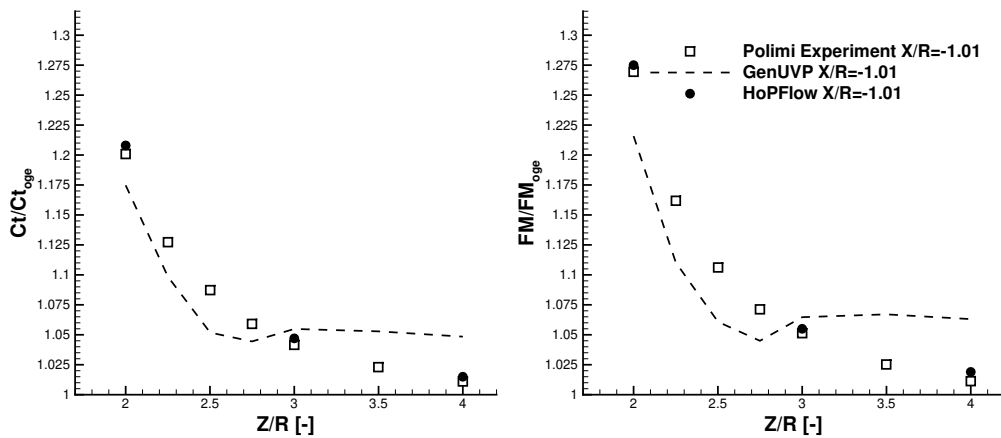
(α΄) Μεταβολές του συντελεστή ώσης συ-
ναρτήσει της θέσης του δρομέα στον z-
άξονα

(β΄) Μεταβολές του συντελεστή FM συ-
ναρτήσει της θέσης του δρομέα στον z-
άξονα

Σχήμα 3.25: Η επίδραση του εμποδίου στο CT και FM του δρομέα σε συ-
νάρτηση με το ύψος αιώρησης από το έδαφος (Z/R). Συγκρίσεις πειραματικών
δεδομένων με προλέξεις του $GenUVP$ και $HoPFlow$ για την περίπτωση $T1$
του $Polimi$.

πεδίο ταχυτήτων των δύο περιπτώσεων. Παρόμοια επίδραση έχει το εμπόδιο και στην
ροπή του δρομέα όπως φαίνεται στο Σχήμα 3.25 (β΄). Στο σχήμα αυτό παρουσιάζεται
η μεταβολή του $Figure\ of\ Merit(FM)$ του δρομέα συναρτήσει της απόστασης από
το έδαφος.

Χρησιμοποιώντας τον $GenUVP$ πραγματοποιήθηκαν προσομοιώσεις για το σύνο-
λο των πειραματικών σημείων που μετρήθηκαν. Η σύγκριση των προλέξεων με τις
μετρήσεις είναι σχετικά καλή, όμως φανερώνει και τις αδυναμίες της μεθόδου. Όπως
φαίνεται από την διακεκομμένη μαύρη καμπύλη του Σχήματος 3.25 η μέθοδος προλέγει
την αύξηση του CT σε σύγκριση με την πτήση OGE, όμως υποεκτιμάει την φόρτιση
του δρομέα όταν αυτός βρίσκεται πολύ κοντά στο κουτί παρόλο που προβλέπεται σωστά
η επιπλέον αύξηση συγκριτικά με την IGE περίπτωση. Ακόμη, για ύψη μεγαλύτερα
του $Z/R = 2.7$ παρατηρείται μία επιπεδοποίηση της καμπύλης σταθεροποιώντας την
επίδραση του εμποδίου περίπου στο 5% ακόμα και για $Z/R = 4$.

Σε αντίθεση με τον $GenUVP$, τα αποτελέσματα του $HoPFlow$ συμφωνούν σε
πολύ μεγάλο βαθμό με τις μετρήσεις. Σε συνέχεια της διαπίστωσης πως η συνε-
κτικότητα του εδάφους διαδραματίζει κομβικό ρόλο στην φόρτιση του δρομέα, διαπι-
στώνεται πως η ανάπτυξη του οριακού στρώματος στο εμπόδιο μεταβάλει αρκετά τα
αποτελέσματα. Για τα τρία σημεία του πειράματος που πραγματοποιήθηκαν προσομοι-
ώσεις ($Z/R = 2, 3.4$) η σύγκριση είναι πολύ καλή τόσο σε μορφή όσο και σε απόλυτες
τιμές. Το $HoPFlow$ προλέγει με ορθό τρόπο την μέγιστη αύξηση του CT (σημείο
$Z/R = 2$), τον ρυθμό μείωσης του CT (σημείο $Z/R = 3$) και το όριο στο οποίο η

επίδραση του εμποδίου παύει να έχει σημαντική τιμή (σημείο $Z/R = 4$).

This page intentionally left blank.

Κεφάλαιο 4

Συμπεράσματα και Μελλοντική Έρευνα

Ο σκοπός της παρούσας εργασίας ήταν α) η σε βάθος διερεύνηση της αλληλεπίδρασης ενός ελικοπτέρου με το έδαφος και παρακείμενα εμπόδια όταν πραγματοποιεί πτήση αιώρησης κοντά σε αυτά και β) η πιστοποίηση δύο υπολογιστικών μεθόδων διαφορετικής πιστότητας ως προς την ορθή πρόλεξη των φορτίων και των πεδίων ροής σε τέτοια προβλήματα αλληλεπίδρασης.

4.1 Συμπεράσματα

Η επίδραση του εδάφους και του εμποδίου στην διαμόρφωση του πεδίου ροής αλλά και στην φόρτιση του ελικοπτέρου πραγματοποιήθηκε χρησιμοποιώντας πειραματικά δεδομένα τριών διαφορετικών πειραμάτων και υπολογιστικά αποτελέσματα από δύο διαφορετικά εργαλεία. Τα συμπεράσματα που εξήχθησαν όσον αφορά το πρόβλημα της αλληλεπίδρασης παρουσιάζονται στην συνέχεια για κάθε περίπτωση ξεχωριστά:

- *OGE*: Τα δεδομένα της συγκεκριμένης περίπτωσης χρησιμοποιήθηκαν για την αδιαστατοποίηση των αποτελεσμάτων των επόμενων περιπτώσεων. Τα πειραματικά αποτελέσματα για το CT συγκρίνονται πολύ καλά με τους υπολογισμούς και από τα δύο εργαλεία ($GenUVP$, $HoPFlow$). Παράλληλα, διαπιστώθηκε πως ενώ η ύπαρξη της ατράκτου στους υπολογισμούς επηρεάζει διαμόρφωση του πεδίου ροής, δεν επηρεάζει σε σημαντικό βαθμό την φόρτιση του κύριου δρομέα.

- *IGE*: Στην περίπτωση που το ελικόπτερο πραγματοποιεί πτήση αιώρησης κοντά στο έδαφος, τα πειράματα παρουσιάζουν περίπου εκθετική αύξηση του CT καθώς η απόσταση από το έδαφος μειώνεται. Η μέγιστη τιμή παρουσιάζεται στο $Z/R = 1$ και είναι ίση με 12.5% περίπου. Η επίδραση του εδάφους παύει να έχει επίπτωση στα φορτία μετά το $Z/R = 4$. Οι προλέξεις του $GenUVP$ είναι σε

πολύ καλή συμφωνία με τα πειράματα παρουσιάζοντας μικρές διαφοροποιήσεις (υποεκτίμηση 2.5% του CT) κυρίως σε μικρά ύψη πτήσης $Z/R < 1.7$. Λόγω του μη συνεκτικού χαρακτήρα της, η μέθοδος αδυνατεί να προσομοιώσει τον σχηματισμό του οριακού στρώματος στο έδαφος με αποτέλεσμα η διαφορετική διαμόρφωση του πεδίου ροής να έχει επίπτωση στην φόρτιση του δρομέα. Α-ντίθετα, η προσομοίωση με το $HoPFlow$ προλέγει με πολύ μεγάλη ακρίβεια το CT (διαφορά στο CT/CT_{OGE} μικρότερη του 0.2%. Μέσα από την ανάλυση της ανάπτυξης της ροής στα αρχικά στάδια της προσομοίωσης παρατηρήθηκε πως οι επαγόμενες ταχύτητες στο επίπεδο του εδάφους οδηγούν στην ανάπτυξη ορια-κού στρώματος το οποίο αλληλεπιδρά με τους στροβίλους των ακροπτερυγίων. Σαν αποτέλεσμα, ο δακτύλιος που δημιουργείται κατά τις πρώτες περιστροφές του δρομέα αναπηδά πάνω στο οριακό στρώμα και τοποθετείται σε υψηλότερη θέση σε σχέση με το έδαφος. Ακόμη, η επίδραση της ατράκτου στα αποτε-λέσματά της φόρτισης είναι αμελητέα παρόλο που η επίδραση στο πεδίο ροής στον ομόρρου του δρομέα είναι σημαντική.

- $T1$: Σε αυτή την περίπτωση το ελικόπτερο πραγματοποιεί πτήση αιώρησης σε σταθερό ύψος πάνω από το έδαφος ($Z/R = 2$ για την περίπτωση του $Polimi$ και $Z/R = 3$ για την $Glasgow$) μεταβάλλοντας την οριζόντια θέση του κατά τον x-άξονα. Αρχικά ο δρομέας τοποθετείται πάνω από το κέντρο του εμποδίου και στην συνέχεια το κέντρο του απομακρύνεται από το εμπόδιο. Στην αρχική του θέση $X/R = -1$ (ακριβώς πάνω από το εμπόδιο παρατηρείται και η μεγαλύτερη αύξηση στα φορτία του CT/CT_{OGE} και FM/FM_{OGE}. Καθώς απομακρύνεται παρατηρείται κατακόρυφη μείωση των φορτίων και για τις δύο πειραματικές διατάξεις. Τα υπολογιστικά μοντέλα αποτυπώνουν πολύ καλά το φαινόμενο και για τις δύο περιπτώσεις. Ο μη συνεκτικός $GenUVP$ αποτελεί αξιόπιστο εργαλείο για την πρόλεξη των φορτίων. Ωστόσο, αδυνατεί να προλέγει ορθά το πεδίο, ειδικά σε περιπτώσεις όπου τα συνεκτικά φαινόμενα είναι έντονα.

- $T2$: Όταν το ελικόπτερο πραγματοποιεί πτήση αιώρησης πάνω από το εμπόδιο μεταβάλλοντας το ύψος του κατά τον z-άξονα, η μορφή της μεταβολής της φόρ-τισης του δρομέα με το ύψος παρουσιάζει ομοιότητες με την περίπτωση IGE. Παρατηρείται μία εκθετική αύξηση του CT καθώς το ελικόπτερο πλησιάζει πιο κοντά στο εμπόδιο. Η μέγιστη αύξηση ($Z/R = 2$ πάνω από το έδαφος) ε-ίναι περίπου 21%. Ο λόγος που αυξάνεται περαιτέρω το CT σε σχέση με την περίπτωση IGE, εντοπίζεται στην αποκόλληση της ροής στις άκρες της πάνω επιφάνειας του εμποδίου που έχουν σαν αποτέλεσμα την δημιουργία περιοχών ανακυκλοφορίας περιμετρικά του εμποδίου. Τα αποτελέσματα που παρήχθησαν με τον $GenUVP$ είναι σχετικά καλά (μέγιστη απόκλιση 4%) καθώς αναπα-ράγουν εν μέρει το φαινόμενο, παρουσιάζουν όμως αρκετές διαφοροποιήσεις τόσο στην μορφή της καμπύλης του CT όσο και στο πεδίο ροής, αφού δεν πε-ριλαμβάνουν τα συνεκτικά φαινόμενα που εμφανίζονται στο εμπόδιο. Από την άλλη πλευρά, οι συγκρίσεις των πειραματικών μετρήσεων με τους υπολογισμούς του $HoPFlow$ είναι πολύ καλές, με αποκλίσεις μικρότερες του 0.1%.

- *T3:* Όταν το ελικόπτερο αιωρείται δίπλα από τον κάθετο τοίχο του εμποδίου μεταβάλλοντας το ύψος πτήσης του σε σχέση με το έδαφος, παρατηρείται η μεγαλύτερη δυσκολία για τα υπολογιστικά εργαλεία να αναπαράγουν τα πειραματικά δεδομένα. Ενώ υπάρχει σαφής εξάρτηση του ύψους πτήσης με την ώση και τη ροπή (καθώς μειώνεται το ύψος αυξάνουν τα φορτία), εντοπίζονται μεταβολές που αποδίδονται στην παρουσία του εμποδίου και την διαμόρφωση της ροής στην ζώνη μεταξύ του δρομέα και του κάθετου τοίχου του εμποδίου. Είναι σαφές πως στην περίπτωση του πειράματος της Γλασκώβης οι μεγαλύτερες διαστάσεις του εμποδίου συγκριτικά με του πειράματος του $Polimi$ επηρεάζουν σε μεγαλύτερο βαθμό τους λόγους CT/CT_{OGE} και FM/FM_{OGE}. Ο $GenUVP$ αδυνατεί να παρακολουθήσει τις μεταβολές των φορτίων με τη θέση του δρομέα λόγω των έντονων συνεκτικών φαινομένων που λαμβάνουν χώρα. Αντίθετα το $HoPFlow$ καταφέρνει να προλέξει σωστά τις μεταβολές των φορτίων, αφού η συνεκτικότητα που εισάγει στα στερεά σύνορα του εδάφους και του εμποδίου συμβάλουν στην σωστή αναπαράσταση του πεδίου ροής και στη θέση των σχηματιζόμενων στροβίλων που επηρεάζουν τη διαμόρφωση των φορτίων του δίσκου του δρομέα.

Όσον αφορά την αξιολόγηση των υπολογιστικών εργαλείων ως προς την ικανότητά τους να επιλύουν τα συγκεκριμένα προβλήματα τα συμπεράσματα είναι τα εξής:

- *GenUVP:* Το συγκεκριμένο υπολογιστικό εργαλείο αποτελεί μία αξιόπιστη λύση για την επίλυση του προβλήματος της αλληλεπίδρασης δρομέα ελικοπτέρου με στερεά σύνορα. Είναι σε θέση να προλέγει τις επιπτώσεις που επιφέρει το έδαφος και το εμπόδιο στην φόρτιση του δρομέα παρόλο που βασίζεται σε μια μη συνεκτική μεθοδολογία. Τα αποτελέσματα εξάγονται σε λίγο χρόνο γεγονός που επιτρέπει την προσομοίωση πληθώρας περιπτώσεων αφού ο κώδικας παραλληλοποιήθηκε σε περιβάλλον MPI και το πεδίο ταχύτητας επιλύεται με την μέθοδο του $Particle\ Mesh$. Ωστόσο, ο μη συνεκτικός χαρακτήρας της μεθόδου είναι και ο λόγος που οι συγκρίσεις με τις πειραματικές μετρήσεις παρουσιάζουν αποκλίσεις στα φορτία αλλά και στην διαμόρφωση του πεδίου σε περιπτώσεις που το ελικόπτερο πραγματοποιεί πτήση αιώρησης πολύ κοντά σε στερεά σύνορα.

- *HoPFlow:* Ο υβριδικός κώδικας συνδυάζει την $Eulerian$ και την $Lagrangian$ εκδοχή των πεδιακών εξισώσεων και με αυτό τον τρόπο εισάγεται στις προσομοιώσεις η συνεκτικότητα του εδάφους και του εμποδίου. Επιλέχθηκε έναντι μίας κλασικής CFD μεθοδολογίας πεπερασμένων όγκων καθώς χειρίζεται πιο αποδοτικά την παρουσία κινούμενων και μη σωμάτων εντός του υπολογιστικού χωρίου. Οι συγκρίσεις των προλέξεων με τις πειραματικές μετρήσεις παρουσιάζουν πολύ μικρές αποκλίσεις, τόσο στα φορτία όσο και στο πεδίο. Η εφαρμογή του επιβεβαίωσε την σημαντική επίδραση της συνεκτικότητας στην πρόλεξη του CT του κύριου δρομέα όταν αυτός βρίσκεται κοντά στο έδαφος και στο εμπόδιο.

53

4.2 Προτάσεις για μελλοντική έρευνα

Οι προτάσεις για μελλοντική έρευνα μπορούν να κατηγοριοποιηθούν ανάλογα με το αν αφορούν τη μεθοδολογία ή εφαρμογές.

Μεθοδολογικές Προτάσεις:

- *Επιλύτης Poisson* Η διαδικασία επίλυσης του πεδίου ταχύτητας πραγματοποιείται μέσω του *Particle Mesh*. Η συγκεκριμένη μέθοδος απαιτεί την χρήση ομοιόμορφου χωρικού πλέγματος καθιστώντας απαγορευτική την πύκνωση του κοντά στα στερεά σύνορα. Για αυτό το λόγο, προτείνεται η αντικατάσταση του *Particle Mesh* από έναν *Poisson* επιλύτη ανομοιόμορφου πλέγματος, είτε η προσθήκη ενός τηλεσκοπικού μηχανισμού στην υπάρχουσα δομή

Προτάσεις εφαρμογής:

- *Εφαρμογή της μεθόδου σε προβλήματα πτήσης αιώρησης που αφορούν ελικόπτερα πλήρους κλίμακας*

- *Έλεγχος των επιπτώσεων του εδάφους και του εμποδίου στην ευστάθεια του ελικοπτέρου*

- *Ανάλυση της πτήσης αιώρησης κοντά στο έδαφος/εμπόδιο με συνθήκες ανέμου*

- *Ανάλυση της πτήσης προσγείωσης ελικοπτέρου*

Bibliography

[1] D. Key, "Analysis of army helicopter pilot error mishap data and the implications for handling qualities," *25th European Rotorcraft Forum, Rome*, 199.

[2] A. Visingardi, F. De Gregorio, T. Schwarz, M. Schmid, R. Bakker, S. Voutsinas, Q. Gallas, R. Boisard, G. Gibertini, D. Zagaglia, G. Barakos, R. Green, G. Chirico, and M. Giuni, "Forces on obstacles in rotor wake – A GARTEUR action group," *43rd European Rotorcraft Forum, Milan*, 2017.

[3] G. Gibertini, D. Grassi, C. Parolini, D. Zagaglia, and A. Zanotti, "Experimental investigation on the aerodynamic interaction between a helicopter and ground obstacles," *Proceedings of the Institution of Mechanical Engineers, Part G: Journal of Aerospace Engineering*, vol. 229, no. 8, pp. 1395–1406, 2015.

[4] D. Zagaglia, M. Giuni, and R. B. Green, "Rotor-obstacle aerodynamic interaction in hovering flight: An experimental survey," *Annual Forum Proceedings - AHS International*, vol. 1, pp. 356–364, 2016.

[5] Q. Gallas, R. Boisard, J.-C. Monnier, J. Pruvost, and A. Gilliot, "Experimental and numerical investigation of the aerodynamic interactions between a hovering helicopter and surrounding obstacles," 2017.

[6] J. Tan, Y. Sun, T. Zhou, N. Barakos G, and R. Green, "Simulation of the aerodynamic interaction between rotor and ground obstacle using vortex method," *CEAS Aeronautical Journal*, 2019.

[7] J.-f. Tan and H.-w. Wang, "Simulating unsteady aerodynamics of helicopter rotor with panel/viscous vortex particle method," *Aerospace Science and Technology*, vol. 30, no. 1, pp. 255–268, 2013.

[8] P. Koumoutsakos, A. Leonard, and F. Pepin, "Boundary conditions for viscous vortex methods," *Journal of Computational Physics*, vol. 113, no. 1, pp. 52–61, 1994.

[9] P. Ploumhans, G. Daeninck, and G. Winckelmans, "Simulation of three-dimensional bluff-body flows using the vortex particle and boundary element methods," *Flow, turbulence and combustion*, vol. 73, no. 2, pp. 117–131, 2004.

[10] P. Poncet, "Topological aspects of three-dimensional wakes behind rotary oscillating cylinders," *Journal of Fluid Mechanics*, vol. 517, pp. 27–53, 2004.

[11] J. Yin and S. Ahmed, "Helicopter main-rotor/tail-rotor interaction," *Journal of the American helicopter society*, vol. 45, no. 4, pp. 293–302, 2000.

[12] J. Yin, B. G. van der Wall, and G. A. Wilke, "Rotor aerodynamic and noise under influence of elastic blade motion and different fuselage modeling," in *40th European Rotorcraft Forum (ERF)*, pp. 2–5, 2014.

[13] J. Yin, B. G. van der Wall, and G. A. Wilke, "Investigation of a simplified aerodynamic modelling technique for noise predictions using fw–h propagation," *CEAS Aeronautical Journal*, vol. 7, no. 4, pp. 551–566, 2016.

[14] T. Andronikos, D. Manolas, V. Riziotis, and S. Voutsinas, "Rotorcraft flight in interaction with obstacles," *43rd European Rotorcraft Forum. CEAS, 12–15 September 2017, Milan, Italy*, 2017.

[15] T. Andronikos, G. Papadakis, V. Riziotis, J. Prospathopoulos, and S. Voutsinas, "Validation of a cost effective method for the rotor-obstacle interaction," *Aerospace Science and Technology*, vol. 113, 2021.

[16] S. G. Voutsinas and D. G. Triantos, "Aeroacoustics of full helicopter configurations using vortex particle flow approximation," in *Proceedings of CEAS Forum on Aeracoustics of Rotors and Propellers, Rome, Italy*, pp. 175–91, DTIC Document, 1999.

[17] G. Gibertini, G. Droandi, D. Zagalia, P. Antoniazza, and A. Catelan, "CFD Assessment of the Helicopter and Ground Obstacles Aerodynamic Interference," *42nd European Rotorcraft Forum. ERF, Lille, France, pp. 553–556*, 2016.

[18] M. Biava, "Rans computations of rotor/fuselage unsteady interactional aerodynamics," *Doctor of Philosophy Thesis, Politecnico di Milano, Milano, Italia*, 2007.

[19] G. Barakos, R. Steijl, K. Badcock, and A. Brocklehurst, "Development of cfd capability for full helicopter engineering analysis," in *31st European Rotorcraft Forum*, vol. 2005, pp. 91–1, Council of European Aerospace Soc. Florence, Italy, 2005.

[20] R. Steijl, G. Barakos, and K. Badcock, "A framework for cfd analysis of helicopter rotors in hover and forward flight," *International journal for numerical methods in fluids*, vol. 51, no. 8, pp. 819–847, 2006.

[21] G. Chirico, D. Szubert, L. Vigevano, and G. N. Barakos, "Numerical modelling of the aerodynamic interference between helicopter and ground obstacles," *CEAS Aeronautical Journal*, vol. 8, no. 4, pp. 589–611, 2017.

[22] S. G. Voutsinas, "Vortex methods in aeronautics: How to make things work," *International Journal of Computational Fluid Dynamics*, vol. 20, no. 1, pp. 3–18, 2006.

[23] S. Voutsinas, M. Belessis, and K. Rados, "Investigation of the yawed operation of wind turbines by means of a vortex particle method," in *AGARD CONFERENCE PROCEEDINGS AGARD CP*, pp. 11–11, AGARD, 1995.

[24] A. J. Chorin, "Numerical study of slightly viscous flow," *Journal of Fluid Mechanics*, vol. 57, no. 04, pp. 785–796, 1973.

[25] E. Rivoalen and S. Huberson, "The particle strength exchange method applied to axisymmetric viscous flows," *Journal of Computational Physics*, vol. 168, no. 2, pp. 519–526, 2001.

[26] C. Hirsch, *Numerical Computation of Internal and External Flows*. Wiley, 1990.

[27] R. J. LeVeque, *Finite volume methods for hyperbolic problems*, vol. 31. Cambridge university press, 2002.

[28] B. Cockburn and C.-W. Shu, "Runge–kutta discontinuous galerkin methods for convection-dominated problems," *Journal of scientific computing*, vol. 16, no. 3, pp. 173–261, 2001.

[29] T. A. Zang, C. L. Streett, and M. Y. Hussaini, "Spectral methods for cfd," 1989.

[30] A. Quarteroni and A. Valli, *Domain decomposition methods for partial differential equations*. Oxford Science Publications, 1999.

[31] D. Mavriplis, "Accurate multigrid solution of the Euler equations on unstructured and adaptive meshes," *AIAA Journal*, vol. 28, pp. 213–221, 1990.

[32] Z. Wang, "A fully conservative interface algorithm for overlapped grids," *Journal of Computational Physics*, vol. 122, no. 1, pp. 96–106, 1995.

[33] R. Steijl and G. Barakos, "Sliding mesh algorithm for cfd analysis of helicopter rotor–fuselage aerodynamics," *International journal for numerical methods in fluids*, vol. 58, no. 5, pp. 527–549, 2008.

[34] S. Cavallo, G. Ducci, G. Barakos, and G. Gibertini, "Cfd analysis of helicopter wakes in ground effect," *European Rotorcraft Forum*, 2018.

[35] T. J. Poinsot and S. Lelef, "Boundary conditions for direct simulations of compressible viscous flows," *Journal of computational physics*, vol. 101, no. 1, pp. 104–129, 1992.

[36] G. Papadakis, *Developement of a hybrid compressible vortex particle method and application to external problems including helicopter flows.* PhD thesis, National Techanical University of Athens, School of Mechanical Engineering, 2014.

[37] G. Papadakis and G. Voutsinas, Spyros, "A strongly coupled eulerian lagrangian method verified in 2d external compressible flows," *Computers & Fluids*, vol. 195, 2019.

[38] S. Huberson, E. Rivoalen, and S. Voutsinas, "Vortex particle methods in aeroacoustic calculations," *Journal of Computational Physics*, vol. 227, no. 21, pp. 9216–9240, 2008.

[39] S. G. Huberson and S. G. Voutsinas, "Particles and grid," *Computers & fluids*, vol. 31, no. 4-7, pp. 607–625, 2002.

[40] P. L. Roe, "Approximate riemann solvers, parameter vectors, and difference schemes," *Journal of computational physics*, vol. 43, no. 2, pp. 357–372, 1981.

[41] V. Venkatakrishnan, "On the Accuracy of Limiters and Convergence to Steady State Solutions," *AIAA paper 93-0880*, 1993.

[42] V. Venkatakrishnan, "Convergence to steady state solutions of the euler equations on unstructured grids with limiters," *Journal of computational physics*, vol. 118, no. 1, pp. 120–130, 1995.

[43] P. Spalart and S. Allmaras, "One-Equation Turbulence Model for Aerodynamic Flows," *Recherche Aerospatiale*, pp. 5–21, 1994.

[44] F. Menter, "Zonal Two Equation k-omega Turbulence Models for Aerodynamic Flows," *AIAA Paper 93-2906*, 1993.

[45] A. Jameson, "Time dependent calculations using multigrid, with applications to unsteady flows past airfoils and wings," *AIAA paper*, vol. 1596, p. 1991, 1991.

[46] S. Ghosal, "An analysis of numerical errors in large-eddy simulations of turbulence," *Journal of Computational Physics*, vol. 125, no. 1, pp. 187–206, 1996.

[47] N. Spyropoulos, J. Prospathopoulos, D. Manolas, G. Papadakis, and V. A. Riziotis, "Development of a fluid structure interaction tool based on an actuator line model," *Journal of Physics: Conference Series*, 2020.

[48] P. Jha and S. Schmitz, "Actuator curve embedding–an advanced actuator line model," *Journal of Fluid Mechanics*, vol. 834, 2018.